Development, Validation and Applications of MRI-Only Treatment Planning in Radiotherapy

Tony Young

B.Med.Rad.Phys.(Hons), M.Sc.

A thesis submitted in fulfilment of the requirements for the degree of

Doctor of Philosophy

Faculty of Science

The University of Sydney

2023

Declaration

This is to certify that to the best of my knowledge, the content of this thesis is my own work. This thesis has not been submitted for any degree or other purposes.

I certify that the intellectual content of this thesis is the product of my own work and that all the assistance received in preparing this thesis and sources have been acknowledged.

Information derived from the published and unpublished work of others has been acknowledged in the text with a list of references given at the end of each chapter.

Some chapters have been published in peer-reviewed journals and other chapters are under review for publication. These are noted in the Publications section following.

Tony Young

26/2/2023

Acknowledgements

This thesis has taken 8 years to produce and would not have happened if not for the support from many different people. Firstly, I would like to give my deepest thanks to my supervisory team, Professor David Thwaites, A/Prof Lois Holloway and A/Prof Jason Dowling. To David, you managed to keep me on track even in retirement (extra thanks for keeping me on as a student post retirement!), and I have appreciated all your advice and mentorship throughout - I will take these with me for the rest of my life. To Lois, your strength and resolve have always been an inspiration to me, and I have always valued your ability to maintain clarity of the bigger picture, both within this project and in life. To Jason, your insights were always invaluable, and I will always appreciate the technical advice and interesting discussions throughout these years.

Thank you to all the staff at Liverpool and Macarthur Cancer Therapy Centres, where I have worked full time as a Radiation Oncology Medical Physics Specialist for the entirety of my PhD candidature. A special thanks must go to the Director of Medical Physics, Gary Goozee, for his encouragement and support in undertaking this endeavor whilst employed full time and maintaining a full clinical workload. Thanks to all my colleagues for their support and assistance across many different projects over the years. An additional thanks to all my collaborators across various hospitals, universities, and companies over the years, this work could never have been completed without your help.

Lastly, a huge thank you to my family and friends. To my wife, Thuy, this would never have been completed without your love, support, encouragement, the clearing out of our social calender for months so I could concentrate on thesis writing, and the many meals. To my parents, thank you for always being there for me, and to my sister, Eva, thanks for keeping it real.

Abstract

Magnetic resonance imaging (MRI) has superior soft tissue visualization to guide radiotherapy treatment planning but does not provide the electron density information required for the dose calculation. Thus, MRI has been used in a complementary way, registering to the gold standard computed tomography (CT) scan. Development of methods to allow accurate planning from the MRI images would remove the requirement for additional (CT) scans as well as improve clinical workflow and remove potential registration errors. Various methods have been reported to generate datasets with electron density information from MRI data, with these being termed substitute, synthetic or pseudo CT (sCT) datasets.

This thesis explores the potential variation in planning and optimization error from MRI-only treatment planning for a range of situations. sCT generation was explored with a deep learning methodology applied to a set of retrospective H&N patient data. A lung MRI sequence was investigated for its potential application for sCT generation, with various methods trialed and assessed for clinical suitability. For an existing sCT generation method used clinically for prostate cancer treatment planning, a time-reduced MRI sequence was investigated, optimizing scan parameters for this by initial assessment in a volunteer cohort, followed by clinical validation in a patient cohort. A pancreas MRI volunteer study was also conducted to investigate internal organ motion effects on treatment planning and potential treatment delivery to assess the suitability of adaptive treatment regimes for pancreatic cancer patients using daily MR imaging.

This work provides evidence that MRI-only treatment planning is achievable and acceptably accurate. This has led to current and future implementations of findings into clinical practice locally with the potential for wider implementation. MRI-only treatment planning in radiotherapy could lead to improved patient outcomes, via both improved target delineation and reduced normal tissue toxicity.

Authorship Attribution Statement

This thesis contains work which was been published and prepared for publication. My contributions to the publications and manuscripts are outlined below:

Chapter 3 was published as

Young, T., Thwaites, D., & Holloway, L. (2018). Assessment of electron density effects on dose calculation and optimisation accuracy for nasopharynx, for MRI only treatment planning. *Australasian Physical & Engineering Sciences in Medicine*, *41*(4), 811-820.

I designed the study, performing all treatment planning and data analysis, and prepared the manuscript.

Chapter 6 was published as

Young, T., Dowling, J., Rai, R., Liney, G., Greer, P., Thwaites, D., & Holloway, L. (2021). Effects of MR imaging time reduction on substitute CT generation for prostate MRI-only treatment planning. *Physical and Engineering Sciences in Medicine*, *44*(3), 799-807.

I designed the study, generated all sCT conversions within a pre-existing framework, performed all treatment planning and data analysis, and prepared the manuscript.

Chapter 7 was accepted for publication and is currently in press as

Young, T., Dowling, J., Rai, R., Liney, G., Greer, P., Thwaites, D., & Holloway, L. (2023) Clinical validation of MR imaging time reduction for Substitute/Synthetic CT Generation for Prostate MRI-only Treatment Planning. *Physical and Engineering Sciences in Medicine*, In Press

I designed the study, performed all treatment planning comparisons and data analysis, and prepared the manuscript.

Work from chapter 8 was submitted as a manuscript to Physical and Engineering Sciences in Medicine and is under review. This under review manuscript is as follows:

Young, T., Lee, M., Johnston, M., Nguyen, T., Ko, R., Arumugam, S. (2023) Assessment of Interfraction Dose Variation in Pancreas SBRT Using Daily Simulation MR Images.

I contributed to the design of the study, contributed significantly to generating workflows and completing contouring work, performed all treatment planning and data analysis, and prepared the manuscript.

In addition, work in Chapters 4 and 5, as well as in the above chapters, has been presented in conference contributions and published abstracts (listed below and noted in the chapter preambles). For all first author presentations, I have been responsible for the work in the same way as in the above. For all non-first author contributions, my roles are listed in the relevant chapter preambles.

Tony Young 26/02/2023

As supervisor for the candidature upon which this thesis is based, I can confirm that the authorship attribution statements above are correct.

David Thwaites

Table of Contents

List of Tables

List of Figures

Research Publications, Presentations and Awards

Publications related to this work during my candidature

Young, T., Thwaites, D., & Holloway, L. (2018). Assessment of electron density effects on dose calculation and optimisation accuracy for nasopharynx, for MRI only treatment planning. *Australasian Physical & Engineering Sciences in Medicine*, *41*(4), 811-820.

Young, T., Dowling, J., Rai, R., Liney, G., Greer, P., Thwaites, D., & Holloway, L. (2021). Effects of MR imaging time reduction on substitute CT generation for prostate MRI-only treatment planning. *Physical and Engineering Sciences in Medicine*, *44*(3), 799-807. Awarded the Kenneth Clarke Journal Award 2022

Young, T., Dowling, J., Rai, R., Liney, G., Greer, P., Thwaites, D., & Holloway, L. (2023) Clinical validation of MR imaging time reduction for Substitute/Synthetic CT Generation for Prostate MRI-only Treatment Planning. *Physical and Engineering Sciences in Medicine*, In Press

Young, T., Lee, M., Johnston, M., Nguyen, T., Ko, R., Arumugam, S. (2023) Assessment of Interfraction Dose Variation in Pancreas SBRT Using Daily Simulation MR Images. *Physical and Engineering Sciences in Medicine, Under Review*

Greer, P., Martin, J., Sidhom, M., Hunter, P., Pichler, P., Choi, J.H., Best, L., Smart, J., **Young, T.**, Jameson, M. and Afinidad, T., (2019) A multi-center prospective study for implementation of an MRI-only prostate treatment planning workflow. *Frontiers in Oncology*, *9*, p.826.

Presentations/Published abstracts related to this work during my candidature

Young, T., Thwaites, D., & Holloway, L., Assessment of Electron Density Effects for MRI Only Treatment Planning. Poster presentation at EPSM 2016 Abstract: *Australasian Physical & Engineering Sciences in Medicine* (2016) 39, 1187

Young, T., Thwaites, D., Dowling, J., Liney, G., Rai, R., Greer, P. and Holloway, L., The Effect of MRI Sequence Variations on Substitute CT Generation for MR-Only Planning. Poster presentation at EPSM 2017 Abstract: *Australasian Physical & Engineering Sciences in Medicine* (2018) 41, 355

Young, T., Dowling, J., Thwaites, D., Kumar, S., Rai, R., Vinod, S., Liney, G., Stemmer, A., Josan, S., Holloway, L., MRI-Only Treatment Planning for Lung Cancer Using a Single MRI Sequence. Oral presentation at EPSM 2018 Abstract: *Australasian Physical & Engineering Sciences in Medicine* (2019) 42: 362-363

Greer, P., Pichler, P., Young, T., Martin, J., Hunter, P., Wratten, C., Denham, J., Holloway, L., Sidhom, M. and Dowling, J., A multi-centre study for implementation of MRI-only prostate planning. Poster presentation at ESTRO 38, 2019 Abstract: *Radiotherapy and Oncology*, *133*, pp.S224-S225.

Young, T., Dowling, J., Rai, R., Liney, G., Greer, P., Thwaites, D. and Holloway, L., Can we reduce imaging time and still generate acceptable Substitute CT for Prostate MRI Only Treatment Planning? Poster presentation at EPSM 2020 Abstract: *Physical and Engineering Sciences in Medicine* (2021) 44, 979

Antunes, J., Pittock, D., Jacobs, P., Nelson, A., Piper, J., Young, T. and Deshpande, S., Deep Learning for MRI-Generated Synthetic CT: Dosimetric Evaluation for RT Planning in Head and Neck Cancers. Poster presentation at AAPM 2022. Abstract: *Medical Physics* 49, (6), pp. E717-E717

Antunes, J., Pittock, D., Jacobs, P., Nelson, A., Piper, J., Young, T. and Deshpande, S., Assessing Multiple MRI sequences in Deep Learning-Based Synthetic CT Generation for MR Only-Guided Radiation Therapy of Head and Neck Cancers. Poster presentation at ASTRO 2022. Abstract: *International Journal of Radiation Oncology, Biology, Physics*, *114*(3), p.e553.

Antunes, J., Pittock, D., Jacobs, P., Chatterjee, K., Nelson, A., Piper, J., Young, T. and Deshpande, S., Comparison of synthetic CTs derived from 2D versus 3D convolutional neural networks via Head and Neck MRIs for RT planning. Oral presentation at EPSM 2022. Abstract: To be published in *Physical and Engineering Sciences in Medicine*

Young, T., Lee, M., Johnston, M., Nguyen, T. Ko, R., Arumugam, S., Dose Variation in Pancreas SBRT – A planning study based on daily MR imaging. Poster presentation at EPSM 2022, awarded EPSM 2022 Best Therapy Poster Prize. Abstract: To be published in *Physical and Engineering Sciences in Medicine*

Awards related to this work during my candidature

EPSM 2022 Best Therapy Poster Prize (awarded by ACPSEM)

Kenneth Clarke Journal Award 2022 for the best paper on original work published in the Australasian Physical and Engineering Sciences in Medicine authored by a member of the ACPSEM in 2021 (awarded by Physical and Engineering Sciences Editorial Board)

Ethics Approvals Related to Work

Work presented in this thesis utilises both volunteer and patient data. As such, appropriate ethics approvals were required for collection and use of this data. The following is a list of ethics approvals relevant to work presented in this thesis. These approvals were granted by the South Western Sydney Local Health District Human Research Ethics Committee.

HREC/13/LPOOL/258 – Quantifying the Clinical Benefit of MRI in Lung Cancer

HREC/15/LPOOL/506 – Magnetic Resonance Imaging in healthy volunteers

HREC/16/LPOOL/41 – Use of multiparametric MRI and FDG PET-CT to evaluate radiological changes after lung stereotactic ablative radiotherapy (SABR)

HREC/18/LPOOL/420 – The NINJA Clinical Trial: Novel Integration of New prostate radiation schedules with adjuvant Androgen deprivation

HREC/2020/ETH01940 – Development of Substitute CT Generation for MRI Only Radiotherapy Planning

1 Introduction and Scope of Work

1.1 Introduction

The use of Magnetic Resonance Imaging (MRI) in radiotherapy has increased over recent years from its beginnings in the 1970s. Since the first MRI images were taken [1, 2], the potential use of MRI in cancer was explored [3]. Computed Tomography (CT) and x-ray imaging have been the mainstay in radiotherapy for disease detection, treatment planning and patient setup and positioning with bony anatomy for many years, however MRI brings some advantages over these modalities. These include providing improved soft tissue definition, as well as potentially providing physiological and biochemical information from magnetic resonance (MR) angiography and spectroscopy [4]. Also, MRI has no radiation dose associated with it as compared to x-ray based imaging, so patients may be scanned multiple times before and after treatment without any concern about imaging dose. These advantages have led to increasing use of MRI images in radiotherapy, initially from diagnostic MRI scanners to aid in treatment planning decisions [4, 5], to the introduction of dedicated MRI scanners, termed MRI-simulators, installed in radiation oncology departments [6-8] and most recently to the development and clinical/commercial availability of hybrid MRI-guided linear accelerators (MRIg-linacs) [9-12].

An MRI-simulator is similar to a CT-simulator, incorporating the additional features that distinguish a radiotherapy CT-simulator from a diagnostic CT scanner, such as external lasers and an indexable flat table top. In addition to these, the dedicated MRI-simulators further differ from diagnostic MRI scanners by incorporating optimised scanning protocols, contrast use, fiducial markers, immobilisation devices and specialised MRI coil placements when required [6, 13-15]. A hybrid MRIg-linac is an in-treatment-room MRI scanner for image guidance combined with a linear accelerator treatment delivery system, providing direct MRI-guided radiotherapy (MRIgRT) including MRI-guided adaptive radiotherapy. The integration of the additional 3D imaging information from MRI into the treatment workflow can provide improved imaging of target and organs at risk and hence greater consistency and accuracy in their delineation [16, 17], as well as the potential for applying radiotherapy in situations where poor imaging might have made radiotherapy use difficult before [18, 19]. MRI use in treatment planning and in adaptive radiotherapy, where a patient's treatment is adapted due to changes in anatomy, position, respiration, motion or setup variations over their time of treatment [20], can bring these advantages through to treatment dosimetry and delivery [21-23]. In addition, the functional imaging capability of MRI holds out promise for biologically-guided and adaptive radiotherapy, allowing new approaches to treatment [24, 25].

MRIg-linacs have been identified as an ideal tool for online adaptive radiation therapy [26, 27], allowing the potential to adapt treatment plans daily. Prior to plan adaptation, adaptive radiation therapy requires precise image guidance and dose verification [20, 28-30]. This has increased the need for accurate image

registration techniques, including non-rigid or deformable image registration (DIR). These enable accurate dose accumulation, summing the dose delivered to the patient over time, to verify the dose received by the patient to guide the plan adaptation required.

However, there are some problems for the use of MRI imaging as the basis of radiotherapy planning and guidance as compared to CT imaging. CT imaging is the current gold standard in radiotherapy, since it provides accurate anatomical definition and bony anatomy, and also directly provides the electron density information which is required for treatment planning calculations. MRI potentially has less accurate geometry (from intrinsic system related and object induced image distortion), does not image bony anatomy well and does not provide electron density information [4, 31].

Due to this, the use of MRI in radiotherapy has more commonly been as a complementary imaging modality to CT imaging. MRI images in radiotherapy have routinely been registered to CT images, a process overlaying one set of images to the other, to gain the advantages of MRI imaging, but also to utilise CT images for treatment planning. However this requires both images to be acquired, needing more resources and a more complicated workflow, and can introduce registration errors due to the possible variation in patient setup and internal organ motion [32]. Increasingly, with the use of MR-simulators and MRIg-linacs, there is a need to be able to use only MRI images for treatment planning and image guidance during treatment, otherwise termed MRI-only radiotherapy [33]. This has required the development of substitute, pseudo, or synthetic CTs (sCT) to be generated, utilising MRI to generate an image which has the electron density information required to enable MRI-only treatment planning [34, 35]. However, this is a recent development, tested only for some anatomical treatment sites and still requiring significant research for development, validation and implementation for widespread clinical use.

1.2 Thesis Motivation

The motivation for this thesis came from working in a radiotherapy centre where MRI had recently been implemented (in 2013) in the form of an MRI-simulator, and where an MRIg-linac, which is now known as the Australian MR-linac project, was in development. Considering these, the increased utilisation of MRI within the centre was a priority. The implementation of MRI-only radiotherapy was seen as part of the future, with work required in the development, implementation and validation of this technique within a clinical setting. The part-time student research work for this thesis began in early 2015.

Additionally, adaptive radiotherapy, as above, is a natural progression in the radiotherapy process. The use of MRI in an adaptive radiotherapy setting is considered a necessity for certain anatomical treatment sites where the additional contrast from MRI is invaluable for accurate delineation of both target and

organs at risk over the course of treatment and contributes to the increased utilisation of MRI within the centre [26, 27].

This work was motivated by a need for tools to allow accurate treatment planning using MRI-only, and to allow online adaptation of these MRI-only treatment plans for an MRIg-linac in a consistent MRI-only radiotherapy environment.

1.3 Aims of Work

This thesis considers the development, application, and validation of MRI use in radiotherapy, with work ranging from development to clinical validation of MRI-only treatment planning for different anatomical treatment sites and application of MRI and MRI-only treatment planning for adaptive radiotherapy.

The research questions considered in this thesis were identified through the growing interest in MRI utilisation within radiotherapy centres. This work aims to broaden the scope of MRI utilisation in radiotherapy, with MRI-only radiotherapy putting MRI at the forefront of diagnosis, treatment planning, and treatment guidance in the form of MRIg-linacs in radiotherapy.

This work aims in general terms to explore some aspects of the development, clinical validation and translation, and application of MRI-only treatment planning for a range of anatomical treatment sites, where the specific aims are detailed in the chapter outlines below.

1.4 Thesis Outline

The chapters of this thesis present work which has been undertaken either for the development of MRI-only radiotherapy, or for the validation of this technique.

Chapter 2 presents a literature review and background to the work presented, especially in regards to MRI use in radiotherapy, and adaptive radiotherapy, for which MRI-only could play a greater role. It includes further details on all the topics introduced briefly in the Introduction section above. Additional specific literature reviews and discussion are presented in each chapter individually.

Chapter 3 presents initial MRI-only work in the head and neck region. The aim of this work was to investigate the effect of incorrect bulk density correction on treatment planning, and plan optimisation. This chapter was published in the journal Physical and Engineering Sciences in Medicine.

Chapter 4 presents clinical validation of a deep learning sCT generation method for head and neck radiotherapy, comparing the sCT generated to both the ground truth CT as well as a CT which has utilised DIR to deform to the MRI. This testing was conducted with MRI data which was not part of

the training cohort. The aim of this work was to validate the sCT technique for radiotherapy treatment planning in a clinical environment, following on from the preliminary previously reported results in work that the current author was involved in [36, 37].

Chapter 5 presents an investigation into sCT generation for lung cancer with a single MRI sequence, with bulk density methods, an atlas based method and a Gaussian Mixture Model (GMM) method attempted with this MRI data. Additionally, different bone models were considered with these methods. The Siemens SpiralVIBE sequence, a Works in Progress (WIP) sequence, was assessed in this study for appropriateness for sCT generation. The aim of this work was to investigate sCT generation using this single sequence for lung cancer, and to assess the suitability of this sequence for sCT generation.

Chapter 6 considers the time reduction of a standard MRI sequence used for sCT generation for prostate cancer patients, with multiple time-reduced sequences tested within a volunteer study. The sCT generated with the time-reduced sequences were compared to the sCT generated with the original standard sequence in terms of anatomical and dosimetric results. The aim of this work was to reduce the time required for an MRI sequence and hence to reduce the potential effect of patient and organ motion, and to investigate the effect on sCT generation in prostate cancer. This chapter was published in the journal Physical and Engineering Sciences in Medicine.

Chapter 7 follows up on the work presented in chapter 6, with the most ideal time-reduced sequence from the volunteer study introduced into a patient study within a clinical trial for real-world clinical validation. The sCTs generated from the time-reduced sequence were tested in a patient cohort against the sCT generated with the standard MRI sequence for anatomical and dosimetric differences. The aim of this study was the clinical validation of the selected time-reduced MRI sequence for sCT generation for clinical translation. This chapter has been submitted to the journal Physical and Engineering Sciences in Medicine and a revision is currently under review.

Chapter 8 presents a study which considers the use of MRI for daily adaptive planning for pancreas stereotactic body radiotherapy (SBRT) treatments. This volunteer study simulated a potential 5 fraction treatment, with volunteers scanned twice a day for 5 days over a 2 week period, with the first scan of the day simulating a daily simulation scan, and the second scan of the day simulating a pre treatment scan. The aim of this study was to investigate the variability of target and OAR volumes for different treatment planning regimens for pancreatic cancer. Part of this aim was to study the potential for a daily MRI simulation scan to be used for adaptive treatment planning purposes prior to treatment on a conventional linac, particularly in the absence of a MRIg-linac, for clinical translation. A secondary aim was to investigate the differences in dose accumulation techniques available utilizing MRI-only treatment planning. Work from this chapter has been prepared for publication.

Chapter 9 summarises the work presented, discussing the main findings of the work. Future directions and further work resulting from that presented is also discussed.

1.5 References

[1] Lauterbur PC. Image formation by induced local interactions: examples employing nuclear magnetic resonance. Nature. 1973;242:190-1.

[2] Mansfield P, Maudsley AA. Medical imaging by NMR. The British Journal of Radiology. 1977;50:188-94.

[3] Damadian R. Tumor detection by nuclear magnetic resonance. Science. 1971;171:1151-3.

[4] Khoo VS, Dearnaley DP, Finnigan DJ, Padhani A, Tanner SF, Leach MO. Magnetic resonance imaging (MRI): considerations and applications in radiotherapy treatment planning. Radiotherapy and Oncology. 1997;42:1-15.

[5] Moerland MA. Magnetic resonance imaging in radiotherapy treatment planning. Medical Physics. 1997;24:336-.

[6] Devic S. MRI simulation for radiotherapy treatment planning. Medical Physics. 2012;39:6701-11.

[7] Liney G, Owen S, Beaumont A, Lazar V, Manton D, Beavis A. Commissioning of a new wide-bore MRI scanner for radiotherapy planning of head and neck cancer. The British Journal of Radiology. 2013;86.

[8] Paulson ES, Erickson B, Schultz C, Li XA. Comprehensive MRI simulation methodology using a dedicated MRI scanner in radiation oncology for external beam radiation treatment planning. Medical Physics. 2015;42:28-39.

[9] Lagendijk JJW, Raaymakers BW, Raaijmakers AJE, Overweg J, Brown KJ, Kerkhof EM, et al. MRI/linac integration. Radiotherapy and Oncology. 2008;86:25-9.

[10] Fallone BG. The Rotating Biplanar Linac–Magnetic Resonance Imaging System. Seminars in Radiation Oncology. 2014;24:200-2.

[11] Keall PJ, Barton M, Crozier S. The Australian Magnetic Resonance Imaging–Linac Program. Seminars in Radiation Oncology. 2014;24:203-6.

[12] Mutic S, Dempsey JF. The ViewRay System: Magnetic Resonance–Guided and Controlled Radiotherapy. Seminars in Radiation Oncology. 2014;24:196-9.

[13] Glide-Hurst CK, Paulson ES, McGee K, Tyagi N, Hu Y, Balter J, et al. Task group 284 report: magnetic resonance imaging simulation in radiotherapy: considerations for clinical implementation, optimization, and quality assurance. Medical Physics. 2021;48:e636-e70.

[14] Paulson ES, Erickson B, Schultz C, Allen Li X. Comprehensive MRI simulation methodology using a dedicated MRI scanner in radiation oncology for external beam radiation treatment planning. Medical Physics. 2015;42:28-39.

[15] Karlsson M, Karlsson MG, Nyholm T, Amies C, Zackrisson B. Dedicated Magnetic Resonance Imaging in the Radiotherapy Clinic. International Journal of Radiation Oncology*Biology*Physics. 2009;74:644-51.

[16] Haie-Meder C, Pötter R, Van Limbergen E, Briot E, De Brabandere M, Dimopoulos J, et al. Recommendations from Gynaecological (GYN) GEC-ESTRO Working Group☆(I): concepts and terms in 3D image based 3D treatment planning in cervix cancer brachytherapy with emphasis on MRI assessment of GTV and CTV. Radiotherapy and Oncology. 2005;74:235-45.

[17] Khoo V, Joon D. New developments in MRI for target volume delineation in radiotherapy. The British Journal of Radiology. 2006;79:S2-S15.

[18] Heerkens HD, Hall W, Li X, Knechtges P, Dalah E, Paulson E, et al. Recommendations for MRI-based contouring of gross tumor volume and organs at risk for radiation therapy of pancreatic cancer. Practical Radiation Oncology. 2017;7:126-36.

[19] Ahmed M, Schmidt M, Sohaib A, Kong C, Burke K, Richardson C, et al. The value of magnetic resonance imaging in target volume delineation of base of tongue tumours–a study using flexible surface coils. Radiotherapy and Oncology. 2010;94:161-7.

[20] Yan D, Vicini F, Wong J, Martinez A. Adaptive radiation therapy. Physics in Medicine & Biology. 1997;42:123.

[21] Metcalfe P, Liney GP, Holloway L, Walker A, Barton M, Delaney GP, et al. The potential for an enhanced role for MRI in radiation-therapy treatment planning. Technol Cancer Res Treat. 2013;12:429-46.

[22] Dirix P, Haustermans K, Vandecaveye V. The Value of Magnetic Resonance Imaging for Radiotherapy Planning. Seminars in Radiation Oncology. 2014;24:151-9.

[23] Acharya S, Fischer-Valuck BW, Kashani R, Parikh P, Yang D, Zhao T, et al. Online magnetic resonance image guided adaptive radiation therapy: first clinical applications. International Journal of Radiation Oncology* Biology* Physics. 2016;94:394-403.

[24] Van der Heide UA, Houweling AC, Groenendaal G, Beets-Tan RG, Lambin P. Functional MRI for radiotherapy dose painting. Magnetic Resonance Imaging. 2012;30:1216-23.

[25] Hunt A, Hansen V, Oelfke U, Nill S, Hafeez S. Adaptive radiotherapy enabled by MRI guidance. Clinical Oncology. 2018;30:711-9.

[26] Winkel D, Bol GH, Kroon PS, van Asselen B, Hackett SS, Werensteijn-Honingh AM, et al. Adaptive radiotherapy: the Elekta Unity MR-linac concept. Clinical and Translational Radiation Oncology. 2019;18:54-9.

[27] Hall WA, Paulson E, Li XA, Erickson B, Schultz C, Tree A, et al. Magnetic resonance linear accelerator technology and adaptive radiation therapy: An overview for clinicians. CA Cancer J Clin. 2022;72:34-56.

[28] Yan D. Treatment strategy for daily image feedback adaptive radiotherapy. The Use of Computers in Radiation Therapy: Springer; 2000. p. 518-20.

[29] Wu QJ, Li T, Wu Q, Yin F-F. Adaptive Radiation Therapy: Technical Components and Clinical Applications. The Cancer Journal. 2011;17:182-9.

[30] Brock K. Adaptive Radiotherapy: Moving Into the Future. Seminars in Radiation Oncology: WB Saunders Ltd; 2019. p. 181-4.

[31] Walker A, Liney G, Metcalfe P, Holloway L. MRI distortion: considerations for MRI based radiotherapy treatment planning. Australas Phys Eng Sci Med. 2014;37:103-13.

[32] Nyholm T, Jonsson J. Counterpoint: Opportunities and Challenges of a Magnetic Resonance Imaging–Only Radiotherapy Work Flow. Seminars in Radiation Oncology. 2014;24:175-80.

[33] Nyholm T, Jonsson J. Counterpoint: opportunities and challenges of a magnetic resonance imaging–only radiotherapy work flow. Seminars in Radiation Oncology: Elsevier; 2014. p. 175-80.

[34] Edmund JM, Nyholm T. A review of substitute CT generation for MRI-only radiation therapy. Radiation Oncology. 2017;12:28.

[35] Owrangi AM, Greer PB, Glide-Hurst CK. MRI-only treatment planning: benefits and challenges. Physics in Medicine & Biology. 2018;63:05TR1.

[36] Antunes J, Pittock D, Jacobs P, Nelson A, Piper J, Young T, et al. Assessing Multiple MRI Sequences in Deep Learning-Based Synthetic CT Generation for MR Only-Guided Radiation Therapy of Head and Neck Cancers. International Journal of Radiation Oncology, Biology, Physics. 2022;114:e553.

[37] Antunes J, Pittock D, Jacobs P, Nelson A, Piper J, Young T, et al. Deep Learning for MRI-Generated Synthetic CT: Dosimetric Evaluation for RT Planning in Head and Neck Cancers. Medical Physics. 2022;49:E717.

2 Background

2.1 Cancer and the Role of Radiotherapy

Cancer remains a leading cause of premature death globally [1], with the International Agency for Research on Cancer's GLOBOCAN 2020 report estimating 19.3 million new cancer cases and almost 10 million cancer deaths occurred in 2020 worldwide [2]. The global cancer burden is rapidly increasing, which is linked to population growth and the advancing age of the population, both of which are associated with socioeconomic development [2, 3].

Cancer is a large group of diseases that can affect any part of the body. Cancer is a disease in which abnormal cells are rapidly created and grow beyond their usual boundaries, able to invade adjoining parts of the body and can spread to other organs via the lymphatic system or blood vessels [4]. Treatment options for cancer can include surgery, chemotherapy or radiotherapy, or a combination of these options, including more recently the combination of radiotherapy with immunotherapy [5]. Radiotherapy is recommended to be utilised in approximately 50% of all cancers [6, 7].

Radiotherapy, or radiation therapy (RT), is the clinical process of using radiation for the treatment of disease, most commonly cancer. Radiotherapy aims to deliver an accurate dose of radiation to a well-defined target volume whilst minimizing dose to healthy normal tissue. The goals of radiotherapy are to eradicate disease, prolong life and/or to improve the quality of life [8].

Modern radiotherapy is a multi-disciplinary process, with the majority of radiotherapy treatments delivered by external beam radiation therapy (EBRT) using linear accelerators (linacs). These treatments are fractionated, that is a fraction of the total dose is delivered per treatment, with treatments over the number of days (or fractions) required to deliver the total dose. Fractionation aims to create a therapeutic window by leveraging differences in radiobiological characteristics between cancers and normal tissue, utilizing normal tissue's superior DNA repair capacity between fractions [9]. The radiotherapy process includes imaging for simulation of treatment, treatment planning and treatment delivery. A simple flowchart of the radiotherapy process from Chandarana et al. [10] is shown in figure 2.1.

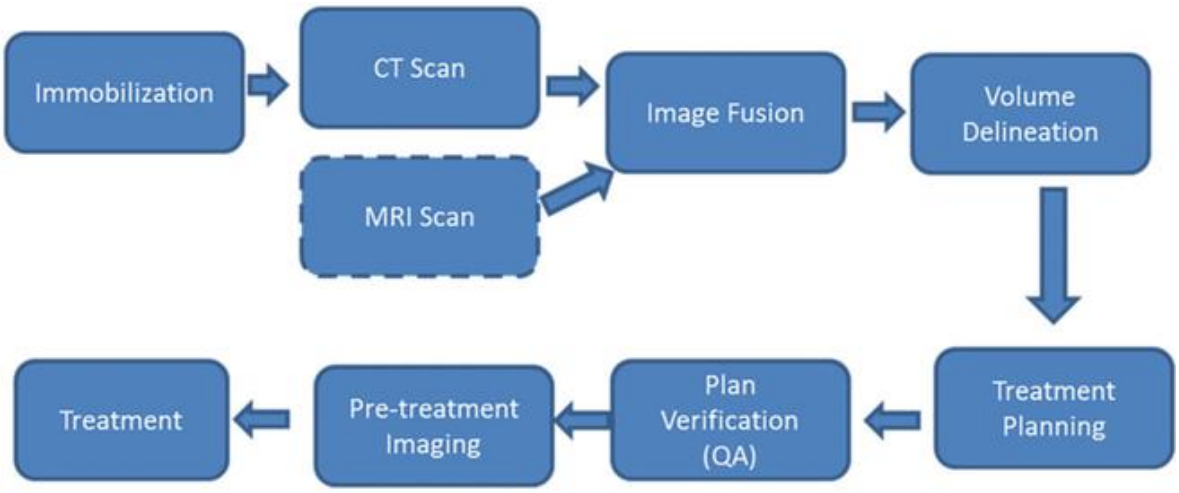

Figure 2.1 - Radiotherapy Simulation, Treatment Planning and Delivery Workflow (from Chandarana et al. [10], with permission from John Wiley and Sons)

The patient simulation process includes the immobilization, simulation imaging (CT and/or MRI), image fusion and volume delineation aspects. Immobilization refers to tools or devices used on the patient to ensure consistent daily patient setup. Simulation imaging is currently almost always computed tomography (CT), though magnetic resonance images (MRI) may also be taken and registered or fused to the CT images, a process of overlaying and matching these scans. The tumour and other target volumes, such as nodal volumes, will be delineated on these scans in addition to nearby organs at risk (OARs) which may need to be accounted for during the treatment planning process to ensure doses received are minimal and acceptable. Treatment delivery from the linac usually utilises multi leaf collimators (MLCs) to create treatment beam shapes and apertures as required. Treatment delivery may utilise 3D conformal radiation therapy (3D-CRT), Intensity Modulated Radiation Therapy (IMRT) or Volumetric Modulated Arc Therapy (VMAT). 3D-CRT involves treatment using static beams of radiation shaped to the target, incident from a few directions. IMRT also uses beams from fixed directions, however the MLCs are used to create multiple apertures over the delivery of the static beam to vary the intensity of the radiation across the beam, creating complex but conformal dose profiles. VMAT combines the use of the varying apertures using the MLCs in conjunction with a rotation of the beam around the patient to deliver dose dynamically with more degrees of freedom [11]. The workflow presented in figure 2.1 may also incorporate a feedback process, where the treatment planning process reoccurs between treatments to adapt treatment plans to variations in target and neighbouring structures [12]. This has been termed adaptive radiotherapy, and may be an online or offline process, either occurring during the patient treatment or between treatment fractions.

Considering the aim of radiotherapy, a fundamental problem is the optimisation between delivering as high a dose as possible into all of the tumour/target volume, with as conformal as possible high dose

distributions, without exceeding the tolerance of nearby healthy tissues, particularly those termed OARs. This problem is different for each patient, as tumours vary in size and location between patients, as well as each patient's individual anatomy. Due to this, geometric and dosimetric precision and accuracy are critical for all aspects of the radiotherapy process. This has led to research into many different aspects of the radiotherapy process, including improved imaging methods for better delineation of targets and OARs for treatment planning, sophisticated plan optimisation and dose calculation algorithms for accurate treatment planning, more complex treatment delivery techniques to achieve better conformality and improved imaging at the point of treatment for verification and adaptation [13]. The use of MRI in radiotherapy has been one such recent development, with applications which range from imaging to guide tumour and OAR delineation, to a pre treatment imager in conjunction with a linac to produce the ultimate adaptive radiotherapy treatment machine. The utility of MRI alone for treatment planning may provide the key to an optimised adaptive radiotherapy process with these newly developed treatment machines and techniques.

2.2 MRI in Radiotherapy

The use of MRI in radiotherapy has increased over recent years. Where CT and x-ray imaging has been a mainstay in radiotherapy for disease detection, treatment planning and patient setup and positioning with bony anatomy for many years, MRI has advantages over these imaging modalities. These include providing improved soft tissue definition as well as physiological and biochemical information potentially being provided with magnetic resonance (MR) angiography and spectroscopy [14]. The integration of the additional 3D imaging information from MRI into the treatment diagnosis workflow has provided greater consistency and accuracy in delineation of tumours and organs at risk in radiation oncology treatment planning [15, 16]. Among the different MRI techniques, there are techniques available which are able to provide physiological and pathological information, such as functional MRI (fMRI), diffusion weighted imaging (DWI) and perfusion weighted imaging (PWI) [17, 18]. Considering DWI in lung, this technique has the potential to provide further information on the state of tumours and their response to treatment [19, 20]. Lastly, as MRI has no radiation dose associated with it as compared to CT scans and x-ray imaging, patients may be scanned a number of times before and after treatment without increasing the risk of secondary cancers, providing the clinician the ability to assess treatment at any time. CT imaging however is the current gold standard in radiotherapy, providing accurate anatomical definition and bony anatomy, as well as providing the electron density information which is required for treatment planning calculations.

MR images are a function of proton densities and tissue relaxation times, with the major source of contrast in clinical MRI being the difference in relaxation times between different tissue types. These contrasts can be due to either proton density (PD), or two characteristic times called spin lattice

relaxation time (T1) or spin-spin relaxation time (T2) weighted. PD is related to the number of hydrogen atoms in a particular volume whereas T1 and T2 depend on the characteristics of different tissues. Fluids have long T1s, and fat based tissues usually have short T1s. T2 is always shorter than T1 for a given tissue. Considering images which focus on each of these contrast mechanisms, in PD images, high PDs produce high signal intensities in the image, while in T2 weighted images, long T2 tissues produce the highest signal intensity, whereas in T1 weighted images long T1 tissues produce the weakest signal, with short T1 signals producing the bright pixels in the image [21]. Common sequences utilised in radiotherapy include VIBE (volumetric interpolated breath hold examination), SPACE (sampling perfection with application optimised constraints using different flip angle evolution) and Dixon sequences. The VIBE sequence produces high resolution images within a 30 second breath hold [22]. The SPACE sequence was developed by Siemens (known as VISTA or CUBE for Philips or GE MRI scanners) and is able to produce 3D isotropic (having the same resolution in all planes) images with good anatomical detail and high spatial resolution [23, 24]. The Dixon sequence utilises the chemical shift between protons of water and fat, generating four types of images from a single Dixon sequence scan – an in-phase image, an out of phase image, water images and fat images [25, 26].

However, MRI has poor imaging of bone and also does not provide any electron density information which is required for dosimetry calculations in current radiotherapy treatment planning systems. MRI has also struggled to challenge CT in radiotherapy due to the presence of intrinsic system-related and object-induced MR image distortions, and the difficulty in integrating and manipulating MR images within radiotherapy treatment planning systems [14].

The advantages of MRI for soft tissue definition and the benefits of MRI-only radiotherapy have been increasingly discussed [27-29]. This has resulted in the development of substitute, pseudo, or synthetic CT (sCT) generation methods, utilising MRI to generate an image which has the electron density information required for radiotherapy dose calculations, which has enabled MRI-only treatment planning. In addition to this, the advantages of MRI have also led to MRI guided linear accelerators (MRIg-linac) being developed and now commercially available, utilising the soft tissue definition and varied contrasts available with MRI for patient setup, target and OAR definition and guidance at radiotherapy treatment [30]. The MRIg-linac provides the means to undertake real time adaptive radiotherapy and offers additional tools which may eventually enable real time tumour tracking and treatment.

2.3 Radiotherapy Simulation

All radiotherapy patients will undergo a simulation session prior to the start of treatment. This may also be referred to as virtual simulation, as this simulation session establishes their treatment position and setup references, as well as required imaging, which represents the "virtual" patient, for radiotherapy treatment planning to occur. Most commonly, CT-simulators are used in radiotherapy. CT images have been the gold standard for radiotherapy treatment planning imaging, providing accurate anatomical information and bony anatomy. The main differences of radiotherapy CT-simulators, when compared to diagnostic CT scanners, are related to the requirements for patient positioning and immobilization, treatment specific scan protocols, increased scan limits, contrast use, placement of localization marks on patient skin, and additional scans to account for motion, i.e. 4D-CT [31].

CT-simulators have different requirements compared to diagnostic CT scanners [31-33]. CT simulators have flat table tops which match the radiotherapy treatment machines, rather than the curved couch tops seen on diagnostic CT. These flat table tops also enable accurate indexing and allow commercially available immobilization devices to be attached, which mirror the treatment machine table top features. External positioning lasers, with a moveable sagittal laser, will also be present with the CT-simulator, allowing positioning of the patient to ensure they are well aligned with no rotation, as well as easier markup of patients for reproducible setup on the treatment machines. As the entire patient external anatomy is required for treatment planning purposes, large bore CT scanners are ideal for use as CT-simulators.

Conventional radiotherapy treatment planning systems (RTPS) currently require a CT dataset for treatment planning dose calculations [34]. The CT-simulator will have a CT number to electron density conversion which may be applied to the corresponding CT images which the dose algorithm will utilize for dose calculations. This CT is also used for volume delineation and generation of the digital reconstructed radiograph (DRR) images which may be used on the linear accelerator as reference images for portal imaging. More commonly, the CT images are used as the reference images to match cone beam CT (CBCT) of the patients each treatment day on conventional linacs [35, 36].

The potential for the use of MRI in radiotherapy has been published and investigated from the 1990s [14, 37]. MRI is used to complement existing CT images, providing additional information used to outline the tumour volume and organs at risk, as well as being able to provide additional information on the movement of mobile organs and tissues in the presence of physiological motion. These additional MR images are fused or registered, a process overlaying and matching images, to the CT scan, with these combined datasets providing the data required for both accurate delineation (MRI) and for dose calculations (CT). However this can introduce registration error, and also results in potential errors due to the possible variation in patient setup and internal organ motion [38].

2.3.1 Dedicated MRI-simulators for Radiotherapy

Dedicated MRI scanners, termed MRI-simulators, for radiotherapy have recently become available in some radiotherapy treatment centres. These dedicated MRI-simulators incorporate the additional features which distinguish a radiotherapy CT-simulator from a diagnostic CT scanner, such as external lasers and an indexable flat table top. In addition to these, the dedicated MRI-simulators further differ from diagnostic MRI scanners by incorporating optimised scanning protocols, specialised contrast use, fiducial markers, immobilisation devices and specialised MRI coil placements when required [39-42].

The increased availability of dedicated MRI-simulators has increased the role of MRI in radiotherapy [43]. The use of external lasers and indexable flat table top, in addition to scanning patients in their treatment position with immobilisation devices present, ensures the accuracy of the MRI scan for registration with the patient's CT scan. In addition to this, optimising MRI sequence protocols to ensure geometric accuracy by reducing geometric distortions and patient artefacts where possible, and the appropriate use and placement of MRI coils for imaging, such as utilising coil bridges and mounts, will ensure patient anatomy is not deformed, further improving registration accuracy [40].

Though there are many difficulties in implementing dedicated MRI simulators in radiotherapy, many studies have taken place which demonstrate that MRI scanners both complement, and have the potential to replace, CT scanners in the radiotherapy process [44-49]. Various studies have demonstrated the potential for MRI-only radiotherapy, with MRI replacing CT use at simulation and tools available for MRI-only treatment planning and reference images available for use for patient setup at treatment on conventional linear accelerators, or even potentially matching with MRI on MRIg-linacs. Edmund et al. [50] conducted a study into the use of CBCT with MRI or CT as reference data. This study has a view on the future of MRI-only radiotherapy, looking at the image guidance impact when MRI is used as reference image data. A comparison was made between using CBCT for patient positioning in MRI-only image guided radiotherapy, and verifying how well this matched a pseudo CT (sCT) generated from MRI datasets, a T1-weighted MRI dataset and the reference CT dataset. From this study, it was seen that there were no significant differences in the pooled CT-CBCT, MRI-CBCT and sCT-CBCT transformations, with maximum deviations of 1 mm and 1 degree. This study concluded that a satisfactory registration between a CBCT and an MRI or sCT can be made without any systematic changes in the transformation directions as compared to a standard CT-CBCT match.

2.4 Radiotherapy Treatment Planning

Computerized systems were introduced in the 1970s, improving accuracy over older manual systems and allowing the ability to flexibly and more rapidly change fields and other planning parameters, reducing the time required to produce a treatment plan [51, 52]. Modern 3D computerized radiotherapy

treatment planning systems (RTPS) are now utilised for all patients' radiotherapy treatments. RTPS are used in external beam radiotherapy, generating the beams required to deliver the required dose distributions for radiotherapy treatments to maximise tumour control whilst minimizing normal tissue doses and dose to surrounding OARs [53]. These systems have developed over time, with the modern RTPS allowing the use of different imaging modalities for target delineation, having more sophisticated dose calculation algorithms, and being capable of more accurate dose calculations required for small fields which may be present in treatment techniques such as Intensity Modulated Radiation Therapy (IMRT) or Volumetric Modulated Arc Therapy (VMAT). These systems also have inverse planning available to optimize these complex treatment plans, generating the shapes required utilizing multi leaf collimators (MLCs) on the linear accelerators to produce a treatment plan meeting the parameters input into the optimizer within the RTPS. With these more complex treatment plans and dose distributions, sophisticated plan evaluation tools are also required, with RTPS providing tools such as dose volume constraints and dose volume histograms (DVH) to assess the generated treatment plan [34, 54, 55]. Conventional RTPS currently require a CT dataset for treatment planning dose calculations, utilizing the electron density information contained within these images [34].

2.4.1 MRI-Only Treatment Planning

The initial use of MRI in radiotherapy was to improve visualisation of anatomy for more accurate target definition and contouring. The superior soft tissue contrast allowed more accurate contouring both of tumour and target volumes, as well as organs at risk. This was enabled through the fusion of the MRI scan with the CT scan. As above, this introduced registration error and also had other potential errors introduced due to the possible variation in patient setup and internal organ motion between scans, producing variations in target and OAR contouring [38].

The gold standard for radiotherapy simulation and treatment planning is CT due to the bony anatomy definition and electron density information for dose calculations. With the advancement of MRI coupled with linear accelerators, the need for MRI-only radiotherapy has emerged. MRI-only radiotherapy with MRIg-linacs will also enable online adaptive radiotherapy. Various methodologies to introduce MRI-only radiotherapy for various treatment sites has been trialled [28, 29, 56, 57]. Methods of estimating electron density information from MRI for both radiation therapy and attenuation correction also need to consider geometric distortion which may be due to magnetic field inhomogeneities, gradient nonlinearity, and patient induced susceptibility [58, 59].

Use of MRI-only in brachytherapy with no inhomogeneity correction is common [60, 61]. The Gynaecological GEC-ESTRO Working group recommend the use of MRI with MR compatible brachytherapy applicators inserted for treatment, due to MRI providing much better tissue contrast to

optimise target delineation and the sparing of organs at risk, i.e. bladder, vagina, rectum and sigmoid colon, which are all more accurately delineated on MRI [15, 62]. In gynaecological brachytherapy, the radiation source is placed in close proximity or within, the target volume in the applicator. Assuming that all soft tissues have the same electron density, using the MR images to plan the brachytherapy treatment is feasible, with very little dosimetric impact or improvement gained from planning on a CT scan with applicators in situ.

In considering the advantages outlined earlier for MRI over CT, moving to MRI-only treatment planning in radiotherapy would remove current registration errors from fusing MRI scans to CT planning scans. These errors are generally reported to be of the order of 2 mm [42, 63]. MRI-only treatment planning would also enable online adaptive radiotherapy in the MRIg-linac setting and remove the need for additional CT scans for adaptive planning. Moving to MRI-only RT would also reduce patient discomfort as well as lower the workload and financial cost of additional scans. Some of the early drawbacks related to the use of MRI-only treatment planning are [14, 37, 42]:

- Poor imaging of bone

- Lack of electron density information from MRI required for dosimetry calculations

- Presence of intrinsic system related and object induced MR image distortions

- Lack of widely available computer software to accurate and reliably integrate and manipulate MR images within existing RT planning systems

More recently, additional drawbacks include [64]:

- Accurate and robust mapping of tissue electron density information

- Characterising the magnitude of the electron return effect for MRI based radiation therapy deliveries (for MRIg-linacs)

Current studies are ongoing looking into resolving these drawbacks. Many of the initial drawbacks have been resolved or improved. There are now many software solutions and tools available to integrate MRI within the radiotherapy treatment planning process, with additional tools available for rigid and deformable registration of MRI with the planning CT scan. Some radiotherapy treatment planning software will now also allow MRI images to be used as the primary data set for radiotherapy planning, with some commercial solutions to deal with the lack of electron density information available. Most treatment planning software also limits the import of non-axial imaging. In terms of poor imaging of bone, Ultrashort Echo Time (UTE) sequences have been demonstrated to provide excellent bony anatomy visualisation [65, 66].

In regard to MRI distortions, much work has been undertaken in quantifying the amount of distortions in MR systems, with vendors offering distortion correction options at the scanner to reduce distortion in images [58, 67]. Phantom studies have been undertaken to benchmark the distortion corrections available from vendors, and to quantify the effect of the residual distortions on patient imaging, tumour and organ delineation and eventual potential radiotherapy planning [48, 58].

Various methods have been investigated to address the lack of electron density information. These datasets generated from MRI have been termed substitute, synthetic or pseudo CT (sCT), with these sCT datasets able to be used in place of the CT scan data for radiotherapy treatment planning [29].

2.4.1.1 sCT Generation and Validation Methods

Various methods have been utilised for sCT generation from MRI data. These various methods include bulk density, atlas based and deep learning methods, or a combination [28, 29, 56, 57, 68, 69]. Some sCT conversion methods have become commercially available from different vendors [47, 70, 71].

The generated sCT is compared to the ground truth CT where possible. Anatomical and dosimetric analysis is undertaken to validate the acceptability of the generated sCT for MRI-only treatment planning use [57, 68]. Common anatomical comparison parameters include a mean error or mean absolute error (MAE) Hounsfield unit (HU) comparison, Hausdorff distance or Dice similarity coefficient (DSC) for comparison of the body anatomy or other selected anatomy which may be delineated for evaluation. Dosimetric comparison, parameters include point dose comparison, DVH comparison or gamma analysis, a tool which takes both dose and distance to agreement (spatial differences) into account.

2.4.1.1.1 Bulk Density

Initial methods considering the use of MRI-only for radiotherapy planning involved comparisons of MRI to CT with very few density corrections. These comparisons involved dosimetric comparisons with either no inhomogeneity corrections, or with anatomy (i.e. tissue, bones or air/gas) contoured and forced to an appropriate density [62, 72]. These initial studies were mostly in brain or prostate cancer treatment. Lee et al. in 2003 [73] showed differences greater than 2% for conformal radiotherapy plans with no inhomogeneity correction, and negligible differences with bulk density assignment for bone in prostate. Chen et al. [74, 75] published a similar study in 2004 considering similar scenarios for prostate IMRT. In the Chen et al. study, the absolute dose agreement for the planning target volume with these IMRT plans was within 2% between CT based and MR based plans, and 3% between measured dose and dose predicted by the TPS in physical phantom measurements. This study did however make note

that the MR imaging based digitally reconstructed radiographs did not provide adequate bony structure information, with this issue requiring further work for MRI to replace CT in the simulation process. More recently Karotki et al. [76] conducted a similar study looking at brain lesions, and Whelan et al., [77] conducted one looking at gynaecological cancers. Jonsson et al. [78] conducted a retrospective study of 40 patients across prostate, lung, head and neck and brain cancer treatment sites. Bulk density corrections were assigned using manual segmentation of bone, tissue, lung and air cavities on the MRI scan, and calculations were made between CT data with and without inhomogeneity corrections, and on MRI or CT data with bulk density assignments. This comparison included the effects of geometric distortion, with MU values of the bulk density assigned plans within 1% of the CT plans with inhomogeneity correction for all patient groups. This study also showed that dose calculations for pelvis treatments were the most sensitive of the sites considered to the choice of bulk density value due to the femoral head and pelvic bone effects within the radiation field.

2.4.1.1.2 Atlas Based Methods

The atlas method involves the application of a previously standardised dataset, an atlas, to deform average anatomical information generated from training datasets to new datasets and applying electron density corrections to produce a sCT dataset. Training pairs of MRI and CT patient scans are co-registered, and then MRI scans are registered into a common reference space, producing an average MRI atlas. An average CT atlas is produced by considering the transformation matrices and deformations which need to be applied to each MRI scan in the training data to produce the average MRI atlas, and applying these same parameters to the corresponding CT scan for the training pair – from these averaged, the average CT atlas is created. To create a sCT for a new MRI scan, the average MRI atlas is registered to the new MRI scan, with these deformations applied to the average CT atlas to produce a corresponding sCT [56]. This concept can be further developed by incorporating multiple atlases, otherwise known as a multi-atlas technique.

Dowling et al. [79] applied this to prostate, using 37 prostate patient data sets to produce a whole pelvis MRI atlas based on manually delineated MRI scans. Along with this, a conjugate electron-density atlas was generated from the co registered CT-MRI scans, with sCT scans for each patient generated by global and non-rigid registration of the MRI atlas to the patient MRI scan, followed by application of the same registration transformations and deformations to the electron density atlas. The generated sCT is then able to be used for both dose planning and DRR generation. A subset of 26 patients was then used for the planning comparison between the sCT and planning CT, with dose differences found to be less than 2% and no significant differences found between the scans' Hounsfield units for organs of interest. The dose difference was attributed to differences in the external contour between the individual patient MRI and CT scans due to slight variations in positioning between the scans, as the MRI scanner

used in the study was a radiology scanner and was not optimised for radiotherapy positioning. This work was further advanced by Dowling et al. [80] automating this sCT generation for the pelvis, and implementing a novel multi atlas method using advanced registration techniques and local weighted voting to automatically map electron density to standard MRI scans. This study produced results of a mean error in Hounsfield units between the sCT and patient CT of less than 1 HU, and the change in monitor units between the sCT based plans against the gold standard CT plan to be less than 1%. The main advantage of this method was that only a single T2 weighted sequence is required for the sCT generation, decreasing scanning time and patient motion.

Similarly, the atlas approach was also applied to the brain by Uh et al. [81]. In this study sCTs were constructed from single or multiple deformed atlas images, using multi-atlas approaches. These included using a single arbitrarily selected atlas, arithmetic mean process using 6 atlases, and pattern recognition with Gaussian process (PGRP) using 6 or 12 atlases. This study found that the atlas approach performed better than assigning a bulk CT number to the entire patient volume, and multiple atlases outperformed the single atlas scheme, though all sCTs agreed well with the planning CT scans for dosimetry, with dosimetric accuracy within 2% for the PTV when multiple atlases were used.

The main drawback in the application of the atlas method is that this technique is computationally intensive due to the number of registrations required [69]. There is also the need for a sufficient amount of data to create an appropriate atlas for a site, with this generic atlas then applied to patient data. Further uncertainty is present in the registration and deformation of the atlas to the patient data set, particularly if the patient is grossly dissimilar to the atlas model or falls outside the bounds of the training data [82].

2.4.1.1.3 Deep Learning Based Methods

There are many different deep learning networks which have been utilised for sCT generation [57, 68, 83-86]. Deep learning allows computational models with multiple processing components with adjustable parameters to learn a representation of data with multiple levels of abstraction [87]. Within this application, the deep learning network essentially learns a complex mapping function which may be applied to an input MR image or images to produce a corresponding CT image. The deep learning architecture utilised for sCT generation have most commonly been either generator only or generative adversarial networks (GAN) and its variants such as cycle-GAN or conditional-GAN. Deep learning models require a large amount of data and computational resources for training, but typically only take a few seconds to generate sCT images.

Generator only architectures which have been used for sCT generation include various convolutional neural networks (CNN), with U-Net one of the most common used. During training of the generator, an objective function called a loss function, which is an intensity based similarity measure between the

generated image (sCT) and the ground truth image (CT), is minimised. Generator only networks are based on convolution encoder-decoder networks, which consist of paired encoder and decoder networks. During encoding, low level feature maps are down sampled to high level feature maps. During decoding, the high level feature maps are upsampled to low level feature maps using the transposed convolutional layer to construct the sCT image [57].

GAN utilises the adversarial learning strategy which was proposed by Goodfellow et al. [88]. This architecture consists of two networks, a generator and a discriminator. The generator produces the sCT images as per its training, whilst the discriminator attempts to determine the probability of whether the sCT has been generated correctly, i.e. as per the training samples, or if it is incorrect or artificial. Training these networks incorporates both real data as well as fake or simulated data which is produced by the generator during the training process. Both networks are trained at the same time with backprojection, with each network becoming better at its given task – the generator better at producing realistic sCT which fools the discriminator, and the discriminator better at detecting fake sCT images as per the real training images [88, 89].

Liu et al. [90] utilized a cycle-GAN architecture to investigate MRI based treatment planning for liver stereotactic body radiotherapy. The cycle-GAN architecture utilises two GANs - one which generates sCT from MRI and another which generates synthetic MRI from sCT (the output of the first GAN). This cohort of 21 patients were used for training, and evaluated by leave one out cross validation (testing with one patient from the cohort and utilizing the remainder for training, and repeating for each patient in the cohort), achieving an MAE of the generated sCT of 72.87 ± 18.16 HU, and achieving an average 1%/1mm gamma pass rate of 99% on the coronal plane intersecting with the isocentre. Dinkla et al. [91] developed and evaluated a patch-based convolutional neural network based on the U-Net architecture for sCT generation for head and neck radiotherapy for an MR-only workflow, with the patch-based deep learning method chosen to improve robustness to abnormal anatomies caused by large tumours, surgical excisions or dental artefacts. This 34 patient retrospective study achieved a mean MAE of 75 ± 9 HU, with dosimetric analysis showing mean deviations of -0.03% ± 0.05% for dose within the body contours. Klages et al. [92] evaluated two different deep learning methodologies, and the effects of multiple combinations of strategies on accuracy for patch based sCT generation in head and neck. Within this study, pix2pix and CycleGan were investigated for sCT generation, with 23 patients used for training, and 8 patients used for independent testing. This study concluded both methods were promising for MRI-only treatment planning for head and neck cancer, with absolute percent dose differences of 2% for all PTV and OAR DVH parameters considered.

2.4.1.1.4 Hybrid sCT Generation Methods

Many sCT generation methods use a combination of the methods previously mentioned, and are sometimes described as voxel based techniques. These methods generate an sCT from MRI utilising a model with a voxel based electron density conversion, removing some uncertainty from the atlas registration and deformation, or the generalisation of a bulk density override. Voxel based methods have the greater potential to produce sCT scans from MRI with accurate estimation of CT information without risk of geometrical inaccuracies. The main challenge for voxel based conversion is the extremely short T2 relaxation time of bone (~0.5ms) which makes separation of bone and air difficult with traditional MR sequences. A current sequence of choice for this conversion is a specialised ultrashort echo time (UTE) MRI sequence as this allows more accurate bony visualisation, particularly in cortical bone, as these sequences sample the free induction decay (FID) rather than a spin or gradient echo.

Different groups have used different approaches to generate voxel to voxel conversion solutions, with studies by Johansson et al. [93, 94], Andreason et al. [95] and Hsu et al. [96] published looking at the head and neck region. These studies used different mathematical models to correlate the MRI scan with an equivalent CT scan and were able to apply an electron density correction voxel by voxel using a combination of methods.

Johansson et al.'s [93] method involved a Gaussian mixture regression (GMR) model linking intensities in reference MR images (two dual echo UTE images with different flip angles and one high resolution T2 weighted image 3D spin echo based sequence) to HU in reference CT images. The derived model was then used to transform sets of MR images into a sCT image. The GMR models the joint distribution of the intensities in the CT and MR images, using the underlying assumption that the images show a discrete number of tissues or clusters. Each cluster is characterised by an intensity value for each image, and due to noise in the images and small variations in the appearance of a tissue type, the samples from a particular tissue will fall in a distribution around the tissue type coordinate. This distribution is approximated by a single multivariate Gaussian. Five patient data sets were analysed in the study and the mean absolute error for the CT number in the sCT images was 137 HU, with the largest errors found at the air tissue and bone tissue interfaces.

Hsu et al. [96] used the potential of probabilistic classification of MRI voxels from multiple contrasts to create a synthetic CT. The method for this study consists of acquiring multiple MRI volumes: T1 weighted, T2 weighted, two echoes from an UTE sequence, and calculated fat and water image volumes using a Dixon method. Probabilistic tissue classification was achieved via fuzzy c-means (FCM) clustering with a spatial constraint, with the FCM algorithm assigning voxels of the images a probability of belonging to a class. Following this, attenuation properties were assigned weights based on the probability of individual tissue classes being present in each voxel. The synthetic CT was then generated

from the sum of attenuation properties in each voxel. This method was found to produce synthetic CTs that were able to distinguish tissues/materials that contribute significantly to attenuation variations seen on CT with reasonable accuracy. The study did however conclude that a single MR image could not sufficiently differentiate all tissue types, and that UTE images increased differentiation of bone from air but could not completely separate air from bone.

Andreason et al. [95] used a "patch" based method in which 3D patches (i.e. small cuboidal image subregions) are extracted from the MRI and a spatially local search for the most similar patches in a preacquired database of labelled MRI scans is performed. The known labels of the resulting database patches are then fused to give the predicted label at each position. To facilitate the spatially local patch search, most patch based methods use a rough linear alignment between the database MRI scans for the MRI to be segmented. The segmented MRI voxel is then applied with the matching CT value from the patch database. This study contained five whole brain RT patients, achieving in regards to dosimetric accuracy, average deviations of less than 0.5% for target coverage.

Commercially available sCT generation software is available from multiple vendors, such as Siemens, Philips and Spectronic Medical [47, 70, 71, 97]. The FDA approved MRCAT package from Philips for use in the male pelvis was one of the first commercial sCT generation algorithms approved. MRCAT uses a T1 weighted mDixon scan sequence, with the different phase images providing different contrasts for tissue classification, in addition to a pelvic bone model atlas [44, 47, 98]. Tyagi et al. [47] evaluated the MRCAT for treatment localisation, distortion analysis and dosimetric accuracy. For this 25 prostate patient study, dosimetric accuracy was reported to be on average within 0.5% for all structures considered through DVH comparison. Similar dosimetric studies in the prostate utilizing MRCAT were also completed by Christianson et al. [44] and Farjam et al. [98] with Christianson et al. reporting a mean pass rate for the body of 98.7% ± 0.9% using a 1%/1mm gamma criteria and Farjam et al. achieving a 1%/1mm gamma pass rate of 90.6% when comparing MRCAT sCT with deformed planning CT.

MRI Planner (Spectronic Medical, Helsingborg, Sweden) is another commercially available sCT generation software. The patient MRI is uploaded to a cloud based conversion service, with the software converting this to sCT based on an automated atlas based conversion method for prostate [71, 99], or a transfer function estimation algorithm in a CNN based method for head and neck [100]. For prostate, a single large field of view (LFOV) T2 fast spin echo sequence is required for this sCT generation, with Persson et al. [46] presenting a dosimetric study of 40 prostate patients utilizing a clinical workflow with this software. Persson et al. reported dose differences between sCT and CT within 2% for most DVH parameters, in addition to global gamma pass rates of above 98% for all patients considering a 2%/1mm gamma criteria. For head and neck, a single T1 weighted Dixon Vibe sequence is required, with Palmer et al. [100] evaluating the MRI Planner software using a 44 head and neck patient cohort.

This study reported a mean MAE of 67 ± 14 HU for overall body when compared to CT, as well as a dose agreement for all DVH volumes considered within 1%.

Siemens has released commercially available MR based synthetic CT with their syngo.via RT Image Suite (VB60). This utilizes an AI based algorithm for brain and pelvis conversions, trained using 6486 CT and MRI image pairs for brain and 9059 for pelvis. This algorithm utilizes two networks, the first a CNN for segmentation of background, bone and soft tissue from the MR images, and the second a conditional GAN for sCT reconstruction. This method reports <1% dose difference for target volumes in both brain and pelvis in the white paper [70]. O'Connor et al. [97] conducted a study using this algorithm for 40 pelvis patients, reporting an average dose difference of 1.2% ± 0.9% (0.8% - 3.9%) between CT and sCT, and a 3%/2mm average gamma pass rate of 99.6% ± 1.0%, which dropped to 84% ± 9.7% for 1%/1mm gamma criteria.

2.5 Radiotherapy Treatment

2.5.1 Hybrid MRI-Linac Systems

The use of Magnetic Resonance Guided Adaptive Radiotherapy as a solution in the future is further discussed by Kupelian and Sonke [101]. With the superior soft tissue contrast available as compared to current available imaging modalities MR has the potential to track more complex structures. The integration of MRI into online adaptive radiotherapy is able to account for both interfraction and intrafraction variations. MRI also offers the ability to image biological and functional aspects of the body. Potentially this allows MRI to provide imaging biomarkers of therapy response of tumour or normal tissue or both, potentially driving adaptive plan modifications to account for these observed therapy responses. This accounts for the potential of MRI to drive biologically based adaptive protocols, able to alter the treatment intent to differentiate between responders and non responders, redistribute the target dose to respond to radioresistant regions, or lower dose constraints to organs at risk with upcoming toxicity. This potentially is the next step in adaptive radiotherapy, moving the technique from one based on anatomical imaging aiming to restore the original treatment plan intent in the presence of anatomical changes, to one which can alter treatment intent based on biological changes. With the further development of MRI-only radiotherapy, the ease of use and potential for this type of more targeted adaptive radiotherapy can be further realised.

With all the additional information, and advantages of MRI, a further development has been the amalgamation of MRI units with therapy devices to produce hybrid systems which allow imaging with MRI, and radiotherapy treatment at the same time. Use of MRI as the treatment imaging modality would provide additional soft tissue anatomy whilst the patient is being treated, with this additional information potentially able to adapt the treatment in real time. These systems have been referred to as

MR-linacs (MRL), MRI guided linacs (MRIg-linac) or hybrid MRI-linac systems. There have been multiple systems which have been in development, or developed and become commercially available, with all having unique design features [102, 103].

The Utrecht group was one of the first groups to publish on an MRI-linac system, with some early studies published in 2007 by Raaijmakers et al. [104] on the experimental verification of magnetic field dose effects for the MRI-accelerator, and in 2008 by Lagendijk et al. [105] on the MRI/linac integration. A proof of concept study was published in 2009 by Raaymakers et al. [106] from the same group, which reported on the production of a prototype MRI-linac, with a modified 6MV Elekta accelerator mounted on a ring around a modified 1.5T Philips Achieva MRI system, which allowed simultaneous irradiation and MR imaging. The radiation beam travels through the closed bore MRI before it enters the patient. This concept is now commercially available from Elekta, known as the Elekta Unity [107, 108]. This system enables MRI guided online adaptive radiotherapy treatment planning through workflows available with the packaged Monaco treatment planning system [109].

Another commercial system as initially discussed by Mutic and Dempsey [110] is the ViewRay system. The original design was a 0.35T MRI coupled with a three headed Co-60 design. The MRI is a vertically gapped (double donut) horizontal solenoid superconducting 0.35T whole body MRI, with a 50cm diameter spherical imaging FOV. The therapy delivery system was a robotic 3 headed Co-60 system, with the 3 sources 120 degrees apart, with this producing a total dose rate comparable to a conventional linear accelerator. The main disadvantages of this system were due to the characteristics of the Co-60 radiation beam and the low, 0.35T field strength of the MRI. The low field strength of the B0 field also provides MRI images with less signal to noise and shorter relaxation times. The main advantage of the use of Co-60 is that the radioactive decay from the source does not interfere with operation of the MRI unit, with the surface dose also lowered by the magnetic field sweeping away contamination electrons. The system also comes with its own online adaptive Monte Carlo based treatment planning system, which is able to calculate dose distributions with and without effects of the magnetic field [111]. The newer system produced by ViewRay is the MRIdian linac, which is a linac combined with a 0.35T MRI, with linac components positioned in areas designed to be shielded from the magnetic field and the RF radiation. This updated system maintains the same 0.35T split superconducting magnet design as the original design, incorporating a linac which generates a 6 MV Flattening Filter Free (FFF) photon beam, and utilises the same treatment planning system for online adaptive planning [112].

Fallone et al. [113] have been working on a whole body Linac-MR at Cross Cancer Institute, Edmonton, Alberta, Canada, now called the Aurora-RT (from MagnetTx Oncology Solutions), which received FDA approval in 2022. This system consists of an isocentrically mounted 6 MV linac that rotates in unison with a biplanar 0.5T MRI in transverse plane. The B0 field and central axis of the 6 MV beam are parallel, with this setup avoiding large increases in dose at tissue/air interfaces and at beam exit due

to the electron return effect. The main magnet field in a biplane open magnet goes from one plane to the other (i.e. the field vector is perpendicular to the planes). The linac can be placed to irradiate either between the MR's magnet planes or poles, or through the central opening of one of the planes, allowing the corresponding radiation field to be either perpendicular or parallel to the main magnetic field, resulting in different physical or clinical properties. The rotation is required to deliver the radiation beam at a particular angle. The system also allows MR during beam on for "live" image guidance of the radiation beam.

An Australian group, headed by Keall et al. [114] are in development of another MRI-linac hybrid system. The Australian MRI Linac program design is a 1T open bore MRI coupled with a 6 MV linac system. This will be able to setup in a perpendicular or inline design approach, allowing both designs to be investigated experimentally as the system is developed. The magnet, produced by Agilent, has an 82cm diameter bore, 50cm gap. The linear accelerator component is from a 6 MV linatron MP industrial linac from Varian, with the Varian Millennium 120 leaf MLC system. The design incorporates patient rotation for treatment, as opposed to the other MRIg-linac designs, or a traditional linac rotating around the static patient [115].

2.6 Adaptation in Radiotherapy

Adaptive radiotherapy (ART) was a term introduced in the mid 1990s [12, 116], to describe a process in which radiation treatment is individualized and adapted over the course of treatment. The earliest published study by Yan et al. [116] describes the term adaptive as initially using the patient population data to identify the sensitivity of different treatment sites to positional variation, followed by using the individual patient position error to modify the treatment parameters, using the example of reshaping MLC fields to improve treatment by either increasing possible dose escalation or reducing the possibility of geometric misses. This concept was further developed with Yan et al.'s publication [12] discussing tracking the status of the treatment process and making decisions when adaptive modifications need to be applied to either the treatment dose and/or field margin, as well as modifying field shape, beam intensity and geometry if necessary. This paper also discussed the optimal modification required, needing knowledge of the treatment dose, tumour dose response and magnitude of the patient variation.

ART is further defined into three components: image guidance, dose verification and plan adaptation [12, 117-119]. For image guidance and dose verification, accurate image registration is a necessity to be able to match the patient's current geometry with their reference geometry for treatment, and to assess the dose delivered on the day. With this information, an assessment can be made if plan adaptation is possible or required.

Since the introduction of the concept of ART, tools have been developed which have improved the nature of ART and have expanded its scope and complexity, as well as fulfilling its premise in each of its components. ART has moved from the realm of offline corrections, that is corrections made between fractions of treatment, to online corrections, that is corrections made to the patient treatment during their treatment delivery [117-119]. Additionally, as the imaging has improved in both the radiotherapy simulation, with the introduction of 4D-CT, MRI simulators, functional imaging techniques such as positron emission tomography (PET) imaging, and the onboard imaging capabilities on the linear accelerators, corrections have become more accurate and complex, potentially incorporating both anatomical and functional-based changes [120, 121]. To enable these corrections, more complex tools and correction methods have been developed. The greatest potential currently lies in the Magnetic Resonance Imaging Guided Linear Accelerator (MRIg-linac), with groups looking at the application of during-treatment MR images to ART [30, 109, 119, 122, 123].

2.6.1 ART Process

The clinical ART process is well described by Green et al. [124]. This publication describes ART as radiotherapy where the delivered dose is monitored for clinical acceptability during the course of treatment and modified as needed with the goal of improving clinical outcomes. ART currently makes use of 4 key processes: imaging, assessment, replanning and quality assurance. ART may be applied at three different timescales: offline between fractions, online immediately prior to a fraction, or real time during a fraction. Figure 2.2 [124] provides an overview of the workflow and tools for the offline and online ART processes. Real time ART requires real time imaging of anatomy to adapt the plan in real time during delivery – this is currently not used clinically due to the additional higher QA burden and automation required. Current clinical practice would be either offline or online corrections, with most current linac based systems using offline corrections, and current MRIg-linacs (and brachytherapy) using online corrections. Varian's Ethos therapy system is a recently approved linac based system which utilises artificial intelligence (AI) based software to perform online adaptive radiotherapy based on daily cone beam CT imaging [125-127]

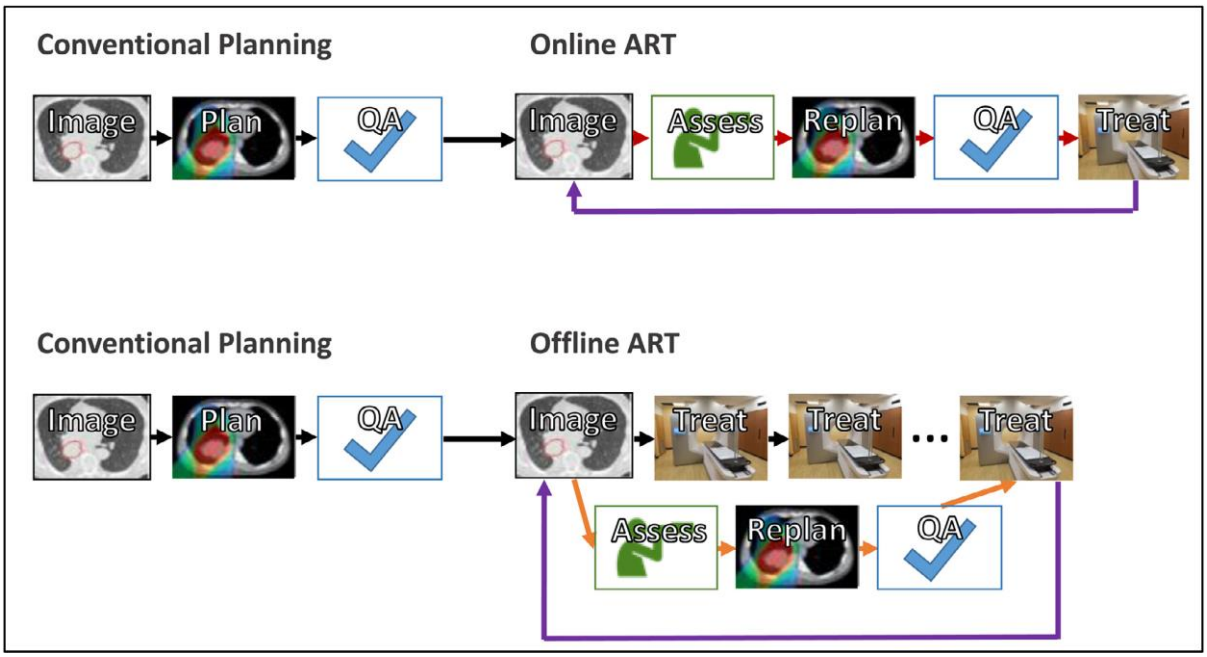

Figure 2.2 - Overview of workflow and tools for offline and online adaptive radiation therapy processes. (from Green et al. [124], with permission from Elsevier)

Offline ART follows a more conventional treatment planning workflow as it is performed generally in the time between fractions (a period of days). Offline ART is commonly used when functional changes in tumour or normal tissue are incorporated into the ART process, allowing the use of cone-beam CT or MRI as an indicator that a change may be required, prior to re-acquiring a new planning CT or MRI scan for replanning. Offline ART does not require any additional clinical or specialized tools which are not already available for use.

For online ART, the patient is imaged in the treatment position immediately prior to delivery, for assessing the need for ART. The replanning and QA is performed all while the patient remains in the treatment position. For this process to be successful it must be highly efficient and fast, and requires specialized, well integrated tools for assessment, replanning and quality assurance. The advantage of online ART is that changes may be immediately adapted to, and treatment delivered.

2.6.2 Image Registration

The need for accurate image registration remains a must for ART. Image registration refers to the process of aligning multiple image datasets. In the ART process this provides a basis for correlation between the initial patient imaging and the patient imaging at time of treatment or analysis. There are two different types of registration modalities – rigid and non-rigid (or deformable) registration algorithms. Rigid registration refers to a registration which uses only translation and/or rotation to align

corresponding image datasets. This registration can be completed by using corresponding points or structures for alignment. Non rigid, otherwise known as deformable, image registration aligns multiple image datasets incorporating shape changes or distortions, able to stretch or morph the images to produce the alignment required.

Rigid registration is commonly used for alignment of daily patient imaging to the reference CT image for pre treatment positioning. Rigid registration is fast and robust for this daily positioning task, however is not able to provide accurate registration in the presence of shape or volume variations and changes [118].

Non-rigid, or Deformable Image Registration (DIR) was introduced to register images with changes in anatomy that rigid registration could not accurately register. The fundamentals of DIR are well described in Chetty et al. [128], with the fundamental challenge being with regard to validation – the ground truth is generally unknown. The paper also breaks down the DIR process into the following three sections:

1 – The transformation model, which is the mathematic model which describes how the source image is altered to match the target image. The output of this transformation model which produces the best mapping between the source and target images is commonly termed the displacement or displacement vector field (DVF).

2 – The similarity metric, which is how well the source (known as primary, reference or fixed) image and the target (secondary or moving) image datasets match. This can be further split into geometric and intensity based metrics.

Geometric based metrics may be defined by anatomical elements defined in both sets of images, such as anatomical landmarks or implanted fiducial markers, and how well they correspond once the transformation model is applied. Limitations of this approach may partly be because the alignment of geometric structures ignores anatomical distortions that may occur in other parts of the images outside of the structures used.

Intensity based metrics align intensity patterns, or grey scale information, between the source and target images, until optimized. Clinically used intensity metrics include sum of squared intensity differences, cross correlation and mutual information. Mutual information is commonly used, with the assumption that the images will be most similar when they are most accurately registered, at which point the mutual information is maximized between the two images.

3 – The optimization model, usually a gradient descent model, which is the strategy used to optimize the transformation model parameters so that the source and target are aligned based on the specified similarity metric. The optimization strategy refers to the mathematical approach used, working to find the best tradeoffs amongst the competing demands to find the best correspondence. Considerations of

the optimization include cost function, transformation, accuracy requirements and possible time constraints.

There are various sources of error in the image registration process which need to be considered, which are across the input, the registration algorithm, and the output. The input, that is the images, have uncertainties such as artefacts due to anatomy (i.e. stents or dental fillings) and motion, artefacts due to acquisition (i.e. MRI distortion) and also large changes in anatomy can be a source of error. With regard to the algorithm, errors can be due to potentially poorly designed optimisers (i.e. solutions found in local minima vs global minima), limitations in the model, or uncertainties in the feature selection or manual contouring of structures used for the registration. The output, that is the registration, may then propagate these errors onwards through the application and use of the registration, i.e. contour propagation, dose accumulation or image guidance [129].

Various DIR error prediction methods have been discussed in the literature [130-138]. The simpler of these follow the similarity metrics used in the algorithms, using criteria such as landmark validation between the datasets, and comparing volumes between the registered datasets to generate Dice similarity coefficients, Hausdorff distance to agreement and image similarity scores, as well as local and target registration error scores. The Jacobian determinant has also been suggested as a quantitative measure of DIR error, identifying the local volume change as a result of the registration. The DVF vector maps may also be reviewed as a quantitative measure for unrealistic deformations which may be applied.

There are various deformable image registration algorithms available, as well as various commercial software solutions, with each algorithm producing varying results [134, 135, 139]. All deformable algorithms generate DVFs which have a level of uncertainty depending on the images, the algorithm itself, tissue changes and the physical fidelity of the deformation field itself. As such, recommendations are that each clinical scenario is assessed [128, 137, 140].

2.6.3 Dose Accumulation

The term ’dose accumulation’ historically referred to summing the dose delivered to the patient over time, and in general is poorly defined. This is due to the patient anatomy potentially changing over time, i.e. tumour regression, weight changes, swelling, changes in edema, and potentially changing during treatment, e.g. breathing motion, bladder and rectal filling. This produces a patient anatomy which differs from the reference anatomy captured at simulation and a treatment dose distribution which is different to that which is planned.

Dose accumulation, in its simplest sense, requires a method to be able to transfer the original planned dose distribution, and on a per treatment fraction basis, apply the corrections required to generate the

dose delivered to the patient for that fraction. These corrected per treatment fraction doses are then summed over the course of treatment.

Some of the earliest publications on dose accumulation referred to the different dose fractionation comparisons and the accumulated dose over time [141, 142]. The earliest dose accumulation publication considering changes to the treatment volume during treatment was by Yan et al. [143], considering the daily setup error and dose delivered to a deforming organ by tracking the position elements of the organ. The daily setup error was generated from daily portal imaging, plus twice weekly CT scans to measure intertreatment organ motion, with the dose accumulation model applied successfully to a rectal wall organ at risk dose over the course of treatment.

In most current practice, dose accumulation makes use of DIR to apply deformation to the original planned dose to map it from the current dataset. A widely used approach is to use the obtained DVF from the DIR to warp the dose grid back to the reference anatomy [129]. Various studies [133, 144-148] have investigated the effect of DIR on the dose accumulation setting using different metrics and definitions. Vickress et al. [145] proposed a method that represented a range of dosimetric uncertainty of DIR error using either landmarks at specific voxels or measures of registration accuracy throughout the volume. This study used 4D-CT images, with landmarks used to match the same point in different phases to characterize DIR error at multiple voxels, to explore the effect on dose accumulation. This was termed the range of dose uncertainty (RDU), which was the maximum and minimum of the doses within a sphere around the corresponding landmark, mapping this across each dataset back to the end expiration phase.

At this point in time, most publications note that deformable dose accumulation is used with caution when applied, and is influenced by a number of factors, including issues related to imaging distortion, noise, artefacts, and tumour and normal tissue motion [128, 140, 143, 145, 149-151].

2.6.4 Clinical Implementation of Adaptive Radiotherapy with regards to DIR and Dose Accumulation

The current best practice of ART in the clinic is generally related to the volumetric changes of the patient's anatomy over the treatment and adapting to this. This includes daily volumetric imaging (CBCT) for patient setup, methods of real time tumour or surface tracking for treatment, and calculation of dose on the dataset of the day for dose assessment prior to any changes to treatment if required. Essentially the imaging obtained produces an imaging feedback loop which is used to assess if replanning is required due to anatomical adaptation or if the original treatment plan is still adequate on the changed anatomy [121, 152, 153].

The AAPM report "Use of image registration and fusion algorithms and techniques in radiotherapy: Report of the AAPM Radiation Therapy Committee Task Group No. 132" provides guidance for the clinical commissioning required for deformable image registration, detailing the testing required for clinical implementation [137]. Dose accumulation is outside the scope of this document.

The clinical recommendations from the TG 132 report are as follows:

1 – Understand the basic image registration techniques and methods of visualizing image fusion

2 – Understand the basic components of the registration algorithm used clinically to ensure its proper use

3 – Perform end to end tests, using a physical phantom, of imaging, registration, and planning/treatment systems if image registration is performed on a standalone system

4 – Perform comprehensive commissioning of image registration using the provided digital phantom data (or similar) as well as clinical data from the user's institution

a. Estimation of registration error should be assessed using a combination of the qualitative and quantitative evaluation tools. Regions with larger estimated errors should be accounted for in the uncertainty margins used

5 – Develop a request and report system to ensure communication and documentation between all users of image registration

6 – Establish a patient specific QA practice for efficient evaluation of image registration results.

These recommendations are for the efficient and safe practice of image registration programs in the clinic. Currently baselines are recommended using both virtual and physical phantoms. Virtual phantoms, that is digital images with a known displacement or DVF, can be used to test deformation algorithms to ensure suitable outputs. For virtual phantoms, current best practice is to ensure the deformation model used to create the phantom is not the same as the model to be tested. The use of physical phantoms allows testing of the entire process, from acquisition to data transfer and import, and image registration. Physical phantoms for DIR testing are generally complex, using motors and computer controllers to deform the shape, and to introduce deformations in a predictable manner. Groups have been working on developing low cost, user friendly phantoms for registration accuracy testing, with new prototypes including tests for rigid image registration for rotation and translation, as well as DIR tests [154].

There are no clinical recommendations for dose accumulation in the clinical setting currently, so such use of dose accumulation should be done with care and consideration of the uncertainties involved.

2.7 The Future of Adaptive Radiotherapy with MRIg-linacs

ART in the future will be based on automatic segmentation, auto planning and real time tracking of the tumour. Keall et al. discussed the future direction of ART, making a see, think and act analogy for real time ART [155]. Within this analogy, the "See" in the future is the technology to locate the target during real time ART, making the reference to conventional linacs and MRIg-linacs having the potential to provide real time imaging to be able to track the tumour at all times of the treatment, in addition to being able to potentially couple this information with surface tracking or markers. The "Think" is in reference to dose calculation during real time ART, considering the future of dose calculation, and dose reconstruction in real time. Currently real time ART provides the means to correct for changes in the target geometry only – if dose was able to be calculated and optimized in real time the potential for higher order corrections would be available. The "Act" analogy refers to technology to hit the target during real time ART, and thus closing the real time ART loop. The earliest example of this would be gating the treatment of the tumour at particular parts of the breathing cycle, with newer potential technologies including MLC tracking or robotic couch tracking. As the technology improves, the potential for sophistication of the ART tools can only increase [119].

Considering this, MRIg-linacs [110, 156, 157] have some advantages over conventional linear accelerators when compared for ART. MRI provides improved soft tissue contrast when compared with CT or x-ray imaging, and is also able to provide some functional imaging techniques which would allow for dose response assessment studies during treatment. Additionally MRI avoids radiation imaging dose exposure when compared to CBCT [123]. The potential use of MRI guidance for proton therapy has also been considered, combining these image guidance advantages with the potential fundamental dosimetric advantages of proton therapy [158, 159].

A publication by Hunt et al. considers the question "Will MRI guided radiotherapy be the ultimate online IGRT solution?" [122]. Clinician led target identification remains one of the weak links in the treatment chain for radiotherapy, with MRI improving inter and intra observer variability for many tumours, and allowing visualization of organs and targets which may not be seen on CT. The addition of onboard functional sequences may provide an additional option for ART in functional adaptation of treatment.

MRI guided adaptive RT has been utilized for a variety of treatment sites on MRIg-linacs, including prostate, oligometastatic lymph nodes, pancreatic tumours, head and neck tumours, rectal cancer, liver, lung and kidney tumours [160, 161]. MRIg-linacs have the ability to provide treatment with online adaptive radiotherapy. In essence, the patient will be scanned, volumed, planned and treated within the one treatment session. This may be crucial in the ability to deliver stereotactic or ablative dose prescriptions safely to target volumes whilst minimizing organ at risk doses, especially for treatment sites which have large intra and inter fraction motion. The most common sites which utilize daily

adaptive treatment include pancreatic and rectal tumours, and lymph nodes due to their close proximity to highly mobile and radiosensitive OARs [160, 162]. The Unity system provides online adaptive treatment planning tools, allowing users to adapt to position (ATP) or adapt to shape (ATS) based on the daily MRI scan taken at treatment [109]. These tools can allow for online plan adaption, with ATP tools allowing reoptimisation of the plan to produce the pre-treatment plan on the new patient position, utilizing rigid registration to match the daily MRI with pre treatment CT. Alternatively, these tools can adapt based off the new patient anatomy and a deformable registration available to adapt contours for plan optimisation in the ATS option.

The combining of MRIg-linacs with MRI-only simulation and treatment planning would provide the next level of adaptive RT. Utilizing the potential of the daily MRI scan for treatment planning directly would remove the requirement to adapt to shape or adapt to position, and allow a truly online adaptive replanning process to occur. The removal of the requirement for a pre treatment planning CT scan would streamline the MRIg-linac workflow, and reduce the registration uncertainties arising from matching the daily MRI to the planning CT, as well as reducing the patient burden of an additional scan. The utilization of MR-only treatment planning is a natural development in MR guided adaptive radiotherapy [163, 164].

2.8 References

[1] Bray F, Laversanne M, Weiderpass E, Soerjomataram I. The ever-increasing importance of cancer as a leading cause of premature death worldwide. Cancer. 2021;127:3029-30.

[2] Sung H, Ferlay J, Siegel RL, Laversanne M, Soerjomataram I, Jemal A, et al. Global cancer statistics 2020: GLOBOCAN estimates of incidence and mortality worldwide for 36 cancers in 185 countries. CA: a cancer journal for clinicians. 2021;71:209-49.

[3] DePinho RA. The age of cancer. Nature. 2000;408:248-54.

[4] Cancer Fact Sheet. World Health Organization; 2022.

[5] DeVita VT, Jr., Rosenberg SA. Two hundred years of cancer research. The New England journal of medicine. 2012;366:2207-14.

[6] Delaney G, Jacob S, Featherstone C, Barton M. The role of radiotherapy in cancer treatment: estimating optimal utilization from a review of evidence-based clinical guidelines. Cancer: Interdisciplinary International Journal of the American Cancer Society. 2005;104:1129-37.

[7] Borras JM, Lievens Y, Dunscombe P, Coffey M, Malicki J, Corral J, et al. The optimal utilization proportion of external beam radiotherapy in European countries: an ESTRO-HERO analysis. Radiotherapy and Oncology. 2015;116:38-44.

[8] Van Dyk J. The Modern Technology of Radiation Oncology. Madison: Medical Physics Publishing. 1999;1.

[9] Ghaderi N, Jung J, Brüningk SC, Subramanian A, Nassour L, Peacock J. A century of fractionated radiotherapy: How mathematical oncology can break the rules. International Journal of Molecular Sciences. 2022;23:1316.

[10] Chandarana H, Wang H, Tijssen R, Das IJ. Emerging role of MRI in radiation therapy. Journal of Magnetic Resonance Imaging. 2018;48:1468-78.

[11] Quan EM, Li X, Li Y, Wang X, Kudchadker RJ, Johnson JL, et al. A comprehensive comparison of IMRT and VMAT plan quality for prostate cancer treatment. International Journal of Radiation Oncology* Biology* Physics. 2012;83:1169-78.

[12] Yan D, Vicini F, Wong J, Martinez A. Adaptive radiation therapy. Physics in Medicine & Biology. 1997;42:123.

[13] Chandra RA, Keane FK, Voncken FE, Thomas CR. Contemporary radiotherapy: Present and future. The Lancet. 2021;398:171-84.

[14] Khoo VS, Dearnaley DP, Finnigan DJ, Padhani A, Tanner SF, Leach MO. Magnetic resonance imaging (MRI): considerations and applications in radiotherapy treatment planning. Radiotherapy and Oncology. 1997;42:1-15.

[15] Haie-Meder C, Pötter R, Van Limbergen E, Briot E, De Brabandere M, Dimopoulos J, et al. Recommendations from Gynaecological (GYN) GEC-ESTRO Working Group☆(I): concepts and terms in 3D image based 3D treatment planning in cervix cancer brachytherapy with emphasis on MRI assessment of GTV and CTV. Radiotherapy and oncology. 2005;74:235-45.

[16] Khoo V, Joon D. New developments in MRI for target volume delineation in radiotherapy. The British Journal of Radiology. 2006;79:S2-S15.

[17] Liney G. MRI in Clinical Practice2006.

[18] Holdsworth SJ, Bammer R. Magnetic resonance imaging techniques: fMRI, DWI, and PWI. Seminars in Neurology: © Thieme Medical Publishers; 2008. p. 395-406.

[19] Ohno Y, Koyama H, Yoshikawa T, Matsumoto K, Aoyama N, Onishi Y, et al. Diffusion-Weighted MRI Versus 18F-FDG PET/CT: Performance as Predictors of Tumor Treatment Response and Patient Survival in Patients With Non–Small Cell Lung Cancer Receiving Chemoradiotherapy. American Journal of Roentgenology. 2012;198:75-82.

[20] Okuma T, Matsuoka T, Yamamoto A, Hamamoto S, Nakamura K, Inoue Y. Assessment of early treatment response after CT-guided radiofrequency ablation of unresectable lung tumours by diffusion-weighted MRI: a pilot study. The British Journal of Radiology. 2009;82:989-94.

[21] McRobbie DW, Moore EA, Graves MJ, Prince MR. MRI from Picture to Proton: Cambridge University Press; 2017.

[22] Rofsky NM, Lee VS, Laub G, Pollack MA, Krinsky GA, Thomasson D, et al. Abdominal MR imaging with a volumetric interpolated breath-hold examination. Radiology. 1999;212:876-84.

[23] Busse RF, Brau AC, Vu A, Michelich CR, Bayram E, Kijowski R, et al. Effects of refocusing flip angle modulation and view ordering in 3D fast spin echo. Magnetic Resonance in Medicine. 2008;60:640-9.

[24] Mugler III JP. Optimized three-dimensional fast-spin-echo MRI. Journal of Magnetic Resonance Imaging. 2014;39:745-67.

[25] Dixon WT. Simple proton spectroscopic imaging. Radiology. 1984;153:189-94.

[26] Ma J. Dixon techniques for water and fat imaging. Journal of Magnetic Resonance Imaging: An Official Journal of the International Society for Magnetic Resonance in Medicine. 2008;28:543-58.

[27] Korsholm M, Waring L, Edmund J. A criterion for the reliable use of MRI-only radiotherapy. Radiation Oncology. 2014;9:16.

[28] Edmund JM, Nyholm T. A review of substitute CT generation for MRI-only radiation therapy. Radiation Oncology. 2017;12:28.

[29] Owrangi AM, Greer PB, Glide-Hurst CK. MRI-only treatment planning: benefits and challenges. Physics in Medicine & Biology. 2018;63:05TR1.

[30] Hall WA, Paulson E, Li XA, Erickson B, Schultz C, Tree A, et al. Magnetic resonance linear accelerator technology and adaptive radiation therapy: An overview for clinicians. CA Cancer J Clin. 2022;72:34-56.

[31] Mutic S, Palta JR, Butker EK, Das IJ, Huq MS, Loo L-ND, et al. Quality assurance for computed-tomography simulators and the computed-tomography-simulation process: report of the AAPM Radiation Therapy Committee Task Group No. 66. Medical Physics. 2003;30:2762-92.

[32] Aird E, Conway J. CT simulation for radiotherapy treatment planning. The British Journal of Radiology. 2002;75:937-49.

[33] Conway J, Robinson M. CT virtual simulation. British Journal of Radiology. 1997;70:S106-S18.

[34] Fraass B, Doppke K, Hunt M, Kutcher G, Starkschall G, Stern R, et al. American Association of Physicists in Medicine Radiation Therapy Committee Task Group 53: quality assurance for clinical radiotherapy treatment planning. Medical Physics. 1998;25:1773-829.

[35] Létourneau D, Wong JW, Oldham M, Gulam M, Watt L, Jaffray DA, et al. Cone-beam-CT guided radiation therapy: technical implementation. Radiotherapy and oncology. 2005;75:279-86.

[36] Van Herk M. Different styles of image-guided radiotherapy. Seminars in Radiation Oncology: Elsevier; 2007. p. 258-67.

[37] Moerland MA. Magnetic resonance imaging in radiotherapy treatment planning. Medical Physics. 1997;24:336-.

[38] Nyholm T, Jonsson J. Counterpoint: Opportunities and Challenges of a Magnetic Resonance Imaging–Only Radiotherapy Work Flow. Seminars in Radiation Oncology. 2014;24:175-80.

[39] Devic S. MRI simulation for radiotherapy treatment planning. Medical Physics. 2012;39:6701-11.

[40] Glide-Hurst CK, Paulson ES, McGee K, Tyagi N, Hu Y, Balter J, et al. Task group 284 report: magnetic resonance imaging simulation in radiotherapy: considerations for clinical implementation, optimization, and quality assurance. Medical Physics. 2021;48:e636-e70.

[41] Paulson ES, Erickson B, Schultz C, Allen Li X. Comprehensive MRI simulation methodology using a dedicated MRI scanner in radiation oncology for external beam radiation treatment planning. Medical Physics. 2015;42:28-39.

[42] Karlsson M, Karlsson MG, Nyholm T, Amies C, Zackrisson B. Dedicated Magnetic Resonance Imaging in the Radiotherapy Clinic. International Journal of Radiation Oncology*Biology*Physics. 2009;74:644-51.

[43] Metcalfe P, Liney GP, Holloway L, Walker A, Barton M, Delaney GP, et al. The potential for an enhanced role for MRI in radiation-therapy treatment planning. Technol Cancer Res Treat. 2013;12:429-46.

[44] Christiansen RL, Jensen HR, Brink C. Magnetic resonance only workflow and validation of dose calculations for radiotherapy of prostate cancer. Acta Oncologica. 2017;56:787-91.

[45] Greer P, Martin J, Sidhom M, Hunter P, Pichler P, Choi JH, et al. A multi-center prospective study for implementation of an MRI-only prostate treatment planning workflow. Frontiers in Oncology. 2019;9:826.

[46] Persson E, Jamtheim Gustafsson C, Ambolt P, Engelholm S, Ceberg S, Bäck S, et al. MR-PROTECT: clinical feasibility of a prostate MRI-only radiotherapy treatment workflow and investigation of acceptance criteria. Radiation Oncology. 2020;15:1-13.

[47] Tyagi N, Fontenla S, Zhang J, Cloutier M, Kadbi M, Mechalakos J, et al. Dosimetric and workflow evaluation of first commercial synthetic CT software for clinical use in pelvis. Physics in Medicine & Biology. 2017;62:2961.

[48] Sun J, Dowling J, Pichler P, Menk F, Rivest-Henault D, Lambert J, et al. MRI simulation: end-to-end testing for prostate radiation therapy using geometric pelvic MRI phantoms. Phys Med Biol. 2015;60:3097-109.

[49] Tenhunen M, Korhonen J, Kapanen M, Seppälä T, Koivula L, Collan J, et al. MRI-only based radiation therapy of prostate cancer: workflow and early clinical experience. Acta Oncologica. 2018;57:902-7.

[50] Edmund JM, Andreasen D, Mahmood F, Van Leemput K. Cone beam computed tomography guided treatment delivery and planning verification for magnetic resonance imaging only radiotherapy of the brain. Acta Oncologica. 2015;54:1496-500.

[51] Bentley R, Milan J. An interactive digital computer system for radiotherapy treatment planning. The British Journal of Radiology. 1971;44:826-33.

[52] Rinks M. Computerised treatment planning systems: where did it all begin? The Radiographer: The Official Journal of the Australian Institute of Radiography. 2012;59:1-4.

[53] Podgorsak EB. Radiation oncology physics: IAEA Vienna; 2005.

[54] Agency IAE. Commissioning and Quality Assurance of Computerized Planning Systems for Radiation Treatment of Cancer. Technical Reports Series No. 430: International Atomic Energy Agency; 2004.

[55] Van Dyk J. Quality assurance of radiation therapy planning systems: current status and remaining challenges. International Journal of Radiation Oncology* Biology* Physics. 2008;71:S23-S7.

[56] Johnstone E, Wyatt JJ, Henry AM, Short SC, Sebag-Montefiore D, Murray L, et al. Systematic Review of Synthetic Computed Tomography Generation Methodologies for Use in Magnetic

Resonance Imaging–Only Radiation Therapy. International Journal of Radiation Oncology• Biology• Physics. 2018;100:199-217.

[57] Boulanger M, Nunes J-C, Chourak H, Largent A, Tahri S, Acosta O, et al. Deep learning methods to generate synthetic CT from MRI in radiotherapy: A literature review. Physica Medica. 2021;89:265-81.

[58] Walker A, Liney G, Metcalfe P, Holloway L. MRI distortion: considerations for MRI based radiotherapy treatment planning. Australas Phys Eng Sci Med. 2014;37:103-13.

[59] Gustafsson C, Nordström F, Persson E, Brynolfsson J, Olsson L. Assessment of dosimetric impact of system specific geometric distortion in an MRI only based radiotherapy workflow for prostate. Physics in Medicine & Biology. 2017;62:2976.

[60] Schmidt MA, Geoffrey SP. Radiotherapy planning using MRI. Physics in Medicine and Biology. 2015;60:R323.

[61] Tanderup K, Viswanathan AN, Kirisits C, Frank SJ. Magnetic Resonance Image Guided Brachytherapy. Seminars in Radiation Oncology. 2014;24:181-91.

[62] Pötter R, Haie-Meder C, Van Limbergen E, Barillot I, De Brabandere M, Dimopoulos J, et al. Recommendations from gynaecological (GYN) GEC ESTRO working group (II): concepts and terms in 3D image-based treatment planning in cervix cancer brachytherapy—3D dose volume parameters and aspects of 3D image-based anatomy, radiation physics, radiobiology. Radiotherapy and Oncology. 2006;78:67-77.

[63] Roberson PL, McLaughlin PW, Narayana V, Troyer S, Hixson GV, Kessler ML. Use and uncertainties of mutual information for computed tomography/magnetic resonance (CT/MR) registration post permanent implant of the prostate. Medical Physics. 2005;32:473-82.

[64] Paulson ES, Erickson B, Schultz C, Li XA. Comprehensive MRI simulation methodology using a dedicated MRI scanner in radiation oncology for external beam radiation treatment planning. Medical Physics. 2015;42:28-39.

[65] Dournes G, Grodzki D, Macey J, Girodet P-O, Fayon M, Chateil J-F, et al. Quiet Submillimeter MR Imaging of the Lung Is Feasible with a PETRA Sequence at 1.5 T. Radiology. 2015;276:258-65.

[66] Hsu S-H, Cao Y, Lawrence TS, Tsien C, Feng M, Grodzki DM, et al. Quantitative characterizations of ultrashort echo (UTE) images for supporting air–bone separation in the head. Physics in Medicine and Biology. 2015;60:2869.

[67] Chen Z, Ma CM, Paskalev K, Li J, Yang J, Richardson T, et al. Investigation of MR image distortion for radiotherapy treatment planning of prostate cancer. Physics in Medicine and Biology. 2006;51:1393.

[68] Spadea MF, Maspero M, Zaffino P, Seco J. Deep learning based synthetic-CT generation in radiotherapy and PET: A review. Medical Physics. 2021;48:6537-66.

[69] Largent A, Barateau A, Nunes J-C, Lafond C, Greer PB, Dowling JA, et al. Pseudo-CT generation for MRI-only radiation therapy treatment planning: comparison among patch-based, atlas-based, and bulk density methods. International Journal of Radiation Oncology* Biology* Physics. 2019;103:479-90.

[70] GmbH SH. MR-only RT planning for brain and pelvis with Synthetic CT White paper.

[71] Persson E, Gustafsson C, Nordström F, Sohlin M, Gunnlaugsson A, Petruson K, et al. MR-OPERA: a Multicenter/Multivendor validation of magnetic resonance Imaging–Only prostate treatment planning using synthetic computed tomography images. International Journal of Radiation Oncology* Biology* Physics. 2017;99:692-700.

[72] Beavis A, Gibbs P, Dealey R, Whitton V. Radiotherapy treatment planning of brain tumours using MRI alone. The British Journal of Radiology. 1998;71:544-8.

[73] Lee YK, Bollet M, Charles-Edwards G, Flower MA, Leach MO, McNair H, et al. Radiotherapy treatment planning of prostate cancer using magnetic resonance imaging alone. Radiotherapy and Oncology. 2003;66:203-16.

[74] Chen L, Price Jr R, Nguyen T, Wang L, Li J, Qin L, et al. Dosimetric evaluation of MRI-based treatment planning for prostate cancer. Physics in Medicine and Biology. 2004;49:5157.

[75] Chen L, Price RA, Wang L, Li J, Qin L, McNeeley S, et al. MRI-based treatment planning for radiotherapy: dosimetric verification for prostate IMRT. International Journal of Radiation Oncology* Biology* Physics. 2004;60:636-47.

[76] Karotki A, Mah K, Meijer G, Meltsner M. Comparison of bulk electron density and voxel-based electron density treatment planning. Journal of Applied Clinical Medical Physics. 2011;12.

[77] Whelan B, Kumar S, Dowling J, Begg J, Lambert J, Lim K, et al. Utilising pseudo-CT data for dose calculation and plan optimization in adaptive radiotherapy. Australas Phys Eng Sci Med. 2015:1-8.

[78] Jonsson J, Karlsson M, Karlsson M, Nyholm T. Treatment planning using MRI data: an analysis of the dose calculation accuracy for different treatment regions. Radiation Oncology. 2010;5:62.

[79] Dowling JA, Lambert J, Parker J, Salvado O, Fripp J, Capp A, et al. An Atlas-Based Electron Density Mapping Method for Magnetic Resonance Imaging (MRI)-Alone Treatment Planning and Adaptive MRI-Based Prostate Radiation Therapy. International Journal of Radiation Oncology*Biology*Physics. 2012;83:e5-e11.

[80] Dowling JA, Sun J, Pichler P, Rivest-Hénault D, Ghose S, Richardson H, et al. Automatic substitute CT generation and contouring for MRI-alone external beam radiation therapy from standard MRI sequences. International Journal of Radiation Oncology • Biology • Physics. 2015.

[81] Uh J, Merchant TE, Li Y, Li X, Hua C. MRI-based treatment planning with pseudo CT generated through atlas registration. Medical Physics. 2014;41:051711.

[82] Dowling JA, Sun J, Pichler P, Rivest-Hénault D, Ghose S, Richardson H, et al. Automatic substitute computed tomography generation and contouring for magnetic resonance imaging (MRI)-Alone external beam radiation therapy from standard MRI sequences. International Journal of Radiation Oncology* Biology* Physics. 2015;93:1144-53.

[83] Bahrami A, Karimian A, Arabi H. Comparison of different deep learning architectures for synthetic CT generation from MR images. Physica Medica. 2021;90:99-107.

[84] Largent A, Barateau A, Nunes J-C, Mylona E, Castelli J, Lafond C, et al. Comparison of deep learning-based and patch-based methods for pseudo-CT generation in MRI-based prostate dose planning. International Journal of Radiation Oncology* Biology* Physics. 2019;105:1137-50.

[85] Li Y, Li W, He P, Xiong J, Xia J, Xie Y. CT synthesis from MRI images based on deep learning methods for MRI-only radiotherapy. 2019 International Conference on Medical Imaging Physics and Engineering (ICMIPE)2019. p. 1-6.

[86] Liu F, Yadav P, Baschnagel AM, McMillan AB. MR-based treatment planning in radiation therapy using a deep learning approach. Journal of Applied Clinical Medical Physics. 2019;20:105-14.

[87] LeCun Y, Bengio Y, Hinton G. Deep learning. Nature. 2015;521:436-44.

[88] Goodfellow I, Pouget-Abadie J, Mirza M, Xu B, Warde-Farley D, Ozair S, et al. Generative adversarial networks. Communications of the ACM. 2020;63:139-44.

[89] Sahiner B, Pezeshk A, Hadjiiski LM, Wang X, Drukker K, Cha KH, et al. Deep learning in medical imaging and radiation therapy. Medical Physics. 2019;46:e1-e36.

[90] Liu Y, Lei Y, Wang T, Kayode O, Tian S, Liu T, et al. MRI-based treatment planning for liver stereotactic body radiotherapy: validation of a deep learning-based synthetic CT generation method. The British Journal of Radiology. 2019;92:20190067.

[91] Dinkla AM, Florkow MC, Maspero M, Savenije MH, Zijlstra F, Doornaert PA, et al. Dosimetric evaluation of synthetic CT for head and neck radiotherapy generated by a patch-based three-dimensional convolutional neural network. Medical Physics. 2019;46:4095-104.

[92] Klages P, Benslimane I, Riyahi S, Jiang J, Hunt M, Deasy JO, et al. Patch-based generative adversarial neural network models for head and neck MR-only planning. Medical Physics. 2020;47:626-42.

[93] Johansson A, Karlsson M Fau - Nyholm T, Nyholm T. CT substitute derived from MRI sequences with ultrashort echo time. Medical Physics. 2011.

[94] Johansson A, Karlsson M, Yu J, Asklund T, Nyholm T. Voxel-wise uncertainty in CT substitute derived from MRI. Medical Physics. 2012;39:3283-90.

[95] Andreasen D, Van Leemput K, Hansen RH, Andersen JA, Edmund JM. Patch-based generation of a pseudo CT from conventional MRI sequences for MRI-only radiotherapy of the brain. Medical Physics. 2015;42:1596-605.

[96] Hsu S-H, Cao Y, Huang K, Feng M, Balter JM. Investigation of a method for generating synthetic CT models from MRI scans of the head and neck for radiation therapy. Physics in Medicine and Biology. 2013;58:8419.

[97] O'Connor LM, Skehan K, Choi JH, Simpson J, Martin J, Warren-Forward H, et al. Optimisation and validation of an integrated magnetic resonance imaging-only radiotherapy planning solution. Physics and imaging in radiation oncology. 2021;20:34-9.

[98] Farjam R, Tyagi N, Deasy JO, Hunt MA. Dosimetric evaluation of an atlas-based synthetic CT generation approach for MR-only radiotherapy of pelvis anatomy. Journal of Applied Clinical Medical Physics. 2019;20:101-9.

[99] Siversson C, Nordström F, Nilsson T, Nyholm T, Jonsson J, Gunnlaugsson A, et al. Technical Note: MRI only prostate radiotherapy planning using the statistical decomposition algorithm. Medical Physics. 2015;42:6090-7.

[100] Palmér E, Karlsson A, Nordström F, Petruson K, Siversson C, Ljungberg M, et al. Synthetic computed tomography data allows for accurate absorbed dose calculations in a magnetic

resonance imaging only workflow for head and neck radiotherapy. Physics and Imaging in Radiation Oncology. 2021;17:36-42.

[101] Kupelian P, Sonke J-J. Magnetic Resonance–Guided Adaptive Radiotherapy: A Solution to the Future. Seminars in Radiation Oncology. 2014;24:227-32.

[102] Hall WA, Paulson ES, van der Heide UA, Fuller CD, Raaymakers BW, Lagendijk JJW, et al. The transformation of radiation oncology using real-time magnetic resonance guidance: A review. European Journal of Cancer. 2019;122:42-52.

[103] Liney GP, Whelan B, Oborn B, Barton M, Keall P. MRI-linear accelerator radiotherapy systems. Clinical Oncology. 2018;30:686-91.

[104] Raaijmakers AJE, Raaymakers BW, Lagendijk JJW. Experimental verification of magnetic field dose effects for the MRI-accelerator. Physics in Medicine and Biology. 2007;52:4283.

[105] Lagendijk JJW, Raaymakers BW, Raaijmakers AJE, Overweg J, Brown KJ, Kerkhof EM, et al. MRI/linac integration. Radiotherapy and Oncology. 2008;86:25-9.

[106] Raaymakers BW, Lagendijk JJW, Overweg J, Kok JGM, Raaijmakers AJE, Kerkhof EM, et al. Integrating a 1.5 T MRI scanner with a 6 MV accelerator: proof of concept. Physics in Medicine and Biology. 2009;54:N229.

[107] Raaymakers BW, Jürgenliemk-Schulz I, Bol G, Glitzner M, Kotte A, Van Asselen B, et al. First patients treated with a 1.5 T MRI-Linac: clinical proof of concept of a high-precision, high-field MRI guided radiotherapy treatment. Physics in Medicine & Biology. 2017;62:L41.

[108] Tijssen RHN, Philippens MEP, Paulson ES, Glitzner M, Chugh B, Wetscherek A, et al. MRI commissioning of 1.5T MR-linac systems – a multi-institutional study. Radiotherapy and Oncology. 2019;132:114-20.

[109] Winkel D, Bol GH, Kroon PS, van Asselen B, Hackett SS, Werensteijn-Honingh AM, et al. Adaptive radiotherapy: the Elekta Unity MR-linac concept. Clinical and Translational Radiation Oncology. 2019;18:54-9.

[110] Mutic S, Dempsey JF. The ViewRay System: Magnetic Resonance–Guided and Controlled Radiotherapy. Seminars in Radiation Oncology. 2014;24:196-9.

[111] Acharya S, Fischer-Valuck BW, Kashani R, Parikh P, Yang D, Zhao T, et al. Online magnetic resonance image guided adaptive radiation therapy: first clinical applications. International Journal of Radiation Oncology* Biology* Physics. 2016;94:394-403.

[112] Klüter S. Technical design and concept of a 0.35 T MR-Linac. Clinical and Translational Radiation Oncology. 2019;18:98-101.

[113] Fallone BG. The Rotating Biplanar Linac–Magnetic Resonance Imaging System. Seminars in Radiation Oncology. 2014;24:200-2.

[114] Keall PJ, Barton M, Crozier S. The Australian Magnetic Resonance Imaging–Linac Program. Seminars in Radiation Oncology. 2014;24:203-6.

[115] Whelan B, Liney GP, Dowling JA, Rai R, Holloway L, McGarvie L, et al. An MRI-compatible patient rotation system — design, construction, and first organ deformation results. Medical Physics. 2017;44:581-8.

[116] Yan D, Jaffray DA, Wong J, Vicini F, Martinez A. Clinical implementation of adaptive radiation therapy. Radiotherapy and Oncology. 1995;37:S61.

[117] Yan D. Treatment strategy for daily image feedback adaptive radiotherapy. The Use of Computers in Radiation Therapy: Springer; 2000. p. 518-20.

[118] Wu QJ, Li T, Wu Q, Yin F-F. Adaptive Radiation Therapy: Technical Components and Clinical Applications. The Cancer Journal. 2011;17:182-9.

[119] Brock K. Adaptive Radiotherapy: Moving Into the Future. Seminars in Radiation Oncology: WB Saunders Ltd; 2019. p. 181-4.

[120] Matuszak MM, Kashani R, Green M, Owen D, Jolly S, Mierzwa M. Functional Adaptation in Radiation Therapy. Seminars in Radiation Oncology: Elsevier; 2019. p. 236-44.

[121] Sonke J-J, Aznar M, Rasch C. Adaptive radiotherapy for anatomical changes. Seminars in Radiation Oncology: Elsevier; 2019. p. 245-57.

[122] Hunt A, Hansen V, Oelfke U, Nill S, Hafeez S. Adaptive radiotherapy enabled by MRI guidance. Clinical Oncology. 2018;30:711-9.

[123] van Herk M, McWilliam A, Dubec M, Faivre-Finn C, Choudhury A. Magnetic Resonance Imaging–Guided Radiation Therapy: A Short Strengths, Weaknesses, Opportunities, and Threats Analysis. International Journal of Radiation Oncology• Biology• Physics. 2018;101:1057-60.

[124] Green OL, Henke LE, Hugo GD. Practical Clinical Workflows for Online and Offline Adaptive Radiation Therapy. Seminars in radiation oncology: Elsevier; 2019. p. 219-27.

[125] Archambault Y, Boylan C, Bullock D, Morgas T, Peltola J, Ruokokoski E, et al. Making on-line adaptive radiotherapy possible using artificial intelligence and machine learning for efficient daily re-planning. Med Phys Int J. 2020;8.

[126] Sibolt P, Andersson LM, Calmels L, Sjöström D, Bjelkengren U, Geertsen P, et al. Clinical implementation of artificial intelligence-driven cone-beam computed tomography-guided online adaptive radiotherapy in the pelvic region. Physics and Imaging in Radiation Oncology. 2021;17:1-7.

[127] Byrne M, Archibald-Heeren B, Hu Y, Teh A, Beserminji R, Cai E, et al. Varian ethos online adaptive radiotherapy for prostate cancer: Early results of contouring accuracy, treatment plan quality, and treatment time. Journal of Applied Clinical Medical Physics. 2022;23:e13479.

[128] Chetty IJ, Rosu-Bubulac M. Deformable Registration for Dose Accumulation. Seminars in radiation oncology: Elsevier; 2019. p. 198-208.

[129] Paganelli C, Meschini G, Molinelli S, Riboldi M, Baroni G. Patient-specific validation of deformable image registration in radiation therapy: Overview and caveats. Medical Physics. 2018;45:e908-e22.

[130] Wang H, Dong L, O'Daniel J, Mohan R, Garden AS, Ang KK, et al. Validation of an accelerated 'demons' algorithm for deformable image registration in radiation therapy. Physics in Medicine and Biology. 2005;50:2887-905.

[131] Schreibmann E, Pantalone P, Waller A, Fox T. A measure to evaluate deformable registration fields in clinical settings. Journal of Applied Clinical Medical Physics. 2012;13:126-39.

[132] Hardcastle N, van Elmpt W, De Ruysscher D, Bzdusek K, Tomé WA. Accuracy of deformable image registration for contour propagation in adaptive lung radiotherapy. Radiation Oncology. 2013;8:243.

[133] Kirby N, Chen J, Kim H, Morin O, Nie K, Pouliot J. An automated deformable image registration evaluation of confidence tool. Physics in Medicine & Biology. 2016;61:N203.

[134] Pukala J, Johnson PB, Shah AP, Langen KM, Bova FJ, Staton RJ, et al. Benchmarking of five commercial deformable image registration algorithms for head and neck patients. Journal of Applied Clinical Medical Physics. 2016;17:25-40.

[135] Broggi S, Scalco E, Belli ML, Logghe G, Verellen D, Moriconi S, et al. A comparative evaluation of 3 different free-form deformable image registration and contour propagation methods for head and neck MRI: the case of parotid changes during radiotherapy. Technology in Cancer Research & Treatment. 2017;16:373-81.

[136] Rigaud B, Simon A, Castelli J, Lafond C, Acosta O, Haigron P, et al. Deformable image registration for radiation therapy: principle, methods, applications and evaluation. Acta Oncologica. 2019:1-13.

[137] Brock KK, Mutic S, McNutt TR, Li H, Kessler ML. Use of image registration and fusion algorithms and techniques in radiotherapy: Report of the AAPM Radiation Therapy Committee Task Group No. 132. Medical Physics. 2017;44:e43-e76.

[138] Obeidat M, Narayanasamy G, Cline K, Stathakis S, Pouliot J, Kim H, et al. Comparison of different QA methods for deformable image registration to the known errors for prostate and head-and-neck virtual phantoms. Biomedical Physics & Engineering Express. 2016;2:067002.

[139] Castadot P, Lee JA, Parraga A, Geets X, Macq B, Grégoire V. Comparison of 12 deformable registration strategies in adaptive radiation therapy for the treatment of head and neck tumors. Radiotherapy and Oncology. 2008;89:1-12.

[140] Murr M, Brock KK, Fusella M, Hardcastle N, Hussein M, Jameson MG, et al. Applicability and usage of dose mapping/accumulation in radiotherapy. Radiotherapy and Oncology. 2023:109527.

[141] Maciejewski B, Withers HR, Taylor JM, Hliniak A. Dose fractionation and regeneration in radiotherapy for cancer of the oral cavity and oropharynx. Part 2. Normal tissue responses: acute and late effects. International Journal of Radiation Oncology* Biology* Physics. 1990;18:101-11.

[142] Thames H, Bentzen S, Turesson I, Overgaard M, Van den Bogaert W. Time-dose factors in radiotherapy: a review of the human data. Radiotherapy and Oncology. 1990;19:219-35.

[143] Yan D, Jaffray D, Wong J. A model to accumulate fractionated dose in a deforming organ. International Journal of Radiation Oncology* Biology* Physics. 1999;44:665-75.

[144] Roussakis Y, Dehghani H, Green S, Webster G. Validation of a dose warping algorithm using clinically realistic scenarios. The British Journal of Radiology. 2015;88:20140691.

[145] Vickress J, Battista J, Barnett R, Yartsev S. Representing the dosimetric impact of deformable image registration errors. Physics in Medicine & Biology. 2017;62:N391.

[146] Qin A, Liang J, Han X, O'Connell N, Yan D. The impact of deformable image registration methods on dose warping. Medical Physics. 2018;45:1287-94.

[147] Takemura A, Nagano A, Kojima H, Ikeda T, Yokoyama N, Tsukamoto K, et al. An uncertainty metric to evaluate deformation vector fields for dose accumulation in radiotherapy. Physics and Imaging in Radiation Oncology. 2018;6:77-82.

[148] Zhang L, Wang Z, Shi C, Long T, Xu XG. The impact of robustness of deformable image registration on contour propagation and dose accumulation for head and neck adaptive radiotherapy. Journal of Applied Clinical Medical Physics. 2018;19:185-94.

[149] Lu W, Mackie TR, Keller H, Ruchala KJ, Olivera GH. A generalization of adaptive radiotherapy and the registration of deformable dose distributions. The Use of Computers in Radiation Therapy: Springer; 2000. p. 521-3.

[150] Jaffray DA, Lindsay PE, Brock KK, Deasy JO, Tomé WA. Accurate accumulation of dose for improved understanding of radiation effects in normal tissue. International Journal of Radiation Oncology* Biology* Physics. 2010;76:S135-S9.

[151] Rigaud B, Klopp A, Vedam S, Venkatesan A, Taku N, Simon A, et al. Deformable image registration for dose mapping between external beam radiotherapy and brachytherapy images of cervical cancer. Physics in Medicine & Biology. 2019;64:115023.

[152] Heukelom J, Fuller CD. Head and Neck Cancer Adaptive Radiation Therapy (ART): Conceptual Considerations for the Informed Clinician. Seminars in Radiation Oncology: Elsevier; 2019. p. 258-73.

[153] Kavanaugh J, Hugo G, Robinson CG, Roach MC. Anatomical Adaptation—Early Clinical Evidence of Benefit and Future Needs in Lung Cancer. Seminars in Radiation Oncology: Elsevier; 2019. p. 274-83.

[154] Wu RY, Liu AY, Wisdom P, Zhu XR, Frank SJ, Fuller CD, et al. Characterization of a new physical phantom for testing rigid and deformable image registration. Journal of Applied Clinical Medical Physics. 2019;20:145-53.

[155] Keall P, Poulsen P, Booth JT. See, Think, and Act: Real-Time Adaptive Radiotherapy. Seminars in Radiation Oncology: Elsevier; 2019. p. 228-35.

[156] Jaffray DA, Carlone MC, Milosevic MF, Breen SL, Stanescu T, Rink A, et al. A Facility for Magnetic Resonance–Guided Radiation Therapy. Seminars in Radiation Oncology. 2014;24:193-5.

[157] Lagendijk JJW, Raaymakers BW, van Vulpen M. The Magnetic Resonance Imaging–Linac System. Seminars in Radiation Oncology. 2014;24:207-9.

[158] Oborn BM, Dowdell S, Metcalfe PE, Crozier S, Mohan R, Keall PJ. Future of Medical Physics: Real-time MRI-Guided Proton Therapy. Medical Physics. 2017;44:e77-e90.

[159] Pham TT, Whelan B, Oborn BM, Delaney GP, Vinod S, Brighi C, et al. Magnetic resonance imaging (MRI) guided proton therapy: A review of the clinical challenges, potential benefits and pathway to implementation. Radiotherapy and Oncology. 2022;170:37-47.

[160] De Mol Van Otterloo S, Christodouleas JP, Blezer EL, Akhiat H, Brown K, Choudhury A, et al. Patterns of Care, Tolerability, and Safety of the First Cohort of Patients Treated on a Novel

High-Field MR-Linac Within the MOMENTUM Study: Initial Results From a Prospective Multi-Institutional Registry. International Journal of Radiation: Oncology-Biology-Physics. 2021.

[161] Strand S, Boczkowski A, Smith B, Snyder JE, Hyer DE, Yaddanapudi S, et al. Analysis of patient-specific quality assurance for Elekta Unity adaptive plans using statistical process control methodology. Journal of Applied Clinical Medical Physics. 2021;22:99-107.

[162] Nierer L, Eze C, da Silva Mendes V, Braun J, Thum P, von Bestenbostel R, et al. Dosimetric benefit of MR-guided online adaptive radiotherapy in different tumor entities: liver, lung, abdominal lymph nodes, pancreas and prostate. Radiation Oncology. 2022;17:1-14.

[163] Jonsson J, Nyholm T, Söderkvist K. The rationale for MR-only treatment planning for external radiotherapy. Clinical and Translational Radiation Oncology. 2019;18:60-5.

[164] Nousiainen K, Santurio GV, Lundahl N, Cronholm R, Siversson C, Edmund JM. Evaluation of MRI-only based online adaptive radiotherapy of abdominal region on MR-linac. Journal of Applied Clinical Medical Physics. 2022:e13838.

3 Assessment of Electron Density Effects on Dose Calculation and Optimisation Accuracy for Nasopharynx, for MRI-Only Treatment Planning

3.1 Presentations and Publications

Initial work was presented at EPSM 2016, Engineering and Physical Sciences in Medicine on 6th – 10th November 2016 in Sydney, Australia under the poster presentation titled "Assessment of Electron Density Effects for MRI Only Treatment Planning". A copy of the accepted abstract is presented in thesis Appendix 1.

This work was published as a scientific paper in Physical and Engineering Sciences in Medicine in 2018. The reference is as follows - Young, T., Thwaites, D. & Holloway, L. Assessment of electron density effects on dose calculation and optimisation accuracy for nasopharynx, for MRI only treatment planning. Australasian Physical & Engineering Sciences in Medicine 41, 811–820 (2018). https://doi.org/10.1007/s13246-018-0675-2

This publication is presented as this chapter. Any additions to the original publication are presented in *italics.*

3.2 Preamble

MRI-only treatment planning generally considers the accuracy of Hounsfield unit (HU) generation and similarity to computed tomography (CT) in assessment of suitability of the synthetic CT (sCT) generated. Very few investigations have been reported into the effect of the potential differences in HU between gold standard CT and generated sCT on treatment plan optimization.

The purpose of this work was to investigate the impact of electron density effects alone on dose calculation and optimization accuracy for nasopharynx head and neck patients. It is challenging to address this with actual sCT data which is also influenced by other potential uncertainties from sCT generation from MRI, such as image distortion, patient setup differences and patient motion. As this work was completed on CT data, with bulk density overrides to assess the potential variation in both dose calculation and optimization accuracy, the potential uncertainty was limited to effects of electron density. This study only focuses on the head and neck region, and areas with larger potential variations in HU may have different optimization differences.

3.3 Publication - Assessment of Electron Density Effects on Dose Calculation and Optimisation Accuracy for Nasopharynx, for MRI Only Treatment Planning

Tony Young

Liverpool and Macarthur Cancer Therapy Centres and Ingham Institute, Sydney, Australia.

Institute of Medical Physics, School of Physics, University of Sydney, Sydney, Australia

Tony.Young@health.nsw.gov.au

David Thwaites

Institute of Medical Physics, School of Physics, University of Sydney, Sydney, Australia.

david.thwaites@sydney.edu.au

Lois Holloway

Liverpool and Macarthur Cancer Therapy Centres and Ingham Institute, Sydney, Australia.

University of New South Wales, Sydney, New South Wales, Australia

Institute of Medical Physics, School of Physics, University of Sydney, Australia.

Centre for Medical Radiation Physics, University of Wollongong, Wollongong,

New South Wales, Australia

lois.holloway@health.nsw.gov.au

Abstract

Introduction

Computed Tomography (CT) is the gold standard for radiotherapy simulation and treatment planning, providing spatial accuracy, bony anatomy definition and electron density information for dose calculations. Magnetic Resonance Imaging (MRI) has been introduced in radiotherapy to improve visualisation of anatomy for accurate target definition and contouring, however lacks electron density information required for dose calculations, with various methods used to overcome this. The aim of this work is to assess the impact on dose calculation accuracy and optimisation results of different

approaches to determine electron density, as could be used in MRI Only treatment planning for nasopharyngeal datasets with VMAT treatment plans.

Method

Volumetric Modulated Arc Therapy (VMAT) plans were created for 10 retrospective Head and Neck (H&N) nasopharyngeal patients. The VMAT plans were generated on the gold standard dataset, the original CT scan. Data sets with no density correction (water equivalent) and two different sets of bulk density correction for bone/air/tissue applied separately were generated for these patients and the VMAT plans were recalculated for each case. Plans were also reoptimised on these data sets, and recalculated. Optimisation error was assessed through Equivalent Uniform Dose (EUD) differences. Additionally, point dose comparison, Dose Volume Histogram (DVH) analysis and gamma analysis of dose were used to assess dose calculation error.

Results

The dose calculation error on average was an increase in EUD whereas the optimisation error on average was a reduction in EUD compared to the original plan for all datasets aside from the bone only override dataset where bone was set to 1.61 g/cm^3. For the optimisation error, the largest mean absolute error (MAE) was 1.88 Gy EUD for the PTV, and 2.21 Gy EUD for the brainstem, for the reoptimisation completed on the air only overridden dataset, and recalculated on the original. Bulk density corrections for bone and air provide dose calculations within 3% of the original treatment plans.

Conclusion

Optimisation errors have the potential to be greater than dose calculation errors if incorrect density corrections are utilized. Electron density correction using a bulk density approach achieves dose calculation uncertainties within 3%, however more advanced approaches, such as a voxel based approach, may improve accuracy and should be considered.

Introduction

Computed Tomography (CT) is the gold standard for radiotherapy simulation and treatment planning, providing spatial accuracy, bony anatomy definition and electron density information for radiotherapy dose calculations. Use of Magnetic Resonance Imaging (MRI) is increasing in radiotherapy as MRI offers improved soft tissue definition for accurate target definition and organ contouring. In

radiotherapy this is achieved by fusion of the MRI scan with the CT scan, introducing registration error and potential errors from possible variations in patient setup and internal organ motion [1]. MRI only radiotherapy treatment planning would remove current registration errors, reported to be of the order of 2 mm [2, 3], and remove the need for additional scans, lowering workload from redundant imaging and financial cost. MRI however lacks electron density information required for radiotherapy dose calculations. With the development of MRI-simulators [4, 5] and on-line MRI guided treatment delivery systems [6-8], the need for MRI-only radiotherapy has emerged and grown. MRI only radiotherapy with MRI-linacs further enable online adaptive radiotherapy. Various methodologies to introduce MRI only radiotherapy for various treatment sites have been trialled [9-15], utilizing the improved anatomical visualization whilst correcting for the lack of electron density information. The varying methods of estimating electron density information from MRI for both radiation therapy and attenuation correction also need to consider geometric distortion, due to magnetic field inhomogeneities, gradient nonlinearity, and patient induced susceptibility.

Initial methods considering the use of MRI only for radiotherapy involved comparisons of MRI to CT with minimal density corrections. These initial studies used manually segmented bulk density corrections for tissue, bone, lung and air, with results reported to be within approximately 2% compared to the same plan applied on a CT dataset [2, 16]. These initial studies were mostly in prostate cancer treatment. Lee et al. in 2003 [17] showed differences greater than 2% for conformal radiotherapy plans with no inhomogeneity correction, and negligible differences with bulk density assignment for bone in prostate. Chen et al. [18, 19] published a similar study in 2004 considering similar scenarios for prostate Intensity Modulated Radiation Therapy (IMRT). In Chen's study, the absolute dose agreement for the planning target volume with these IMRT plans was within 2% between CT based and MRI based plans, and 3% between phantom-measured dose and dose predicted by the TPSs. This study did however make note that the MR imaging based digitally reconstructed radiographs did not provide adequate bony structure information, with this issue requiring further work for MRI to replace CT in the simulation process. More recently Karotki et al. [20] conducted a similar study for brain lesions, and Whelan et al., [21] considered gynaecological cancers. Jonsson et al. [22] conducted a retrospective study of 40 patients across prostate, lung, head and neck (H&N) and brain cancer treatment sites. Bulk density corrections were assigned using manual segmentation of bone, tissue, lung and air cavities on the MRI scan, and calculations were made between CT data with and without inhomogeneity corrections, and on MRI or CT data with bulk density assignments. This comparison included the effects of geometric distortion, with values of the bulk density assigned plans within 1% of the CT plans with inhomogeneity correction for all patient groups. This study also showed that of the treatment sites considered dose calculations for prostate treatments were the most sensitive to the choice of bulk density value due to the femoral head and pelvic bone effects to the radiation field. Additionally, Karotki et al. considered electron density for MRI planning, comparing homogenous and bulk density corrected plans for H&N

[20]. This study concluded that for H&N treatment plans, variations in PTV coverage of greater than 2% were observed for the homogenous plans in 7/10 patients, with these variations reducing to within 2% when bulk density corrections were applied. Further work includes an atlas based electron density mapping method to automatically segment and apply the appropriate bulk density correction, with some success reported for prostate cases [9]

The accuracy in the bulk density corrections will affect the accuracy of the final dose calculation. AAPM Report No. 85, report of TG-65 "Tissue inhomogeneity corrections for megavoltage photon beams" [23] discusses the influence of CT number variations, stating accurate dose calculation not only requires an accurate calculation algorithm or model of the machine data, but also an accurate calibration of Hounsfield Unit (HU) for CT based inhomogeneity corrections prior to dose calculation. Chu et al. [24] studied the variation of CT number and the effect of this variation on photon dose calculations. This study found that the dose uncertainty, due to CT number uncertainty, for a 6 MV beam is less than 2% up to a 20 cm depth. Additionally, dose calculations were conducted for changes of 20 HU in soft tissue and 250 HU for bone in brain, lung, and pelvis cases. These HU changes produced a change in MU of less than 1% in the brain, and less than 2% in the lung and pelvis cases. Cozzi et al. [25] compared an average calibration table provided by the manufacturer against a measured customer calibration. A difference in HU for high density materials was found of approximately 300 HU, with the maximum dosimetric error determined to be 2%, with on average the error being below 1% for the conformal treatment plans considered. In essence, the effect of electron density uncertainties has relatively minor effects on the accuracy of the dose calculation.

The assessment of optimisation error, that is the impact on the optimisation result due to errors in the electron density, is often overlooked when considering dose accuracy in these studies. Whelan et al. [21] assessed optimisation error in cervix treatment plans, finding that optimisation errors in their study were greater than dose calculation errors alone, with the largest optimisation errors occurring in the least heavily weighted organs in the inverse planning prescription. The study did conclude that the optimisation error, although not resulting in an incorrect record of dose, resulted in a sub optimal plan, and should be considered when assessing impact of electron density. The impact of an optimisation error due to uncertainties in electron density has not been previously considered for H&N plans.

The current study investigated the effect of optimising VMAT treatment plans on datasets with varying electron density corrections as applied to H&N CT images for dose calculation, as well as the clinical impact of variations in density correction for dose calculation. The impact of the variations will be useful in the assessment of conversion accuracy of MRI datasets for MRI only treatment planning and gives information on the robustness of the results using the initial set.

Method

Data Set Creation

Ten retrospective Head and Neck (H&N) nasopharyngeal patients with their original CT datasets were used for the study. Bone and air within the datasets were contoured. The original datasets, with these contours, were density corrected in various ways to produce image data sets with different electron density (ED) features as per table 3.1. Two sets of bulk density values were used for bone and air respectively – the first set used a value of 1.61 g/cm^3 as recommended by ICRU 46 for cranium bone [26, 27] and 0.001 g/cm^3 for air. To test robustness to density values, a second set of values was used, with 1.3 g/cm^3 being a mid range bone density as per CT to ED conversion phantoms [28], and 0.3 g/cm^3 chosen as a quite different value, however one still found in the body where tissue and air are mixed.

Table 3.1 - Data sets used in the study.

Dataset	Description	
Original CT	The original CT data set – gold standard electron density data	
Homogenous	Entire patient data set ED changed to water equivalent value of 1 g/cm^3	
	Set 1	Set 2
Bone Only Override	Bones set to an ED of 1.61 g/cm^3. The rest of the patient data set was set to ED of 1 g/cm^3.	Bones set to an ED of 1.3 g/cm^3. The rest of the patient data set was set to ED of 1 g/cm^3.
Air Only Override	Air set to an ED of 0.001 g/cm^3. The rest of the patient data set was set to ED of 1 g/cm^3.	Air set to an ED of 0.3 g/cm^3. The rest of the patient data set was set to ED of 1 g/cm^3.
Bone and Air Override	Bones set to an ED of 1.61 g/cm^3. Air set to an ED of 0.001 g/cm^3. The rest of the patient data set was set to an ED of 1 g/cm^3.	Bones set to an ED of 1.3 g/cm^3. Air set to an ED of 0.3 g/cm^3. The rest of the patient data set was set to an ED of 1 g/cm^3.

Treatment Planning

All patients had clinically acceptable Volumetric Modulated Arc Therapy (VMAT) plans created using the Pinnacle TPS (v9.10) on the original CT data set. These plans were recalculated on the additional data sets listed in table 3.1. Plans were also reoptimised on the homogenous, bone only override and air only override data sets with no change in the original prescription values for target and organs at risk which produced the clinically acceptable plan on the original CT dataset. The plans were re-optimised

until an equivalent coverage to the original plan was reached, or the optimisation reached a plateau. This reoptimised plan was then recalculated on the original CT data set to assess optimisation error. *All plans were calculated using the Pinnacle Adaptive Convolution algorithm.* Combinations are shown in Table 3.2.

Table 3.2 - Different plan optimisation and dose calculation combinations investigated.

Plan Label	Plan Optimisation	Plan Dose Calculation
Case 1 (Original plan)	Correct electron density	Correct electron density
Case 2 (Dose calculation error)	Correct electron density	Incorrect electron density
Case 3 (Optimisation and dose calculation error)	Incorrect electron density	Incorrect electron density
Case 4 (Optimisation error)	Incorrect electron density	Correct electron density

Analysis

All newly created plans were compared to the original plan on the original CT using 3DVH software (v3.0) (Sun Nuclear, FL). These new plans were assessed for dose calculation and optimisation error through point dose comparison, Dose Volume Histogram (DVH) analysis and global gamma analysis of dose. The isocentre point dose as well as a dose point in the high dose planning target volume (PTV) were compared. The high dose point was placed centrally within the high dose target volume away from heterogeneity. Additionally, plans were compared by assessing Equivalent Uniform Dose (EUD) differences using in-house MATLAB code, with a tissue parameter "a" value of -10 for the PTV volume and 7 for the brainstem [21, 29, 30]. All plans were compared against the original treatment plan with the correct electron density (case 1).

Results

Point Dose Comparison for Density Overridden Plans (Case 2)

Isocentre point dose results for the different data sets with varying densities overridden were all within 4% when compared to the original CT dataset, as shown in table 3.3. Variations for the high dose point dose were of similar magnitude to the isocentre point, as shown in table 3.4.

Table 3.3 - Isocentre Point Dose Comparison for different density corrected plans (Set 1/Set 2).

Patient	1	2	3	4	5	6	7	8	9	10
Homogenous	-0.28%	1.29%	2.08%	2.62%	0.25%	1.50%	1.83%	1.54%	1.72%	3.40%
Bone Only Override	-0.07% / -0.37%	-1.37% / 0.06%	-2.63% / -0.29%	-1.27% / 0.74%	0.46% / 0.36%	-1.21% / 0.17%	-1.07% / 0.45%	-0.06% / 0.78%	0.90% / 1.33%	-1.30% / 0.97%
Air Only Override	-0.46% / -0.54%	1.03% / 1.09%	2.16% / 2.13%	3.09% / 2.96%	1.69% / 1.07%	1.43% / 1.43%	1.68% / 1.72%	1.07% / 1.64%	1.82% / 1.74%	3.10% / 3.20%
Bone and Air Override	-0.24% / -0.36%	-1.62% / -0.13%	-2.60% / -0.25%	-0.79% / 1.09%	1.65% / 1.15%	-1.32% / 0.09%	-1.21% / 0.34%	-0.48% / 0.87%	1.01% / 1.35%	-1.58% / 0.77%

Table 3.4 - High Dose Point Dose Differences within the PTV for different density corrected plans (Set 1/Set 2).

Patient	1	2	3	4	5	6	7	8	9	10
Homogenous	-1.17%	3.27%	1.87%	2.99%	3.87%	2.94%	2.99%	-0.65%	2.36%	2.89%
Bone Only Override	0.11% / -0.33%	0.88% / 2.09%	-0.98% / 0.45%	0.58% / 1.82%	1.52% / 2.80%	-0.74% / 1.11%	-0.66% / 1.16%	-2.55% / -1.62%	0.77% / 1.59%	0.21% / 1.55%
Air Only Override	-0.69% / -0.98%	3.24% / 3.26%	3.40% / 2.96%	2.98% / 3.01%	3.86% / 3.93%	3.10% / 3.06%	3.10% / 3.08%	2.94% / 1.91%	2.13% / 2.20%	2.77% / 2.81%
Bone and Air Override	0.61% / -0.33%	0.83% / 2.08%	0.47% / 1.50%	0.49% / 1.83%	1.41% / 2.73%	-0.70% / 1.16%	-0.54% / 1.26%	0.88% / 0.89%	0.57% / 1.44%	0.10% / 1.48%

Global Gamma Results for Density Overridden Plans (Case 2)

Global gamma results using re-calculated plans were acceptable meeting a 95% pass rate using a 3%/3mm gamma criteria with a 10% dose threshold (Table 3.5). These gamma results improved in the bone and air override data sets for set 2 only as they are closest to the original fully corrected CT datasets. On average, the gamma results for set 2 datasets were better than set 1 datasets.

Table 3.5 - 3%/3mm Global Gamma Results (% of points passing) for the Different Density Corrected Plans (Set 1/Set 2).

Patient	1	2	3	4	5	6	7	8	9	10
Homogenous	99.7	99.6	99.6	99.3	99.0	99.3	99.4	99.3	97.7	99.4
Bone Only Override	99.5/ 98.0	99.2/ 99.9	99.6/ 99.8	99.0/ 99.7	99.2/ 99.6	99.3/ 99.7	99.5/ 99.7	97.6/ 99.2	99.5/ 99.7	99.2/ 99.8
Air Only Override	98.2/ 99.9	98.4/ 99.2	99.3/ 99.5	97.6/ 98.8	97.8/ 98.6	98.1/ 99.0	98.0/ 99.2	98.3/ 98.8	96.5/ 97.1	97.7/ 98.9
Bone and Air Override	98.1/ 100	99/ 99.9	99.4/ 99.9	98.2/ 99.8	95.0/ 99.6	98.5/ 99.8	98.3/ 99.7	98.7/ 99.6	98.5/ 99.7	98.1/ 99.8

Reoptimised Plans on Density Corrected Datasets Results (Case 3)

Reoptimised plans on the different density corrected data sets showed large discrepancies when compared to the clinically accepted distributions in the original plans. Large variations were observed in the DVH distributions for some organs at risk, i.e. brainstem. The PTV DVH results show only minor differences as plans were reoptimised until similar target coverage was achieved (if possible). Patient 1 and 4 set 2 DVH distributions for PTV and brainstem are shown (Figure 3.1). Additionally, the 3D dose difference for the plan reoptimised on the homogenous data set for set 1 compared to the original plan for patient 1 is shown (Figure 3.2) as an example of the regions of difference for the worst case scenario.

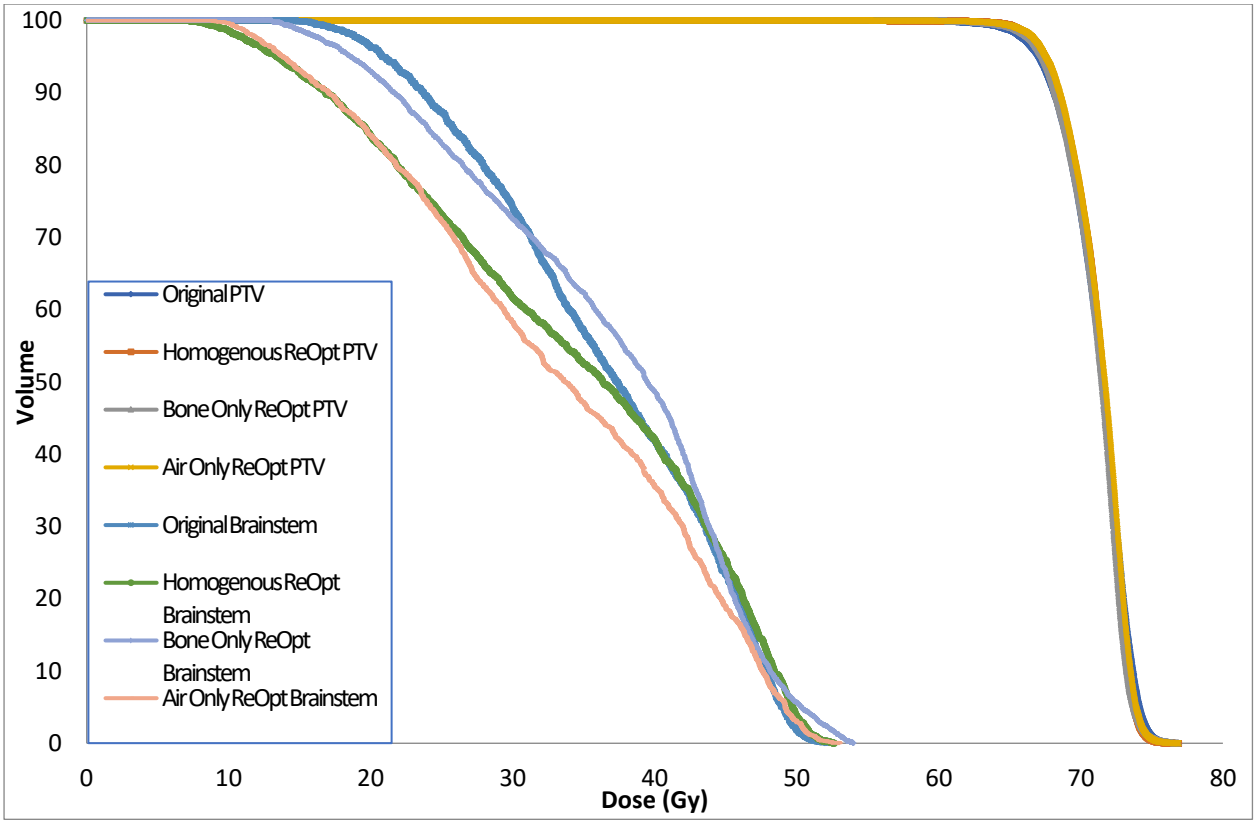

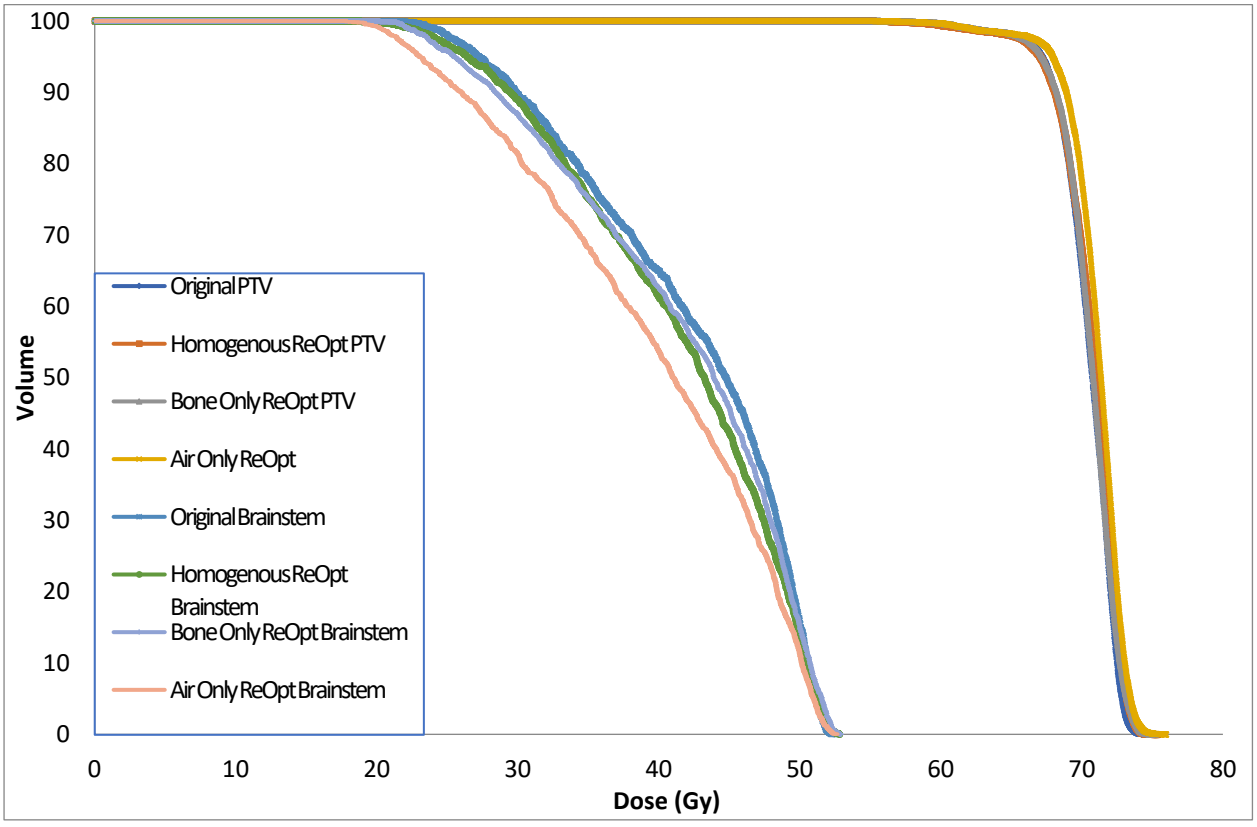

Figure 3.1 - Patient 1 (top) and Patient 4 (bottom) PTV and Brainstem DVH Comparison Between Different Reoptimised Plans on Different Density Corrected Datasets.

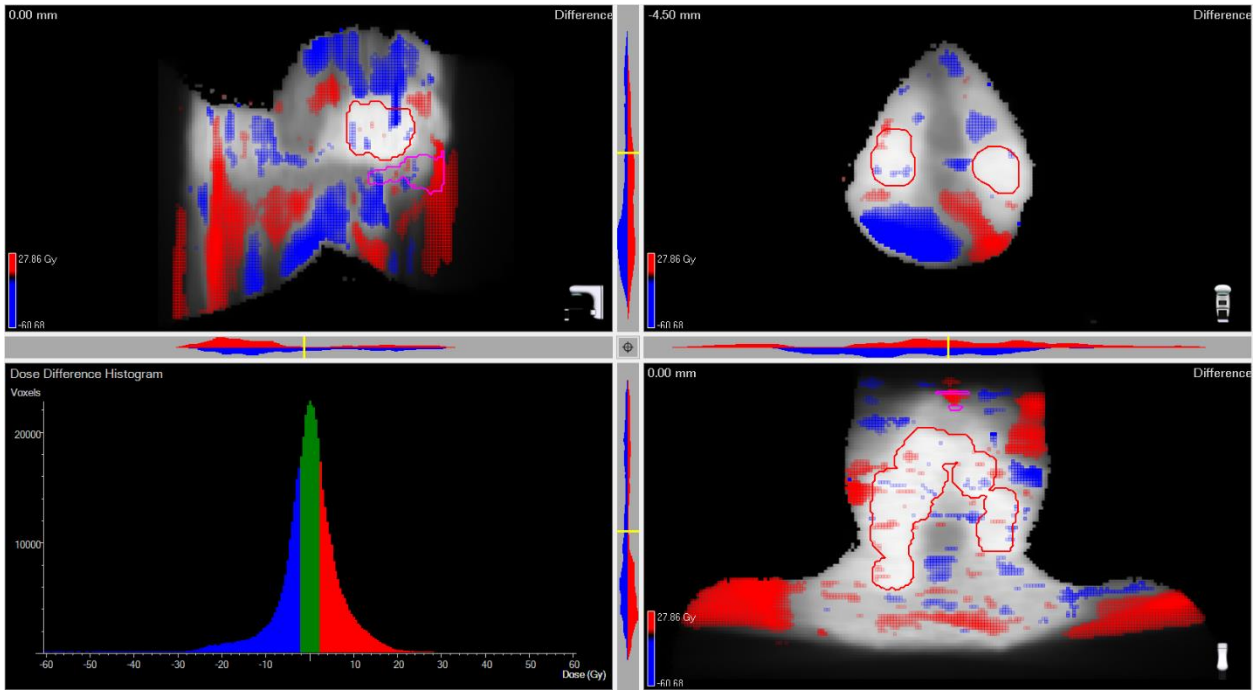

Figure 3.2 - Patient 1 Dose Differences for Homogenous Reoptimised plan compared to the Original Plan. Isocentre axial slice is shown as well as PTV and brainstem volumes.

EUD Results (Case 4)

The EUD values were calculated for the PTV and brainstem volumes, and compared back to the original plan. For the PTV volume, the largest differences were found in the reoptimised plans that were recalculated on the original datasets, with these EUD values also tending to be lower than the original plan. The largest mean absolute error (MAE) for the PTV was for the reoptimisation completed on the Air only overridden dataset for set 1, and recalculated on the original dataset, with a MAE of 1.88 Gy EUD. For the brainstem, the largest MAE was 2.21 Gy EUD for the reoptimisation completed on the air only overridden dataset for set 2 and recalculated on the original dataset. On average, for set 1, the PTV dose calculation error was 0.41 Gy and the average optimisation error was -0.80 Gy. The brainstem average dose calculation error was 0.45 Gy and the average optimisation error was -0.41 Gy. For set 2, the PTV dose calculation error was 0.94 Gy, and the optimisation error was -1.15 Gy. The brainstem average dose calculation error was 0.77 Gy, and average optimisation error was -1.20 Gy. The dose calculation error on average was an increase in EUD whereas the optimisation error on average was a reduction in EUD compared to the original plan, with these results displayed in figure 3.3 (*it may be noted that in these plots the whiskers indicate the range of data within ± 1.5 of the interquartile range and any data outside this are removed and considered as outliers. All boxplots within this thesis are presented in this way*). The only dataset which did not follow this trend was the bone override dataset with the set 1 density values, with this relationship reversed.

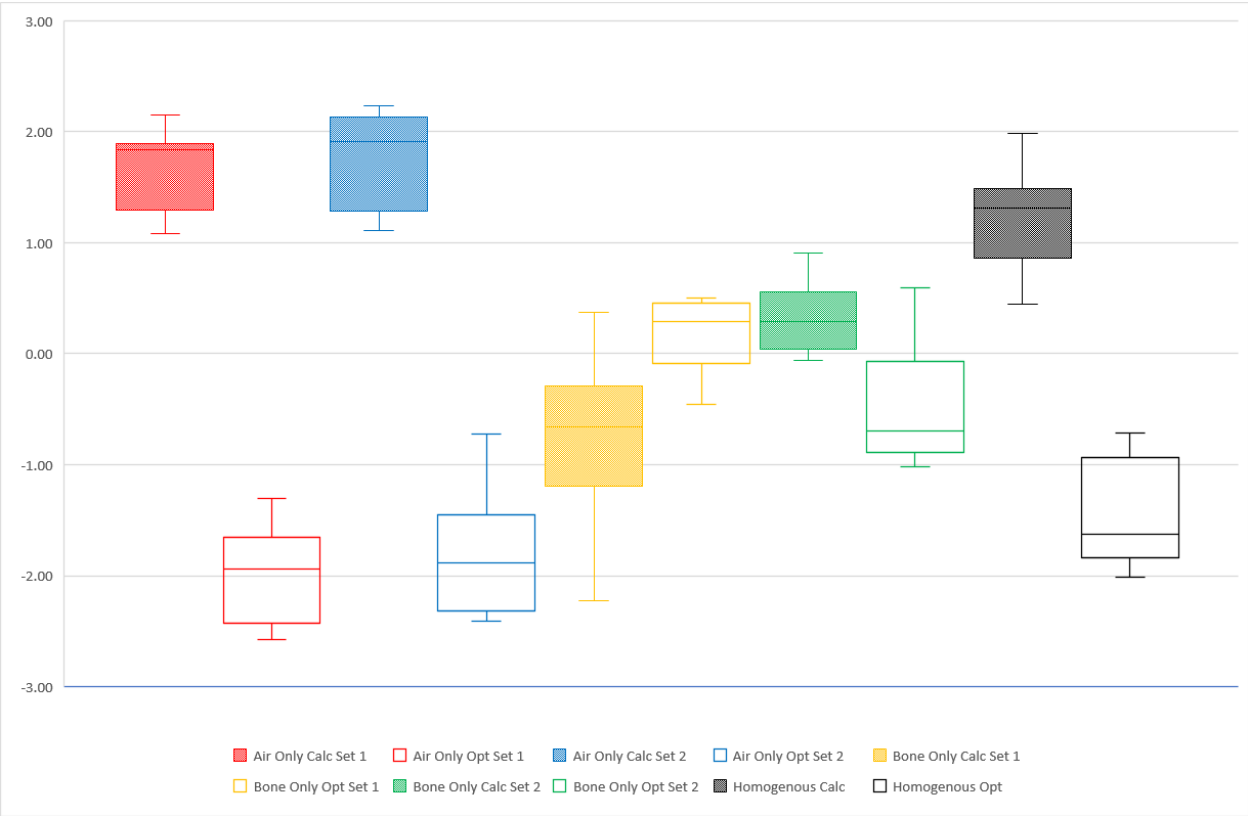

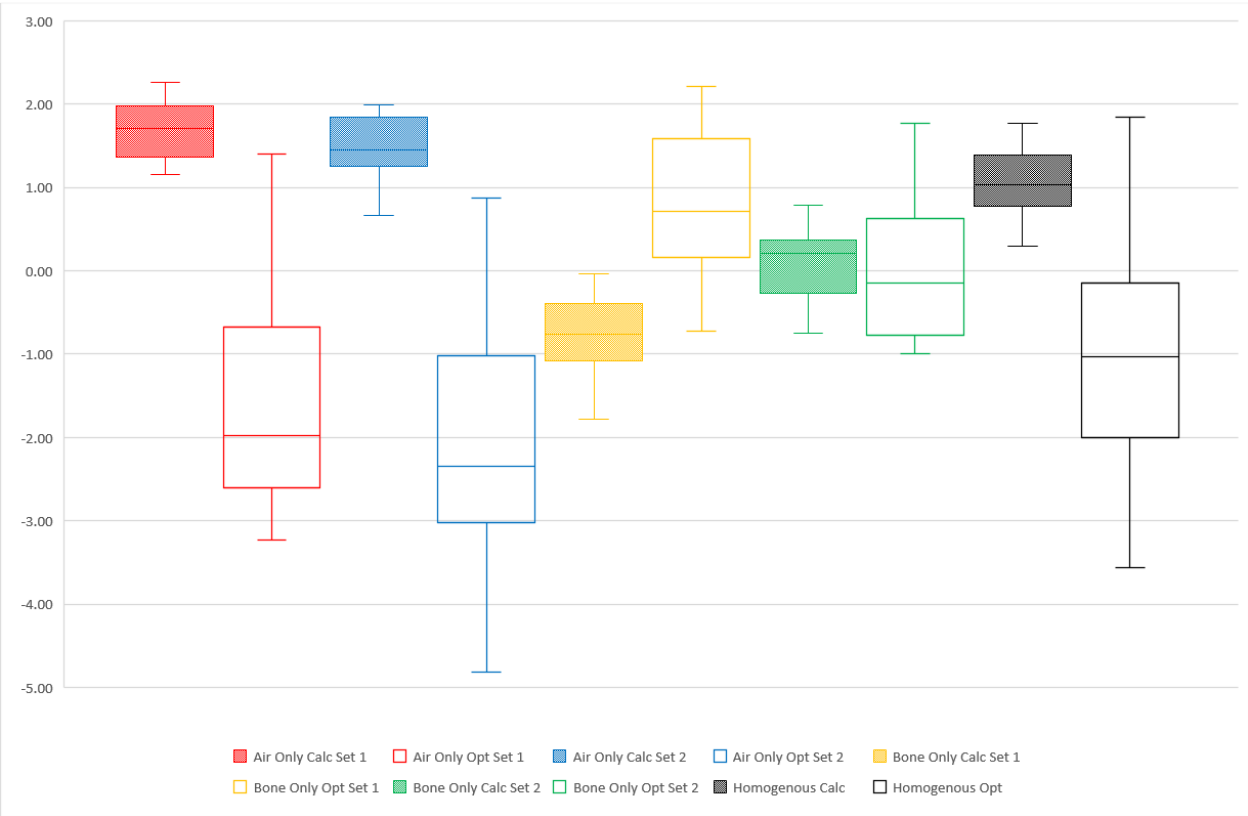

Figure 3.3 - EUD Calculation and Optimisation Errors for PTV (top) and Brainstem (bottom). The central line is the median, the "box" is the 25th and 75th quartiles of the data and the "whiskers" represent the data range *within ± 1.5 IQR (interquartile range) with any data outside of this presented as outliers. All boxplots within this thesis are presented in this way.*

Discussion

Density correction of planning data, as may be utilized for MRI only planning, can influence both the dose calculation accuracy and the plan optimisation. Considering these, the dose calculation accuracy will directly affect the patient clinical treatment, as this may alter the delivery of the correct dose to the patient, however the optimisation error is more difficult to quantify. The optimisation error will potentially produce a suboptimal plan, if it can be considered that planning on the gold standard fully density corrected dataset would produce an optimal treatment plan.

For all cases considered, bulk density corrections for bone and air provide dose calculations within 4% of the original treatment plans with appropriate corrections and typically within 3%. Patient 10 had the largest variation in isocentre point dose, of up to 3.5% when compared with the original density corrected plan. This was slightly higher than reported in previous publications [18, 20, 31] however this was due to the isocentre point being located on a bone/tissue interface. Global gamma results for all density overridden plans met a 95% 3%/3mm pass rate. This is expected as the dose calculation differences for the datasets were generally within 3% and in the majority of cases within 2%. The gamma results for set 2 were on average better than set 1. This however was not reflected for all patients for the point dose comparison.

Reoptimised plans with the same original prescription on different density corrected datasets displayed large discrepancies in various DVH distributions. This indicates that incorrect bulk density correction may have a large effect on the optimisation parameters required for a suitable treatment plan, with the original parameters producing a suboptimal plan.

Considering the optimisation error, the largest optimisation errors were observed in the homogenous dataset, that is where the entire density was corrected to a density of 1. *As displayed in figure 3.2, the greatest variations were seen outside the target volumes in normal tissue, particularly at the periphery of the patient, with the optimisation driven to produce the same target coverage in a different way.* This dataset varies the most from the fully corrected dataset, and generally resulted in the largest differences in gamma results, as well as having the largest difference in MAE for the PTV volume. This indicates that the larger the variation from the correct densities in the dataset, the larger the potential differences in the optimisation, as mentioned previously [21].

EUD values indicated that the largest variations for the PTV and the brainstem were for plans which were reoptimised on the incorrect density data, and then recalculated on the original density corrected dataset. The magnitude of average EUD differences was also greater for optimisation errors compared to dose calculation errors for these datasets. For tumours, EUD represents the uniform dose which leads to the same probability of local control as the actual non-uniform dose distribution [29], with the reoptimised plans on average produced lower EUD values, which would represent lower probability of local control. Further on EUD, the dose calculation error on average was an increase in EUD whereas

the optimisation error on average was a reduction in EUD compared to the original plan. This indicates that incorrectly density corrected plans generally produce plans which overestimate the target dose, whilst reoptimized plans using the original optimisation parameters on the different density corrected datasets, produce plans which underestimate the target dose. Additionally, the air only overridden and homogenous data set produced EUD difference values which were much greater than the bone only overridden data set. These two data sets differ the greatest when compared to the original data set, and produced the greatest errors in optimisation and dose calculation error. The only dataset which did not follow this relationship was the bone only overridden dataset with the set 1 density values. It must be considered however that the average difference for dose calculation and optimisation error was under 0.5 Gy for both the PTV and brainstem.

This study investigates only dosimetric and optimisation errors due to differences in electron density values for conversion of MRI datasets for dose calculation. An additional limitation of MRI only treatment planning relates to the geometric inaccuracy which may be present in the MRI imaging, which would then be inherent in the converted scans for dose calculation and optimisation. A study by Walker et al. [32] investigated the distortion across multiple scanner FOVs, with distortions varying between scanners, scan sequence and distance from the centre of the bore. The study reported results of average distortions within 2 mm generally for the phantom used, with the largest discrepancy of 4.1 mm at the edge of the bore. H&N imaging however as would be used for the current study, would be located within 20 cm of the centre of the MRI bore, and as reported by Walker et al., would not expect to have distortions exceeding 1 mm.

Conclusion

Optimisation errors have the potential to be greater than dose calculation errors if incorrect density corrections are utilized. Electron density correction using a bulk density approach achieves dose calculation uncertainties within 3%, however more advanced approaches, such as a voxel based approach, may improve accuracy and should be considered.

References

[1] Nyholm T, Jonsson J. Counterpoint: Opportunities and Challenges of a Magnetic Resonance Imaging–Only Radiotherapy Work Flow. Seminars in Radiation Oncology. 2014;24:175-80.

[2] Karlsson M, Karlsson MG, Nyholm T, Amies C, Zackrisson B. Dedicated Magnetic Resonance Imaging in the Radiotherapy Clinic. International Journal of Radiation Oncology*Biology*Physics. 2009;74:644-51.

[3] Roberson PL, McLaughlin PW, Narayana V, Troyer S, Hixson GV, Kessler ML. Use and uncertainties of mutual information for computed tomography/magnetic resonance (CT/MR) registration post permanent implant of the prostate. Medical Physics. 2005;32:473-82.

[4] Liney G, Owen S, Beaumont A, Lazar V, Manton D, Beavis A. Commissioning of a new wide-bore MRI scanner for radiotherapy planning of head and neck cancer. The British Journal of Radiology. 2013;86.

[5] Metcalfe P, Liney GP, Holloway L, Walker A, Barton M, Delaney GP, et al. The potential for an enhanced role for MRI in radiation-therapy treatment planning. Technol Cancer Res Treat. 2013;12:429-46.

[6] Raaymakers BW, Lagendijk JJW, Overweg J, Kok JGM, Raaijmakers AJE, Kerkhof EM, et al. Integrating a 1.5 T MRI scanner with a 6 MV accelerator: proof of concept. Physics in Medicine and Biology. 2009;54:N229.

[7] Fallone BG. The Rotating Biplanar Linac–Magnetic Resonance Imaging System. Seminars in Radiation Oncology. 2014;24:200-2.

[8] Mutic S, Dempsey JF. The ViewRay System: Magnetic Resonance–Guided and Controlled Radiotherapy. Seminars in Radiation Oncology. 2014;24:196-9.

[9] Dowling JA, Lambert J, Parker J, Salvado O, Fripp J, Capp A, et al. An Atlas-Based Electron Density Mapping Method for Magnetic Resonance Imaging (MRI)-Alone Treatment Planning and Adaptive MRI-Based Prostate Radiation Therapy. International Journal of Radiation Oncology*Biology*Physics. 2012;83:e5-e11.

[10] Kapanen M, Collan J, Beule A, Seppälä T, Saarilahti K, Tenhunen M. Commissioning of MRI-only based treatment planning procedure for external beam radiotherapy of prostate. Magnetic Resonance in Medicine. 2013;70:127-35.

[11] Korsholm M, Waring L, Edmund J. A criterion for the reliable use of MRI-only radiotherapy. Radiation Oncology. 2014;9:16.

[12] Yu H, Caldwell C, Balogh J, Mah K. Toward Magnetic Resonance–Only Simulation: Segmentation of Bone in MR for Radiation Therapy Verification of the Head. International Journal of Radiation Oncology* Biology* Physics. 2014;89:649-57.

[13] Dowling JA, Sun J, Pichler P, Rivest-Hénault D, Ghose S, Richardson H, et al. Automatic substitute computed tomography generation and contouring for magnetic resonance imaging (MRI)-Alone external beam radiation therapy from standard MRI sequences. International Journal of Radiation Oncology* Biology* Physics. 2015;93:1144-53.

[14] Edmund JM, Nyholm T. A review of substitute CT generation for MRI-only radiation therapy. Radiation Oncology. 2017;12:28.

[15] Guerreiro F, Burgos N, Dunlop A, Wong K, Petkar I, Nutting C, et al. Evaluation of a multi-atlas CT synthesis approach for MRI-only radiotherapy treatment planning. Physica Medica. 2017;35:7-17.

[16] Lambert J, Greer PB, Menk F, Patterson J, Parker J, Dahl K, et al. MRI-guided prostate radiation therapy planning: Investigation of dosimetric accuracy of MRI-based dose planning. Radiotherapy and Oncology. 2011;98:330-4.

[17] Lee YK, Bollet M, Charles-Edwards G, Flower MA, Leach MO, McNair H, et al. Radiotherapy treatment planning of prostate cancer using magnetic resonance imaging alone. Radiotherapy and Oncology. 2003;66:203-16.

[18] Chen L, Price Jr R, Nguyen T, Wang L, Li J, Qin L, et al. Dosimetric evaluation of MRI-based treatment planning for prostate cancer. Physics in Medicine and Biology. 2004;49:5157.

[19] Chen L, Price RA, Wang L, Li J, Qin L, McNeeley S, et al. MRI-based treatment planning for radiotherapy: dosimetric verification for prostate IMRT. International Journal of Radiation Oncology* Biology* Physics. 2004;60:636-47.

[20] Karotki A, Mah K, Meijer G, Meltsner M. Comparison of bulk electron density and voxel-based electron density treatment planning. Journal of Applied Clinical Medical Physics. 2011;12.

[21] Whelan B, Kumar S, Dowling J, Begg J, Lambert J, Lim K, et al. Utilising pseudo-CT data for dose calculation and plan optimization in adaptive radiotherapy. Australas Phys Eng Sci Med. 2015:1-8.

[22] Jonsson J, Karlsson M, Karlsson M, Nyholm T. Treatment planning using MRI data: an analysis of the dose calculation accuracy for different treatment regions. Radiation Oncology. 2010;5:62.

[23] Papanikolaou N, Battista JJ, Boyer AL, Kappas C, Klein E, Mackie TR, et al. Tissue inhomogeneity corrections for megavoltage photon beams. AAPM Task Group. 2004;65:1-142.

[24] Chu JC, Ni B, Kriz R, Saxena VA. Applications of simulator computed tomography number for photon dose calculations during radiotherapy treatment planning. Radiotherapy and Oncology. 2000;55:65-73.

[25] Cozzi L, Fogliata A, Buffa F, Bieri S. Dosimetric impact of computed tomography calibration on a commercial treatment planning system for external radiation therapy. Radiotherapy and Oncology. 1998;48:335-8.

[26] White G, Wilson I. Photon, electron, proton and neutron interaction data for body tissues. ICRU Report. 1992;46.

[27] Jonsson JH, Karlsson MG, Karlsson M, Nyholm T. Treatment planning using MRI data: an analysis of the dose calculation accuracy for different treatment regions. Radiation Oncology (London, England). 2010;5:62-.

[28] Constantinou C, Harrington JC, DeWerd LA. An electron density calibration phantom for CT-based treatment planning computers. Medical Physics. 1992;19:325-7.

[29] Gay HA, Niemierko A. A free program for calculating EUD-based NTCP and TCP in external beam radiotherapy. Physica Medica. 2007;23:115-25.

[30] Niemierko A. Reporting and analyzing dose distributions: a concept of equivalent uniform dose. Medical Physics. 1997;24:103-10.

[31] Stanescu T, Hans-Sonke J, Stavrev P, Fallone BG. 3T MR-based treatment planning for radiotherapy of brain lesions. Radiology and Oncology. 2006;40.

[32] Walker A, Liney G, Metcalfe P, Holloway L. MRI distortion: considerations for MRI based radiotherapy treatment planning. Australas Phys Eng Sci Med. 2014;37:103-13.

4 Clinical Validation of a Deep Learning Synthetic CT Generation Method for Head and Neck Cancer

4.1 Presentations related to this work

Initial related work was presented at AAPM 2022, American Association of Physicists in Medicine on 10 – 14 July 2022 in Washington, DC, USA as a poster presentation under the title "Deep Learning for MRI-Generated Synthetic CT: Dosimetric Evaluation for RT Planning in Head and Neck Cancers".

Additional related work was presented at ASTRO 2022, American Society for Radiation Oncology on 23 – 26 October 2022 in San Antonio, USA as a poster presentation under the title "Assessing Multiple MRI sequences in Deep Learning-Based Synthetic CT Generation for MR Only-Guided Radiation Therapy of Head and Neck Cancers".

Further related work was presented at EPSM 2022, Engineering and Physical Sciences in Medicine on 13th – 16th November 2022 in Adelaide, Australia under the oral presentation "Comparison of synthetic CTs derived from 2D versus 3D convolutional neural networks via Head and Neck MRIs for RT planning".

Copies of the accepted abstracts are presented in thesis appendix 2.

These presentations relate to the model development and training of the deep learning model for head and neck synthetic CT generation utilised in this chapter. As a co-author on these works, I contributed to the design of the study, gained hospital ethics approvals for the study to occur (as primary investigator from the hospital), curated the data used for model training in the study, assisted in analysis of results, and review of the abstracts and presentations.

The work presented in this chapter follows on from the work in these presentations, with this chapter considering the clinical validation of the developed deep learning model for sCT generation for head and neck cancer. I led, planned, and carried out this clinical validation work.

4.2 Introduction

Magnetic resonance imaging (MRI) use in head and neck cancer has been shown to improve delineation of target volumes, providing additional soft tissue contrast which is unable to be seen with CT [1-3]. For nasopharyngeal carcinoma and other tumours around the skull base, MRI offers improved evaluation of the skull base for early marrow invasion, for intracranial extension and perineural involvement. MRI is also superior for evaluating intracranial and intraorbital extent of sinunasal tumours and allows differentiation of solid enhancing tumour in the paranasal sinuses. Also, due to the

soft tissue contrast, it may be useful for mapping extent of deep soft tissue invasion and for the detection of small tumours in the tonsils. The soft tissue contrast advantage has been seen in nasopharyngeal cancer [4], where in comparison with CT, MRI produced target volumes which were 74% larger and did not always include the targets generated from CT. Similar results were also seen for tongue tumours [5], with the gross tumour volumes found to be delineated much larger on MRI than on CT. MRI in the head and neck region also has a robustness to dental artefacts [6].

Additionally, the potential for molecular imaging with MRI has increased the modality's value to the radiotherapy process. Diffusion weighted imaging (DWI) may detect differences in the tissue microenvironment from random displacement of water molecules. DWI is achieved by placing two additional diffusion sensitizing gradients on each side of the 180 degree radiofrequency (RF) pulse of a spin echo sequence [7], which produces a signal loss proportional to the amount of movement and the strength of the gradient. These differences are quantified as the apparent diffusion coefficients (ADC), which are inversely correlated with tissue cellularity [1, 8].

MRI however is inferior to CT in taking a much longer time to acquire scans, and suffers from motion artefacts from breathing, carotid artery pulsations and swallowing which may degrade image quality [2, 3]. All patients need to be evaluated for MR safety, and any implanted metallic hardware may produce susceptibility artefacts where there is a complete loss of signal around the implant.

With the emergence of magnetic resonance guidance for image guided radiotherapy through the development of MRI guided linear accelerators (MRIg-linacs), the potential for adaptive treatment for head and neck cancer has been raised [9].

Generating accurate sCT for the head and neck anatomy is challenging for a number of reasons [10, 11]. Though the head/brain region is reasonably simple enough in terms of geometry and conversion, the majority of the difficulty lies from the oral cavity region into the neck region. This area has a mixture of bone and air present, both of which have a low intensity in MRI images, making them difficult to separate for automated methods. MRI simulation in the neck region generally focusses on a reduced field of view (FOV) to ensure adequate image quality, and thus this region may not provide accurate dose calculation as the shoulders and part of the patient external body contour is truncated. There may also be large differences in neck flexion or the position of the patient jaw between different imaging sessions, i.e., between the CT and the MRI simulation sessions. This makes registration methods difficult, as well as introducing additional uncertainty in the dose comparison.

There have been a few different studies looking at sCT generation for head and neck cancer. Farjam et al. [11] investigated a multi-atlas approach with local registration goodness weighting for MRI based electron density mapping for head and neck anatomy. Hsu et al. [12] studied the potential of probabilistic classification of voxels from multiple MRI sequences and contrasts to generate synthetic CTs, using fuzzy c-means clustering with a spatial constraint to classify tissues. A further study was

conducted utilizing ultra short echo time (UTE) MRI in the head and neck for bone classification, investigating the potential of UTE for bone generation accuracy in synthetic CT generation [13]. A bulk density methodology was applied by Zheng et al. [14], utilizing a UTE/Dixon sequence combination for sCT generation, with this combination improving both bone and air contrast in MRI.

Deep learning techniques for sCT generation from MRI data has also been trialed, with recent reviews of deep learning methodologies for synthetic CT generation in radiotherapy published [15-17]. Palmer et al. [18] evaluated a commercial convolution neural network based algorithm (MRI Planner from Spectronic Medical AB, Helsingborg, Sweden) for a 44 head and neck patient cohort, achieving statistically equivalent dosimetric results in their comparison of sCT and CT based treatment plans. Dinkla et al. [19] developed and evaluated a patch based convolutional neural network based on the U-Net architecture for sCT generation for head and neck radiotherapy for an MRI-only workflow, with the patch based deep learning method chosen to improve robustness to abnormal anatomies caused by large tumours, surgical excisions or dental artefacts. Klages et al. [20] evaluated two different deep learning methodologies, and the effects of multiple combination of strategies on accuracy for patch based sCT generation in head and neck. Within this study, pix2pix and CycleGan was investigated for sCT generation, concluding that both methods were promising for MRI-only treatment planning for head and neck cancer. Qi et al. [21] proposed multiple sCT prediction models using cGAN and U-Net networks and explored the effect of multi MR sequences on sCT accuracy in the head and neck region.

Common deep learning techniques for image synthesis included U-Nets and generative adversarial networks (GANs). These networks belong to the class of Convolution Neural Networks (CNNs) where convolutional filters are combined through weights, or parameters, learnt during training. Depth is provided using multiple layers of filters [22]. These networks have been found useful for medical image synthesis where it may be formulated as an image-to-image translation problem, where a model that maps an input image (i.e. A) to a target image (i.e. B) has to be found [23]. U-Net presents an encoding and a decoding path with additional skip connections to extract and reconstruct image features, learning to translate from domains A to B. In the simplest GAN architecture, two networks are competing. A generator is trained to obtain synthetic images similar to the input set, and a discriminator that is trained to classify whether the synthetic image is real or fake, improving the generator's performance [15]. The U-Net framework [24] has previously been used for organ segmentation [25-27] as well as synthetic CT generation [15, 16] due to its preservation of high level contextual information via skip connections between the encoder and decoder. U-Net works well with paired MR-CT training pairs as it is shallower and less complex than networks better suited to unpaired images such as some types of generative adversarial networks [16, 21], and has faster evaluation times, requires less memory and has a reduced likelihood of artefacts or artificial material being introduced [28]. These deep learning networks can also be applied using 2D or 3D approaches, with 2D using individual slices and training performed considering only transverse, sagittal or coronal images, whilst 3D considers volumes as input, either the

whole 3D volume or 3D patches [17]. 2D approaches were initially favoured due to the computational power required and the higher number of samples required for training a larger number of parameters in a 3D architecture. However as computing power has increased and 3D approaches have been optimized, 3D approaches have been shown to have increased accuracy when compared to 2D approaches [15, 29].

Various methods have been utilised to reduce the effect of differences in setup, particularly for neck and jaw anatomy between MRI and CT scans. One published method was to modify the body contour of the sCT to resemble that of CT, and to apply a bulk density override to the additional soft tissue inside, and air outside the body contour [18]. More commonly, deformable image registration is used to deform the CT to the MRI or sCT, or the MRI or sCT to the CT prior to comparison with the generated sCT [11, 19, 20].

Hsu et al. [12] concluded that based on their study a single MRI image volume may not be sufficient to differentiate all tissue types, especially for differentiating bone from air. The Dixon sequence [30-32] makes use of the chemical shift between protons of water and fat. This technique uses two separate images with a modified spin echo pulse sequence, with one a conventional spin echo image with water and fat signals in phase, and the other acquired with the readout gradient slightly shifted so that the water and fat signals are 180 degrees out of phase. From these images, a water only and a fat only image can be generated, with the water only image commonly used for fat suppression. From the single Dixon sequence scan, four types of images are produced – an in-phase image (equivalent to non fat suppressed anatomical images), an out of phase image, water images (equivalent to fat suppressed) and fat images (equivalent to water suppressed). For head and neck cancer imaging, the Dixon sequence has been used as it suppresses the signal from fat, which has the advantage of suppressing artefacts due to high fat signals, to improve T2 contrast between fatty and non fatty tissues and to enable detection of enhancing tumours hidden in fatty tissue [33, 34]. Due to the multiple image contrasts produced from a single Dixon sequence, it has been investigated for use in MRI based PET attenuation correction for hybrid PET/MRI systems [35-37] as well as suitability for sCT generation [12, 18-21, 38].

This chapter considers the clinical validation of a deep learning sCT generation method in collaboration with a commercial software partner. This includes the assessment of Hounsfield unit (HU) accuracy and external body anatomical accuracy, in addition to dosimetric accuracy of this methodology.

4.3 Method

A cohort of 20 retrospective head and neck patient data sets were used for clinical validation of a deep learning sCT generation technique. These head and neck patients all had multiple planning target volumes (PTV), with these receiving 70/63/56Gy in 35 fractions. These patients were treated between

2015 – 2021 and were planned for treatment using the Pinnacle Treatment Planning System (various versions of software). These patients all received a CT scan on a Philips Big Bore CT scanner, as well as an MRI simulation session on a Siemens Skyra 3T MRI scanner. Within the MRI simulation session, different sequence combinations were received by the patients as the scan protocol changed over time and was dependent on whether contrast was received, the tumour type and tumour location. Patients were scanned on MRI with the same immobilization as on CT, and generally with any buildup or bolus material as per their treatment setup, though this was sometimes missing from the scan.

The deep learning model was generated by MIM Software Inc through a research partnership agreement, with local ethics approval (HREA 2020/ETH01940). This model was trained on a separate 26 patient dataset with various combinations of Dixon MRI sequences with treatment planning CT scans [39]. This training dataset was captured from the same centre and MRI scanner and had no overlap with the clinical validation cohort of patients. The training data was pre-processed using MIM Software (v6.9 MIM Software Inc, Cleveland Ohio), with a software mask of each patient generated on the CT images to remove the thermoplastic mask, treatment couch and other patient immobilization devices from the images, with CT pixels outside this set to -1024 HU. The CT was registered to a primary MRI sequence to preserve MR image quality and FOV, with a global rigid registration followed by a deformable image registration used to align these image pairs.

The sCT generator comprised of a U-Net deep learning architecture with skip connections designed for a variable subset of MR inputs. This implementation of U-Net consisted of 4 encoding layers and 4 decoding layers with skip connections from layer i to layer n - i, where n is the total number of layers. The network was adapted to allow for variable number of input channels, C, which are the subset of C images made up of different MR sequences.

The model was designed for variable subsets of MRI inputs. For model training, 14 unique combinations of MRI sequences were tested [39]. This included single sequence inputs, all Dixon phases for a particular MRI protocol, and combining protocols. For each combination, approximately 85% (N=21) of the MR-CT pairs were used for model training. U-Net training was on a 2D basis, where a single slice of an image volume is one sample. All model training was fixed at 50 epochs. A customized L1 loss (Eq. 1) was used by weighting (w) the mean pixel-wise error ($L1$) within distinct regions of anatomical material. Air to soft tissue, and soft tissue to bone boundaries were isolated using empirically determined HU intensity thresholds of -400 and 100 HU, respectively. The MIM proprietary weighting scheme (at the time of writing still commercially confidential) prioritized correctness in the bone regions, as bone loss had the greatest effect on later dose estimation accuracy.

$$Loss = L1_{bone} * w_{bone} + L1_{soft\ tissue} * w_{soft\ tissue} + L1_{air} * w_{air} \quad (1)$$

The trained sCT generator was then utilized on the 20 patient cohort for this study, which had a range of available Dixon MRI datasets available per patient. The number of sequences available and the number of patients is shown in table 4.1. Patients had a combination of sequences available, with T1 weighted Dixon sequences captured pre and post contrast, T2 weighted Dixon sequence or single phases from the Dixon sequence available. Some patients had only the water (w) or in phase images from the corresponding Dixon sequence available for use, as opposed to all Dixon phases available, as designated by the appropriate subscript in table 4.1.

Table 4.1 - Clinical Patient cohort MRI Sequence combinations

MRI Sequences	Number of Sequences	Number of patients
$T1pre_{all} + T1post_{all} + T2_{all}$	12	4
$T1pre_{all} + T2_{all}$	8	1
$T1_{all} + T2_{in} + T2_{W}$	6	3
$T1pre_{in} + T1post_{W} + T2_{in} + T2_{W}$	4	10
$T1pre_{in} + T1post_{W} + T2_{in}$	3	2

The original patient CT datasets were cropped to match the MRI dataset FOV to produce a comparable ground truth CT scan which could be used for dose calculation. Generally as the MRI FOV was smaller than the CT scan, the shoulder anatomy of the patient was cropped, and the scan length truncated to match the MRI scan length. The original treatment plan was then recalculated within the Pinnacle TPS (v16.20) on the cropped CT scan to allow comparison with the generated sCT from the MRI scan.

Additionally, a different approach to assessment where another iteration of the cropped CT was generated by deforming the original CT to the MRI dataset was considered. The MIM Maestro deformation algorithm, the VoxAlign Deformation Engine was used for this. For multi-modality deformable registration, the VoxAlign Deformation Engine utilises a free form deformation that uses a feature similarity scoring metric, maximising the correspondence of high-dimensional feature descriptors computed by evaluating each image voxel in the context of neighbouring voxels [40]. This algorithm was used to produce a cropped, deformed CT scan. This may produce better results compared to the generated sCT as it is deformed to match the anatomy at the time of the MRI scan. The original treatment plan was also recalculated on this dataset for comparison.

The sCT was compared to both cropped (cCT) and deformed (dCT) original CT for HU accuracy within the external mask of the reference CT (cropped or cropped and deformed), with mean absolute error (MAE) reported. The cropped external contours were also compared for Hausdorff distance (HD) agreement, mean distance to agreement (MDA) and Dice similarity coefficient (DSC). For dose

comparisons, the sCT was rigidly registered to the corresponding cCT and dCT dataset. Point dose comparison was completed between the plans calculated on each dataset. For some plans the isocentre point was also used as the weight point for reporting purposes, though in other plans the isocentre is placed in the neck in between the neck node target regions. For these cases an additional weight point (WP) is placed within the high dose target region and reported. The average point dose differences have been reported in addition to absolute dose differences to give an indication of the magnitude of difference. Global gamma analysis and dose volume histogram (DVH) analysis of the PTV volumes and the surrounding organs at risk (OAR) was also completed. Each PTV was included in the DVH comparison, with the D98 (i.e. dose to 98% of the volume), D95, D50 and D2 compared for the PTV70, and only D95, D50 and D2 compared for the PTV63 and PTV56. Due to the location of these target volumes, these had the largest uncertainties due to the cropping process and were often at the peripherals of the patient volume. In regards to the OAR comparison, both parotid gland mean doses were compared as well as the maximum dose of the spinal cord (SC), the brainstem (BS) and the mandible.

4.4 Results

All patient sequence combinations were able to be used to generate a corresponding sCT, regardless of the combination of Dixon sequences.

The HU comparison of the generated sCT for all patients to both the cCT and dCT datasets is shown in figure 4.1. On average for the cCT, the HU MAE was 130.01 ± 26.85 HU (99.51 – 196.01) and on average for the dCT, the HU MAE was 119.74 ± 45.14 HU (74.97 – 233).

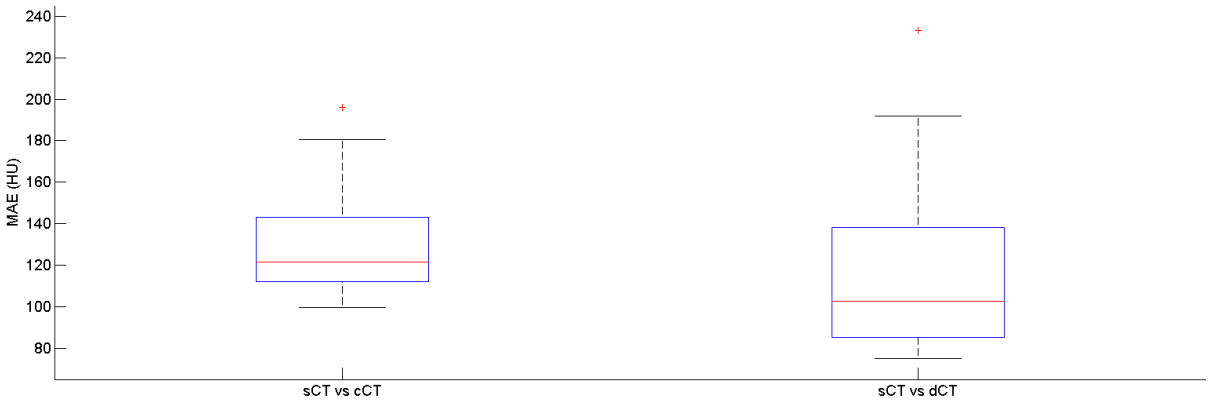

Figure 4.1 - HU MAE for both the cCT and the dCT compared to the sCT.

The external body contour was also compared between the cCT, dCT and the sCT, with the results for HD, MDA and DSC presented in figures 4.2 and 4.3. When comparing the external contour of the sCT

to the cCT, the mean HD was 19.06 mm ± 8.90 mm, the mean MDA was 2.12 mm ± 1.12 mm and the mean DSC was 0.963 ± 0.016 for the 20 patient cohort. When comparing the external contour of the sCT to the dCT, the results were improved, with an average HD of 14.93 mm ± 7.88 mm, an MDA of 1.15 mm ± 0.94 mm and a mean DSC of 0.969 ± 0.017.

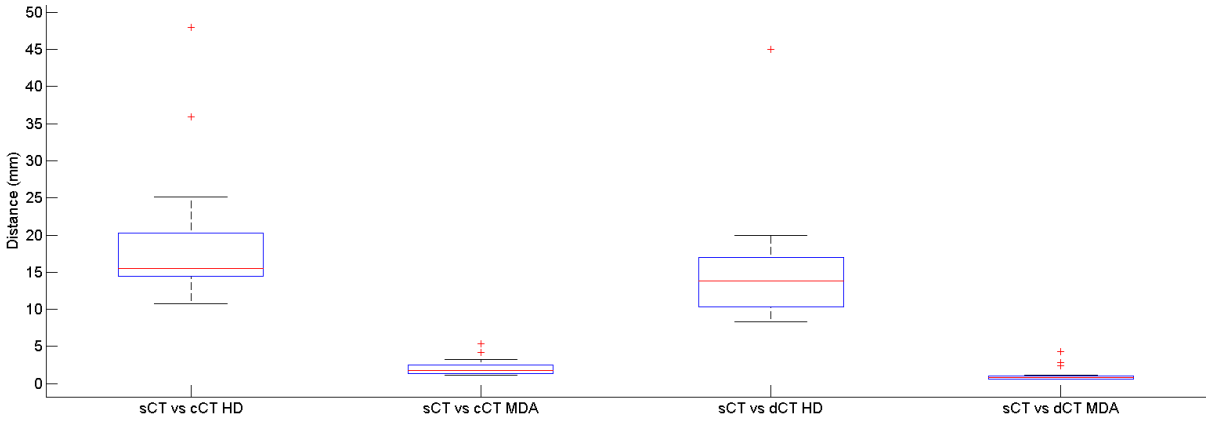

Figure 4.2 - Comparison of External contour Hausdorff Distance (HD) and Mean Distance to Agreement (MDA) for sCT vs cCT and sCT vs dCT.

Figure 4.3 - Comparison of External contour DSC for sCT vs cCT and sCT vs dCT.

Point dose comparison was completed, comparing the maximum calculated dose in the dataset, the isocentre point dose and the weight point dose where present. These results are presented in figure 4.4 and tables 4.2 and 4.3. Table 4.2 presents a summary of the point dose differences, whilst table 4.3 presents a summary of the absolute point dose differences.

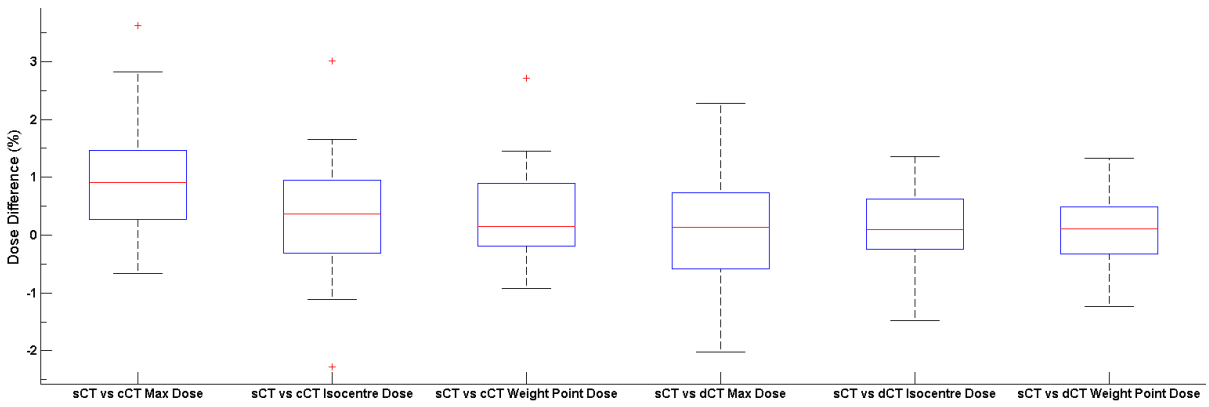

Figure 4.4 - Point dose comparison of the sCT to the cCT and dCT.

Table 4.2 - Summary of Point Dose differences.

	sCT to cCT Point Dose Difference			sCT to dCT Point Dose Difference		
	Max	Iso	WP	Max	Iso	WP
Average	1.00%	0.30%	0.42%	0.14%	0.10%	0.08%
StDev	1.04%	1.10%	0.94%	0.98%	0.75%	0.68%
Min	-0.66%	-2.28%	-0.92%	-2.02%	-1.48%	-1.24%
Max	3.62%	3.01%	2.72%	2.28%	1.36%	1.33%

Table 4.3 - Summary of Point Dose Absolute Differences.

	sCT to cCT Point Dose Absolute Difference			sCT to dCT Point Dose Absolute Difference		
	Max	Iso	WP	Max	Iso	WP
Average	1.11%	0.85%	0.79%	0.76%	0.56%	0.57%
StDev	0.91%	0.74%	0.64%	0.61%	0.49%	0.36%
Min	0.04%	0.15%	0.01%	0.02%	0.02%	0.04%
Max	3.62%	3.01%	2.72%	2.28%	1.48%	1.33%

Gamma analysis results are shown in figure 4.5 and table 4.4. On average the sCT when compared to the dCT had a slightly higher gamma pass rate result than the sCT compared to the cCT, with the dCT having a 3%/3mm global gamma pass rate of 98.42% ± 1.28% whilst the cCT had a 3%/3mm global gamma pass rate of 97.58% ± 1.61%. If the gamma tolerances are reduced to 1%/1mm, the dCT comparison had a higher average gamma pass rate of 88.34% ± 9.05% when compared to the cCT of 79.70% ± 9.88%.

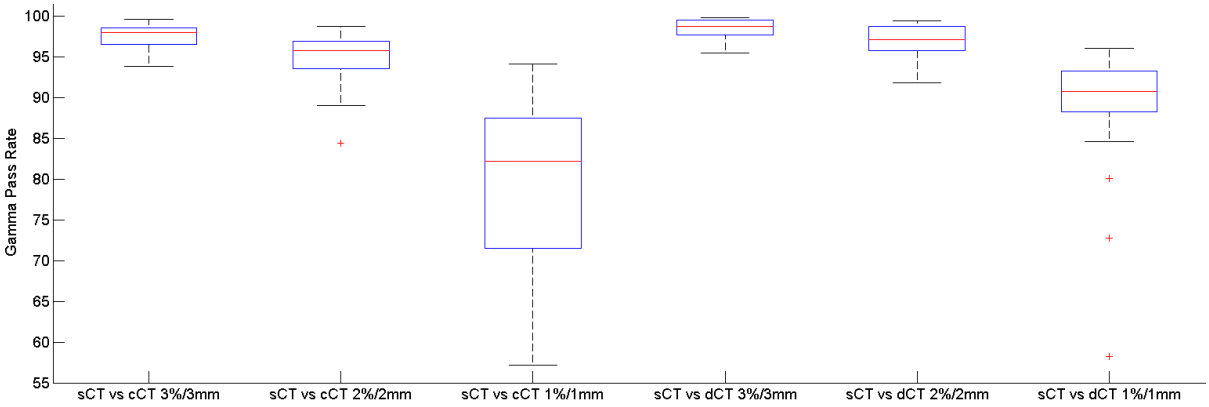

Figure 4.5 - Gamma Analysis results for sCT vs cCT and sCT vs dCT.

Table 4.4 - Gamma Analysis summary for sCT vs cCT and sCT vs dCT.

	sCT to cCT Gamma (%)			sCT to dCT Gamma (%)		
	3%-3mm	2%-2mm	1%-1mm	3%-3mm	2%-2mm	1%-1mm
Average	97.58	94.70	79.70	98.42	96.74	88.34
StDev	1.61	3.65	9.88	1.28	2.37	9.05
Min	93.84	84.45	57.17	95.49	91.80	58.21
Max	99.65	98.77	94.10	99.85	99.40	96.08

The DVH comparison is presented in the following figures and tables. For the sCT vs cCT DVH analysis, the PTV and OAR analysis is presented in figures 4.6 and 4.7 respectively. For the sCT vs dCT analysis, the PTV and OAR analysis is presented in figures 4.8 and 4.9 respectively. A summary of the average PTV and OAR DVH dose differences is shown in tables 4.5 and 4.6.

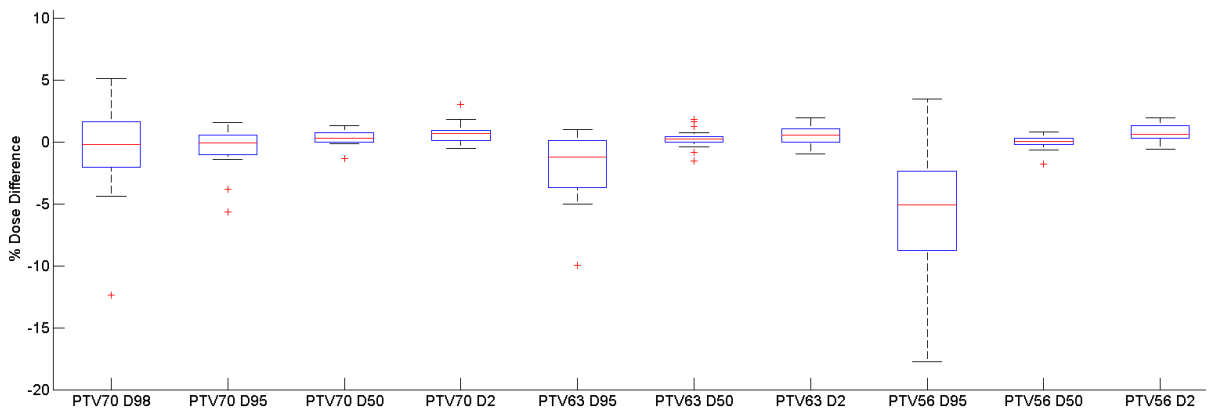

Figure 4.6 - sCT vs cCT PTV DVH Analysis. Outliers not shown in the image include data points for the PTV70 D98 at 27.63% and 39.13%, as well as for PTV56 D95 at -70.35%.

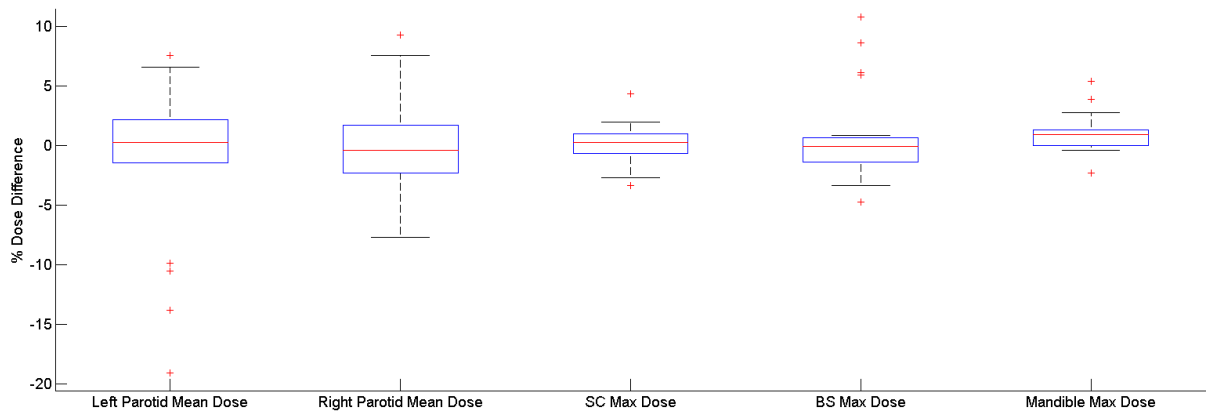

Figure 4.7 - sCT vs cCT OAR DVH Analysis.

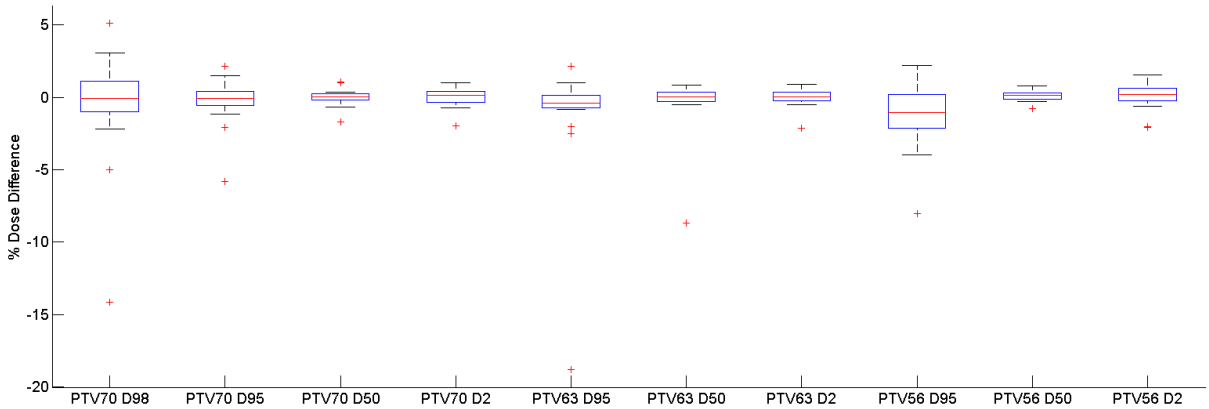

Figure 4.8 - sCT vs dCT PTV DVH Analysis.

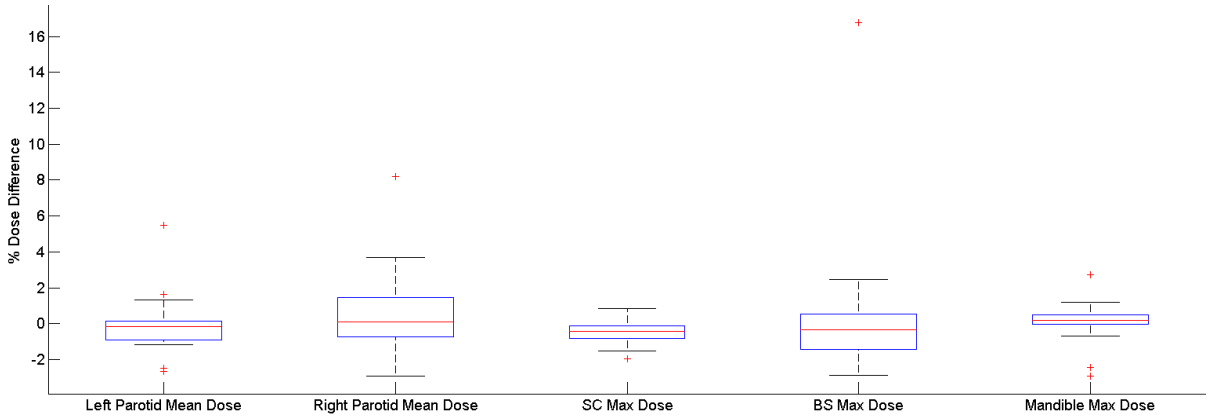

Figure 4.9 - sCT vs dCT OAR DVH Analysis.

Table 4.5 - Average PTV DVH Dose Differences.

	PTV70 D98	PTV70 D95	PTV70 D50	PTV70 D2	PTV63 D95	PTV63 D50	PTV63 D2	PTV56 D95	PTV56 D50	PTV56 D2
sCT vs cCT Average	0.01%	-0.44%	0.34%	0.71%	-1.96%	0.28%	0.49%	-8.68%	0.02%	0.81%
sCT vs cCT StDev	11.58%	1.71%	0.58%	0.78%	2.70%	0.77%	0.84%	15.28%	0.56%	0.71%
sCT vs dCT Average	-0.67%	-0.25%	-0.01%	0.05%	-1.22%	-0.36%	0.00%	-1.17%	0.11%	0.09%
sCT vs dCT StDev	3.86%	1.59%	0.57%	0.66%	4.26%	1.99%	0.63%	2.30%	0.35%	0.93%

Table 4.6 - Average OAR DVH Dose Differences.

	L Parotid mean	R Parotid mean	SC max	BS max	Mandible max
sCT vs cCT Average	-1.49%	0.31%	0.20%	0.81%	1.04%
sCT vs cCT StDev	6.94%	4.14%	1.67%	4.12%	1.67%
sCT vs dCT Average	-0.12%	0.63%	-0.47%	0.44%	0.13%
sCT vs dCT StDev	1.71%	2.55%	0.70%	4.23%	1.21%

Table 4.7 - Average Absolute PTV DVH Dose Differences.

	PTV70 D98	PTV70 D95	PTV70 D50	PTV70 D2	PTV63 D95	PTV63 D50	PTV63 D2	PTV56 D95	PTV56 D50	PTV56 D2
sCT vs cCT Average	5.57%	1.11%	0.50%	0.78%	2.33%	0.58%	0.79%	9.06%	0.37%	0.88%
sCT vs cCT StDev	10.08%	1.35%	0.44%	0.70%	2.37%	0.57%	0.56%	15.05%	0.41%	0.61%
sCT vs dCT Average	2.09%	0.88%	0.35%	0.49%	1.63%	0.71%	0.42%	1.81%	0.29%	0.68%
sCT vs dCT StDev	3.29%	1.34%	0.44%	0.44%	4.11%	1.89%	0.47%	1.81%	0.21%	0.61%

Table 4.8 - Average Absolute OAR DVH Dose Differences.

	L Parotid mean	R Parotid mean	SC max	BS max	Mandible max
sCT vs cCT Average	4.62%	3.05%	1.20%	2.69%	1.38%
sCT vs cCT StDev	5.28%	2.72%	1.14%	3.17%	1.39%
sCT vs dCT Average	1.07%	1.71%	0.67%	2.09%	0.78%
sCT vs dCT StDev	1.32%	1.95%	0.51%	3.67%	0.91%

The PTV DVH dose agreement was within 1% for all PTVs considering D50 and D2 as shown in table 4.7. Larger discrepancies were seen at the high dose DVH parameters particularly compared to the cCT when considering absolute differences, with the PTV70 D98 being on average 5.57% ± 10.08% different whilst the average difference when compared to the dCT was 2.09% ± 3.29%. Large discrepancies also occurred for the D95 for the PTV56, with a result of 9.06% ± 15.05% when compared with the cCT, and 1.81% ± 1.81% when compared to the dCT. OAR agreement was also improved when considering the agreement with the dCT, especially when comparing average absolute differences in the mean parotid doses, as shown in table 4.8.

4.5 Discussion

The U-Net deep learning technique was used in an sCT generator which was able to convert the various Dixon scan combinations to a sCT for treatment planning. Depending on the combination of MRI sequences available within the training cohort, different models were able to be applied which best matched the MRI sequence mix for each individual patient case for sCT conversion.

Previous initial validation of this model was presented [39] however the data utilized for this validation was part of the training data cohort, with 5 patients used for validation. That initial study reported an average MAE ranging from 78.9 – 86.5 HU, and a high average 3%/3mm gamma pass rate result which ranged from 99.5% to 99.8%. There was a small correlation of improved results with increased number of sequences, though this improvement was only minor. These previous results are slightly better than the results achieved in this wider study, with this potentially being due to the overlap of training and validation data in the initial study, and differences in sequences available. Additionally, the average MAE is reported as the entire dataset, and not just within the patient external contour, which will produce a better average MAE due to the background correlation.

Point dose results and gamma results within this study are in good agreement considering the results presented in tables 4.2 and 4.4. From the gamma results presented in figure 4.5, some data points may be seen to be outliers, which produces the variations in mean gamma results when compared to table 4.4. These point dose and gamma results indicate that the largest differences in HU may be in regions with the largest change in HU from region to region, such as at edges of the dataset where there is increased artefact present, with the differences in external contour also supporting this, or at air or bone interfaces. The use of DIR can lead to unexpected and unnatural deformations applied to datasets. Figure 4.10 provides an example of this, with this being one of the outlier results in regards to the HU comparison. The red contour is the external contour from the deformed CT, which does not match any of the other datasets due to the deformations applied. This can be seen particularly on the first transverse slice of the dataset (shown in figure 4.10), as well as the large section as the inferior edge of the dataset above the chest.

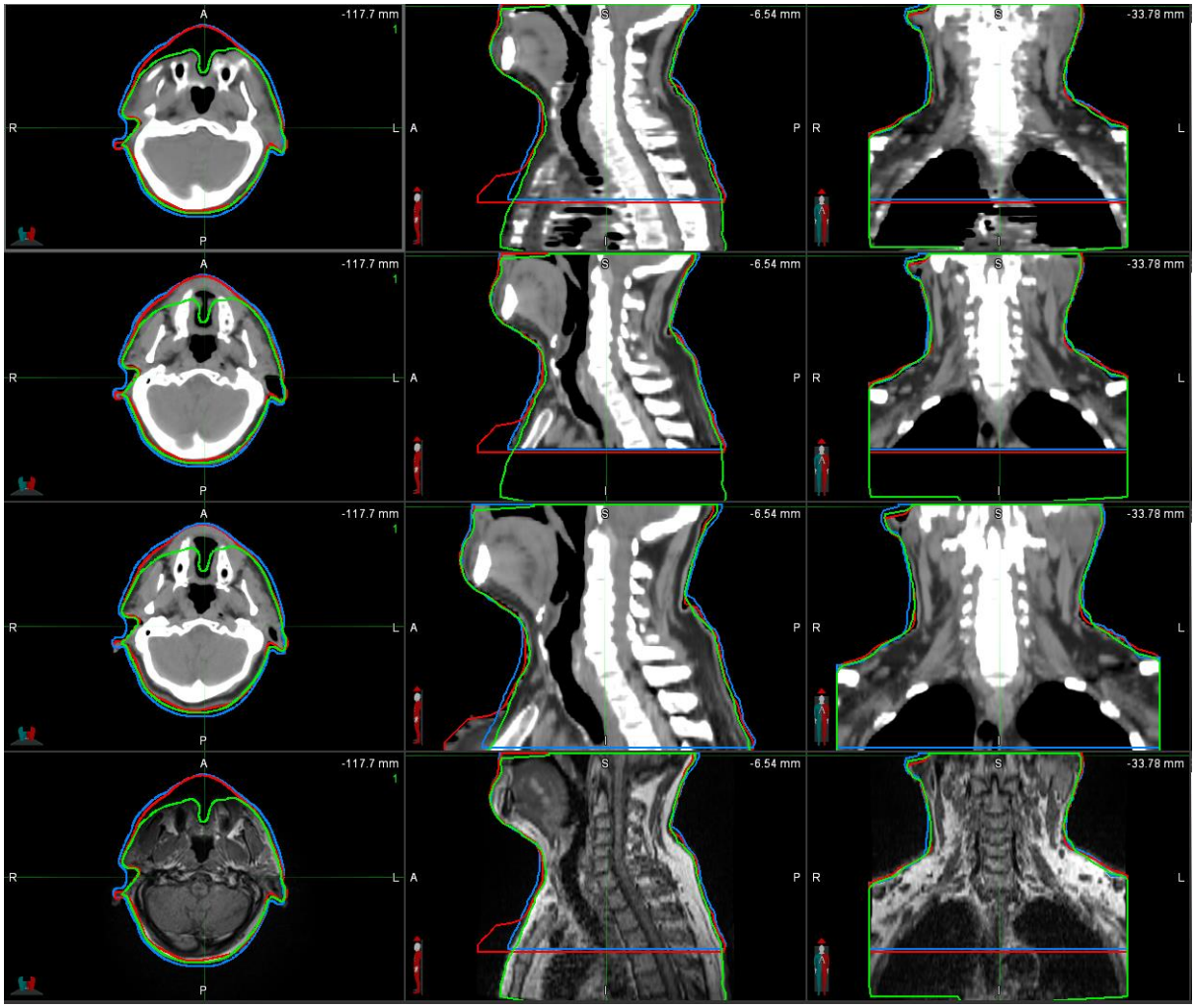

Figure 4.10 - Example of an outlier patient geometry due to DIR. From top row to bottom row, sCT top row, rigid CT 2nd row, deformed CT 3rd row, MRI sequence 4th row.

Some variations at the edges of the image were due to the registration of the images required for plan comparison. As we are comparing sCT generated from MRI images which may be taken at a different time point to the reference CT scan, the patient setup and internal anatomy may vary slightly when comparing these images. The registrations applied were a best match of the datasets, however some uncertainty would be present due to this. Additionally, the cropping of the images would have increased the uncertainty of the imaging at the edge of the field of view, and also altered some of the low dose targets which may have extended beyond the FOV compared. A study by Palmer et al. [18] minimized the variations in patient positioning between MRI and CT by modifying the body contour of the sCT to resemble that of CT, and applying a bulk density override to the additional soft tissue inside, and to air outside the body contour.

Previous studies utilizing different deep learning techniques have reported slightly improved results when compared to the anatomical and dosimetric results presented in this study. Palmer et al. [18] evaluated a commercial convolution neural network based algorithm from MRI Planner (Spectronic Medical AB, Helsingborg, Sweden), achieving relative absorbed dose agreement for all DVH volumes considered within 1%, in addition to a mean MAE of 67 ± 14 HU for overall body. It should be noted that this is a commercial algorithm with current regulatory approval, so it would be expected that it has had a much larger amount of training data available, as well as multi-centre validation prior to approval. MRI Planner also recommends use of a T1 weighted Dixon Vibe (3D spoiled GRE) sequence for sCT conversion, which takes approximately 10 minutes to acquire. The Dixon sequences utilized in the current work took between 1 minute to 3 minutes to capture for each sequence, depending on FOV and whether it was T1 or T2 contrast. The Dixon sequences captured for the current work were small FOV scans utilized for target and organ at risk contouring purposes, and were not captured specifically for sCT generation purposes. Dinkla et al. [19] also achieved similar results of a mean MAE within the body contours of 75 ± 9 HU with mean deviations of -0.03% ± 0.05% for dose within the body contours and -0.07% ± 0.22% inside the >90% dose volumes using a patch based deep neural network, which used the U-Net architecture and was composed of 14 layers. This study utilized a 34 patient cohort, with training completed on 22 datasets and a three fold cross validation was performed to analyse all 34 patients. This study also had similar mean gamma pass rate results, with pass rates of 95.6% ± 2.9% (87.5% - 98.6%) and 98.7% ± 1.4% (93.0% - 99.7%) for 2%/2mm and 3%/3mm gamma criteria and noted similar variations in the mean dose to parotid glands of 1.58% ± 2.09%.

Klages et al. [20] evaluated two different deep learning methodologies (pix2pix and CycleGAN), utilizing 23 head and neck patient mDixon MR and CT images as training data, with an additional 8 head and neck patient datasets used for independent testing. Klages et al. reported MAE results for both cross validated patients (i.e. the training cases) and for the independent testing set. Cross validated MAE results within the whole head and neck region were 66.9 ± 7.3 HU (pix2pix) and 82.3 ± 6.4 HU (CycleGAN), with these results increasing to 94.0 ± 10.6 HU (pix2pix) and 102.9 ± 14.7 HU (CycleGAN) for the independent test cases. Both methods were also reported to have absolute percent dose differences of 2% or less for all PTV and OAR DVH parameters considered. Qi et al. [21] completed their analysis with only a rigid registration, comparing a 4 channel GAN (pix2pix) and a 4 channel U-Net model. The study used multi-channel images as model input, i.e. multiple image sequences and contrasts, and achieved better accuracy than using a single MR sequence image as input. The study concluded that T1 weighted images are more suitable for head and neck region sCT prediction, and that the pix2pix was able to generate sCT images much closer to the actual CT images, retained more image details and was less blurred than the U-Net model due to the additional discriminator in the GAN. Qi et al. utilized multiple channel images similar to the current work presented, with 30 patients used for training and 15 patients used for testing. The Qi et al. study achieved

a MAE within the body of 69.98 ± 12.02 HU for their 4-channel pix2pix model, and 71.31 ± 12.40 HU for their 4-channel U-Net model. Both models achieved mean dose differences to the high dose PTV within 1%, in addition to a 2%/2mm gamma pass rate of 99.32% ± 0.34% (98.90% – 99.70%) for the 4 channel pix2pix, and 99.02% ± 0.39% (98.31% – 99.51%) for the 4 channel U-Net model.

The sCT compared to the dCT had the best dosimetric results in the current work for the majority of patients, especially for DVH results. This was expected as the dCT more closely matched the MRI scan used to generate the subsequenct sCT. Though the cCT had inferior results, the variations in set up between the MRI and CT scans likely contributed to the rigid registration unable to more closely register the cCT with the sCT as opposed to the dCT which was the CT deformed to the original MRI scan.

The largest variations in dosimetric results were seen for structures close to the skin surface of the patient, such as some of the low dose PTV volumes (PTV63 and PTV56) and the parotids. As there were differences in the MRI, and thus generated sCT in terms of the neck flexion, this produced a slightly different external contour, which led to some of the parotid contours extended outside the external contour. This produced the large discrepancies for some patient results in regards to the mean parotid results. These discrepancies were due to one limitation of this validation work in regards to the smaller FOV in the MRI scans. To allow more accurate comparisons, the CT data, including target and OAR volumes, were required to be cropped in order to match. In addition to this, as data at the edge of an sCT image has the greatest uncertainty due to border effects from the training of a deep learning model [19], these various issues combined likely contributed to the large variations seen for the affected DVH volumes, in particular the PTV56 and parotid results.

It should be noted that 11 patients within the patient cohort utilized in the current work for clinical validation had dental implants. Though this could be manually accounted for in treatment planning, this could not be incorporated into the HU analysis, and would have some affect on the HU agreement due to both the difference due to the dental implant as well as the artefact generated in the CT scan that is not present in the MRI scan, and subsequently generated sCT. This does however show the ability of the sCT generated from the MRI to remove the effect of dental filling artefacts as noted in previous studies [21].

Considering the previously published results, it should be noted that this deep learning model has the potential to be improved, or an alternative deep learning methodology may be more appropriate. Otherwise further sophistication could be added to the current deep learning model which may improve the anatomical and dosimetric agreement, such as incorporating additional data to the training network or utilizing alternate loss functions which may produce superior sCT images [16, 41]. Alternate, newly developed deep learning models such as the various GAN models discussed previously may be able to further improve sCT generation, utilizing additional steps and layers in the sCT generator to produce a further improved sCT [15, 16, 42, 43]. The current limitations of training a deep learning model should

also be considered. Training is performed on a specific set of images which utilize a fixed scan protocol, with each scan ideally having the same scan parameters and capturing the same anatomy and FOV within each paired MRI and CT scan. If a scan protocol is adapted over time, retraining of the model with more appropriate training data would be required [19, 20, 22]. Additionally, if incorporation of dosimetric validation results into the training, or retraining, of a model were possible, this process may be sped up or the need for large amounts of training data may be reduced.

One limitation of this model is that it utilizes only a small FOV in regards to the MRI data, adding uncertainty to the training of the model due to the FOV mismatch between MRI and CT. This study approached that limitation by cropping the CT to the MRI FOV for comparison of the models. Other studies which did not capture the full patient anatomy in the MRI approached this issue by either padding out the FOV of the sCT to match the CT, filling this with either a bulk density correction or incorporating the CT data by stitching the missing regions into the new sCT [18, 44]. It could be considered that specific data should be captured for deep learning methodologies which incorporate the appropriate FOV and anatomy for treatment planning purposes and would be a future work. Further collaboration with the commercial partner, MIM Software Inc, is planned regarding this with a prospective study in the discussion phase for the capture of an appropriate large FOV MRI sequence for sCT generation.

4.6 Conclusion

The U-Net framework produces acceptable clinical dosimetric results for generating head and neck sCT datasets for radiotherapy treatment planning within the current limitations of the approach. However, the work shows that there is still potential for improvement in the sCT images and scope for further work. One necessary requirement for wider application for accurate radiotherapy treatment planning in this site is the availability of an accurate, artefact-free large FOV MRI incorporating the entire patient anatomy.

4.7 References

[1] Grégoire V, Langendijk JA, Nuyts S. Advances in radiotherapy for head and neck cancer. Journal of Clinical Oncology. 2015;33:3277-84.

[2] Junn JC, Soderlund KA, Glastonbury CM. Imaging of head and neck cancer with CT, MRI, and US. Seminars in Nuclear Medicine: Elsevier; 2021. p. 3-12.

[3] Wippold FJ. Head and neck imaging: the role of CT and MRI. Journal of Magnetic Resonance Imaging: An Official Journal of the International Society for Magnetic Resonance in Medicine. 2007;25:453-65.

[4] Emami B, Sethi A, Petruzzelli GJ. Influence of MRI on target volume delineation and IMRT planning in nasopharyngeal carcinoma. International Journal of Radiation Oncology* Biology* Physics. 2003;57:481-8.

[5] Ahmed M, Schmidt M, Sohaib A, Kong C, Burke K, Richardson C, et al. The value of magnetic resonance imaging in target volume delineation of base of tongue tumours–a study using flexible surface coils. Radiotherapy and Oncology. 2010;94:161-7.

[6] Liney G, Owen S, Beaumont A, Lazar V, Manton D, Beavis A. Commissioning of a new wide-bore MRI scanner for radiotherapy planning of head and neck cancer. The British Journal of Radiology. 2013;86.

[7] Stejskal E. Use of spin echoes in a pulsed magnetic-field gradient to study anisotropic, restricted diffusion and flow. The Journal of Chemical Physics. 1965;43:3597-603.

[8] Leibfarth S, Winter RM, Lyng H, Zips D, Thorwarth D. Potentials and challenges of diffusion-weighted magnetic resonance imaging in radiotherapy. Clinical and Translational Radiation Oncology. 2018;13:29-37.

[9] Boeke S, Mönnich D, Van Timmeren JE, Balermpas P. MR-guided radiotherapy for head and neck cancer: current developments, perspectives, and challenges. Frontiers in Oncology. 2021;11:616156.

[10] Burgos N, Cardoso MJ, Guerreiro F, Veiga C, Modat M, McClelland J, et al. Robust CT synthesis for radiotherapy planning: application to the head and neck region. International Conference on Medical Image Computing and Computer-Assisted Intervention: Springer; 2015. p. 476-84.

[11] Farjam R, Tyagi N, Veeraraghavan H, Apte A, Zakian K, Hunt MA, et al. Multiatlas approach with local registration goodness weighting for MRI-based electron density mapping of head and neck anatomy. Medical Physics. 2017;44:3706-17.

[12] Hsu S-H, Cao Y, Huang K, Feng M, Balter JM. Investigation of a method for generating synthetic CT models from MRI scans of the head and neck for radiation therapy. Physics in Medicine and Biology. 2013;58:8419.

[13] Hsu S-H, Cao Y, Lawrence TS, Tsien C, Feng M, Grodzki DM, et al. Quantitative characterizations of ultrashort echo (UTE) images for supporting air–bone separation in the head. Physics in Medicine and Biology. 2015;60:2869.

[14] Zheng W, Kim JP, Kadbi M, Movsas B, Chetty IJ, Glide-Hurst CK. Magnetic Resonance–Based Automatic Air Segmentation for Generation of Synthetic Computed Tomography Scans in the Head Region. International Journal of Radiation Oncology* Biology* Physics. 2015;93:497-506.

[15] Spadea MF, Maspero M, Zaffino P, Seco J. Deep learning based synthetic-CT generation in radiotherapy and PET: A review. Medical Physics. 2021;48:6537-66.

[16] Boulanger M, Nunes J-C, Chourak H, Largent A, Tahri S, Acosta O, et al. Deep learning methods to generate synthetic CT from MRI in radiotherapy: A literature review. Physica Medica. 2021;89:265-81.

[17] Sahiner B, Pezeshk A, Hadjiiski LM, Wang X, Drukker K, Cha KH, et al. Deep learning in medical imaging and radiation therapy. Medical Physics. 2019;46:e1-e36.

[18] Palmér E, Karlsson A, Nordström F, Petruson K, Siversson C, Ljungberg M, et al. Synthetic computed tomography data allows for accurate absorbed dose calculations in a magnetic resonance imaging only workflow for head and neck radiotherapy. Physics and Imaging in Radiation Oncology. 2021;17:36-42.

[19] Dinkla AM, Florkow MC, Maspero M, Savenije MH, Zijlstra F, Doornaert PA, et al. Dosimetric evaluation of synthetic CT for head and neck radiotherapy generated by a patch-based three-dimensional convolutional neural network. Medical Physics. 2019;46:4095-104.

[20] Klages P, Benslimane I, Riyahi S, Jiang J, Hunt M, Deasy JO, et al. Patch-based generative adversarial neural network models for head and neck MR-only planning. Medical Physics. 2020;47:626-42.

[21] Qi M, Li Y, Wu A, Jia Q, Li B, Sun W, et al. Multi-sequence MR image-based synthetic CT generation using a generative adversarial network for head and neck MRI-only radiotherapy. Medical Physics. 2020;47:1880-94.

[22] LeCun Y, Bengio Y, Hinton G. Deep learning. Nature. 2015;521:436-44.

[23] Yu B, Wang Y, Wang L, Shen D, Zhou L. Medical image synthesis via deep learning. Deep Learning in Medical Image Analysis. 2020:23-44.

[24] Ronneberger O, Fischer P, Brox T. U-net: Convolutional networks for biomedical image segmentation. International Conference on Medical Image Computing and Computer-Assisted Intervention: Springer; 2015. p. 234-41.

[25] Nikolov S, Blackwell S, Zverovitch A, Mendes R, Livne M, De Fauw J, et al. Clinically applicable segmentation of head and neck anatomy for radiotherapy: deep learning algorithm development and validation study. Journal of Medical Internet Research. 2021;23:e26151.

[26] Tang H, Chen X, Liu Y, Lu Z, You J, Yang M, et al. Clinically applicable deep learning framework for organs at risk delineation in CT images. Nature Machine Intelligence. 2019;1:480-91.

[27] Zhu W, Huang Y, Zeng L, Chen X, Liu Y, Qian Z, et al. AnatomyNet: deep learning for fast and fully automated whole-volume segmentation of head and neck anatomy. Medical Physics. 2019;46:576-89.

[28] Arjovsky M, Bottou L. Towards principled methods for training generative adversarial networks. arXiv preprint arXiv:170104862. 2017.

[29] Zhou X, Yamada K, Kojima T, Takayama R, Wang S, Zhou X, et al. Performance evaluation of 2D and 3D deep learning approaches for automatic segmentation of multiple organs on CT images. Medical Imaging 2018: Computer-Aided Diagnosis: Spie; 2018. p. 520-5.

[30] Dixon WT. Simple proton spectroscopic imaging. Radiology. 1984;153:189-94.

[31] Ma J. Dixon techniques for water and fat imaging. Journal of Magnetic Resonance Imaging: An Official Journal of the International Society for Magnetic Resonance in Medicine. 2008;28:543-58.

[32] Chiabai O, Van Nieuwenhove S, Vekemans M-C, Tombal B, Peeters F, Wuts J, et al. Whole-body MRI in oncology: can a single anatomic T2 Dixon sequence replace the combination of T1 and STIR sequences to detect skeletal metastasis and myeloma? European Radiology. 2023;33:244-57.

[33] Jensen K, Al-Farra G, Dejanovic D, Eriksen JG, Loft A, Hansen CR, et al. Imaging for target delineation in head and neck cancer radiotherapy. Seminars in Nuclear Medicine: Elsevier; 2021. p. 59-67.

[34] Widmann G, Henninger B, Kremser C, Jaschke W. MRI sequences in head & neck radiology–state of the art. RöFo-Fortschritte auf dem Gebiet der Röntgenstrahlen und der bildgebenden Verfahren: © Georg Thieme Verlag KG; 2017. p. 413-22.

[35] Berker Y, Franke J, Salomon A, Palmowski M, Donker HC, Temur Y, et al. MRI-based attenuation correction for hybrid PET/MRI systems: a 4-class tissue segmentation technique using a combined ultrashort-echo-time/Dixon MRI sequence. Journal of Nuclear Medicine. 2012;53:796-804.

[36] Eiber M, Martinez-Möller A, Souvatzoglou M, Holzapfel K, Pickhard A, Löffelbein D, et al. Value of a Dixon-based MR/PET attenuation correction sequence for the localization and evaluation of PET-positive lesions. European Journal of Nuclear Medicine and Molecular Imaging. 2011;38:1691-701.

[37] Wagenknecht G, Kaiser H-J, Mottaghy FM, Herzog H. MRI for attenuation correction in PET: methods and challenges. Magnetic Resonance Materials in Physics, Biology and Medicine. 2013;26:99-113.

[38] Olin AB, Thomas C, Hansen AE, Rasmussen JH, Krokos G, Urbano TG, et al. Robustness and generalizability of deep learning synthetic computed tomography for positron emission tomography/magnetic resonance imaging–based radiation therapy planning of patients with head and neck cancer. Advances in Radiation Oncology. 2021;6:100762.

[39] Antunes J, Pittock D, Jacobs P, Nelson A, Piper J, Young T, et al. Assessing Multiple MRI Sequences in Deep Learning-Based Synthetic CT Generation for MR Only-Guided Radiation Therapy of Head and Neck Cancers. International Journal of Radiation Oncology, Biology, Physics. 2022;114:e553.

[40] Piper J, Richmond, J, Nelson A, VoxAlign Deformation Engine. Cleveland, OH: MiM Software Inc. 2018.

[41] Largent A, Barateau A, Nunes J-C, Mylona E, Castelli J, Lafond C, et al. Comparison of deep learning-based and patch-based methods for pseudo-CT generation in MRI-based prostate dose planning. International Journal of Radiation Oncology* Biology* Physics. 2019;105:1137-50.

[42] Bahrami A, Karimian A, Arabi H. Comparison of different deep learning architectures for synthetic CT generation from MR images. Physica Medica. 2021;90:99-107.

[43] Li Y, Li W, He P, Xiong J, Xia J, Xie Y. CT synthesis from MRI images based on deep learning methods for MRI-only radiotherapy. 2019 International Conference on Medical Imaging Physics and Engineering (ICMIPE)2019. p. 1-6.

[44] Thummerer A, De Jong BA, Zaffino P, Meijers A, Marmitt GG, Seco J, et al. Comparison of the suitability of CBCT-and MR-based synthetic CTs for daily adaptive proton therapy in head and neck patients. Physics in Medicine & Biology. 2020;65:235036.

5 Lung MRI-Only Treatment Planning using a Single MRI Sequence

5.1 Presentations

This work was presented as an oral presentation in 2018 at EPSM 2018, Engineering and Physical Sciences in Medicine on 31st October 2018 in Adelaide, Australia. A copy of the accepted abstract is presented in thesis Appendix 3.

5.2 Introduction

With the advent of hybrid Magnetic Resonance Imaging guided Linear Accelerators (MRIg-linacs) in radiotherapy, as well as the increase in use of MRI-simulators, the requirement for treatment planning using only Magnetic Resonance Imaging (MRI) has arisen. The current gold standard for treatment planning is Computed Tomography (CT) as this imaging modality provides electron density information directly required for radiotherapy dose calculations, which MRI is not able to provide. MRIg-linacs will enable online adaptive radiotherapy with MRI imaging, which will require MRI-only treatment planning. MRI-only radiotherapy planning studies for various treatment sites have been published utilising various methodologies to correct for the lack of electron density information [1-7]. Any methods of estimating electron density information from MRI need to consider geometric distortion due to magnetic field inhomogeneities, gradient nonlinearity, and patient induced susceptibility.

The use of MRI for lung imaging has been limited due to a number of challenges, including the low proton density of lung and the presence of cardiac and respiratory motion in the imaging area. Lung tissue also presents additional susceptibility artefacts due to the numerous air-tissue interfaces and magnetic heterogeneity due to microscopic tissue heterogeneity [8-10]. In lung, the current gold standard is CT imaging, with its superior image contrast and spatial resolution to that of MRI. However MRI provides superior soft tissue definition, anatomical and functional imaging options, and a radiation free alternative to CT.

For this study, a developmental works in progress MRI sequence was used – the SpiralVIBE sequence. This sequence produces 3D ultrashort echo time (UTE) images under free breathing using a prototype spoiled gradient echo sequence utilizing a variable TE stack-of-spirals trajectory. It incorporates a volumetric interpolated breath-hold examination (VIBE) under free breathing, incorporating navigator scans for respiratory gating. UTE is a critical factor in improving the quality of lung imaging due to the short T2 and T2* values in lung. The stack-of-spirals acquisition allows 3D imaging to be achieved with high read out efficiency, reducing the scan time required [8, 10, 11].

The SpiralVIBE sequence used was originally described by Qian et al. [11], introducing an acquisition weighted stack-of-spirals for fast high resolution 3D UTE MR imaging by modifying the acquisition weighted data collection technique. This technique was adapted from a technique previously used in MR microscopy [12] and spectroscopic imaging [13], using a selective radiofrequency (RF) pulse and a slab select gradient to excite a segment of the object rather than the whole object. Additional changes to the sequence by Qian et al. include shortening the refocussing lobe of the slab select gradient by lowering the amplitude and replacing the in plane phase encodings with spiral trajectories to accelerate in plane data collection. Off-resonance induced image blurring and T2-induced signal decay were minimised by selecting the proper number of spirals used, and the modified technique acquires data at a delay varying only with the duration of slice encoding, referred to as acquisition weighted stack of spirals. This acquisition weighted stack of spirals pulse sequence had independent selection between in-plane resolution and slice thickness, and thus was capable of generating high in-plane resolution (under 1mm) while keeping slice thickness unchanged, and maintaining short total scan time.

The SpiralVIBE sequence used in this study differs from the original technique of Qian et al as it utilises a 60 μs non selective rectangular pulse to achieve echo times (TE) of 50 μs. Images were also acquired in a coronal orientation to minimise the number of through plane encoding steps. Additionally, the sequence utilises navigator scans based off the liver phase for respiratory gating, with the navigator scans and imaging scans using the same excitation pulse and repetition time (TR) to sustain steady state, with this information generating scans at inspiration during a free breathing acquisition [10].

This work investigated the various methods of synthetic CT (sCT) generation from a single MRI sequence for lung cancer, and the suitability of the SpiralVIBE MRI sequence was tested for MRI-only treatment planning. The sCT will provide electron density information required for radiotherapy treatment planning calculations and will enable MRI-only radiotherapy. For any such method of sCT generation, the dosimetric accuracy of the method must be assessed against the current CT gold standard. As such, these results will determine the suitability of the SpiralVIBE sequence for sCT generation and MRI-only treatment planning.

5.3 Method

Eleven lung cancer patients' datasets were available for use in this study. These clinical patients underwent a CT simulation session for treatment planning in the treatment position with arms above their head, as well as an MRI simulation session in which their scanned position varied between arms up and arms by the side. 3D UTE images were acquired on a Siemens MAGNETOM Skyra 3T MRI Simulator under free breathing using the prototype spoiled gradient echo sequence utilizing a variable TE stack-of-spirals trajectory (SpiralVIBE). The SpiralVIBE parameters used for these scans are displayed in table 5.1, with an example of the SpiralVIBE images shown in Figure 5.1.

Table 5.1 - SpiralVIBE parameters used in this study.

Parameters	SpiralVIBE
TR/TE (ms)	2.97/0.05
Frequency field of view (FOV) (mm)	480
Average FOV in slice direction (mm)[a]	288
Acquisition orientation	Coronal
Flip angle	5
In-plane resolution acquired (mm)	1.5 x 1.5
Base resolution	320
Slice thickness (mm)	1.5
Bandwidth (Hz/Px)	NA
Acquisition time (s)	295
Spiral interleaves	504

[a]FOV in slice direction = (slice thickness × no. of slices), this is variable per patient depending on the number of slices acquired.

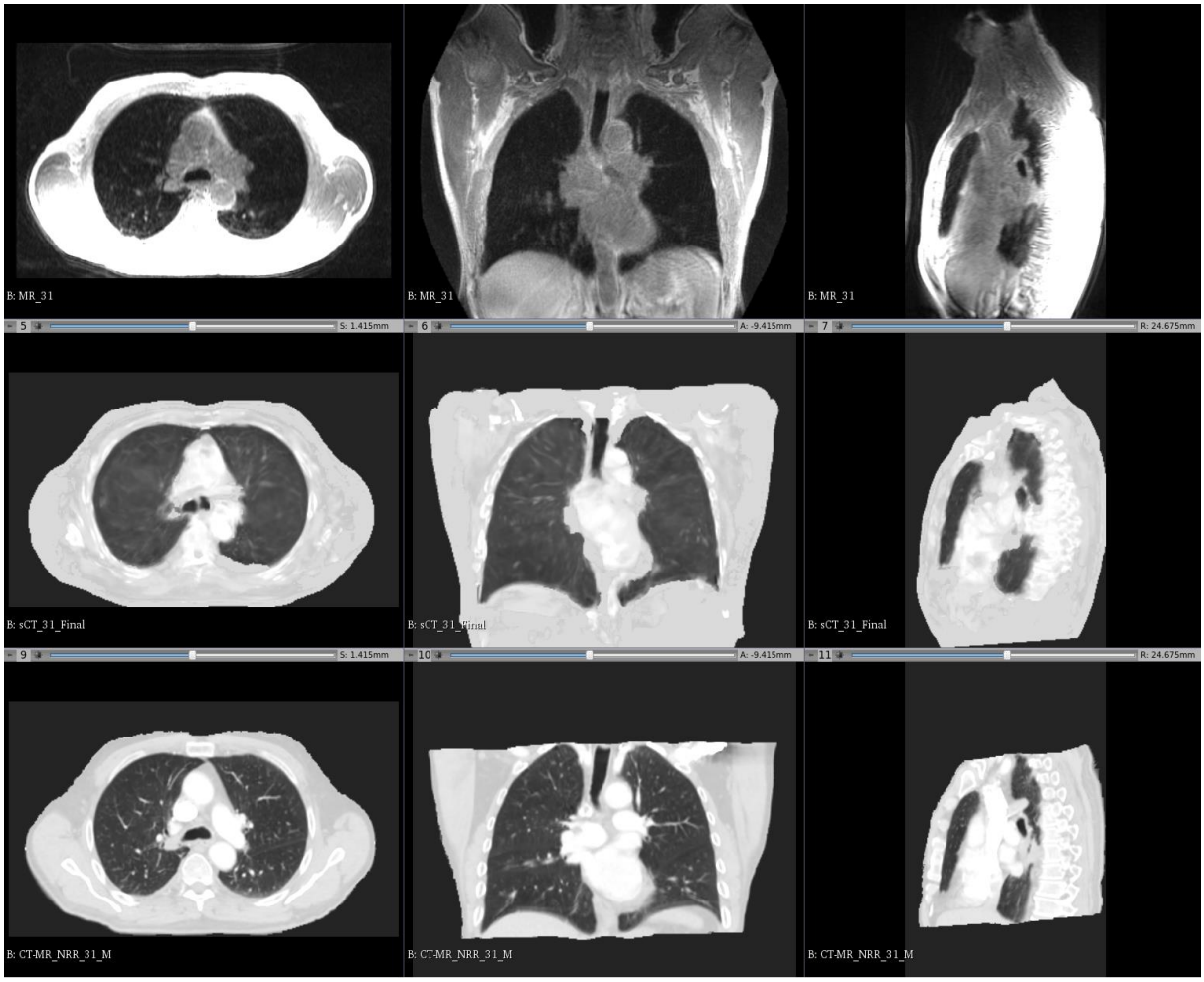

Figure 5.1 - A patient example of the SpiralVIBE MRI (top row), the generated sCT using the atlas method (middle row) and the corresponding patient CT scan (bottom row).

A number of sCT conversion methods were investigated using the available lung datasets. These included bulk density corrections, an atlas conversion method and a Gaussian Mixture Model (GMM) conversion method. All conversion methods were compared to the gold standard CT scan captured for patient treatment planning. MIMvista (v6.8.5) was used to contour the patient external and the lung contours on the SpiralVIBE MRI scans for bulk density correction, and to assist the conversion accuracy in the atlas method. For the atlas approach and GMM approach, a Hounsfield unit (HU) comparison was completed. For all sCT conversion methods investigated, a point dose and a 2%/2mm global gamma comparison for each plan calculated on the sCT dataset compared to the plan calculated on the original CT was completed. The original clinically accepted treatment plan generated on the original CT scan was used for all patients and was copied to all addition sCT datasets for calculation. All treatment planning was carried out using the Pinnacle Treatment Planning System (v16.02)

5.4 sCT Conversion Methodology and Results

5.4.1 Bulk density

Bulk density correction involves the application of density overrides for different areas of the scan to appropriate densities, and has worked well for other treatment sites, in particular for brain and pelvis where the anatomy is fixed [14-17]. This can include tissue overrides as well as density overrides for different anatomy such as bone or lung. This method however does remove inhomogeneity in regards to tissue density, and forces a single density to an area.

5.4.1.1 Bulk Density with CT Datasets

Initially, bulk density corrections were applied to the original treatment plans on the original patient planning CT scan. Within this work, a first order correction was completed with only the patient external contour density overridden initially. A second order correction was then considered by applying an additional density override on the contoured lung volume. For these, the patient external contour and the clinically contoured lung volumes had bulk density corrections applied of 1 g/cm^3 and 0.26 g/cm^3 respectively as per the International Commission on Radiation Units and Measurements (ICRU) report 46 recommendations [18], with a dataset generated with only the patient external contour bulk density override applied (first order correction), and a second data set with both the patient external contour and the lung contour bulk density override applied (second order correction). As these contours are generated on the original CT scan, there were no differences due to registration and patient motion and they provided a baseline for expected agreement with this methodology. The original treatment plan was calculated on these new bulk density applied datasets and compared to the treatment plan calculated on the original CT dataset.

Table 5.2 - Point dose results for CT bulk density and CT external only datasets.

Patient	CT Bulk Density	CT External Only
Lung_19	1.38%	-4.23%
Lung_20	3.18%	-4.31%
Lung_21	0.19%	-4.50%
Lung_23	2.75%	-2.47%
Lung_26	3.10%	-0.85%
Lung_27	0.80%	-13.35%
Lung_28	1.92%	2.88%
Lung_29	0.73%	-1.73%
Lung_30	1.29%	-4.89%
Lung_31	1.19%	-11.89%
Lung_33	1.49%	-9.30%
Average	1.64%	-4.97%

Table 5.3 - Gamma results for CT bulk density and CT external only datasets.

Patient	CT Bulk Density (%)	CT External Only (%)
Lung_19	89.4	57.9
Lung_20	74.7	64.7
Lung_21	73.3	20.3
Lung_23	84.2	62.2
Lung_26	76.0	52.8
Lung_27	72.4	19.6
Lung_28	87.6	70.0
Lung_29	96.6	65.7
Lung_30	87.1	51.3
Lung_31	86.8	31.9
Lung_33	85.3	41.3
Average	83.0	48.9

The results for the point dose and gamma pass rates for the CT bulk density and CT external only datasets are shown in tables 5.2 and 5.3. The bulk density results for only the CT External contour overridden were quite poor, with the point dose results ranging from -13.35% to -0.85% with an average of -4.97%, and the gamma pass rates ranging from 19.6% to 65.7% with an average of 48.9% for a 2%/2mm gamma tolerance. For the bulk density results with both the CT external contour and the lung volume overridden, the results were much improved. The point dose results ranged from 0.19% to 3.10% with an average agreement of 1.64%, and the 2%/2mm gamma pass rates ranged from 73.3% to 96.6% with an average pass rate of 83%.

5.4.1.2 Bulk Density with MRI Datasets

A similar approach to bulk density correction was then applied to the MRI data to test suitability of the methodology for sCT generation. The patient external contour and the lungs were manually contoured and then densities of 1g/cm^3 and 0.26g/cm^3 were applied for the patient external volume and the lungs respectively as per ICRU 46 recommendations [18]. The plans were calculated with only the patient external contour density applied and considering the patient volume only as tissue, and also with both the patient external contour and the lung densities applied. The original treatment plan was calculated on these new data sets and compared to the treatment plan calculated on the original CT dataset. Table 5.4 and table 5.5 presents the point dose results and the 2%/2mm global gamma results for the MRI bulk density and MRI external only datasets with the original treatment plan recalculated, and compared to the original CT dataset results.

Table 5.4 - Point dose results for MRI bulk density and MRI external only datasets.

Patient	MRI Contours Bulk Density	MRI External Only
Lung_19	3.90%	-4.92%
Lung_20	2.54%	-5.14%
Lung_21	-3.06%	-7.56%
Lung_23	1.88%	-1.60%
Lung_26	3.06%	-0.99%
Lung_27	-0.05%	-13.82%
Lung_28	4.36%	4.36%
Lung_29	-0.93%	-3.59%
Lung_30	-1.26%	-7.30%
Lung_31	0.19%	-12.93%
Lung_33	0.90%	-9.17%
Average	1.05%	-5.70%

Table 5.5 – 2%/2mm Global Gamma results for MRI contours and MRI External only datasets.

Patient	MRI Contours Bulk Density (%)	MRI External Only (%)
Lung_19	72.7	56.1
Lung_20	87.7	58.8
Lung_21	76.7	10.9
Lung_23	84.0	59.0
Lung_26	77.9	48.0
Lung_27	74.0	17.9
Lung_28	52.2	38.3
Lung_29	76.2	48.5
Lung_30	85.6	40.6
Lung_31	85.1	30.1
Lung_33	79.6	41.6
Average	77.4	40.9

Similar to the same approach on the CT scans, the bulk density results for only the MRI external contour were also quite poor, with the point dose results ranging from -13.82% to -0.99% with an average of -5.70%. The 2%/2mm gamma pass rates ranged from 10.9% to 58.8% with an average pass rate of 40.9%. For the bulk density results with both the MRI external contour and lung volume overridden, the results were improved compared to the MRI external contour only results. The point dose results ranged from -3.06% to 3.90% with an average of 1.05%, and the 2%/2mm gamma pass rate ranged from 52.2% to 87.7% with an average of 77.4%. These results vary more than the CT bulk density results due to registration and anatomy differences between the CT and MRI scans.

5.4.1.3 Bulk Density with MRI Data with a Bone Model

A 5 patient subset of the study data was used to attempt the automation of the bulk density process and the introduction of a bone model into the conversion process. This subset of patients was chosen to be the patient group where the MRI data patient geometry matched the CT treatment geometry (arms up position). A threshold based autocontouring method was used to generate both the external volume and the lung volumes to automate the bulk density conversion process. These then had densities of 1g/cm^3 and 0.26g/cm^3 applied for the patient external volume and the lungs respectively as per ICRU 46 recommendations [18].

Additionally, a bone model was applied to this small subset of data in an attempt improve the accuracy of the sCT generation and the dose calculation accuracy. An atlas of 10 patient data sets, with each MRI co-registered to each CT scan in the set was used for this. To apply the bone model to a new case, all atlas cases were rigidly registered to the new case, and the atlas case with the best match based on mutual information was selected. This atlas case was then rigidly registered with the new case, and voxels over 200HU (bone) were transferred to the new case as the bone model. This bone model was applied to this subset for both the auto contoured datasets and manually contoured datasets as per the previous section. The original treatment plan was calculated on these new data sets and compared to the treatment plan calculated on the original CT dataset. Table 5.6 and table 5.7 present the point dose results and 2%/2mm global gamma results for the bulk density methodology with a bone model applied as well as the results with the MRI auto contours.

Table 5.6 - Point Dose Results for the Bulk Density Methodology with a Bone Model applied.

Patient	MRI Manual Contours with Bones	MRI Auto Contours with Bones	MRI Auto Contours with No Bones
Lung_19	-1.80%	-3.08%	-2.76%
Lung_26	-3.84%	-2.08%	1.41%
Lung_27	-9.47%	-3.74%	-3.88%
Lung_31	-3.00%	-1.24%	-0.57%
Lung_33	-5.62%	-2.65%	1.03%
Average	-4.74%	-2.56%	-0.95%

Table 5.7 - 2%/2mm Global Gamma Results for the Bulk Density Methodology with a Bone Model applied.

Patient	MRI Manual Contours with Bones (%)	MRI Auto Contours with Bones (%)	MRI Auto Contours with No Bones (%)
Lung_19	77.0	55.0	55.1
Lung_26	64.3	81.6	88.9
Lung_27	42.1	73.6	71.7
Lung_31	62.1	69.0	73.3
Lung_33	49.0	44.9	36.0
Average	58.9	64.8	65.0

For 4 out of the 5 patients used in this subset, the applied bone model agreement with the original plan calculated on original CT scan produced worse results when compared to the non-bone model datasets for the point dose results. For the 2%/2mm gamma results, the bone model produced worse results on 3 out of the 5 patients used in this subset when compared to the non bone model datasets.

The applied bone model was found to be lacking in accuracy, generally extending into the lung or being in the wrong location. Additionally the vertebral bodies seemed to appear twisted or distorted to fit the new patient geometry. This indicates that the matched atlas case was not ideal, though could be improved with a larger atlas to cover a greater number of patient sizes. Figure 5.2 shows an example of the bone model applied.

Deformable registration was also attempted for the registration of the unseen case to the atlas case. However this produced unrealistic skewed bone contours which were no better than using the closest rigid registration case.

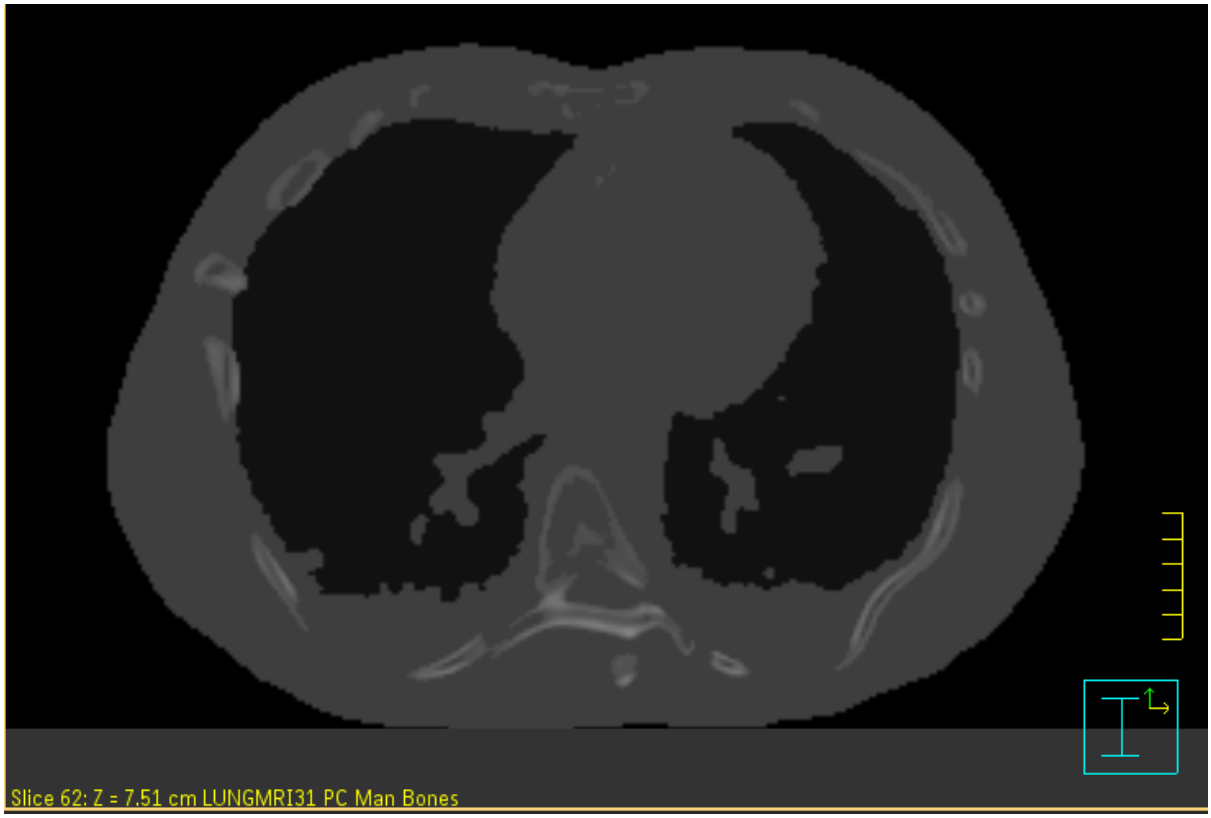

Figure 5.2 - Patient 31 dataset with bone model applied screenshot.

The automatic thresholding worked for most patients, however failed for one patient that had some MRI signal in one of their lungs, possibly due to previous lung collapse. As such this lung was not auto thresholded correctly, and was considered tissue in that dataset. This can be seen in figure 5.3.

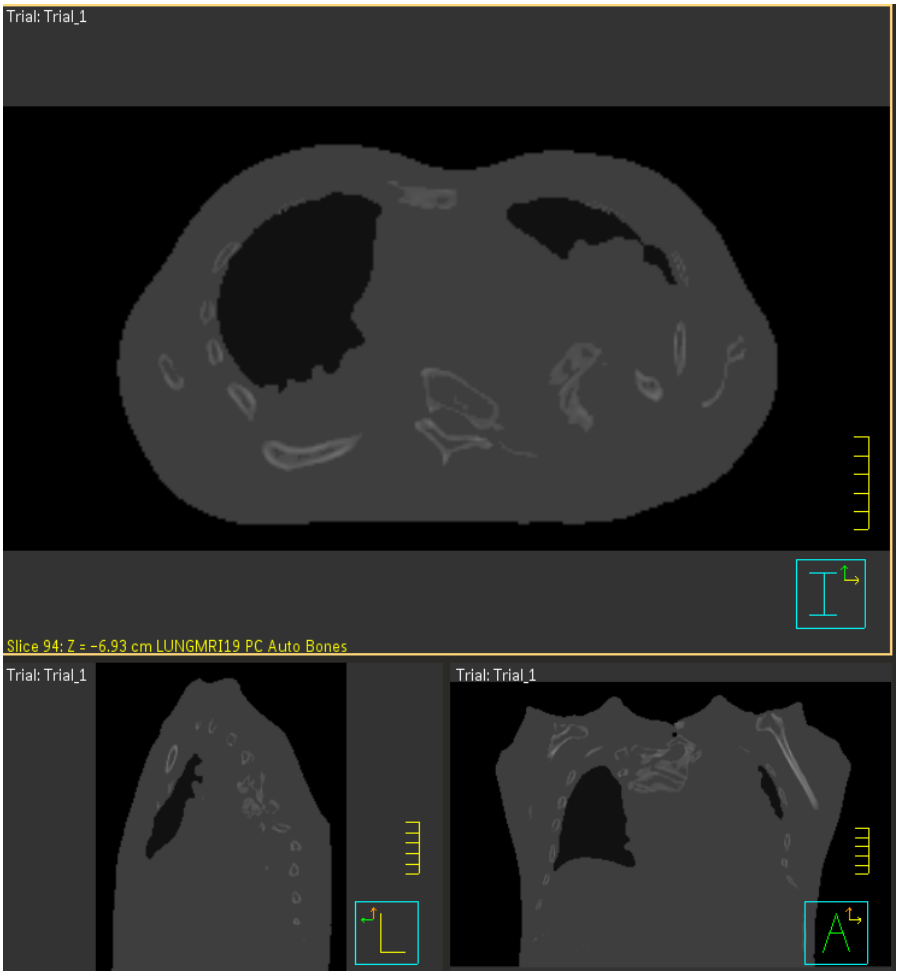

Figure 5.3 - Patient 19 dataset with missing lung screenshot.

5.4.1.4 Distorted CT using a Deformable Registration to the MRI

A distorted CT dataset was created from deformable registration to the MRI scan. This was completed as an indication of the differences between the MRI scan and the CT scan, removing differences in sCT conversion as the original CT and associated densities are still present, though distorted to match the difference in datasets. This was completed on the same subset of 5 patients as used in the previous section which had MRI and CT scans in matching arms up setup positions.

The original CT was registered to the MRI using a deformable registration method. This was based on a cubic B-spline free-deformation model using a normalized mutual information metric from a non-commercial open source software, NiftyReg version 1.3.9 [19]. The deformations from this registration were then applied to the original CT scan. The original treatment plan was calculated on the new deformed CT scan and compared to the original CT scan.

Table 5.8 - Distorted CT compared to CT Point Dose and 2%/2mm Global Gamma Results.

Patient	Point Dose	Gamma (%)
Lung_19	-1.62%	89.7
Lung_26	0.07%	89.7
Lung_27	1.51%	89.7
Lung_31	-0.62%	90.2
Lung_33	0.32%	89.6
Average	-0.07%	89.8

Table 5.8 presents the point dose results and the 2%/2mm global gamma results for these distorted CT datasets compared to the original CT. The point dose results were all within ± 2%, and the 2%/2mm gamma results ranged from 89.6% to 90.2%. This indicates that for this subset of patients, at best a 90.2% 2%/2mm gamma result could be achieved based off the difference in patient anatomy between the CT and MRI scans. This would be due to the differences in lung volume due to the SpiralVIBE scan triggering on the exhale portion of the breathing cycle, which produces a smaller lung volume. The CT scan used for treatment was the average scan generated from the 4D-CT scan, which is an average of all scans acquired during the patient breathing cycle and would produce a lung volume which is larger than that produced in the SpiralVIBE MRI scan.

5.4.2 Atlas Conversion

Atlas Based sCT conversion makes use of image registration to map information from an atlas set of co-registered CT-MR scans across to the new MRI scan. The atlas conversion technique used for this work was adapted from the publication by Dowling et al [20], which was validated for the male pelvis. This methodology additionally made use of manually generated contours to refine the approach.

The MRI images were pre processed using an N4 bias field correction [21] to reduce the signal inhomogeneity across the images. The N4 bias field correction is freely available as part of the open source Insight Toolkit of the National Institutes of Health, and uses a robust B-spline approximation algorithm to correct a range of bias modulation. The CT images were then co-registered to the MRI images, before the conversion was completed as per Dowling et al. [20]. Using a leave one out approach, all other cases were registered to the target MRI using a rigid registration followed by a diffeomorphic demons registration, with a local weighted voting approach used. The diffeomorphic demons registration used is an efficient non parametric diffeomorphic deformable image registration algorithm based on Thirion's demons algorithm [22]. This produced the datasets which are reported here as Atlas

1. These initial results with atlas 1 were poor due to differences in arm position, errors in CT-MR and MR-MR registration and differences in FOV, which lead to incorporating manual body and lung contours as an additional step. This additional step ensured that errors in local weighted voting which produced erroneous air pockets were suitably filled with a soft tissue intensity. This additional step produced the datasets reported as Atlas 2. An example of the SpiralVIBE images, and subsequence Atlas sCT conversion along with the original CT data is shown in figure 5.1.

The main issues with this atlas approach are that it is time consuming, as it requires all the registrations for the atlas, and still required manual lung and external contours to be completed. Additionally the bones were also poorly defined on these atlas based sCTs. Table 5.9 presents the results for the HU comparison of the Atlas 2 sCT datasets with the CT datasets, presenting the Mean Absolute Error (MAE) and the standard deviation.

Table 5.9 - HU MAE for the Atlas Conversion Methodology.

Patient	Atlas 2 MAE HU	St Dev
Lung_19	125.74	146.14
Lung_20	105.13	132.26
Lung_21	185.92	245.98
Lung_23	135.01	222.13
Lung_26	127.34	165.84
Lung_27	158.97	214.44
Lung_28	279.71	331.14
Lung_29	98.71	136.67
Lung_30	294.20	325.16
Lung_31	117.91	157.66
Lung_33	152.93	215.50
Average	161.96	208.45

The average HU MAE within the patient external contour for Atlas 2 was 161.96 HU and ranged from 98.71 HU to 294.20 HU from table 5.9. In other reported anatomical sites, sCTs have been generated for the prostate within 100 HU and for the brain within 150 HU [5, 23-25]. The HU MAE achieved for the atlas conversion methodology, though somewhat higher than those reported elsewhere, appears reasonable considering the difference in the CT and MRI scans due to the motion and patient position for some scans.

Tables 5.10 and 5.11 present the point dose results and the 2%/2mm global gamma results for the original treatment plans recalculated on the new atlas generated sCT datasets. These results are given for both the atlas methods described earlier.

Table 5.10 - Point Dose Results for the Atlas Conversion Methodology.

Patient	%Diff Atlas 2	%Diff Atlas 1
Lung_19	-1.07%	-1.26%
Lung_20	2.89%	4.81%
Lung_21	-0.72%	0.48%
Lung_23	-0.69%	-2.37%
Lung_26	-0.70%	-0.98%
Lung_27	-4.50%	-5.41%
Lung_28	3.65%	2.07%
Lung_29	0.64%	-0.06%
Lung_30	-2.27%	-2.38%
Lung_31	-0.71%	-1.81%
Lung_33	-1.10%	-2.58%
Average	-0.42%	-0.86%

Table 5.11 - 2%/2mm Global Gamma Results for the Atlas Conversion Methodology.

Patient	Atlas 2 (%)	Atlas 1 (%)
Lung_19	79.3	80.7
Lung_20	68.9	57.9
Lung_21	56.7	55.5
Lung_23	85.9	83.2
Lung_26	82.5	78.5
Lung_27	69.1	57.0
Lung_28	50.1	51.9
Lung_29	72.8	72.4
Lung_30	77.2	70.0
Lung_31	79.0	77.4
Lung_33	78.8	68.9
Average	72.8	68.5

The point dose results for atlas 1 varied from -5.41% to 2.07% with an average of -0.86%, while for atlas 2 the point dose results varied from -4.50% to 3.65% with an average of -0.42%. The 2%/2mm gamma pass rates ranged from 51.9% to 83.2% with an average pass rate of 68.5% for Atlas 1, whilst ranging from 50.1% to 85.9% with an average of 72.8% for Atlas 2. When comparing the results for Atlas 2 to Atlas 1, improvement in the point dose was seen in 8 out of the 11 patients, and for 9 out of the 11 patients in regards to the 2%/2mm gamma pass rates. In regards to clinical pass rates, it could be considered that the point dose should agree within ±2%. For Atlas 1, 5 out of 11 patients, and for Atlas 2, 7 out of the 11 patients meet this clinical point dose criteria.

5.4.3 GMM Conversion

A Gaussian Mixture Model (GMM) is a probabilistic model that assumes all data is generated from a mixture of a finite number of Gaussian distributions with unknown parameters. An example may be represented schematically as in figure 5.4. A GMM may be applied to an image dataset as a thresholding tool, and has been used in brain MR images previously [26-28].

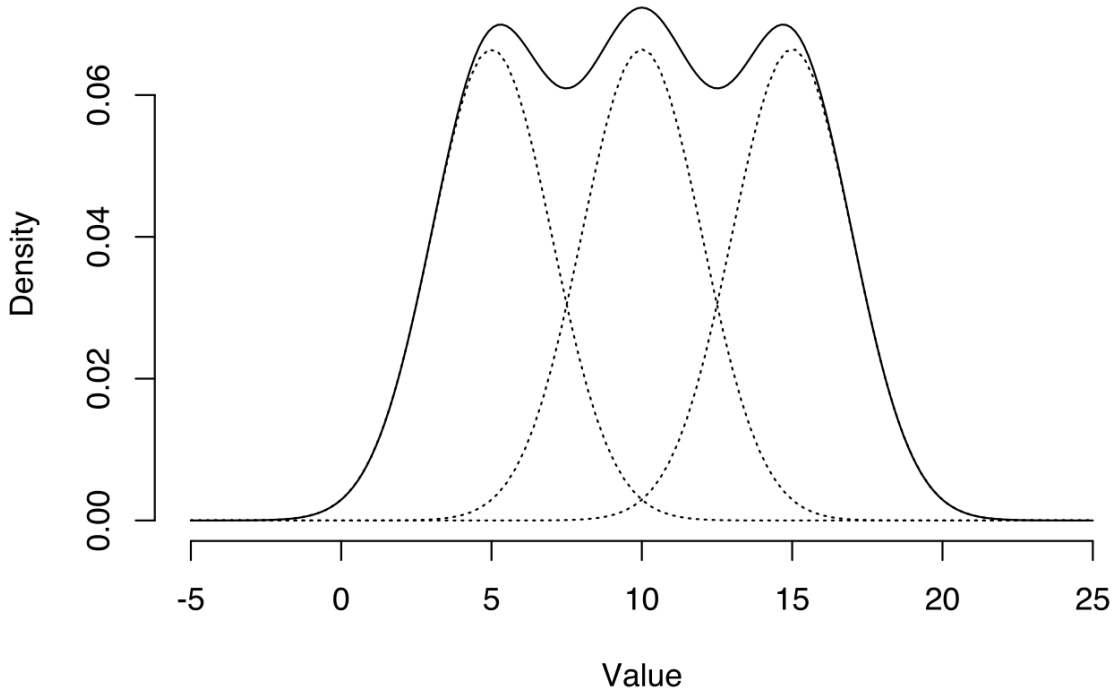

Figure 5.4 - Example of how a Gaussian Mixture Model (GMM) operates, with 3 Gaussian distributions making up the model shown. Figure from Wikipedia, available under the Creative Commons Attribution License.

The MRI images were pre-processed using an N4 bias field correction [21] to reduce the signal inhomogeneity across the images. The CT images were then co-registered to the MRI images with a rigid and a free form deformation registration. An initial training step was undertaken to generate a 10 bin model trained to convert GMM probabilities into CT HU. Following the initial training step, each new MRI was separated into a 3 class GMM, with each class representing three different volumes with probabilities as can be seen in figure 5.5. For these datasets, class 0 was air, class 1 was tissue and class 2 was bright tissue or artefact due to the signal inhomogeneity across the dataset. For each voxel in each volume, the mean HU for each bin (based off the probability from the initial training step) is mapped across from the trained model, and then the three volumes are combined, with the air class having priority. An exemplar patient is used for the bone model – the MRI from this patient is registered using a rigid and diffeomorphic demons registration to the target MRI. From this mapped CT-MR registration, the bones (in a HU range of 300-1000) are mapped to the resulting volume. The advantage of this conversion is that there is no contouring required and so it is relatively fast (when compared to the atlas approach).

For the GMM conversion methodology, 3 out of the 11 patients failed to convert correctly. An example of this is shown in figure 5.6. This was due to the signal inhomogeneity of the image, which was not

able to be corrected for through image pre-processing prior to beginning the conversion process. As such, when class separation was attempted this lack of signal was mistaken for the air class, and the resultant sCT is of air throughout the centre of the patient dataset.

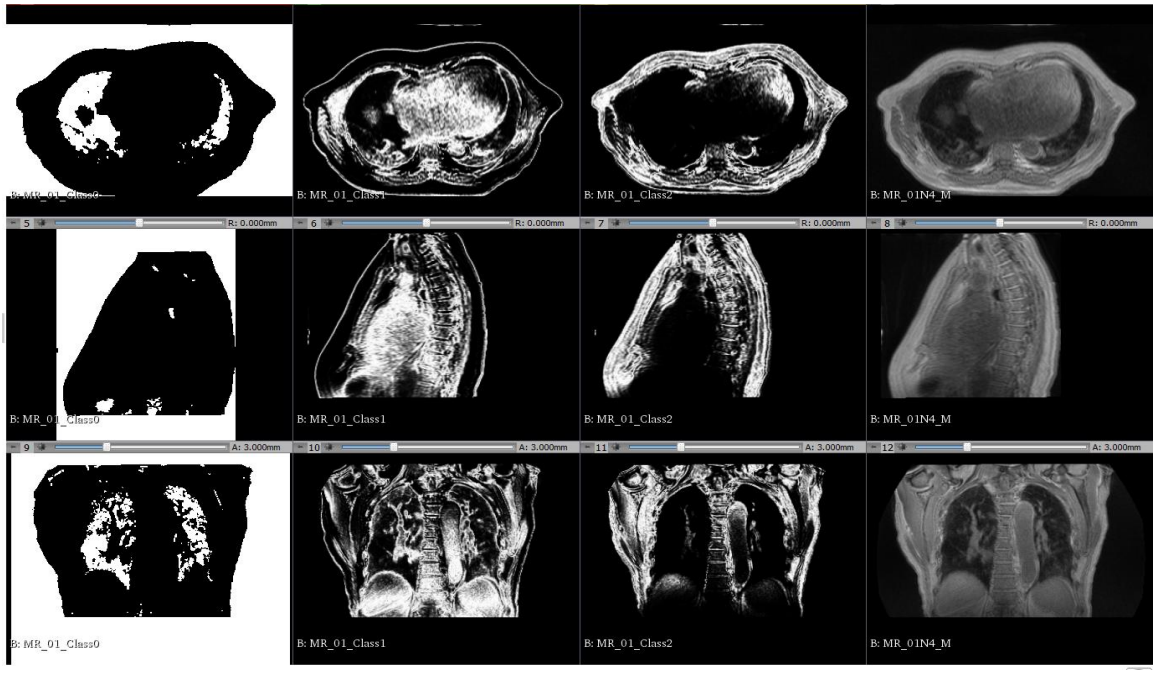

Figure 5.5 - A display of the 3 class GMM separation where class 0 is air, class 1 is tissue and class 2 is bright tissue, some of which is artefact, with the final column being the N4 bias field corrected MRI.

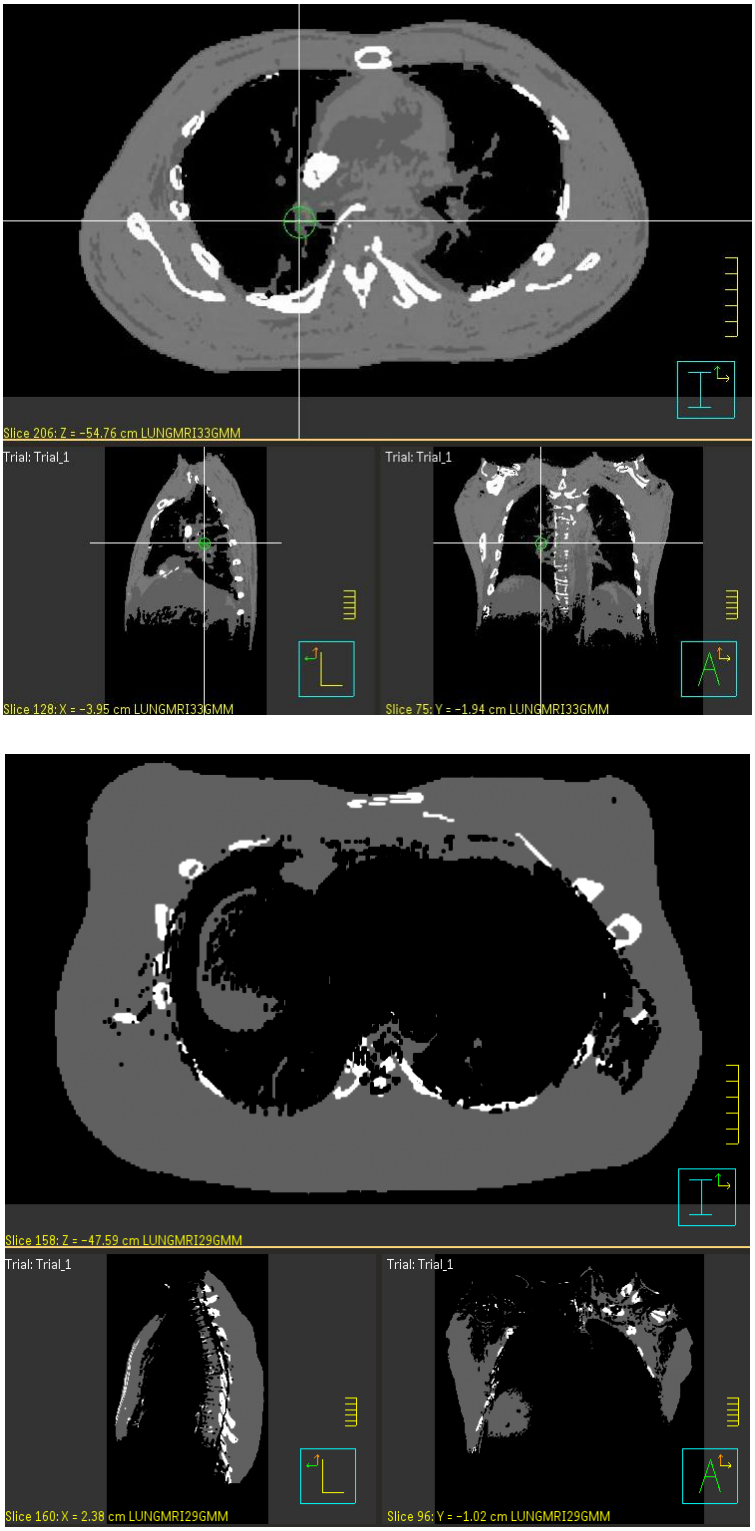

Figure 5.6 - Examples of a successful sCT conversion using the GMM methodology (top) and an unsuccessful conversion (bottom).

Table 5.12 - HU MAE for the GMM Conversion Methodology.

Patient	GMM MAE HU	St Dev
Lung_19	148.04	213.39
Lung_20	163.37	203.12
Lung_21	191.46	254.75
Lung_23	143.55	186.07
Lung_26	126.20	172.32
Lung_27	139.26	175.16
Lung_28	266.48	322.22
Lung_29	379.86	337.19
Lung_30	285.55	317.45
Lung_31	155.53	239.80
Lung_33	207.17	261.51
Average	200.59	243.91

Table 5.12 presents the results for the HU comparison of the GMM sCT datasets with the CT datasets, presenting the Mean Absolute Error (MAE) and the standard deviation. As previously mentioned, in other reported anatomical sites, sCTs have been generated for the prostate within 100 HU and for the brain within 150 HU [5, 23-25]. The MAE HU for the GMM conversion method was on average 200.59 HU and ranged from 126.20 to 379.86 HU. These high differences are due to this conversion method failing for several patients.

Table 5.13 - Point Dose Results for the GMM Conversion Methodology.

Patient	%Diff
Lung_19	-2.47%
Lung_20	
Lung_21	-0.29%
Lung_23	-0.24%
Lung_26	0.70%
Lung_27	-2.13%
Lung_28	
Lung_29	
Lung_30	-2.06%
Lung_31	0.19%
Lung_33	-1.42%
Average	-0.96%

Table 5.14 - 2%/2mm Global Gamma Results for the GMM Conversion Methodology.

Patient	2%2mm Pass Rate (%)
Lung_19	76.0
Lung_20	
Lung_21	57.9
Lung_23	62.2
Lung_26	89.7
Lung_27	76.1
Lung_28	
Lung_29	
Lung_30	66.1
Lung_31	75.4
Lung_33	79.9
Average	72.9

Tables 5.13 and 5.14 present the point dose results and the 2%/2mm global gamma results for the GMM conversion methodology compared to the original CT results. Considering only the GMM conversions which were successful, the point dose results ranged from -2.47% to 0.70% with an average of -0.96%. Similarly for the 2%/2mm gamma results, the results ranged from 57.9% to 89.7%, with an average pass rate of 72.9%. If the additional conversions which did not convert correctly were considered then these values would be much lower. If considering a common clinical pass rate of ±2% for the point dose, only 5 out of the 11 patients met this criteria.

The use of an exemplar bone model for this conversion method was not successful, with the model placed in the incorrect position for most patients. This may be seen in figure 5.7. The vertebral body was incorrectly placed and the ribs in the bone model appeared within the patient lungs for the majority of patients.

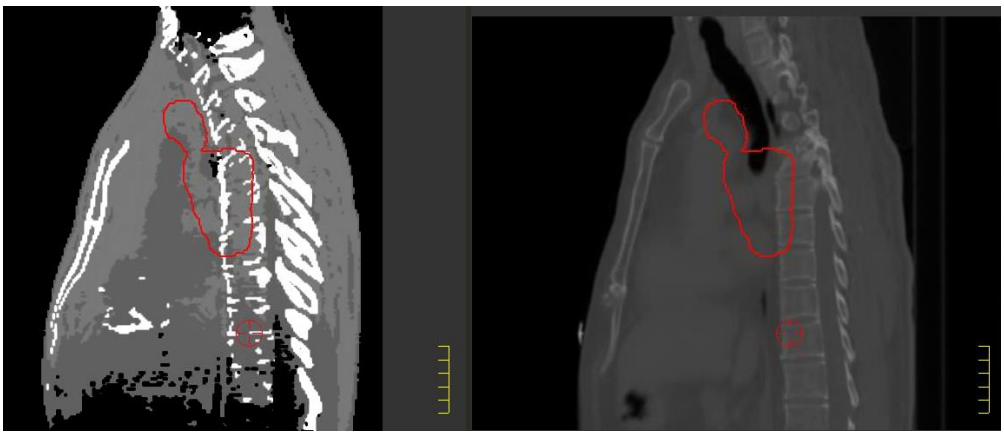

Figure 5.7 - Bone registration from a single exemplar patient.

5.5 Discussion

Various methodologies were used with the MRI data to produce sCT datasets and were compared to the original treatment plan calculated on the patient CT images. Unfortunately the MRI sequence used was shown not to be ideal for use in this manner when compared to the patient CT images and the treatment plans calculated on these. This is due to the signal inhomogeneity across the images which was not able to be suitably processed out, which made it difficult to successfully apply the sCT generation methodologies investigated. Additionally, the inherent differences in lung volume, and the patient external volume in the images due to the SpiralVIBE sequence triggering on the exhale phase, when compared to the treatment CT scan, contributed to the differences in the treatment plan calculation results. Potentially a 4D-MRI approach may be suitable for sCT generation if signal homogeneity can be maintained across the images.

The SpiralVIBE sequence was considered suitable due to the large FOV capturing the entire thorax anatomy as required for treatment planning in a single free breathing sequence. Previous studies had investigated the diagnostic accuracy of this sequence, with a study by Cha et al [8] finding good airway depiction, pulmonary vascular depiction and mediastinal evaluation, concluding that this sequence could be a potential alternative to chest CT. This sequence also scored well in a local volunteer observer study by Kumar et al. [10] in regards to edge detection, artefacts, image noise and overall image quality. However the SpiralVIBE sequence was not able to be converted into suitable sCT images for treatment planning when compared with the gold standard treatment CT images.

In regards to the sCT generation methods attempted, it does not appear that any of those tested produced suitable results for clinical radiotherapy treatment planning. Development and application of machine learning and deep learning methodologies currently show promise for accurate conversion of MRI to sCT [29-33]. For all methodologies, none met a 2% point dose criteria for all patients studied. Additionally, the 2%/2mm gamma pass rate on average was quite low, on average falling under 73% for all methodologies investigated. This gamma pass rate would not be acceptable in regard to clinical criteria.

The bulk density assignment in lung did not produce acceptable results. Previous studies have also concluded that the bulk density approach may not be appropriate for lung cancer, and that a voxel based method is likely required for dosimetrically accurate MR-based planning [34]. This study by Prior et al. [34], found noticeable differences in the internal target volume (ITV) and planning target volume (PTV) dose volume parameters, when comparing CT based planning and "simulated MRI-based plans" which had bulk density forced on the original CT, with dose volume parameters investigated ranging from 4% – 9.8% and 0.3% – 19.6% for the ITV and PTV respectively. As Prior et al's study is wholly based off CT imaging, with bulk density correction applied, it should be noted that no registration error would be present. It should also be considered that a study by Jonsson et al. [35] concluded the opposite to Prior et al., obtaining acceptable results through bulk density correction in the lung using monitor unit (MU) comparison for the same dose. For the MRI bulk density corrected data set compared to the CT dataset, the mean change in MU was 0.2%, and ranged from -0.6% to 0.9% for a 10 patient data set in this study. One difference between the studies is that Jonsson's study ignored the effect of bone anatomy in the MRI bulk density corrected datasets, comprising only of tissue and air, whereas Prior's study included bone anatomy in their CT bulk density correction. Prior et al.'s publication considers Jonsson et al.'s study in the discussion, and does state that it was surprising that they did not observe a larger variation, especially considering the presented case within their paper and the isodose location across vertebrae. Prior et al. does state that not considering the vertebral bone may be an important factor in explaining why Jonsson et al. did not observe the same variations as they have published.

The multi atlas approach used within this chapter did not yield acceptable results. This may possibly have been improved if there were a greater number of patients within the atlas, and if patient scan positions were consistent for all patients between CT and MRI. The addition of manual external and lung contours improved the multi atlas conversion slightly, and this conversion process was able to convert all patients to reasonable sCT datasets as opposed to the GMM conversion. The atlas approach was used by Wang et al. [36] with positron emission tomography (PET)/MR and PET/CT data in a feasibility study using mock target volumes in the lung. Wang et al used attenuation maps derived from a breath hold mDixon sequence in addition to a model based bone segmentation to generate sCT datasets for 11 patients, achieving 2%/2mm gamma pass rates greater than 99%, and mean PTV dose agreement of on average -1.2% ± 0.3%. However, it should be considered that these results were obtained after a non rigid registration was performed between the sCT and the CT before treatment planning, removing registration differences and setup differences between the scans. For all work presented in this chapter, only rigid registrations were used to align the sCT and CT datasets for comparison.

The use of an exemplar bone model as part of the GMM conversion method, that is the bone model from a single patient, was not ideal as shown in figure 5.7. The exemplar patient did not match the anatomy of the other patients closely enough and the spine and bones were incorrectly located within the sCT. The attempt of generating a bone model based off an atlas methodology was also unsuccessful. The difficulty in producing an accurate bone model for sCT for lung has a number of contributing factors, including low MRI signal from bone. Previous studies have attempted to use shape models to generate vertebral bodies [37, 38], using a spine mask shape and removing other known structures from within the area. Some success has been reported using an automatic atlas based segmentation of bones and lungs for generation of sCT of the whole abdomen in pediatric patients with abdominal tumours [39], though this was a larger atlas of 30 patients. Potentially, the addition of an extra MRI sequence which may generate signal from bone [40] may be useful.

Further attempts were made in-house to improve the GMM conversion using only 10 patient datasets with their arms in the treatment position. This was coded using python and ITK, with an N4 bias correction applied before a GMM was applied to split the patient datasets into 3 classes. The initial attempt was made to use bulk density for density overrides, with an additional attempt of using CT-MR co-registered pairs and linear regression to obtain a model for converting density to intensity. This additional work was unsuccessful in improving the conversion, with variations in GMM class extraction due to variation in signal between patients being the primary issue. This further impacted any attempts to generate a reasonable model for density correction. The signal inhomogeneity was not able to be improved with image processing for these scans. Previous studies have demonstrated similar methodologies in the lung or abdomen may work, with a study by Hsu et al. [37, 38] using both the in-phase, fat and water images from a mDixon sequence as well as fuzzy c-means clustering in addition to

intensity thresholding and shape models to generate probability maps representing fat, high density tissue, spine, air and lungs.

SpiralVIBE is triggered on the liver phase – which is close to the exhale phase of the lung. This means that when compared to the lung volume obtained in the average CT, the lung volume from the SpiralVIBE is much smaller. This produces difficulties in registration of the SpiralVIBE scan and/or generated sCT dataset as this inherent difference will be carried from the MRI to the sCT, which increases the uncertainty in the comparison to the ground truth CT scan. This inherent difference in the lung volume and poor bone definition, in addition to the signal inhomogeneity across the MRI images, makes the use of SpiralVIBE for sCT generation difficult. A more suitable sequence, such as a 4D MRI sequence, may provide accurate imaging of the lungs throughout the breathing cycle, and an average 4D MRI dataset, and subsequent generated sCT, may be more suitable for planning and comparison with the 4D average CT [41].

5.6 Conclusion

The SpiralVIBE sequence was ultimately not ideal for use in this setting. As lung is a moving organ, and the SpiralVIBE triggers on a specific phase of the breathing cycle, there were inherent variations when compared to the CT gold standard for radiotherapy treatment planning. This indicates the need for a more suitable MRI sequence – possibly a 4D MRI sequence to allow the possibility of correlating average or motion compensated CT scans with similar MRI scans.

The sCT generation methods investigated did not produce sCT datasets suitable for clinical use with the SpiralVIBE sequence. Further work is required in this space to develop more sophisticated conversion methodologies to produce accurate and clinically acceptable sCT for use.

5.7 References

[1] Dowling JA, Lambert J, Parker J, Salvado O, Fripp J, Capp A, et al. An Atlas-Based Electron Density Mapping Method for Magnetic Resonance Imaging (MRI)-Alone Treatment Planning and Adaptive MRI-Based Prostate Radiation Therapy. International Journal of Radiation Oncology*Biology*Physics. 2012;83:e5-e11.

[2] Kapanen M, Collan J, Beule A, Seppälä T, Saarilahti K, Tenhunen M. Commissioning of MRI-only based treatment planning procedure for external beam radiotherapy of prostate. Magnetic Resonance in Medicine. 2013;70:127-35.

[3] Korsholm M, Waring L, Edmund J. A criterion for the reliable use of MRI-only radiotherapy. Radiation Oncology. 2014;9:16.

[4] Yu H, Caldwell C, Balogh J, Mah K. Toward Magnetic Resonance–Only Simulation: Segmentation of Bone in MR for Radiation Therapy Verification of the Head. International Journal of Radiation Oncology* Biology* Physics. 2014;89:649-57.

[5] Dowling JA, Sun J, Pichler P, Rivest-Hénault D, Ghose S, Richardson H, et al. Automatic substitute computed tomography generation and contouring for magnetic resonance imaging (MRI)-Alone external beam radiation therapy from standard MRI sequences. International Journal of Radiation Oncology* Biology* Physics. 2015;93:1144-53.

[6] Edmund JM, Nyholm T. A review of substitute CT generation for MRI-only radiation therapy. Radiation Oncology. 2017;12:28.

[7] Guerreiro F, Burgos N, Dunlop A, Wong K, Petkar I, Nutting C, et al. Evaluation of a multi-atlas CT synthesis approach for MRI-only radiotherapy treatment planning. Physica Medica. 2017;35:7-17.

[8] Cha MJ, Park HJ, Paek MY, Stemmer A, Lee ES, Park SB, et al. Free-breathing ultrashort echo time lung magnetic resonance imaging using stack-of-spirals acquisition: a feasibility study in oncology patients. Magnetic Resonance Imaging. 2018;51:137-43.

[9] Kumar S, Liney G, Rai R, Holloway L, Moses D, Vinod SK. Magnetic resonance imaging in lung: a review of its potential for radiotherapy. The British Journal of Radiology. 2016;89:20150431.

[10] Kumar S, Rai R, Stemmer A, Josan S, Holloway L, Vinod S, et al. Feasibility of free breathing Lung MRI for Radiotherapy using non-Cartesian k-space acquisition schemes. The British Journal of Radiology. 2017;90:20170037.

[11] Qian Y, Boada FE. Acquisition-weighted stack of spirals for fast high-resolution three-dimensional ultra-short echo time MR imaging. Magnetic Resonance in Medicine: An Official Journal of the International Society for Magnetic Resonance in Medicine. 2008;60:135-45.

[12] Song HK, Wehrli FW. Variable TE gradient and spin echo sequences for in vivo MR microscopy of short T2 species. Magnetic Resonance in Medicine. 1998;39:251-8.

[13] Robson MD, Tyler DJ, Neubauer S. Ultrashort TE chemical shift imaging (UTE-CSI). Magnetic Resonance in Medicine: An Official Journal of the International Society for Magnetic Resonance in Medicine. 2005;53:267-74.

[14] Chen L, Price Jr R, Nguyen T, Wang L, Li J, Qin L, et al. Dosimetric evaluation of MRI-based treatment planning for prostate cancer. Physics in Medicine and Biology. 2004;49:5157.

[15] Chen L, Price RA, Wang L, Li J, Qin L, McNeeley S, et al. MRI-based treatment planning for radiotherapy: dosimetric verification for prostate IMRT. International Journal of Radiation Oncology* Biology* Physics. 2004;60:636-47.

[16] Stanescu T, Hans-Sonke J, Stavrev P, Fallone BG. 3T MR-based treatment planning for radiotherapy of brain lesions. Radiology and Oncology. 2006;40.

[17] Eilertsen K, Nilsen Tor Arne Vestad L, Geier O, Skretting A. A simulation of MRI based dose calculations on the basis of radiotherapy planning CT images. Acta Oncologica. 2008;47:1294-302.

[18] White G, Wilson I. Photon, electron, proton and neutron interaction data for body tissues. ICRU Report. 1992;46.

[19] Modat M, Ridgway GR, Taylor ZA, Lehmann M, Barnes J, Hawkes DJ, et al. Fast free-form deformation using graphics processing units. Computer Methods and Programs in Biomedicine. 2010;98:278-84.

[20] Dowling JA, Sun J, Pichler P, Rivest-Hénault D, Ghose S, Richardson H, et al. Automatic substitute CT generation and contouring for MRI-alone external beam radiation therapy from standard MRI sequences. International Journal of Radiation Oncology • Biology • Physics. 2015.

[21] Tustison NJ, Avants BB, Cook PA, Zheng Y, Egan A, Yushkevich PA, et al. N4ITK: improved N3 bias correction. IEEE transactions on medical imaging. 2010;29:1310-20.

[22] Vercauteren T, Pennec X, Perchant A, Ayache N. Diffeomorphic demons: Efficient non-parametric image registration. NeuroImage. 2009;45:S61-S72.

[23] Andreasen D, Van Leemput K, Hansen RH, Andersen JA, Edmund JM. Patch-based generation of a pseudo CT from conventional MRI sequences for MRI-only radiotherapy of the brain. Medical Physics. 2015;42:1596-605.

[24] Johansson A, Karlsson M, Nyholm T. CT substitute derived from MRI sequences with ultrashort echo time. Medical Physics. 2011;38:2708-14.

[25] Koivula L, Guerreiro F, Raaymakers BW, Korhonen J. EP-2086: Synthetic CT generation from standard T2-weighted MR image – lung, vertebrae, and liver targets. Radiotherapy and Oncology. 2018;127:S1145-S6.

[26] Greenspan H, Ruf A, Goldberger J. Constrained Gaussian mixture model framework for automatic segmentation of MR brain images. IEEE transactions on medical imaging. 2006;25:1233-45.

[27] Huang Z-K, Chau K-W. A new image thresholding method based on Gaussian mixture model. Applied Mathematics and Computation. 2008;205:899-907.

[28] Ji Z, Xia Y, Sun Q, Chen Q, Xia D, Feng DD. Fuzzy Local Gaussian Mixture Model for Brain MR Image Segmentation. IEEE Transactions on Information Technology in Biomedicine. 2012;16:339-47.

[29] Kazemifar S, McGuire S, Timmerman R, Wardak Z, Nguyen D, Park Y, et al. MRI-only brain radiotherapy: Assessing the dosimetric accuracy of synthetic CT images generated using a deep learning approach. Radiotherapy and Oncology. 2019;136:56-63.

[30] Li Y, Li W, He P, Xiong J, Xia J, Xie Y. CT synthesis from MRI images based on deep learning methods for MRI-only radiotherapy. 2019 International Conference on Medical Imaging Physics and Engineering (ICMIPE)2019. p. 1-6.

[31] Massa HA, Johnson JM, McMillan AB. Comparison of deep learning synthesis of synthetic CTs using clinical MRI inputs. Physics in Medicine & Biology. 2020;65:23NT03.

[32] Liu J, Pan Y, Li M, Chen Z, Tang L, Lu C, et al. Applications of deep learning to MRI images: A survey. Big Data Mining and Analytics. 2018;1:1-18.

[33] Lenkowicz J, Votta C, Nardini M, Quaranta F, Catucci F, Boldrini L, et al. A deep learning approach to generate synthetic CT in low field MR-guided radiotherapy for lung cases. Radiotherapy and Oncology. 2022;176:31-8.

[34] Prior P, Chen X, Gore E, Johnstone C, Li XA. Is bulk electron density assignment appropriate for MRI-only based treatment planning for lung cancer? Medical Physics. 2017;44:3437-43.

[35] Jonsson J, Karlsson M, Karlsson M, Nyholm T. Treatment planning using MRI data: an analysis of the dose calculation accuracy for different treatment regions. Radiation Oncology. 2010;5:62.

[36] Wang H, Chandarana H, Block KT, Vahle T, Fenchel M, Das IJ. Dosimetric evaluation of synthetic CT for magnetic resonance-only based radiotherapy planning of lung cancer. Radiation Oncology. 2017;12:108.

[37] Hsu S, Peng Q, Tomé W. On the generation of synthetic CT for a MRI-only radiation therapy workflow for the abdomen. Journal of Physics: Conference Series: IOP Publishing; 2019. p. 012011.

[38] Hsu SH, DuPre P, Peng Q, Tomé WA. A technique to generate synthetic CT from MRI for abdominal radiotherapy. Journal of Applied Clinical Medical Physics. 2020;21:136-43.

[39] Guerreiro F, Koivula L, Seravalli E, Janssens GO, Maduro JH, Brouwer CL, et al. Feasibility of MRI-only photon and proton dose calculations for pediatric patients with abdominal tumors. Physics in Medicine & Biology. 2019;64:055010.

[40] Hsu S-H, Cao Y, Lawrence TS, Tsien C, Feng M, Grodzki DM, et al. Quantitative characterizations of ultrashort echo (UTE) images for supporting air–bone separation in the head. Physics in Medicine and Biology. 2015;60:2869.

[41] Stemkens B, Paulson ES, Tijssen RH. Nuts and bolts of 4D-MRI for radiotherapy. Physics in Medicine & Biology. 2018;63:21TR01.

6 Effects of MR Imaging Time Reduction on Substitute CT Generation for Prostate MRI-Only Treatment Planning

6.1 Presentations and Publications

Initial work was presented at EPSM 2017, Engineering and Physical Sciences in Medicine on 29th October – 1st November 2017 in Hobart, Australia under the poster presentation titled "The Effect of MRI Sequence Variations on Substitute CT Generation for MR-Only Planning".

Follow up work was presented at EPSM 2020, Engineering and Physical Sciences in Medicine on 2nd – 4th November 2020 under the poster presentation titled "Can we reduce imaging time and still generate acceptable Substitute CT for Prostate MRI Only Treatment Planning?".

A copy of these accepted conference abstracts is presented in thesis appendix 4.

This work was published as a scientific paper in Physical and Engineering Sciences in Medicine in 2021. The full reference is as follows: Young, T., Dowling, J., Rai, R. et al. Effects of MR imaging time reduction on substitute CT generation for prostate MRI-only treatment planning. Physical and Engineering Sciences in Medicine. 44, 799–807 (2021). https://doi.org/10.1007/s13246-021-01031-0

This publication won the 2022 Kenneth Clarke Journal Award for best paper on original work published in the Australasian Physical and Engineering Sciences in Medicine journal authored by a member of the ACPSEM in 2021. This publication is presented as the chapter. Any additions to the original publication are presented in *italics*.

6.2 Preamble

Prostate magnetic resonance imaging (MRI)-only radiotherapy has become clinically available in recent years. Commercial solutions are available for synthetic CT (sCT) generation from different MRI vendors and companies, utilizing different MRI sequences and sCT generation methodologies. All available solutions make use of a particular MRI sequence, with set sequence parameters to ensure appropriate MRI image quality for accurate sCT generation.

This study investigated the effects of time reduction on an MRI sequence used for sCT generation for prostate MRI-only treatment planning. The aim of the time reduction of the MRI sequence was to reduce the potential effects of patient and organ motion on the scan, as well as the impact on the patient. For a multi-atlas sCT generation methodology, the benchmarked MRI sequence had various parameters adjusted to reduce the MRI sequence imaging time. These time-reduced MR images were then

converted to sCT and compared to the sCT generated with the original MRI sequence for both anatomical and dosimetric parameters.

6.3 Publication - Effects of MR Imaging Time Reduction on Substitute CT Generation for Prostate MRI-Only Treatment Planning

Tony Young

Liverpool and Macarthur Cancer Therapy Centres and Ingham Institute, Sydney, Australia.

Institute of Medical Physics, School of Physics, University of Sydney, Sydney, Australia

Tony.Young@health.nsw.gov.au

Jason Dowling

CSIRO Health and Biosecurity, The Australian e-Health & Research Centre, Australia

South Western Sydney Clinical School, University of New South Wales, Australia

Institute of Medical Physics, University of Sydney, Australia

School of Mathematical and Physical Sciences, University of Newcastle, Australia

Centre for Medical Radiation Physics, University of Wollongong, Wollongong,

New South Wales, Australia

Jason.Dowling@csiro.au

Robba Rai

Liverpool and Macarthur Cancer Therapy Centres and Ingham Institute, Sydney, Australia.

University of New South Wales, Sydney, New South Wales, Australia

Robba.Rai@health.nsw.gov.au

Gary Liney

Liverpool and Macarthur Cancer Therapy Centres and Ingham Institute, Sydney, Australia

University of New South Wales, Sydney, New South Wales, Australia

Centre for Medical Radiation Physics, University of Wollongong, Wollongong,

New South Wales, Australia

Gary.Liney@health.nsw.gov.au

Peter Greer

Calvary Mater Newcastle Hospital, Newcastle, New South Wales, Australia

School of Mathematical and Physical Sciences, University of Newcastle, Australia

peter.greer@newcastle.edu.au

David Thwaites

Institute of Medical Physics, School of Physics, University of Sydney, Sydney, Australia.

david.thwaites@sydney.edu.au

Lois Holloway

Liverpool and Macarthur Cancer Therapy Centres and Ingham Institute, Sydney, Australia.

University of New South Wales, Sydney, New South Wales, Australia

Institute of Medical Physics, School of Physics, University of Sydney, Australia.

Centre for Medical Radiation Physics, University of Wollongong, Wollongong,

New South Wales, Australia

lois.holloway@health.nsw.gov.au

Abstract

Introduction

The introduction of MRI linear accelerators (MR-linacs) and the increased use of MR imaging in radiotherapy, requires improved approaches to MRI-only radiotherapy. MRI provides excellent soft tissue visualisation but does not provide any electron density information required for radiotherapy dose calculation, instead MRI is registered to CT images to enable dose calculations. MRI-only radiotherapy

eliminates registration errors and reduces patient discomfort, workload and cost. Electron density requirements may be addressed in different ways, from manually applying bulk density corrections, to more computationally intensive methods to produce substitute CT datasets (sCT), requiring additional sequences, increasing overall imaging time. Reducing MR imaging time would reduce potential artefacts from intrafraction motion and patient discomfort. The aim of this study was to assess the impact of reducing MR imaging time on a hybrid atlas-voxel sCT conversion for prostate MRI-only treatment planning, considering both anatomical and dosimetric parameters.

Method

10 volunteers were scanned on a Siemens Skyra 3T MRI. Sequences included the 3D T2-weighted (T2-w) SPACE sequence used for sCT conversion as previously validated against CT, along with variations to this sequence in repetition time (TR), turbo factor, and combinations of these to reduce the imaging time. All scans were converted to sCT and were compared to the sCT from the original SPACE sequence, evaluating for anatomical changes and dosimetric differences for a standard prostate VMAT plan.

Results

Compared to the previously validated T2-w SPACE sequence, scan times were reduced by up to 80%. The external volume and bony anatomy were compared, with all but one sequence meeting a DICE coefficient of 0.9 or better, with the largest variations occurring at the edges of the external body volume. The generated sCT agreed with the gold standard sCT within an isocentre dose of 1% and a gamma pass rate of 99% for a 1%/1mm gamma tolerance for all but one sequence.

Conclusion

This study demonstrates that the MR imaging sequence time was able to be reduced by approximately 80% with similar dosimetric results.

Keywords – MRI-Only, sCT, Prostate

Introduction

Magnetic Resonance Imaging (MRI) utilisation in radiotherapy is increasing with MRI-simulators and other MR imaging becoming more widely available for treatment planning and with the introduction of MRI linear accelerators (MR-linacs). Radiotherapy treatment planning currently uses Computed Tomography (CT) imaging as the gold standard as it provides bony anatomical information in addition to electron density information required for treatment planning calculations. MRI is used to complement the existing CT images, providing excellent soft tissue visualisation which may be used to guide the contouring of the target and organs at risk. These MRI images are registered to the CT images, introducing registration error and potentially also errors due to variations in patient setup and internal organ motion [1, 2].

Completing radiotherapy treatment with only MR imaging has become a possibility in recent years. Termed MRI-only radiotherapy [2-11], this process of radiotherapy without use of CT imaging, but only MRI, removes registration errors between CT and MRI, and has been reported to reduce patient discomfort, workload and the cost of additional scans [12-14]. However, MRI does not provide any electron density information required for dose calculations, with various methods proposed and developed to address this. These methods to convert MR image data to Hounsfield Units (HU) generate datasets which have been referred to as substitute, synthetic or pseudo CT images (sCT), and include bulk density or voxel based corrections, atlas methods, hybrid voxel and atlas methods and deep learning algorithms [15-17].

Current MRI sequences used for sCT generation can take several minutes to be completed [18], increasing the potential for artefacts due to patient and organ motion. The reduction of MR imaging time would produce a reduction in costs, allow greater patient throughput and comfort and reduce the potential effects of patient or organ motion [19]. However in MRI there is a trade off between scan time reduction and image quality, with the potential for loss of image contrast, signal to noise ratio and resolution along with an increased risk of artefacts [20]. With the advent of MR-linacs, fast MRI sequences able to be used for patient simulation, sCT generation and treatment planning, as well as patient setup for radiotherapy treatment would enable online adaptive planning and facilitate a move to a MRI-only radiotherapy process rather than the current practice requiring a pre-treatment CT scan [21].

Theoretically, MR imaging time is a function of repetition time (TR), the number of signal averages and the phase encoding matrix size necessary to produce the desired spatial resolution in the required Field of View (FOV) [22, 23]. Fast spin echo imaging also has potential for time reduction in applying longer echo train lengths (turbo factor) [24-27], with the imaging time function being divided by this factor. Additionally, as image information in an MRI is acquired in k-space, other methods of reducing the acquisition time are available by manipulating or undersampling the data collected. Undersampled k-space data will introduce potential artefacts into the images; however, with additional information

applied during the Fourier transform, reconstructed images of acceptable quality may be obtained. This is the basic premise of both partial Fourier imaging and parallel imaging [22, 28, 29].

This study investigates the effect of adjusting sequence parameters to reduce MR imaging time, and the impact on a previously validated hybrid atlas-voxel sCT conversion in regard to sCT generation accuracy and dosimetric effects in treatment planning based on this.

Method

Ten male volunteers were scanned on a Siemens (Erlangen, Germany) Skyra 3T MRI with a flat radiotherapy couch and coil mounts. Volunteer Body Mass Index (BMI) ranged from 22.3 to 30.1 and volunteers were scanned with empty bladders for comfort. The "Original" planning MRI sequence validated against CT from Dowling et al [30] was a 3D T2 weighted isotropic SPACE (Sampling Perfection with Application optimised Contrasts using different flip angle Evolution) sequence which covered the entire pelvis. The scan limits began at L5/S1 and ended at pubic symphysis in the craniocaudal direction, to ensure that the entire bladder and distal rectum was included in the scan length. Additional SPACE sequences covering the same FOV and scan length that had variations to the original sequence parameters in repetition time (TR), turbo factor, partial Fourier acceleration, parallel imaging acceleration, and a combination of these to reduce the sequence imaging time were considered here. The sequences, with variations to the original sequence and average scan time, are listed in table 6.1.

Table 6.1 - Sequence parameters and the average scan time.

MRI Sequence	Average TR (ms)	Turbo factor	Partial Fourier	Imaging Acceleration Factor	Average Scan Time (min:sec)
T2_SPACE_Original	1700	80	7/8	4	5:04
T2_SPACE_TR1200	1200	80	7/8	4	3:34
T2_SPACE_TR800	800	80	7/8	4	2:23
T2_SPACE_TURBO160	1700	160	7/8	4	2:33
T2_SPACE_TURBO300	1700	300	7/8	4	1:26
T2_SPACE_5-8PF	1700	80	5/8	4	3:39
T2_SPACE_p6_6-8FT_Turbo120_TR1200	1200	120	6/8	6	1:19
T2_SPACE_p6_6-8FT_Turbo120_TR900	900	120	6/8	6	1:00

For all image sequences, a minimum FOV of 420 mm in the AP and LR directions, and voxel size of 1.6x1.6x1.6 mm^3 was achieved with the same values used for original and modified sequences for each volunteer. In the CC direction, 128 slices were captured using these sequence parameters, with this reduced to 120 slices if the system required due to SAR limitations. Where possible, all other parameters, as per the original sequence, were maintained in each modified sequence, with changes only in the relevant parameters being tested. Table 6.1 provides sequence pre-set parameters which were only modified if required by the system.

All MRI datasets were converted to sCT using a hybrid atlas-voxel method as described in Dowling et al. [30]. All generated sCT were compared to the sCT generated using the original sequence. Mean absolute error (MAE) and standard deviation in HU for the generated sCT for each sequence was obtained from comparison to the original sequence generated sCT, with the body mask from the original sequence sCT used. Additionally, an anatomical comparison was done for the body volume and automatically generated bones using volume differences, Hausdorff distance and DICE comparison.

A single arc Volumetric Arc Therapy (VMAT) prostate treatment plan was generated on the original sCT using the Pinnacle Treatment Planning System (v16.21; Philips Healthcare, Andover, MA). The bladder, rectum and a PTV volume expanded from the prostate were contoured on the original MRI sequence, and were used by the departmental clinical auto planning procedure to create a 78Gy in 39 fraction treatment plan. The auto planning procedure aims to meet a D95 of 78Gy to the PTV whilst minimising rectum and bladder dose. This treatment plan was copied to each sCT and recalculated with fixed monitor units (MU). As all images were completed during the same session with the same scan

centre, no registration was required between sequences/sCT for comparison. The isocentre point dose was compared, as well as a 1%/1mm global gamma analysis of the dose distribution for each recalculated treatment plan against the original plan. Additionally, the DVH for the PTV, rectum and bladder volume from the original dataset were compared for the plan re-calculated on each dataset. The DVH parameters reported are used for clinical reporting and were clinical DVH criteria in the auto planning procedure.

Results

The proposed sequences were able to be completed on all volunteers, though some modifications to sequences were required by the system. This was to ensure SAR requirements were not exceeded, and involved slight adjustments to flip angles, or for one volunteer, an increase in TR for the low TR sequences. As such the TR800 sequence and the TR900 sequence were unable to be completed for this volunteer, having to be increased to TR935 and TR988 respectively.

All sequences used were able to be converted to sCT as per the published procedure [30]. A mid scan slice of each MRI sequence for a sample volunteer and the subsequently generated sCT is shown in Figure 6.1.

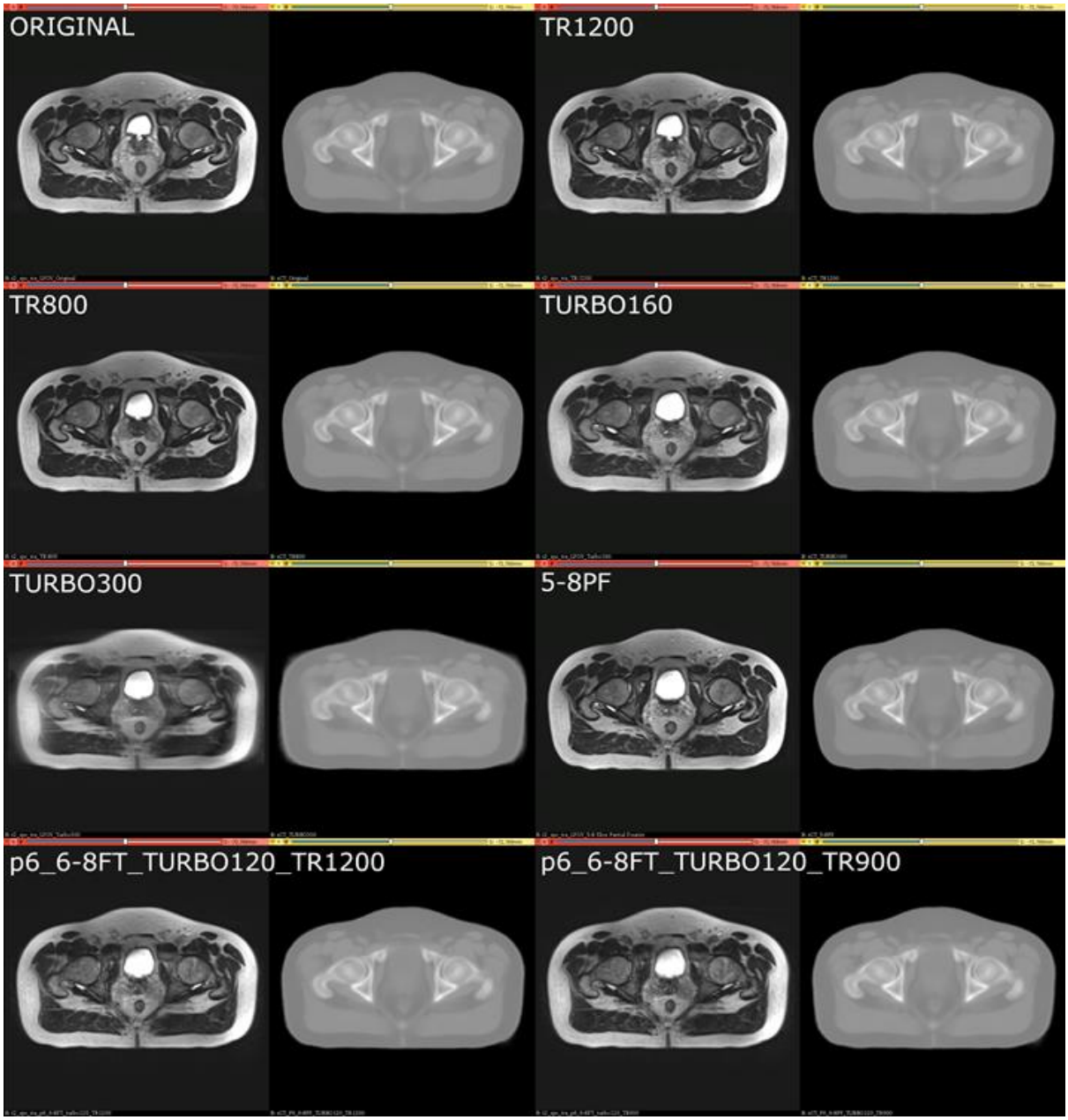

Figure 6.1 - A mid dataset slice of each MRI sequence and the corresponding generated sCT slice for a sample volunteer.

Mean absolute error (MAE) and standard deviation in HU for the generated sCT for each sequence were obtained from comparison to the original sequence generated sCT with the body mask from the original sequence sCT used (Figure 6.2). The TURBO300 scan *derived sCTs* showed the largest MAE in HU compared to the original sequence. For all other sequences, the *average* MAE was within 40 HU.

a)

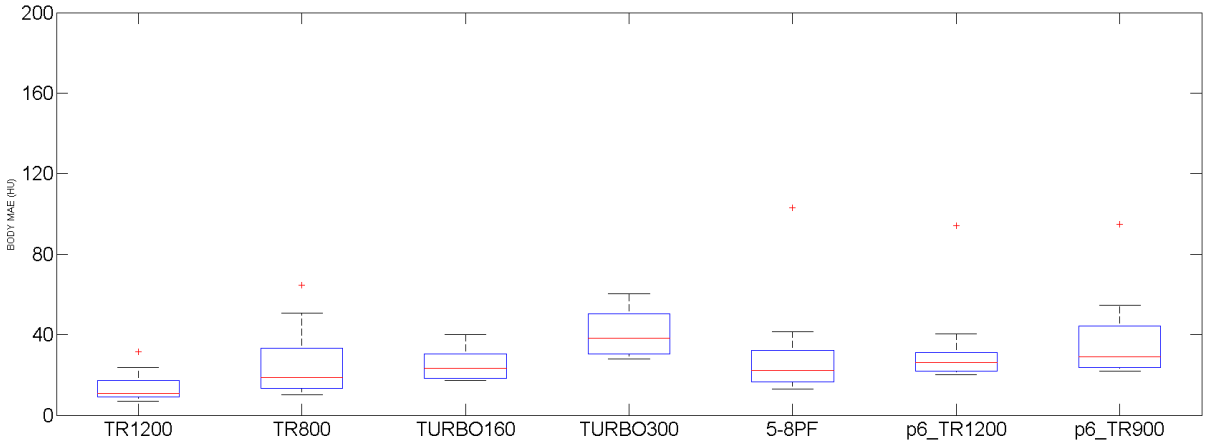

b)

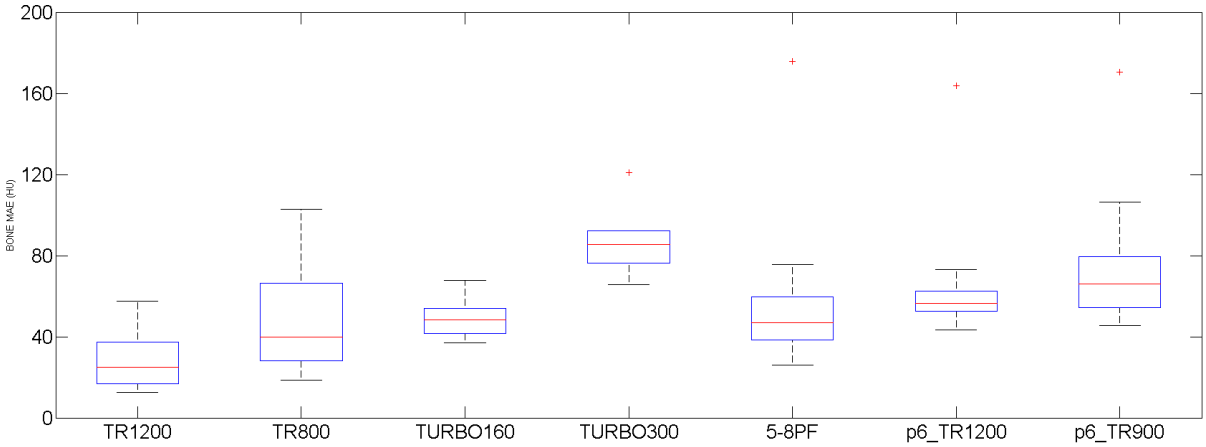

Figure 6.2 - Mean Absolute Error (MAE) of HU of each generated sCT compared to the sCT generated from the original MRI sequence for a) entire body and b) automatic bone contours. Note the TURBO300 has a single outlier.

Most sequences produced a body volume within 2% of the original sequence, as shown in Table 6.2. The TURBO300 sequence gave values greater than this. In regards to the volume of the bones within the dataset, large variations were observed in the TURBO300 sequence, with the TR1200, TURBO160 and p6_6-8FT_TR1200 sequence all within 2% of the original sequence on average.

Table 6.2 - Average volume absolute percentage difference comparison, average mean Hausdorff distance and average DICE results for the automatic body and bone contours for the generated sCT compared to the original sequence generated sCT. All errors are 1 SD, ranges are given in brackets.

	Body Volume % Difference	Body Mean Hausdorff (mm)	Body DICE	Bone Volume % Difference	Bone Mean Hausdorff (mm)	Bone DICE
TR1200	0.51% ± 0.67% (0.09%:2.27%)	0.72 ± 0.29 (0.51:1.42)	0.991 ± 0.003 (0.983:0.993)	1.60% ± 2.87% (0.07%:9.68%)	0.64 ± 0.25 (0.47:1.31)	0.953 ± 0.015 (0.916:0.966)
TR800	1.97% ± 2.68% (0.44%:8.18%)	1.10 ± 0.91 (0.53:3.25)	0.984 ± 0.013 (0.955:0.993)	3.19% ± 3.97% (0.41%:12.66%)	0.77 ± 0.30 (0.48:1.45)	0.943 ± 0.020 (0.902:0.964)
TURBO160	0.73% ± 0.51% (0.01%:1.93%)	1.18 ± 0.38 (0.87:2.13)	0.985 ± 0.004 (0.977:0.989)	1.90% ± 2.62% (0.03%:9.03%)	0.78 ± 0.23 (0.55:1.32)	0.943 ± 0.015 (0.914:0.956)
TURBO300	7.14% ± 3.21% (4.72%:15.07%)	4.86 ± 2.06 (3.08:9.82)	0.946 ± 0.025 (0.887:0.968)	5.01% ± 4.85% (0.26%:15.78%)	2.00 ± 1.06 (1.03:4.55)	0.869 ± 0.062 (0.717:0.927)
5-8PF	1.31% ± 1.47% (0.05%:4.54%)	1.13 ± 0.98 (0.54:3.62)	0.985 ± 0.013 (0.950:0.993)	2.22% ± 2.53% (0.27%:8.94%)	1.10 ± 1.15 (0.53:4.29)	0.921 ± 0.075 (0.714:0.962)
p6_6-8FT_Turbo120_TR1200	1.68% ± 0.48% (1.01%:2.68%)	1.57 ± 0.76 (1.03:3.49)	0.980 ± 0.011 (0.952:0.988)	1.78% ± 2.83% (0.08%:9.66%)	1.19 ± 1.03 (0.60:4.04)	0.916 ± 0.065 (0.735:0.951)
p6_6-8FT_Turbo120_TR900	1.65% ± 0.46% (1.04%:2.21%)	1.79 ± 0.86 (1.05:3.50)	0.977 ± 0.013 (0.951:0.987)	2.58% ± 3.36% (0.08%:10.31%)	1.29 ± 1.04 (0.61:4.14)	0.909 ± 0.065 (0.730:0.951)

The majority of the sequences achieved a greater than 0.98 DICE coefficient for the body contour compared to the original, with a mean Hausdorff value of less than 2mm. The DICE coefficient for the bone contours was greater than 0.90 for the same majority, with a mean Hausdorff value of less than 2 mm.

All datasets which were a variation of the original SPACE sequence had an isocentre point dose value within 2.5% of the original plan, with the majority on average within ±1%, as shown in Figure 6.3 and Table 6.3. For a 1%/1mm global gamma index tolerance within the original sequence body contour as reference, most sequences had a greater than 99.9% pass rate, apart from the TURBO300 sequence (Table 6.3).

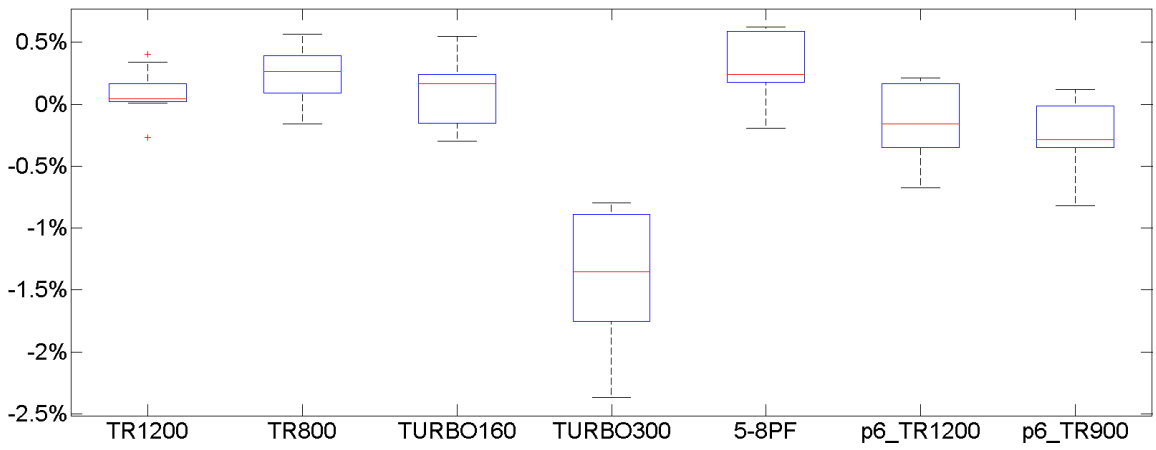

Figure 6.3 - Range of isocentre point dose differences for the VMAT plan generated on the original sequence sCT and recalculated on all other datasets for each volunteer. The dose difference was a comparison to the original sequence sCT.

Table 6.3 - Average dosimetric results for each sequence sCT compared back to the original sequence sCT. All errors are 1 SD, ranges are given in brackets.

sCT	Isocentre Average % Dose Difference	1%/1mm Average Gamma Passrate (%)
TR1200	0.10% ± 0.19% (-0.27%:0.4%)	99.99 ± 0.02 (99.95:100)
TR800	0.24% ± 0.22% (-0.16%:0.57%)	99.96 ± 0.10 (99.68:100)
TURBO160	0.12% ± 0.28% (-0.30%:0.55%)	99.97 ± 0.04 (99.85:100)
TURBO300	-1.39% ± 0.52% (-2.37%:-0.79%)	79.22 ± 15.02 (50.21:98.23)
5-8PF	0.30% ± 0.27% (-0.19%:0.62%)	99.92 ± 0.14 (99.54:100)
p6_6-8FT_Turbo120_TR1200	-0.14% ± 0.29% (-0.67%:0.21%)	99.97 ± 0.03 (99.91:100)
p6_6-8FT_Turbo120_TR900	-0.26% ± 0.31% (-0.82%:0.12%)	99.93 ± 0.13 (99.56:100)

DVH analysis was completed with each *recalculated* treatment plan compared to the original treatment plan *calculated* on the *sCT generated from the* original *SPACE* sequence dataset. Table 6.4 displays the average for the 10 volunteers for each DVH statistic. In regard to the PTV DVH statistics reported, on average the differences compared to the original dataset were within 0.5% for all sequences except for the TURBO300 sequence. On average, all sequences except for the TURBO300 sequence were within 2% for the bladder and rectum V40 and V65 DVH points.

Table 6.4 - DVH Comparison of the PTV, Bladder and Rectum. These values are averaged across the 10 volunteers, with errors reported as 1SD. The range of differences across the dataset for each sequence is also reported.

	TR1200	TR800	TURBO160	TURBO300	5-8PF	p6_6-8FT_Turbo120_TR1200	p6_6-8FT_Turbo120_TR900
PTV							
D98	0.11% ± 0.14% (-0.05%:0.35%)	0.16% ± 0.18% (-0.21%:0.41%)	0.00% ± 0.21% (-0.33%:0.34%)	-1.55% ± 0.73% (-3.01%:-0.41%)	0.26% ± 0.23% (-0.15%:0.59%)	-0.27% ± 0.23% (-0.76%:0.06%)	-0.35% ± 0.23% (-0.83%:-0.03%)
D95	0.11% ± 0.12% (-0.03%:0.28%)	0.17% ± 0.16% (-0.15%:0.36%)	0.00% ± 0.20% (-0.29%:0.31%)	-1.52% ± 0.74% (-3.02%:-0.37%)	0.26% ± 0.22% (-0.15%:0.55%)	-0.28% ± 0.22% (-0.74%:0.01%)	-0.34% ± 0.23% (-0.83%:-0.08%)
D50	0.11% ± 0.11% (-0.02%:0.33%)	0.21% ± 0.15% (-0.06%:0.45%)	0.09% ± 0.19% (-0.20%:0.43%)	-1.31% ± 0.63% (-2.47%:-0.25%)	0.33% ± 0.21% (-0.09%:0.65%)	-0.18% ± 0.20% (-0.64%:0.10%)	-0.26% ± 0.24% (-0.75%:0.08%)
D2	0.11% ± 0.12% (-0.02%:0.34%)	0.21% ± 0.15% (-0.02%:0.49%)	0.11% ± 0.19% (-0.14%:0.47%)	-1.25% ± 0.62% (-2.38%:-0.14%)	0.33% ± 0.18% (-0.02%:0.61%)	-0.17% ± 0.19% (-0.55%:0.17%)	-0.26% ± 0.22% (-0.63%:0.10%)
RECTUM							
V40	0.03% ± 0.32% (-0.48%:0.52%)	0.05% ± 0.32% (-0.33%:0.64%)	0.02% ± 0.43% (-0.52%:0.75%)	-3.38% ± 5.49% (-18.76%:-0.37%)	0.22% ± 0.39% (-0.22%:0.98%)	-0.53% ± 0.22% (-0.92%:-0.18%)	-0.51% ± 0.29% (-0.87%:-0.08%)
V65	-0.35% ± 0.58% (-1.74%:0.25%)	-0.22% ± 0.50% (-0.93%:0.70%)	-0.52% ± 0.44% (-1.26%:0.17%)	-4.87% ± 3.02% (-10.69%:-1.41%)	0.39% ± 0.84% (-0.94%:1.92%)	-1.55% ± 0.86% (-3.60%:-0.52%)	-1.48% ± 0.83% (-3.02%:-0.52%)
BLADDER							
V40	0.06% ± 0.24%	0.24% ± 0.26%	0.26% ± 0.19%	-1.18% ± 0.92%	0.38% ± 0.29%	-0.09% ± 0.25%	-0.16% ± 0.33%

	TR1200	TR800	TURBO160	TURBO300	5-8PF	p6_6-8FT_Turbo120_TR1200	p6_6-8FT_Turbo120_TR900
	(-0.38%:0.45%)	(-0.13%:0.66%)	(-0.04%:0.69%)	(-3.13%:0.17%)	(-0.30%:0.79%)	(-0.63%:0.34%)	(-0.80%:0.24%)
V65	0.34% ± 0.46% (-0.28%:1%)	0.60% ± 0.50% (-0.22%:1.33%)	0.47% ± 0.39% (-0.11%:0.97%)	-2.92% ± 1.82% (-5.98%:0.31%)	0.98% ± 0.49% (-0.14%:1.73%)	-0.13% ± 0.41% (-1.02%:0.46%)	-0.27% ± 0.50% (-1.02%:0.50%)

Discussion

This study investigated the potential of MR imaging time reduction and the effect on the sCT generated due to the change in image quality. Image quality reduction is acceptable as this sequence is used purely for dose calculation. *It may be noted that within an overall MRI-only simulation session* other more appropriate MRI sequences *are captured for* volume definition *and* patient setup *as* required. *This allows optimisation of MRI sequences to specific application requirements to best utilise the enhanced soft tissue contrast capabilities.*

For one volunteer, the TR800 and p6_6-8FT_Turbo120_TR900 sequences were not able to be completed due to SAR (Specific Absorption Rate related to radiofrequency absorption in tissue) warnings. For this volunteer, the TR had to be increased to TR935 and TR988 respectively for the scan sequences to fall within SAR levels. Additionally, these 2 sequences along with the TURBO300 sequence required slight adjustments to flip angle for each volunteer. As such these low TR levels would not be considered for clinical implementation as they may require adjustment on a per patient basis.

The BMI range for volunteers in this study was 22.3 to 30.1. This is on average lower than previously reported clinical trial patient cohorts, having a mean of 28.5 with a range of 19 – 39 [18]. As such some further adjustments may be required for patients with a greater BMI.

There may be considerable trade offs in reducing MRI imaging time, and the impact of the effect of parameter changes to the original sequence should be considered. Reducing TR, that is the repetition time, produces an image that is more T1 weighted, with greater contrast between fat and water/tissue [23]. Adjusting the partial Fourier factor changes the amount of k-space data required in the phase encoding direction, and has the practical effect of reducing the signal to noise ratio [28]. Increasing the turbo factor, that is increasing the echo train length, increases the number of echoes. Though this has the effect of reducing imaging time, it can create artefacts, reduce signal to noise, degrade image contrast and cause blurring [31]. These factors due to the change in sequence parameter may produce an MRI image which would not produce an accurate sCT.

It should be considered that the comparison for this study is between sCT and gold standard sCT, whereas the gold standard for other sCT studies is true CT. The latter was not possible in the current work, as it was a volunteer study in healthy volunteers. *However, the use of the gold standard sCT in this study provides a more appropriate comparison, as it removes the potential registration errors with a CT scan.*

For this atlas method Dowling et al [30] achieved a MAE of 40.5 ± 8.2 HU when comparing the generated sCT back to the matching patient CT within the patient's body contour. Additionally from this study, the automatic bone contours had a DSC of 0.91 ± 0.03 when compared to the original CT bone manual contours. Farjam et al achieved a MAE of 54.67 for the entire CT comparing the

commercially available Philips Ingenia generated MRCAT (MR for Calculating ATtenuation) synthetic CT scan back to the corresponding deformed planning CT [32]. In comparison, the current study achieved a MAE 40 HU for the majority of sequences, and a DSC 0.980 or better for suitable sequences for the body contour, and 0.9 or better for the bone contours when compared to the original sequence sCT.

Different methodologies have been used for sCT generation. Chen et al [8] use a bulk density assignment for prostate IMRT plans to achieve a dose difference of 2.5% between sCT and CT. Dowling et al [6, 30] used an automatic atlas method in the prostate achieving a point dose agreement of 0.3% ± 0.8% between sCT and CT, with gamma results meeting a mean pass rate of 95% for 1%/1mm gamma tolerance. There is commercial software available, with the FDA approved MRCAT package from Philips, which generates an sCT using the different phase images acquired using a T1 weighted mDixon scan sequence [32-34]. This T1 weighted mDixon scan sequence is reported to take approximately 3.20 minutes [33]. Tyagi, et al [34] evaluated the MRCAT for treatment localisation, distortion analysis and dosimetric accuracy. In regards to dosimetric accuracy compared to CT, all structures were reported to be on average within 0.5% utilising DVH comparison. Christiansen, et al [33] also conducted a dosimetric comparison between MRCAT CT and CT scans using gamma analysis, reporting median values of 100% for all evaluated structures using a 1%/1mm gamma criteria*, and a mean body gamma pass rate of 98.7% using a 1%/1mm gamma criteria*. The study does state that some individual structures yielded pass rates below 95% due to rectal air present on CT but not on the sCT. Farjam et al [32] achieved a 1%/1mm gamma pass rate of 90.6% when comparing MRCAT CT and deformed planning CT. The isocentre point dose results for the current study were largely within 1% for most sequences, and gamma results for a 1%/1mm tolerance were better than 99% for suitable sequences when compared to the original sequence sCT. Persson, et al [35] presented a clinical workflow incorporating the commercial synthetic CT generation software MriPlanner (Spectronic Medical, Helsingborg, Sweden). This software requires only a single LFOV T2 fast spin echo sequence which is reported to take 7 minutes scan time, with this scan uploaded into a cloud based conversion service and converted to sCT based off an automated atlas based conversion method [36, 37]. A dose difference between sCT and CT was found to be within 2% for most DVH parameters for patients within the study, with some outliers for some DVH parameters for 3 patients due to rectal gas present in the CT images but not the MRI/sCT images. Additionally, global gamma pass rates were above 98% for all patients down to a 2%/1mm global gamma criteria.

Each volunteer completed a single imaging session of approximately 25 minutes to obtain the eight MRI sequences. As such there would be varying effects of potential volunteer motion and internal organ motion over the course of the session. Although motion effects on the results weren't investigated separately, the small differences in point doses and the high gamma pass rate indicate that such effects would at most be small in this healthy volunteer cohort and would not impact on the conclusions.

However as all images were completed during the same session with the same scan centre, no registration was required between sequences/sCT for comparison as would be required if CT was the gold standard. Additionally there were no distortion assessments for the new sequences which would be available with CT comparison, though vendor distortion corrections were enabled for all scans. The gold standard original sCT sequence has been benchmarked against CT, achieving a DSC of 1.00±0.00 for the body contour comparing the automatic organ contouring with gold standard expert manual contours [30]. This was used for body contour volume and Hausdorff and DICE comparisons, which demonstrated comparable results to previous studies.

The MRI sequence imaging time was able to be reduced from over 5 minutes for the original MRI SPACE sequence to just over 1 minute. Considering the benchmarking of the original sequence against CT in Dowling et al [30], for anatomical factors, a benchmark MAE of 40.5 could be considered when comparing the generated sCT back to the original sequence generated sCT in addition to a DICE score of 0.91 for the bones. For dosimetric factors an isocentre point dose agreement benchmark of 0.3% ± 0.8% could be considered in addition to a 1%/1mm gamma pass rate of 95%. All sequences except for the TURBO300 sequence met these anatomical and dosimetric criteria in comparison to the generated sCT with the sCT generated with the original MRI sequence. Although the sCT from the original MRI sequence were already benchmarked back to CT, giving an indirect comparison of these sCT to CT, further work would be required to determine clinical acceptability directly against CT scans, using patient studies and including consideration of the appropriateness of the generated sCT to be used for DRR generation in addition to reference imaging for patient setup and verification.

From this study, considering the results and likelihood of on-the-fly sequence adjustments required, the use of the TURBO160 sequence or p6_6-8FT_Turbo120_TR1200 sequence for sCT generation using this hybrid atlas-voxel method would result in a 50-74% time reduction with similar dosimetric results. In regards to the p6_6-8FT_Turbo120_TR1200 sequence rectum V65 DVH comparison results, two volunteers had rectum V65 differences greater than 2%. This was due to the small volume of the rectum and the low absolute doses, with absolute differences of less than 0.3Gy compared to the original sequence. It should be noted that these results are only applicable for this sCT conversion methodology, and changes in MR image quality may influence other sCT conversion methodologies differently. Additionally, this study provides a framework for potential timing studies for MRI-only planning, or for assessment of sequences used for daily positioning on MR-linacs in terms of dose calculation accuracy. Further assessment of the selected sequence would be required prior to clinical use, with a comparison for a number of patients with gold standard clinical CT comparison being ideal.

Conclusion

The MR imaging sequence time was able to be reduced by approximately 80% with similar dosimetric results. For suitable MRI sequences, the generated sCT agreed with the gold standard sCT within an isocentre dose of 1% and a gamma pass rate of 99% for a 1%/1mm gamma tolerance.

Ethics Declarations

None

Conflict of Interest

Authors declare no conflicts of interest

Research involving humans and animal rights

Volunteer data obtained for this study was acquired with local ethics committee approval (HREC/15/LPOOL/506).

Reference

[1] Nyholm T, Jonsson J. Counterpoint: Opportunities and Challenges of a Magnetic Resonance Imaging–Only Radiotherapy Work Flow. Seminars in Radiation Oncology. 2014;24:175-80.

[2] Owrangi AM, Greer PB, Glide-Hurst CK. MRI-only treatment planning: benefits and challenges. Physics in Medicine & Biology. 2018;63:05TR1.

[3] Stanescu T, Kirkby C, Wachowicz K, Fallone BG. Developments in MRI-based radiation treatment planning. In: Dössel O, Schlegel W, editors. World Congress on Medical Physics and Biomedical Engineering, September 7 - 12, 2009, Munich, Germany: Springer Berlin Heidelberg; 2009. p. 821-4.

[4] Johansson A, Karlsson M Fau - Nyholm T, Nyholm T. CT substitute derived from MRI sequences with ultrashort echo time. Medical Physics. 2011.

[5] Karotki A, Mah K, Meijer G, Meltsner M. Comparison of bulk electron density and voxel-based electron density treatment planning. Journal of Applied Clinical Medical Physics. 2011;12.

[6] Dowling JA, Lambert J, Parker J, Salvado O, Fripp J, Capp A, et al. An Atlas-Based Electron Density Mapping Method for Magnetic Resonance Imaging (MRI)-Alone Treatment Planning and Adaptive MRI-Based Prostate Radiation Therapy. International Journal of Radiation Oncology*Biology*Physics. 2012;83:e5-e11.

[7] Greer PB, Martin J, Sidhom M, Hunter P, Pichler P, Choi JH, et al. A multi-center prospective study for implementation of an MRI-only prostate treatment planning workflow. Frontiers in Oncology. 2019;9:826.

[8] Chen L, Price Jr R, Nguyen T, Wang L, Li J, Qin L, et al. Dosimetric evaluation of MRI-based treatment planning for prostate cancer. Physics in Medicine and Biology. 2004;49:5157.

[9] Korhonen J, Kapanen M, Keyriläinen J, Seppälä T, Tuomikoski L, Tenhunen M. Absorbed doses behind bones with MR image-based dose calculations for radiotherapy treatment planning. Medical Physics. 2013;40:011701.

[10] Kapanen M, Collan J, Beule A, Seppälä T, Saarilahti K, Tenhunen M. Commissioning of MRI-only based treatment planning procedure for external beam radiotherapy of prostate. Magnetic Resonance in Medicine. 2013;70:127-35.

[11] Jonsson JH, Karlsson MG, Karlsson M, Nyholm T. Treatment planning using MRI data: an analysis of the dose calculation accuracy for different treatment regions. Radiation Oncology. 2010;5:62-.

[12] Karlsson M, Karlsson MG, Nyholm T, Amies C, Zackrisson B. Dedicated Magnetic Resonance Imaging in the Radiotherapy Clinic. International Journal of Radiation Oncology*Biology*Physics. 2009;74:644-51.

[13] Roberson PL, McLaughlin PW, Narayana V, Troyer S, Hixson GV, Kessler ML. Use and uncertainties of mutual information for computed tomography/magnetic resonance (CT/MR) registration post permanent implant of the prostate. Medical Physics. 2005;32:473-82.

[14] Jonsson J, Nyholm T, Söderkvist K. The rationale for MR-only treatment planning for external radiotherapy. Clinical and Translational Radiation Oncology. 2019;18:60-5.

[15] Edmund JM, Nyholm T. A review of substitute CT generation for MRI-only radiation therapy. Radiation Oncology. 2017;12:28.

[16] Johnstone E, Wyatt JJ, Henry AM, Short SC, Sebag-Montefiore D, Murray L, et al. Systematic review of synthetic computed tomography generation methodologies for use in magnetic resonance imaging–only radiation therapy. International Journal of Radiation Oncology* Biology* Physics. 2018;100:199-217.

[17] Han X. MR-based synthetic CT generation using a deep convolutional neural network method. Medical Physics. 2017;44:1408-19.

[18] Greer P, Martin J, Sidhom M, Hunter P, Pichler P, Choi JH, et al. A multi-center prospective study for implementation of an MRI-only prostate treatment planning workflow. Frontiers in Oncology. 2019;9:826.

[19] Liney GP, Moerland MA. Magnetic Resonance Imaging Acquisition Techniques for Radiotherapy Planning. Seminars in Radiation Oncology. 2014;24:160-8.

[20] Mekle R, Wu EX, Meckel S, Wetzel SG, Scheffler K. Combo acquisitions: balancing scan time reduction and image quality. Magnetic Resonance in Medicine: An Official Journal of the International Society for Magnetic Resonance in Medicine. 2006;55:1093-105.

[21] Prior P, Chen X, Botros M, Paulson ES, Lawton C, Erickson B, et al. MRI-based IMRT planning for MR-linac: comparison between CT-and MRI-based plans for pancreatic and prostate cancers. Physics in Medicine & Biology. 2016;61:3819.

[22] Feinberg DA, Hale JD, Watts JC, Kaufman L, Mark A. Halving MR imaging time by conjugation: demonstration at 3.5 kG. Radiology. 1986;161:527-31.

[23] McRobbie DW, Moore EA, Graves MJ, Prince MR. MRI from Picture to Proton: Cambridge University Press; 2017.

[24] Hennig J, Nauerth A, Friedburg H. RARE imaging: a fast imaging method for clinical MR. Magnetic Resonance in Medicine. 1986;3:823-33.

[25] Hennig J, Friedburg H. Clinical applications and methodological developments of the RARE technique. Magnetic Resonance Imaging. 1988;6:391-5.

[26] Constable RT, Anderson AW, Zhong J, Gore JC. Factors influencing contrast in fast spin-echo MR imaging. Magnetic Resonance Imaging. 1992;10:497-511.

[27] Jones KM, Mulkern R, Schwartz RB, Oshio K, Barnes PD, Jolesz F. Fast spin-echo MR imaging of the brain and spine: current concepts. AJR American Journal of Roentgenology. 1992;158:1313-20.

[28] Hollingsworth KG. Reducing acquisition time in clinical MRI by data undersampling and compressed sensing reconstruction. Physics in Medicine and Biology. 2015;60:R297-R322.

[29] Griswold MA, Jakob PM, Heidemann RM, Nittka M, Jellus V, Wang J, et al. Generalized autocalibrating partially parallel acquisitions (GRAPPA). Magnetic Resonance in Medicine. 2002;47:1202-10.

[30] Dowling JA, Sun J, Pichler P, Rivest-Hénault D, Ghose S, Richardson H, et al. Automatic substitute computed tomography generation and contouring for magnetic resonance imaging (MRI)-Alone external beam radiation therapy from standard MRI sequences. International Journal of Radiation Oncology* Biology* Physics. 2015;93:1144-53.

[31] Mugler III JP. Optimized three-dimensional fast-spin-echo MRI. Journal of Magnetic Resonance Imaging. 2014;39:745-67.

[32] Farjam R, Tyagi N, Deasy JO, Hunt MA. Dosimetric evaluation of an atlas-based synthetic CT generation approach for MR-only radiotherapy of pelvis anatomy. Journal of Applied Clinical Medical Physics. 2019;20:101-9.

[33] Christiansen RL, Jensen HR, Brink C. Magnetic resonance only workflow and validation of dose calculations for radiotherapy of prostate cancer. Acta Oncologica. 2017;56:787-91.

[34] Tyagi N, Fontenla S, Zhang J, Cloutier M, Kadbi M, Mechalakos J, et al. Dosimetric and workflow evaluation of first commercial synthetic CT software for clinical use in pelvis. Physics in Medicine & Biology. 2017;62:2961.

[35] Persson E, Jamtheim Gustafsson C, Ambolt P, Engelholm S, Ceberg S, Bäck S, et al. MR-PROTECT: clinical feasibility of a prostate MRI-only radiotherapy treatment workflow and investigation of acceptance criteria. Radiation Oncology. 2020;15:1-13.

[36] Persson E, Gustafsson C, Nordström F, Sohlin M, Gunnlaugsson A, Petruson K, et al. MR-OPERA: a Multicenter/Multivendor validation of magnetic resonance Imaging–Only prostate treatment planning using synthetic computed tomography images. International Journal of Radiation Oncology* Biology* Physics. 2017;99:692-700.

[37] Siversson C, Nordström F, Nilsson T, Nyholm T, Jonsson J, Gunnlaugsson A, et al. Technical Note: MRI only prostate radiotherapy planning using the statistical decomposition algorithm. Medical Physics. 2015;42:6090-7.

7 Clinical validation of MR imaging time reduction for Substitute/Synthetic CT Generation for Prostate MRI-only Treatment Planning

7.1 Presentations and Publications

This work was accepted as a scientific paper in Physical and Engineering Sciences in Medicine journal in 2023. The article is currently in press. The current reference for this article is as follows: Young, T., Dowling, J., Rai, R. et al. Clinical validation of MR imaging time reduction for substitute/synthetic CT generation for prostate MRI-only treatment planning. Physical and Engineering Sciences in Medicine (2023). https://doi.org/10.1007/s13246-023-01268-x

This publication is presented as the chapter. Any additions to the original publication are presented in *italics.*

7.2 Preamble

Synthetic CT (sCT) generation from magnetic resonance imaging (MRI) can vary between volunteer and patient cohorts due to the differences in patient anatomy, including age, height and weight ranges. As such, studies involving volunteer data may not necessarily have results which exactly mirror those expected when clinical patients are considered due to these cohort differences.

This study was a follow up study to the publication in the previous chapter considering volunteers, with the aim of this study being the clinical validation of the selected time-reduced MRI sequence for sCT generation for clinical translation. This study investigated the effects of MR imaging time reduction on sCT generation for prostate MRI-only treatment planning for a clinical cohort of patients enrolled in an MRI-only study. As the patients were on an MRI-only study, the generated sCT for the time-reduced MRI sequence was compared back to the sCT generated with the standard MRI sequence utilized within the clinical MRI-only study. This study provides a potential framework for future studies which investigate incremental improvements in either sCT generation or MRI sequence time for MRI-only treatment planning studies as these studies may not necessarily include a gold standard CT image, but rather a baseline or standard MRI/sCT image.

7.3 Publication - Clinical validation of MR imaging time reduction for Substitute/Synthetic CT Generation for Prostate MRI-only Treatment Planning

Tony Young

Liverpool and Macarthur Cancer Therapy Centres and Ingham Institute, Sydney, Australia.

Institute of Medical Physics, School of Physics, University of Sydney, Sydney, Australia

Tony.Young@health.nsw.gov.au

Jason Dowling

CSIRO Health and Biosecurity, The Australian e-Health & Research Centre, Australia

South Western Sydney Clinical School, University of New South Wales, Australia

Institute of Medical Physics, University of Sydney, Australia

School of Mathematical and Physical Sciences, University of Newcastle, Australia

Centre for Medical Radiation Physics, University of Wollongong, Wollongong,

New South Wales, Australia

Jason.Dowling@csiro.au

Robba Rai

Liverpool and Macarthur Cancer Therapy Centres and Ingham Institute, Sydney, Australia.

University of New South Wales, Sydney, New South Wales, Australia

Robba.Rai@health.nsw.gov.au

Gary Liney

Liverpool and Macarthur Cancer Therapy Centres and Ingham Institute, Sydney, Australia

University of New South Wales, Sydney, New South Wales, Australia

Centre for Medical Radiation Physics, University of Wollongong, Wollongong,

New South Wales, Australia

Gary.Liney@health.nsw.gov.au

Peter Greer

Calvary Mater Newcastle Hospital, Newcastle, New South Wales, Australia

School of Mathematical and Physical Sciences, University of Newcastle, Australia

peter.greer@newcastle.edu.au

David Thwaites

Institute of Medical Physics, School of Physics, University of Sydney, Sydney, Australia.

david.thwaites@sydney.edu.au

Lois Holloway

Liverpool and Macarthur Cancer Therapy Centres and Ingham Institute, Sydney, Australia.

University of New South Wales, Sydney, New South Wales, Australia

Institute of Medical Physics, School of Physics, University of Sydney, Australia.

Centre for Medical Radiation Physics, University of Wollongong, Wollongong,

New South Wales, Australia

lois.holloway@health.nsw.gov.au

Abstract

Introduction

Radiotherapy treatment planning based only on magnetic resonance imaging (MRI) has become clinically achievable. Though computed tomography (CT) is the gold standard for radiotherapy imaging, directly providing the electron density values needed for planning calculations, MRI has superior soft tissue visualisation to guide treatment planning decisions and optimisation. MRI-only planning removes the need for the CT scan, but requires generation of a substitute/synthetic/pseudo CT (sCT) for electron density information. Shortening the MRI imaging time would improve patient comfort and reduce the likelihood of motion artefacts. A volunteer study was previously carried out to

investigate and optimise faster MRI sequences for a hybrid atlas-voxel conversion to sCT for prostate treatment planning. The aim of this follow-on study was to clinically validate the performance of the new optimised sequence for sCT generation in a treated MRI-only prostate patient cohort.

Method

10 patients undergoing MRI-only treatment were scanned on a Siemens Skyra 3T MRI as part of the MRI-only sub-study of the NINJA clinical trial (ACTRN12618001806257). Two sequences were used, the standard 3D T2-weighted SPACE sequence used for sCT conversion which has been previously validated against CT, and a modified fast SPACE sequence, selected based on the volunteer study. Both were used to generate sCT scans. These were then compared to evaluate the fast sequence conversion for anatomical and dosimetric accuracy against the clinically approved treatment plans.

Results

The average Mean Absolute Error (MAE) for the body was 14.98 ± 2.35 HU, and for bone was 40.77 ± 5.51 HU. The external volume contour comparison produced a Dice Similarity Coefficient (DSC) of at least 0.976, and an average of 0.985 ± 0.004, and the bony anatomy contour comparison a DSC of at least 0.907, and an average of 0.950 ± 0.018. The fast SPACE sCT agreed with the gold standard sCT within an isocentre dose of -0.28% ± 0.16% and an average gamma pass rate of 99.66% ± 0.41% for a 1%/1 mm gamma tolerance.

Conclusion

In this clinical validation study, the fast sequence, which reduced the required imaging time by approximately a factor of 4, produced an sCT with similar clinical dosimetric results compared to the standard sCT, demonstrating its potential for clinical use for treatment planning.

Keywords – MRI-Only, sCT, Prostate

Introduction

Radiotherapy treatment planning based only on magnetic resonance imaging (MRI), or MRI-only radiotherapy, has recently become clinically achievable [1-4]. Treatment planning requires electron density information for dose calculation, which is conventionally acquired from computed tomography (CT), but which MRI scans do not provide directly. However, substitute, synthetic, or pseudo CT (sCT) scans generated from specific MRI sequences are able to provide electron density information [5-7]. These sCT scans are validated against CT scans and their use removes the need to acquire a pre-treatment CT scan.

There are various approaches which have been utilised for sCT generation, such as bulk density correction methods, atlas methods, deep learning algorithms or a combination of these approaches. Bulk density correction requires only segmentation of the MRI, with appropriate density values applied to these segmentations for dose calculation [8]. Atlas or multi atlas methodologies have been successfully utilised in the male pelvis [9, 10], where training sets of registered CT-MRI image pairs are used to produce an average CT-MRI atlas. The advantages of this method include a robustness to artefacts and intensity differences between images, and realistic anatomical deformation due to the use of prior training information, with the main disadvantage of the method being that images that fall outside the bounds of the atlas training data may be unable to be matched appropriately [11]. Commercially available sCT generation software has used a combination of atlas and bulk density assignment methods for prostate sCT generation [12-14]. Deep learning and artificial intelligence (AI) methods have also been utilised for prostate sCT generation, with these techniques able to be used in combination with others for image segmentation and tissue classification [15-19]; however they require a large amount of data and resources for training, but are much faster than the atlas method for sCT generation, taking typically in the order of seconds compared to minutes.

Within an MRI simulation session for MRI-only radiotherapy treatment planning, various MRI sequences may be captured for specific visualisation, such as fiducial marker identification, or target and organ at risk delineation purposes in addition to any particular sequence or sequences required for specific sCT generation methods. The MR imaging portion of the simulation session can take a significant amount of time [1, 14], especially when compared to a CT simulation session in which only a single CT scan may be required for both anatomical information and treatment planning. Any reduction in MR imaging time for a sequence would reduce the overall simulation time, and reduce the potential for patient motion or organ variation, in particular prostate motion, bladder filling and rectal and bowel gas changes over the simulation session [20-22], as well as reduce patient discomfort and increase MRI scanner utilisation [23]. Time reduction in MRI sequences however could impact image quality, reducing signal to noise ratio, image contrast and resolution [24-28], the effect of which should be considered in the application of each particular sequence. Additionally, to improve online adaptation of treatment plans for patient treatment on MRI linear accelerators, any time reduction which causes no

change in treatment plan dosimetric quality would benefit the patient, reducing their treatment time and increasing patient comfort and tolerance for treatment [29-31]

Previously, a volunteer study was conducted investigating the effects of MRI sequence time reduction on sCT generation for prostate MRI-only treatment planning and to determine a suitable sequence [32]. This follow-up study aims to clinically apply and validate the previously determined optimal fast MRI sequence with a prospective patient cohort undergoing MRI-only radiotherapy treatment planning. The sCT generated from the new fast MRI sequence with clinical patient data is evaluated by comparison both anatomically and dosimetrically to the current established and validated sCT generation method utilising the standard MRI sequence. This study will determine whether the new fast sequence can be utilised clinically in sCT generation for future MRI-only radiotherapy.

Method

Ten prostate radiotherapy patients were included in the study. These patients were recruited to the NINJA (Novel Integration of New prostate radiation therapy schedules with adjuvant Androgen deprivation) clinical trial (ACTRN12618001806257) which had local ethics approval (HREC/18/LPOOL/420), investigating stereotactic radiotherapy to the prostate comparing monotherapy against a virtual high dose rate brachytherapy boost regimen. This clinical trial also contains an MRI-only planning sub-study, demonstrating the ability to fully transition centres from CT- to MRI-based prostate radiotherapy planning, which these patients were enrolled into. Patients in this trial were prescribed either 40 Gy in 5 fractions or a stereotactic boost of 20 Gy in 2 fractions followed by a standard 36 Gy in 12 fractions, with treatment plans consisting of two VMAT arcs. The patients involved in the current study were part of the MRI-only planning sub-study, and scanned on a Siemens (Erlangen, Germany) Skyra 3T MRI with a flat radiotherapy couch and body coil mounted on coil mounts as per trial protocol. Patient age ranged from 60 – 72, and Body Mass Index (BMI) ranged from 23.1 to 32, with a mean of 27.1.

The standard planning MRI sequence as used for the clinical trial was a 3D T2-weighted isotropic SPACE (Sampling Perfection with Application optimised Contrasts using different flip angle Evolution) sequence which covered the entire pelvis, with scan limits from L5/S1 to the pubic symphysis. This sequence was previously validated against CT by Dowling et al [11], and has an average scan time of 5 minutes and 4 seconds. A time-reduced MRI sequence was achieved by varying a combination of repetition time (TR), turbo factor, partial Fourier acceleration and parallel imaging acceleration, following the findings from the volunteer study [21], reducing the average scan time to 1 minute and 19 seconds. The sequence parameters are displayed in table 7.1, with further detail available in Young et al [32].

Table 7.1 - MRI sequence parameters which differed between the standard and fast T2 SPACE and the average scan time for each sequence.

MRI Sequence	Average TR (ms)	Turbo factor	Partial Fourier	iPAT Acceleration Factor	Average Scan Time (min:sec)
Standard T2 SPACE	1700	80	7/8	4	5:04
Fast T2 SPACE	1200	120	6/8	6	1:19

MRI sequences were converted to sCT using a hybrid atlas-voxel method as described in Dowling et al [11], with the converted Fast SPACE (F-sCT) compared to the Standard SPACE (S-sCT) conversion. Mean Absolute Error (MAE) for HU for the entire body, along with tissue and bones only was calculated by comparing the F-sCT to the S-sCT with the auto-segmented body and bone masks from the S-sCT. An anatomical comparison of the body and bone volumes between the generated sCT was completed considering volume differences, mean Hausdorff distance and Dice Similarity Coefficient (DSC) comparison.

Treatment planning for these patients was completed on the S-sCT using the Pinnacle Treatment Planning System (v16.21; Philips Healthcare, Andover, MA) utilising the auto-planning module for beam optimisation. Patient treatment plans met all trial guidelines, with each treatment plan consisting of two full Volumetric Arc Therapy (VMAT) treatment beams. Each patient's corresponding clinically approved treatment plan was copied to the F-sCT and recalculated for comparison of isocentre point dose, a 1%/1mm global gamma comparison and DVH analysis of the PTV, bladder and rectum.

Results

The Fast sequence scan was able to be completed on all patients with no modifications required by the system. This sequence was able to be converted to sCT as per Dowling et al [11], with no additional artefacts seen in qualitative review of the fast MRI sequence scan or converted F-sCT. An example of the standard MRI and fast MRI, as well as the corresponding S-sCT and F-sCT can be seen in figure 7.1.

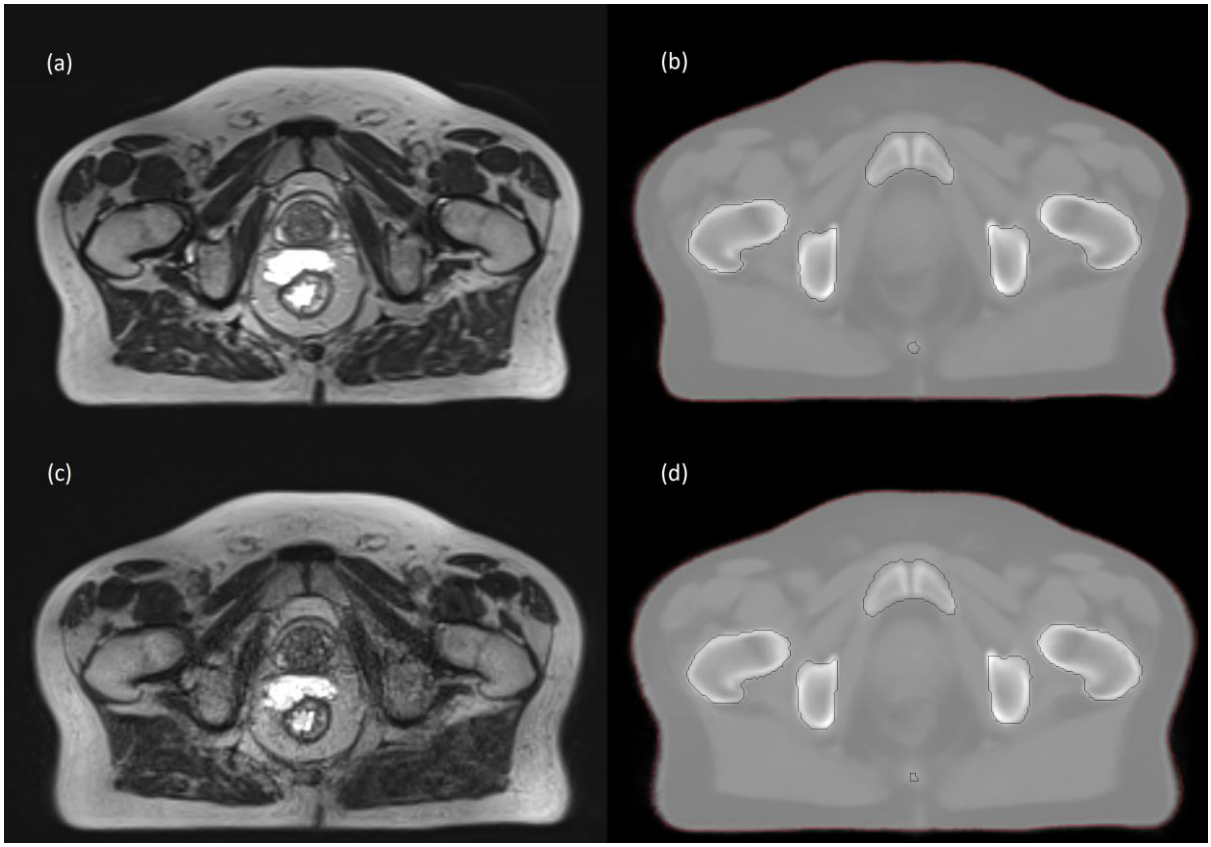

Figure 7.1 - An example of the (a) standard MRI and (b) S-sCT and the (c) fast MRI and (d) F-sCT for the same corresponding slice for one patient. The body and bone masks are also displayed on the sCT slices in (b) and (d).

The mean absolute error (MAE) in HU over the ten patients for the F-sCT compared to the S-sCT with the body and bone masks from the S-sCT, in addition to tissue only, is shown in figure 7.2. The average MAE for the body was 14.98 ± 2.35 HU, for tissue only was 12.68 ± 2.75 HU, and for the bone was 40.77 ± 5.51 HU.

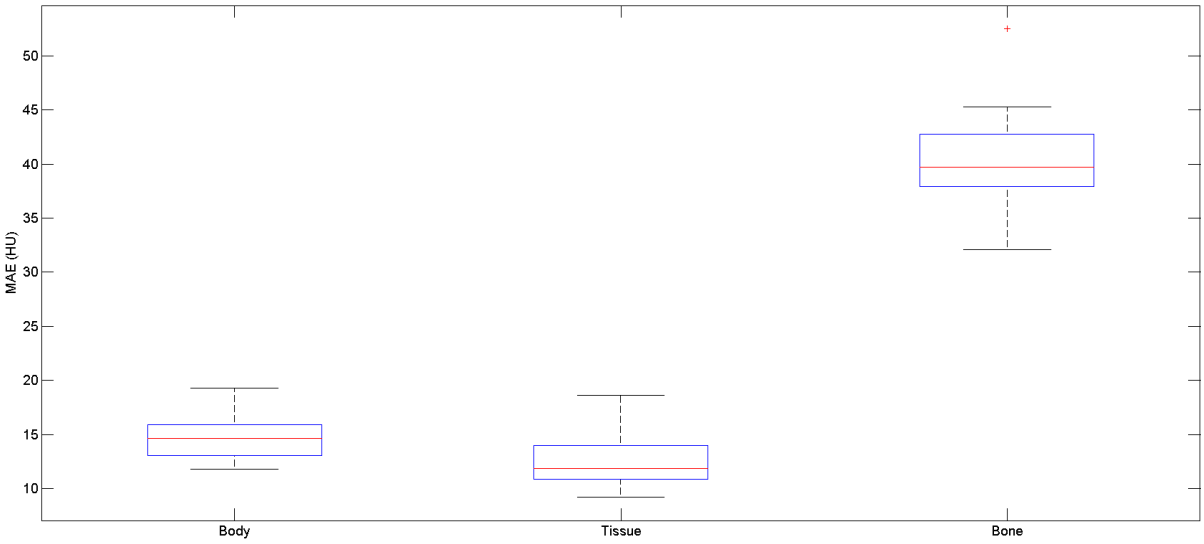

Figure 7.2 - Mean Absolute Error (MAE) of HU for the generated sCT from the fast MRI sequence compared to the sCT generated from the standard MRI sequence for all patients for the within-the-body contour, the automatic bone contour, and for tissue only.

Table 7.2 - Volume percentage difference, mean Hausdorff distance and DSC results for automatic body and bone contours for the generated sCT for the fast MRI sequence compared to the standard sequence generated sCT for all patients.

Patient	Body Volume % Difference	Body Mean Hausdorff (mm)	Body DSC	Bone Volume % Difference	Bone Mean Hausdorff (mm)	Bone DSC
1	-0.03%	0.76	0.990	-3.82%	0.71	0.948
2	3.99%	1.48	0.976	0.70%	1.29	0.907
3	2.26%	0.97	0.988	1.61%	0.43	0.967
4	1.13%	0.98	0.988	-0.25%	0.42	0.964
5	2.43%	1.24	0.986	-0.82%	0.71	0.937
6	0.22%	0.90	0.988	-5.23%	0.69	0.942
7	2.89%	1.24	0.984	0.98%	0.43	0.963
8	-1.17%	1.21	0.987	-2.65%	0.54	0.960
9	3.28%	1.47	0.982	1.79%	0.49	0.960
10	0.70%	1.65	0.981	0.74%	0.61	0.949

The volume percentage difference, mean Hausdorff distance and DSC results for both the body and bone contour comparison can be seen in table 7.2. The average body volume difference was 1.57% ± 1.65%, whilst the average bone volume difference was -0.69% ± 2.42%. The mean Hausdorff value was less than 2 mm for both the body and bone volumes, with the body contour comparison producing

a DSC of at least 0.976, and an average of 0.985 ± 0.004, and the bone contour producing a DSC of at least 0.907, and an average of 0.950 ± 0.018.

Table 7.3 - Dosimetric Results for all patient plan comparisons. The isocentre point dose was compared, as well as 1%/1 mm Global Gamma analysis for the clinical plan from the S-sCT recalculated on the F-sCT.

Patient	Isocentre Point Dose	1%1mm Gamma (%)
1	-0.20%	99.10
2	-0.23%	98.87
3	-0.35%	99.56
4	-0.17%	99.89
5	-0.43%	100.00
6	-0.45%	99.39
7	-0.27%	99.93
8	0.07%	100.00
9	-0.42%	100.00
10	-0.31%	99.89

Table 7.3 shows dosimetric results. The isocentre point dose agreement for the clinical plan recalculated on the F-sCT was on average -0.28% ± 0.16%, and within ±0.5% of the S-sCT. The 1%/1 mm global Gamma pass rate was on average 99.66% ± 0.41%, with only one patient achieving below a 99% pass rate. The DVH dose differences are shown in figure 7.3. The PTV DVH statistics reported, on average, were within 0.5%, with an average difference of -0.27% ± 0.18%. The bladder and rectum D50 were within ±2% on average, with the rectum D50 average difference being -0.08 ± 0.40%, and the bladder D50 average difference being 0.08% ± 1.10%.

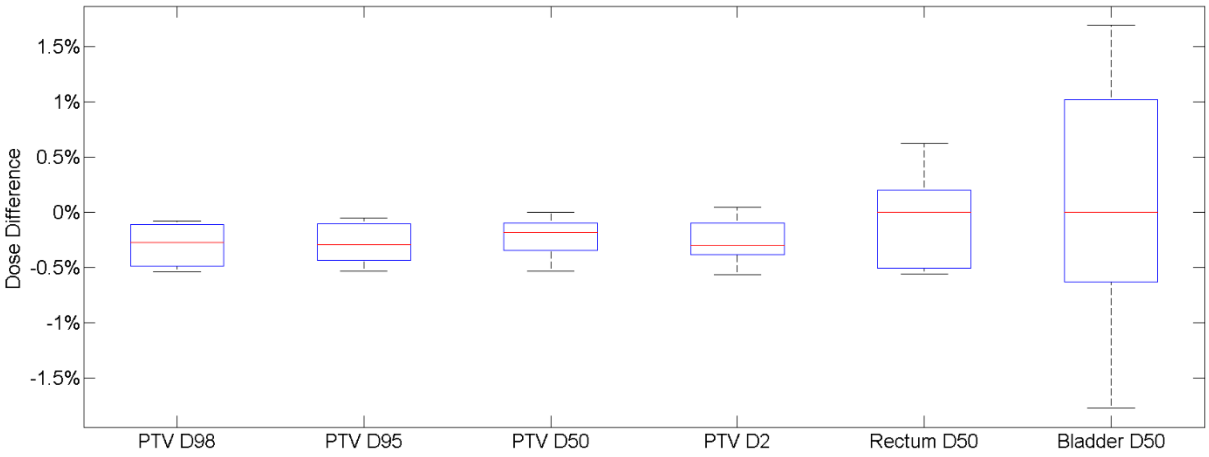

Figure 7.3 - DVH comparison of PTV parameters and the rectum and bladder D50 for the recalculated treatment plans on the F-sCT compared to calculated on the S-sCT. This figure shows the percentage difference for each parameter for all patients.

Discussion

This study demonstrates clinical application and validation of the results from the previous volunteer study. It provides clinical data, using a patient cohort, regarding a time-reduced MRI sequence for sCT generation for prostate MR-only treatment planning. In an MRI-only workflow, additional sequences *are* required for volume definition as image contrast and resolution may be enhanced or targeted to the anatomy, or functional sequences may provide additional guidance. The time reduction and associated reduction in image quality for the sCT sequence may be appropriate if anatomical and dose differences in the generated sCT for treatment planning are considered acceptable.

The potential trade-offs between reducing MR imaging time and the effects on the MR image quality and subsequent sCT generation accuracy should be considered [32]. A reduction in TR will produce an image with increased contrast between water and fat, being more T1-weighted [25]. An increase in the echo train length, the turbo factor, may increase the potential for artefacts, reducing signal-to-noise and image contrast and causing blurring in the image [33]. Changes in the partial Fourier factor may produce a time reduction in the scan by reducing the amount of k-space data acquired in the phase encoding direction, producing an image with a reduced signal-to-noise ratio [28]. Increasing the imaging acceleration factor will also alter the k-space data acquired, which may produce aliasing artefacts and reduce signal-to-noise [26, 34, 35]. Qualitative comparison of the fast MRI and standard MRI patient images did show a decreased signal-to-noise and some blurring in the fast MRI images, as can be seen in the MRI images in figure 1. However, these issues did not significantly affect the generated sCT for this cohort of patients.

The clinical study results compare favourably with our previously reported volunteer study [32]. In that, the fast sequence achieved an average body MAE of 33.66 ± 22.04 HU and an average bone MAE of

67.34 ± 34.84 HU. The body DSC was 0.980 ± 0.011 and the bone DSC was 0.916 ± 0.065. In terms of the results for these same anatomical regions, the current patient study resulted in an average MAE for the body of 14.98 ± 2.35 HU, and for the bone of 40.77 ± 5.51 HU, in addition to a body DSC result of 0.985 ± 0.004, and the bone contour producing a DSC result of 0.950 ± 0.018. These HU and anatomical results showed better agreement in the clinical patient study than those achieved in the volunteer study. This may be due to the fast sequence being captured immediately after the standard sequence, as opposed to larger time differences within the volunteer study. From the volunteer study, the isocentre average point dose difference was -0.14% ± 0.29%, with an average 1%/1mm Gamma pass rate of 99.97 ± 0.03, and an average PTV DVH difference of -0.22% ± 0.21%. From the current patient study, the isocentre average point dose difference was -0.28% ± 0.16%, with an average 1%/1mm Gamma pass rate of 99.66% ± 0.41%, and an average PTV DVH difference of -0.27% ± 0.18%. The current patient study has comparable dosimetric results, with the slight reduction in gamma pass rate potentially due to the increased treatment plan complexity. The volunteer study treatment plans consisted of a single VMAT arc designed to deliver 78 Gy in 39 fractions, i.e., a conventional 2 Gy per fraction plan. The clinical study treatment plans are for hypofractionated treatment regimes, delivering a much higher dose per fraction compared to the plans in the volunteer study.

As discussed previously in Young et al [32], from the benchmarking of the standard sequence against CT in Dowling et al [11], for anatomical factors, a MAE of 40.5, along with a DSC score of 0.91 for bones could be considered for comparing generated sCT back to the standard sequence sCT. An isocentre point dose agreement benchmark of 0.3% ± 0.8% along with a 1%/1mm global gamma pass rate of 95% could also be considered for dosimetric factors. In the current patient study, the fast sequence generated sCT met both these criteria for anatomical and dosimetric agreement.

The current study considers a comparison of sCT with a gold standard sCT. A more appropriate comparison would be true CT, but the study utilised patient data from an MRI-only sub-study within a clinical trial, so capturing an additional CT was not possible or within the study guidelines. *However, the use of the gold standard sCT in this study provides a more appropriate comparison, as it removes the potential registration errors with a CT scan.* However, as the S-sCT approach was previously benchmarked against CT, it could be considered that this was an indirect comparison of sCT to CT. As sCT use for treatment planning and MRI-only radiotherapy becomes more common, further adjustments or improvements in sCT may need to be considered without the availability of a corresponding CT scan. In these cases similar comparisons may be appropriate in assessing suitability of a new sCT.

Conclusion

In this clinical validation study, the fast sequence, which reduced the required imaging time by approximately a factor of 4, produced an sCT with similar clinical dosimetric results compared to the standard sCT, demonstrating its potential for clinical use for treatment planning.

Declarations

Funding

The authors received no funding for this study.

The NINJA Trial receives some grant funding from Cancer Australia (GA52651)

Conflicts of Interest

Authors declare no conflicts of interest. Liverpool Cancer Therapy Centre has a master research agreement with Siemens, unrelated to this study.

Research Involving Humans and Animal Rights

Patient data was acquired with local ethics committee approval, HREC/18/LPOOL/420

This clinical trial is registered with ANZCTR (ACTRN12618001806257)

Consent to Participate

Informed consent was obtained from all individual participants included in the study.

Consent to Publish

The authors affirm that human research participants provided informed consent for publication of data.

Data Availability

Due to the nature of this research, participants of this study did not agree for their data to be shared publicly, so supporting data is not available.

Reference

[1] Greer P, Martin J, Sidhom M, Hunter P, Pichler P, Choi JH, et al. A multi-center prospective study for implementation of an MRI-only prostate treatment planning workflow. Frontiers in Oncology. 2019;9:826.

[2] Persson E, Gustafsson C, Nordström F, Sohlin M, Gunnlaugsson A, Petruson K, et al. MR-OPERA: a Multicenter/Multivendor validation of magnetic resonance Imaging–Only prostate treatment planning using synthetic computed tomography images. International Journal of Radiation Oncology* Biology* Physics. 2017;99:692-700.

[3] Stanescu T, Kirkby C, Wachowicz K, Fallone BG. Developments in MRI-based radiation treatment planning. In: Dössel O, Schlegel W, editors. World Congress on Medical Physics and Biomedical Engineering, September 7 - 12, 2009, Munich, Germany: Springer Berlin Heidelberg; 2009. p. 821-4.

[4] Tenhunen M, Korhonen J, Kapanen M, Seppälä T, Koivula L, Collan J, et al. MRI-only based radiation therapy of prostate cancer: workflow and early clinical experience. Acta Oncologica. 2018;57:902-7.

[5] Johnstone E, Wyatt JJ, Henry AM, Short SC, Sebag-Montefiore D, Murray L, et al. Systematic review of synthetic computed tomography generation methodologies for use in magnetic resonance imaging–only radiation therapy. International Journal of Radiation Oncology* Biology* Physics. 2018;100:199-217.

[6] Edmund JM, Nyholm T. A review of substitute CT generation for MRI-only radiation therapy. Radiation Oncology. 2017;12:28.

[7] Spadea MF, Maspero M, Zaffino P, Seco J. Deep learning based synthetic-CT generation in radiotherapy and PET: A review. Medical Physics. 2021;48:6537-66.

[8] Chen L, Price Jr R, Nguyen T, Wang L, Li J, Qin L, et al. Dosimetric evaluation of MRI-based treatment planning for prostate cancer. Physics in Medicine and Biology. 2004;49:5157.

[9] Dowling JA, Lambert J, Parker J, Salvado O, Fripp J, Capp A, et al. An Atlas-Based Electron Density Mapping Method for Magnetic Resonance Imaging (MRI)-Alone Treatment Planning and Adaptive MRI-Based Prostate Radiation Therapy. International Journal of Radiation Oncology*Biology*Physics. 2012;83:e5-e11.

[10] Siversson C, Nordström F, Nilsson T, Nyholm T, Jonsson J, Gunnlaugsson A, et al. Technical Note: MRI only prostate radiotherapy planning using the statistical decomposition algorithm. Medical Physics. 2015;42:6090-7.

[11] Dowling JA, Sun J, Pichler P, Rivest-Hénault D, Ghose S, Richardson H, et al. Automatic substitute computed tomography generation and contouring for magnetic resonance imaging (MRI)-Alone external beam radiation therapy from standard MRI sequences. International Journal of Radiation Oncology* Biology* Physics. 2015;93:1144-53.

[12] Farjam R, Tyagi N, Deasy JO, Hunt MA. Dosimetric evaluation of an atlas-based synthetic CT generation approach for MR-only radiotherapy of pelvis anatomy. Journal of Applied Clinical Medical Physics. 2019;20:101-9.

[13] Tyagi N, Fontenla S, Zhang J, Cloutier M, Kadbi M, Mechalakos J, et al. Dosimetric and workflow evaluation of first commercial synthetic CT software for clinical use in pelvis. Physics in Medicine & Biology. 2017;62:2961.

[14] Persson E, Jamtheim Gustafsson C, Ambolt P, Engelholm S, Ceberg S, Bäck S, et al. MR-PROTECT: clinical feasibility of a prostate MRI-only radiotherapy treatment workflow and investigation of acceptance criteria. Radiation Oncology. 2020;15:1-13.

[15] Tahri S, Barateau A, Cadin C, Chourak H, Ribault S, Nozahic F, et al. A high-performance method of deep learning for prostate MR-only radiotherapy planning using an optimized Pix2Pix architecture. Physica Medica. 2022;103:108-18.

[16] Farjam R, Nagar H, Kathy Zhou X, Ouellette D, Chiara Formenti S, DeWyngaert JK. Deep learning-based synthetic CT generation for MR-only radiotherapy of prostate cancer patients with 0.35T MRI linear accelerator. Journal of Applied Clinical Medical Physics. 2021;22:93-104.

[17] Maspero M, Savenije MH, Dinkla AM, Seevinck PR, Intven MP, Jurgenliemk-Schulz IM, et al. Dose evaluation of fast synthetic-CT generation using a generative adversarial network for general pelvis MR-only radiotherapy. Physics in Medicine & Biology. 2018;63:185001.

[18] Boulanger M, Nunes J-C, Chourak H, Largent A, Tahri S, Acosta O, et al. Deep learning methods to generate synthetic CT from MRI in radiotherapy: A literature review. Physica Medica. 2021;89:265-81.

[19] Shafai-Erfani G, Wang T, Lei Y, Tian S, Patel P, Jani AB, et al. Dose evaluation of MRI-based synthetic CT generated using a machine learning method for prostate cancer radiotherapy. Medical Dosimetry. 2019;44:e64-e70.

[20] Liney GP, Moerland MA. Magnetic Resonance Imaging Acquisition Techniques for Radiotherapy Planning. Seminars in Radiation Oncology. 2014;24:160-8.

[21] Chen Z, Yang Z, Wang J, Hu W. Dosimetric impact of different bladder and rectum filling during prostate cancer radiotherapy. Radiation Oncology. 2016;11:1-8.

[22] Ten Haken R, Forman J, Heimburger D, Gerhardsson A, McShan D, Perez-Tamayo C, et al. Treatment planning issues related to prostate movement in response to differential filling of the rectum and bladder. International Journal of Radiation Oncology* Biology* Physics. 1991;20:1317-24.

[23] Owrangi AM, Greer PB, Glide-Hurst CK. MRI-only treatment planning: benefits and challenges. Physics in Medicine & Biology. 2018;63:05TR1.

[24] Mekle R, Wu EX, Meckel S, Wetzel SG, Scheffler K. Combo acquisitions: balancing scan time reduction and image quality. Magnetic Resonance in Medicine: An Official Journal of the International Society for Magnetic Resonance in Medicine. 2006;55:1093-105.

[25] McRobbie DW, Moore EA, Graves MJ, Prince MR. MRI from Picture to Proton: Cambridge University Press; 2017.

[26] Deshmane A, Gulani V, Griswold MA, Seiberlich N. Parallel MR imaging. Journal of Magnetic Resonance Imaging. 2012;36:55-72.

[27] Fellner C, Fellner F, Schmitt R, Helmberger T, Obletter N, Böhm-jurkovic H. Turbo spin-echo sequences in magnetic resonance imaging of the brain: Physics and applications. Magnetic Resonance Materials in Physics, Biology and Medicine. 1994;2:51-9.

[28] Hollingsworth KG. Reducing acquisition time in clinical MRI by data undersampling and compressed sensing reconstruction. Physics in Medicine and Biology. 2015;60:R297-R322.

[29] Boldrini L, Cusumano D, Cellini F, Azario L, Mattiucci GC, Valentini V. Online adaptive magnetic resonance guided radiotherapy for pancreatic cancer: state of the art, pearls and pitfalls. Radiation Oncology. 2019;14:1-6.

[30] Stan JH, Joanne MVdV, Jan JWL, Marco van V, Bas WR. The feasibility of utilizing pseudo CT-data for online MRI based treatment plan adaptation for a stereotactic radiotherapy treatment of spinal bone metastases. Physics in Medicine and Biology. 2014;59:7383.

[31] Magallon-Baro A, Milder MT, Granton PV, Nuyttens JJ, Hoogeman MS. Comparison of daily online plan adaptation strategies for a cohort of pancreatic cancer patients treated with SBRT. International Journal of Radiation Oncology* Biology* Physics. 2021;111:208-19.

[32] Young T, Dowling J, Rai R, Liney G, Greer P, Thwaites D, et al. Effects of MR imaging time reduction on substitute CT generation for prostate MRI-only treatment planning. Physical and Engineering Sciences in Medicine. 2021;44:799-807.

[33] Mugler III JP. Optimized three-dimensional fast-spin-echo MRI. Journal of Magnetic Resonance Imaging. 2014;39:745-67.

[34] Griswold MA, Jakob PM, Heidemann RM, Nittka M, Jellus V, Wang J, et al. Generalized autocalibrating partially parallel acquisitions (GRAPPA). Magnetic Resonance in Medicine. 2002;47:1202-10.

[35] Wright KL, Harrell MW, Jesberger JA, Landeras L, Nakamoto DA, Thomas S, et al. Clinical evaluation of CAIPIRINHA: comparison against a GRAPPA standard. Journal of Magnetic Resonance Imaging. 2014;39:189-94.

8 Assessment of MRI-Only Adaptive Radiotherapy for Pancreas Cancer

8.1 Presentations

Initial work was presented at EPSM 2022, Engineering and Physical Sciences in Medicine on 13th – 16th November 2022 in Adelaide, Australia under the poster presentation titled "Dose Variation in Pancreas SBRT – A planning study based on daily MR imaging". This poster presentation was awarded best poster in any field of physical science and engineering related to therapeutic radiation at EPSM 2022.

A copy of this accepted conference abstract is presented in thesis appendix 5.

This work has been submitted as a scientific paper to the Physical and Engineering Sciences in Medicine journal and is currently under review.

8.2 Introduction

Pancreatic Cancer is associated with significant morbidity and mortality, with the treatment outcomes remaining poor compared to other cancers. Most pancreatic cancer patients present with locally advanced or metastatic disease, with tumours often unresectable due to local invasion of adjacent structures. Even in patients with resectable disease, the 5 year overall survival is less than 25% [1].

The use of hypofractionated Stereotactic Body Radiotherapy (SBRT) of 1-5 fractions to treat pancreatic cancer has shown improved local control [2-4]. Radiotherapy for pancreatic cancer is challenging due to the close proximity of several organs at risk (OARs) to the pancreas, such as the duodenum, small bowel and stomach. In addition to this, the target volume may have large inter- and intra-fraction variations due to body contour changes, internal organ motion and changes, and respiratory motion [5]. Respiratory motion alone has the potential to produce intrafraction target motion of the order of 10 - 20 mm [6]. Day to day interfraction motion can produce variations and displacements of greater than 10 mm for surrounding duodenum, small bowel and stomach in pancreatic cancer radiotherapy [7, 8]. The addition of magnetic resonance imaging (MRI) guided radiotherapy has also improved the potential of online adaptive radiotherapy for pancreatic cancer [9], with MRI providing high resolution images with superior soft tissue contrast compared to CT [10]. This soft tissue contrast is necessary as there may be considerable interfraction position variation of the target and organs at risk relative to bony anatomy [11, 12], and it aids in target delineation, resulting in smaller target volumes and reducing interobserver variation [13].

The advent of adaptive treatment planning has also been required to counter the intrafraction motion within the abdomen which may affect the delivery of radiation to pancreatic cancer. There have been studies attempting to quantify allowable motion to maintain appropriate dose distributions in pancreatic cancer radiotherapy treatment, and the clinical effects due to the inter- and intra-fraction motion [5, 11, 14-16].

With the introduction of hybrid MRI-guided linac (MRIg-linac) systems, the ability to deliver online MRI-guided adaptive radiotherapy has become more common [9, 17-21]. These systems facilitate the adaptation of treatment plans to accommodate daily position variations, however have strict time constraints as the patient remains on the table in the treatment position whilst plan adaptation occurs. These systems still require treatment planning to occur on a reference CT scan however, with the daily adaptation of treatment plan based off the change in treatment volumes and OAR volumes from the captured MRI guidance scan.

The use of various deformable image registration (DIR) algorithms for dose accumulation has been investigated for numerous treatment sites [22-24]. Deformable dose accumulation provides a methodology to account for total cumulative dose delivered to the different anatomy in each treatment fraction, attempting to correct for the motion and deformation of organs and structures to accurately measure the actual dose delivered to the target and organs. A widely used approach is to obtain a deformation vector field (DVF), which describes the vector applied to each voxel from the DIR, to warp the dose grid back to the reference anatomy [25]. The accuracy of the deformable dose mapping and accumulation is dependant on the integrity of the DVF generated during DIR, with any errors and uncertainties in the DVF being propagated to the dose mapping [22]. The Raystation treatment planning system (TPS) has the hybrid intensity and structure based DIR algorithm, otherwise known as ANACONDA [26]. ANACONDA is an acronym of Anatomically Constrained Deformation Algorithm and uses a combination of image intensity information and anatomical/contour information. Contours are incorporated in the ANACONDA objective function by chamfer matching, which basically matches segmented features onto an image [27], with the objective function a linear combination of three non-linear terms – an image similarity term, looking at whether the reference and deformed target image are voxel wise “similar”; a grid regularization term, to create a smooth and invertible grid; and a penalty term when controlling structures are used.

In the diagnosis and staging of pancreatic cancer, MRI is considered superior when compared to ultrasound or CT imaging due to the enhanced soft tissue contrast provided [28-30]. The utilisation of MRI for pancreatic cancer patients is recommended, with the superior soft tissue contrast providing advantages for contouring of both the target volume and the surrounding OARs [31]. Considering this, the aim of this study was to investigate the variability of target and OAR volumes for different treatment planning regimens for pancreatic cancer, as part of an evaluation of the feasibility of utilizing treatment

day MRI scans from an MRI simulator for daily adaptive planning. Additionally, a secondary aim was to investigate the differences in dose accumulation techniques available utilizing MRI-only treatment planning.

8.3 Method

Ten volunteers were scanned on a Siemens (Erlangen, Germany) Skyra 3T MRI with a flat radiotherapy couch and coil mounts. Volunteer ages ranged from 25 to 47 with a median age of 35, and Body Mass Index (BMI) ranged from 19.7 to 29 with a median BMI of 24. Volunteers were scanned in full body vacuum bags for all sessions for setup consistency. Each volunteer was scanned over two sessions per day over 5 days to simulate a potential pancreas SBRT treatment regime, with a daily simulation scan for treatment planning, and a pre-treatment scan for adaptive planning and treatment. The second imaging session for each day was approximately three hours after the first imaging session. Volunteers were given instructions allowing only one cup of liquid and a small snack between scans, though compliance with these instructions was not strictly enforced being a volunteer study.

Each MRI scanning session consisted of the following scans as presented in table 8.1 - a T1 weighted transverse VIBE with Dixon (16 second exhale breath hold), T2 weighted interleaved TruFISP (3 orthogonal planes) (1 minute CINE) and a T1 weighted transverse 4D-MRI (5-6 minutes). Only the VIBE scan and the 4D MRI scan were used for this study.

Table 8.1 - MRI scanning session sequences, use and time taken.

Scan	Use	Time
T1 weighted transverse VIBE with Dixon (16 second exhale breath hold)	Anatomical contouring, treatment planning	~20 s
T2 weighted interleaved TruFISP (3 orthogonal planes) (1 minute CINE)	2D motion assessment	~1 minute
T1 weighted transverse 4D-MRI	3D motion assessment, ITV generation	~5-6 minutes

All scans were contoured and planned in the Raystation (RaySearch Laboratories, Stockholm, Sweden) TPS (version 10b). The water only images from the T1 weighted VIBE Dixon MRI sequence were used for treatment planning. The images from the first imaging session of the first day (D1S1) were considered the primary planning images for each volunteer. A Radiation Oncologist (RO) contoured a hypothetical tumour volume in the head region of the pancreas, with the last 2 cm of the pancreas used

as the Gross Tumour Volume (GTV) volume, as well as the nearby critical organs (i.e. stomach, duodenum). All other OARs required were contoured by Radiation Therapists (RTs) and physicists. The 4D MRI was used to generate an Internal Target Volume (ITV) from the GTV, which covered the movement of the GTV over the volunteer breathing cycle, with a 5 mm expansion applied to the ITV to generate the Planning Target Volume (PTV). The ITV generation using the 4D MRI sequence has been validated against CT previously [32].

Initially, each session on each day was registered to the D1S1 dataset using a rigid registration which focused on the pancreas, vertebral body, and kidney Regions of Interest (ROIs). Similarly, the second session of each day was registered to the first session as well. The ITV and nearby OARs were assessed for volume change, Dice similarity coefficient (DSC) and Hausdorff distance for each day, as well as compared to the primary planning images.

To enable treatment planning on the MRI images, density overrides were applied to the external contour (1 g/cm^3) and vertebral body (1.12 g/cm^3) as per the International Commission on Radiation Units and Measurements (ICRU) Report 46 recommendations. An initial validation of 10 retrospective pancreatic cancer patients was completed to benchmark the accuracy of the bulk density applied for treatment planning. For this comparison, the retrospective patient clinically approved treatment plan was recalculated on the same dataset with the external contour and vertebral body density overridden. Point dose comparison and 2%/2mm global gamma comparison was completed to assess the accuracy of the recalculation compared to the gold standard CT calculation for the clinically approved treatment plan.

The treatment plan was generated following the current departmental protocols on the D1S1 dataset. These clinical goals have been taken from the MASTERPLAN clinical trial (ACTRN12619000409178) and are presented in tables 8.2 and 8.3. Three different adaptive treatment methods were considered in this study and are presented in figure 8.1. This treatment plan was propagated via the rigid registration to all other imaging sessions and recalculated. This treatment plan was assessed for whether adaptation was required for the following imaging sessions to simulate a fractionated treatment schedule. Each imaging session was additionally registered using ANACONDA with the primary planning images, using the pancreas as the controlling ROI for this DIR. This allowed dose accumulation of the registered sessions. The plan recalculated on the 2nd session of each imaging day was taken as the “treatment” fraction (S2), with these 5 sessions accumulated on the primary planning images to produce a simulated treatment dose. This simulated treatment dose was compared with the original plan calculated on the primary planning images. This assessment was through DVH comparison of the PTV D95 (i.e. dose to 95% of the volume), ITV D99 and the duodenum and small bowel OAR volumes (Max D0.5cc dose, i.e. maximum dose to 0.5cc of the volume).

Table 8.2 - Planning Target Volume clinical goals from the MASTERPLAN Clinical Trial.

Parameter	Per Protocol	Minor Variation	Major variation
PTV40_EVAL D90%	> 100%	90-99%	< 90%
PTV40 D99%	>30Gy	25-30Gy	<25Gy
ITV D99%	>33Gy	30-33Gy	<30Gy
Max Dose (D0.5cc)	110-130%	130-140% OR <110%	>140%

Table 8.3 - OAR clinical goals considered for this study, taken from the MASTERPLAN Clinical Trial.

Organ	Constraint	Per Protocol	Minor Variation	Major Variation
Duodenum	Dmax (0.5cc)	<33Gy	≤35Gy	>35Gy
	V30	<5cc	5-10cc	>10cc
Stomach	Dmax (0.5cc)	<33Gy	≤35Gy	>35Gy
	V30	<5cc	5-10cc	>10cc
Small Bowel	Dmax (0.5cc)	<33Gy	≤35Gy	>35Gy
	V30	<5cc	5-10cc	>10cc
Combined Kidneys	V12Gy	<25%	25-30%	>30%
Liver	V12Gy	<40%	≤50%	>50%

The first imaging session of each day was also replanned as would occur with a daily simulation and adaptive treatment planning (S1), and corresponding treatment (S2) later that day. This method was utilised as it was the potential clinical translation of this work, with patients undergoing a daily MRI simulation session followed by radiotherapy on a conventional linear accelerator. The treatment plan generated on the first session of each day was propagated to the second session and recalculated, with the doses accumulated to represent daily replanning and treatment. In addition, a treatment plan was generated on the second session of each day, with the doses accumulated to indicate online (on table) treatment adaptation. This also was completed to ensure that the clinical goals were able to be met on that dataset. Both instances were compared with the treatment plan generated on the primary planning images through DVH comparison. The DVH comparison was also used to assess acceptability against the clinical goals outlined in tables 8.2 and 8.3, with the number of acceptable treatment fractions assessed. For the OAR clinical goals, a 0.5 cc maximum dose constraint and/or a volumetric dose

constraint, i.e. where V30 refers to the volume (can be specified as a percentage or cubic cm, cc) of the OAR receiving 30 Gy or higher, are considered.

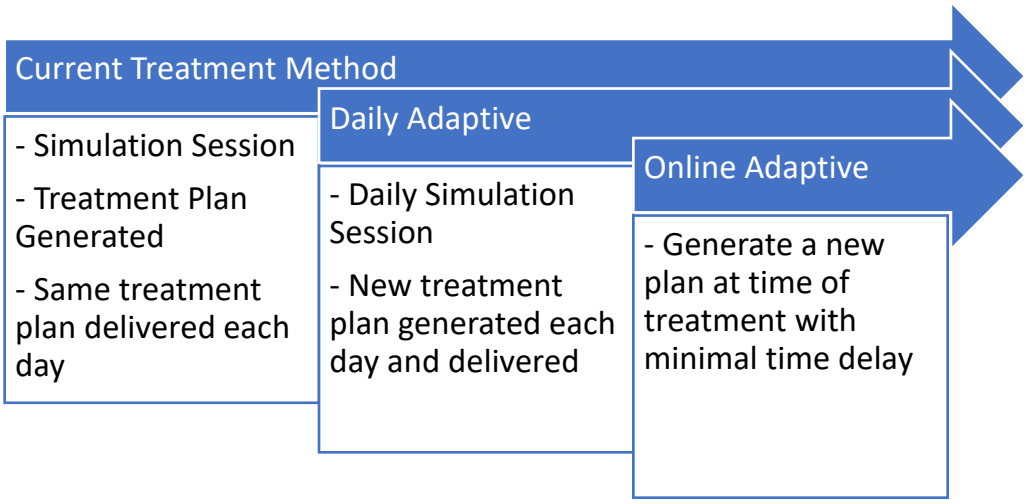

Figure 8.1 - Summary of the different mock adaptive treatment methods considered in this study.

8.4 Results

8.4.1 Initial validation of density override technique using retrospective patient data

The initial comparison of the clinical treatment plan calculated on the original patient CT to that calculated on the bulk density applied CT images is shown in table 8.4. The isocentre point doses agreed on average 0.01% ± 1.06%, with all cases lying within ±2% and the 2%/2mm global gamma results were on average 99.14% ± 0.97%, with all cases meeting a global gamma of greater than 97%. These results indicated that the bulk density values to be applied to the MRI scans for treatment planning, and which are recommended by ICRU 46, are reasonable for use for this patient anatomy.

Table 8.4 - Retrospective Patient Clinical Plan Comparison of bulk density datasets to original CT.

Retrospective Patient	Isocentre Point Dose Difference	2%/2mm Global Gamma Comparison (%)
1	-1.35%	97.43
2	1.93%	99.22
3	0.32%	99.98
4	-0.30%	99.77
5	-0.57%	99.92
6	-0.19%	99.15
7	-0.52%	97.63
8	1.77%	98.47
9	-0.82%	99.78
10	-0.17%	100
Average	0.01%	99.14
SD	1.06%	0.97

8.4.2 Volume Comparison

ITV volume variations over the course of the mock treatment were quite high for both comparison with the D1S1 baseline scan and the daily S1 scan for each volunteer. Figure 8.2 shows the day to day average variations and average absolute variations for both mock treatment scenarios across all volunteers. Figure 8.3 shows the day to day variation, and figure 8.4 shows the variation for each volunteer. Figures 8.2a and 8.3a display the same data as per figures 8.2 and 8.3 but with two outliers removed that are outside ± 1.5 IQR (interquartile range). The generated ITV was compared from the D1S1 reference scan to all other days. On average, the variation was -0.85% ± 23.68%. Considering average magnitude, the ITV size varied on average 22.44% ± 13.28% (1.61% - 56.27%). The generated ITV was also compared each day between the two daily imaging sessions, to simulate a daily simulation session and treatment. This variation was on average 7.30% ± 45.58%, and when magnitude only is considered, the average magnitude was 25.83% ± 37.48% (0.89% - 242.66%).

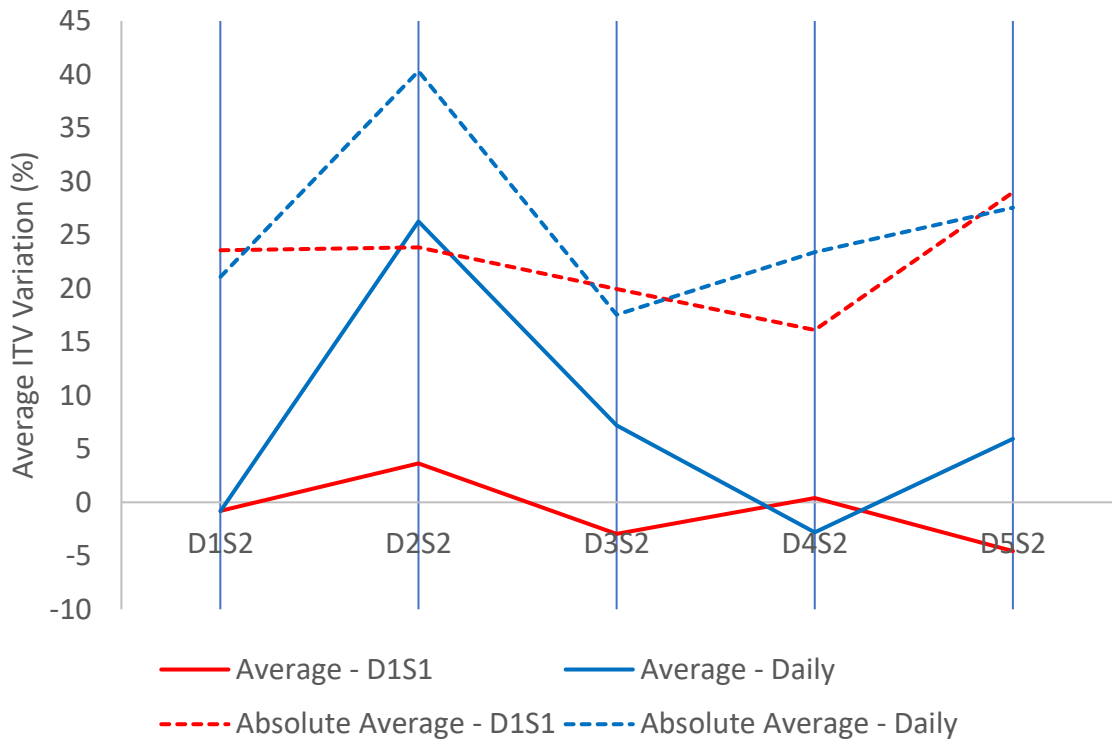

Figure 8.2 - Average ITV variations by day considering a reference (D1S1) scan or a daily reference (Daily) scan. Both average and average absolute differences are considered.

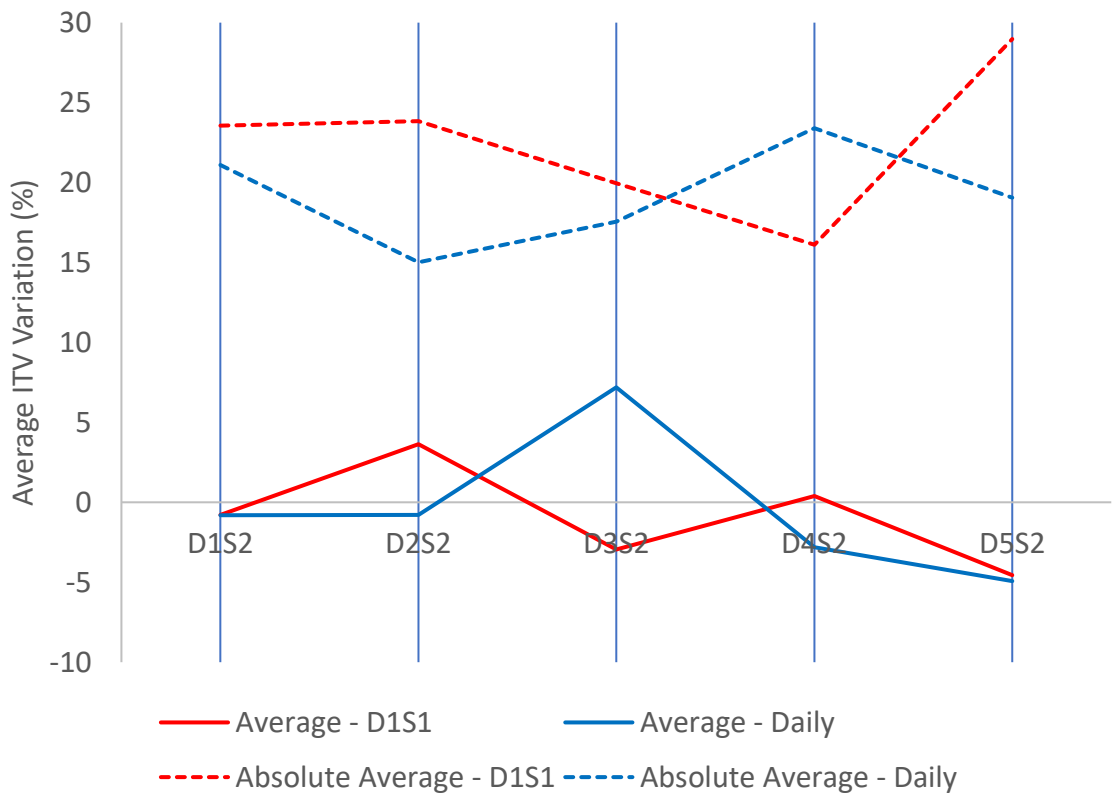

Figure 8.3a - Average ITV variations by day considering a reference (D1S1) scan or a daily reference (Daily) scan with outliers removed. Both average and average absolute differences are considered.

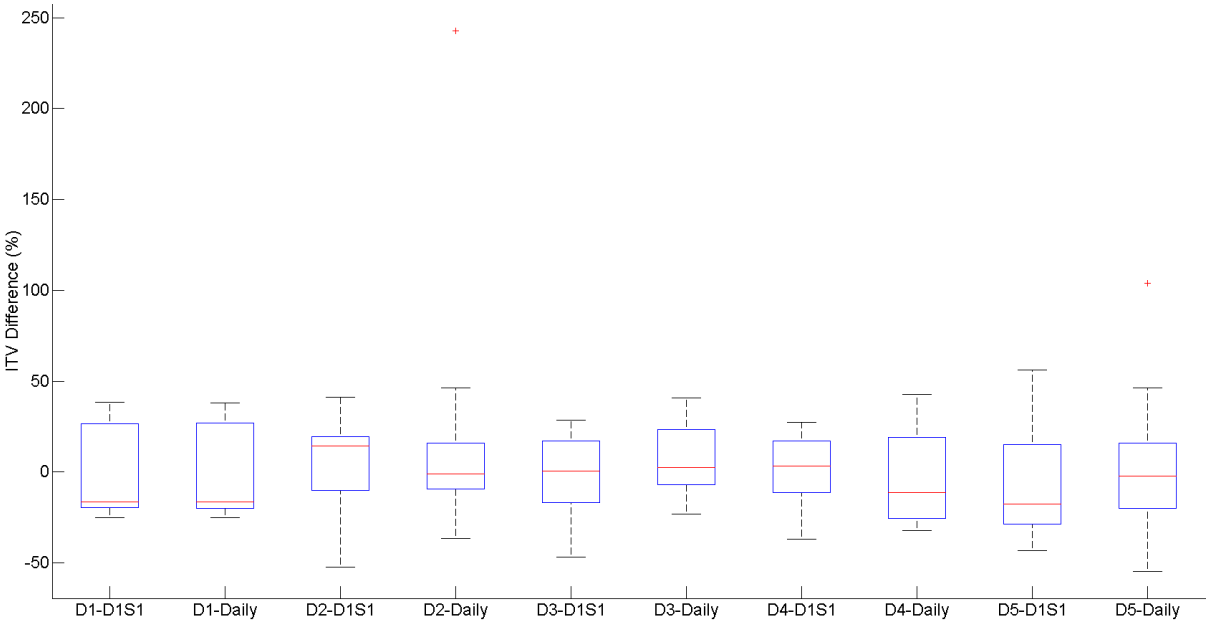

Figure 8.4 - ITV Variations by day considering a reference (D1S1) scan or a daily reference (Daily) scan. There are outliers for both the D2 and D5 daily comparison which skew the average for these days.

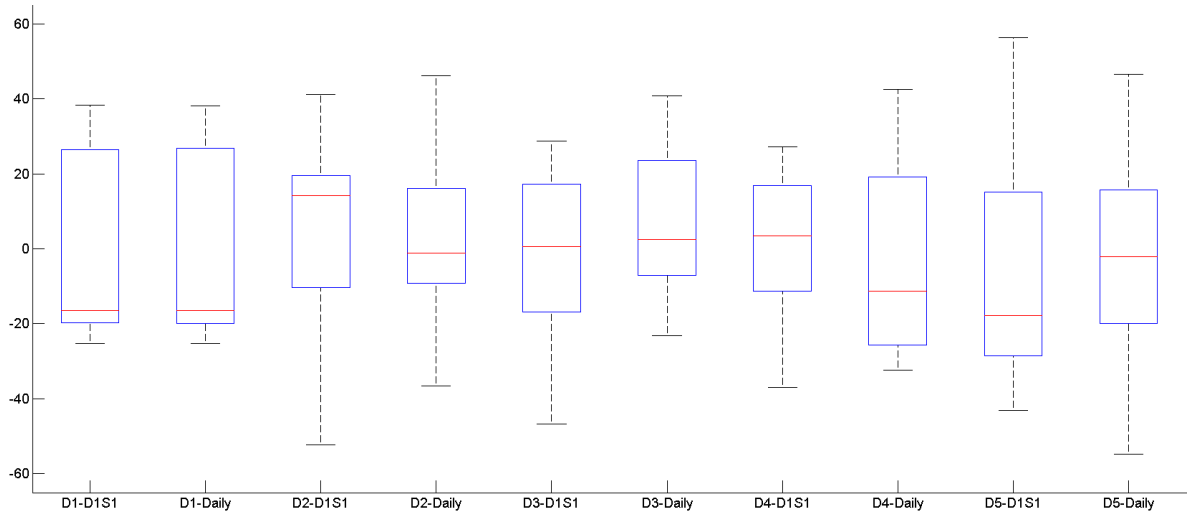

Figure 8.5a - ITV Variations by day considering a reference (D1S1) scan or a daily reference (Daily) scan. The outliers for both the D2 and D5 daily comparison have been removed.

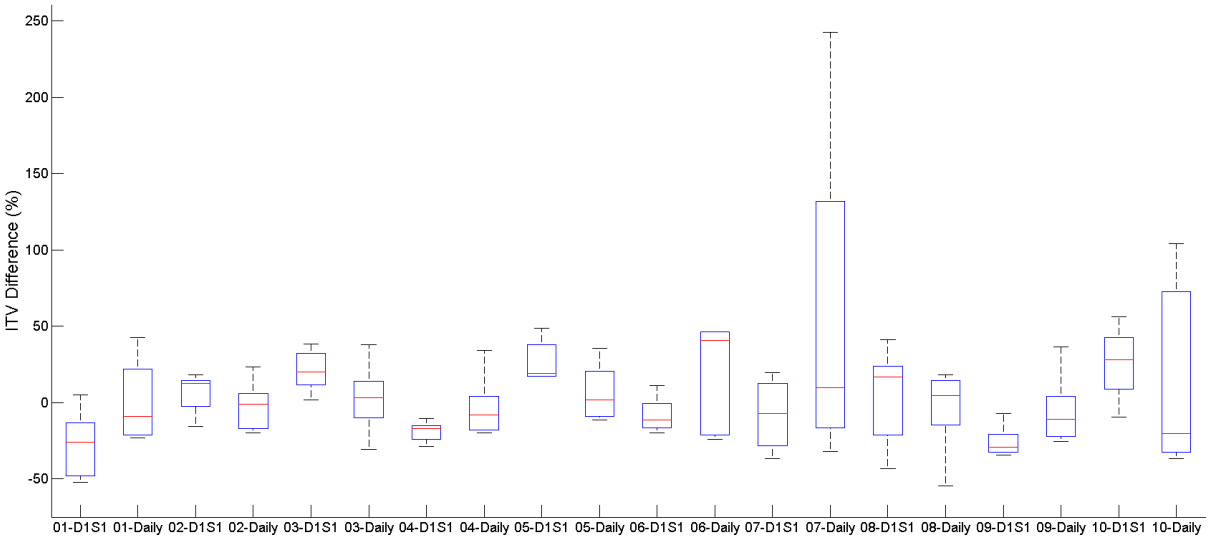

Figure 8.6 - ITV Variations for each volunteer considering a reference (D1S1) scan or a daily reference (Daily) scan. Volunteers 07 and 10 show large daily variations in ITV.

Contour assessment was also undertaken considering the GTV, ITV and the surrounding organs at risk for the second imaging session of each day for when a single reference scan is considered and also for a daily reference scan. The results for the average across the 10 volunteer dataset, considering the DSC, mean Hausdorff agreement and the volume change for both comparisons is shown in table 8.5. Figures 8.5 and 8.6 display the DSC and Hausdorff results for all volunteers. When the volume change is considered, the absolute volume changes are also smaller when a daily reference is considered. The external volume DSC is similar for both when compared to a D1S1 scan and to a daily scan, with a result of 0.959 ± 0.021 and 0.968 ± 0.009 respectively. The variation in internal volumes indicates the effect of internal organ motion and interfraction motion.

Table 8.5 - Contour comparison results when considering a single reference scan (D1S1) or a daily S1 reference scan (daily). The average DSC, Hausdorff distance and volume changes for various volumes are presented.

	External	GTV	ITV	Duoden-um	Pancreas	Small Bowel	Stomach
VS D1S1 Volumes							
Average DSC	0.959	0.521	0.594	0.542	0.686	0.569	0.654
StDev DSC	0.021	0.152	0.158	0.097	0.087	0.206	0.073
Average Hausdorff (mm)	11.39	3.74	3.66	4.55	2.89	10.18	6.63
StDev Hausdorff (mm)	3.44	1.55	1.69	1.52	0.78	9.29	2.49
Average Volume Change	0.20%	-5.90%	-0.25%	-4.44%	3.30%	73.86%	-9.68%
StDev Volume Change	2.61%	16.20%	19.70%	24.19%	20.01%	217.14%	43.76%
Average Absolute Volume Change	1.78%	14.33%	16.56%	19.66%	12.79%	91.02%	39.14%
StDev Absolute Volume Change	1.82%	8.54%	9.14%	13.32%	15.19%	209.77%	17.79%
VS Daily S1 Volume							
Average DSC	0.968	0.538	0.615	0.585	0.722	0.653	0.704
StDev DSC	0.009	0.139	0.141	0.108	0.061	0.071	0.076
Average Hausdorff (mm)	10.94	3.48	3.41	4.03	2.58	7.10	5.14
StDev Hausdorff (mm)	3.33	1.60	1.67	1.83	0.65	1.69	1.31
Average Volume Change	0.41%	4.50%	8.00%	-3.78%	-2.89%	3.55%	1.29%
StDev Volume Change	0.94%	21.97%	18.95%	10.49%	7.93%	15.08%	41.80%
Average Absolute Volume Change	0.88%	14.49%	11.45%	8.62%	6.63%	13.32%	31.42%
StDev Absolute Volume Change	0.46%	16.49%	16.86%	6.58%	4.83%	6.66%	25.53%

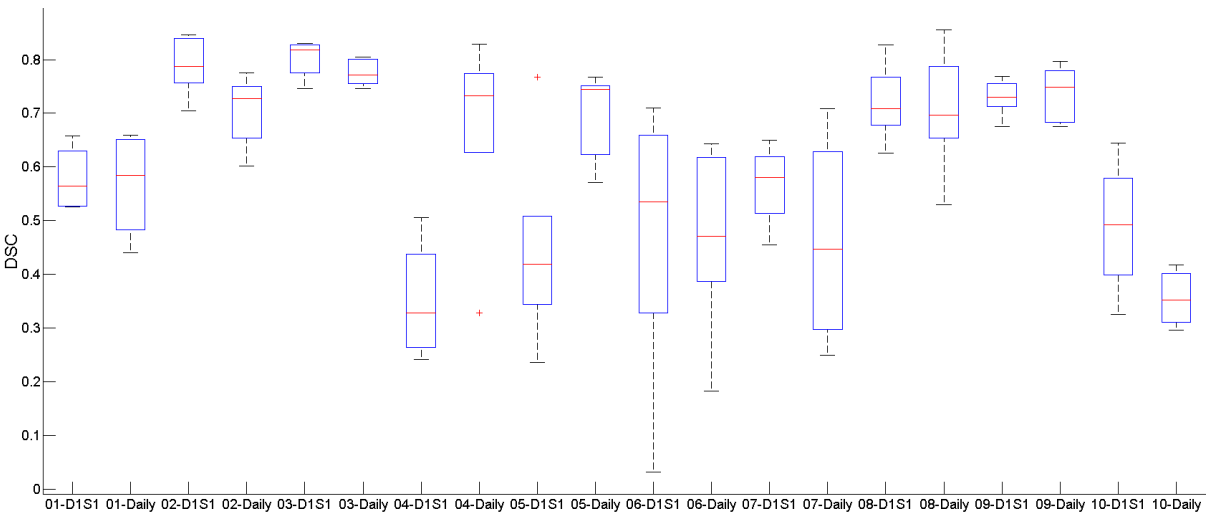

Figure 8.7 - DSC variation for each patient ITV. Both sets of results comparing a single reference scan (D1S1) or a daily S1 reference scan (daily) are presented.

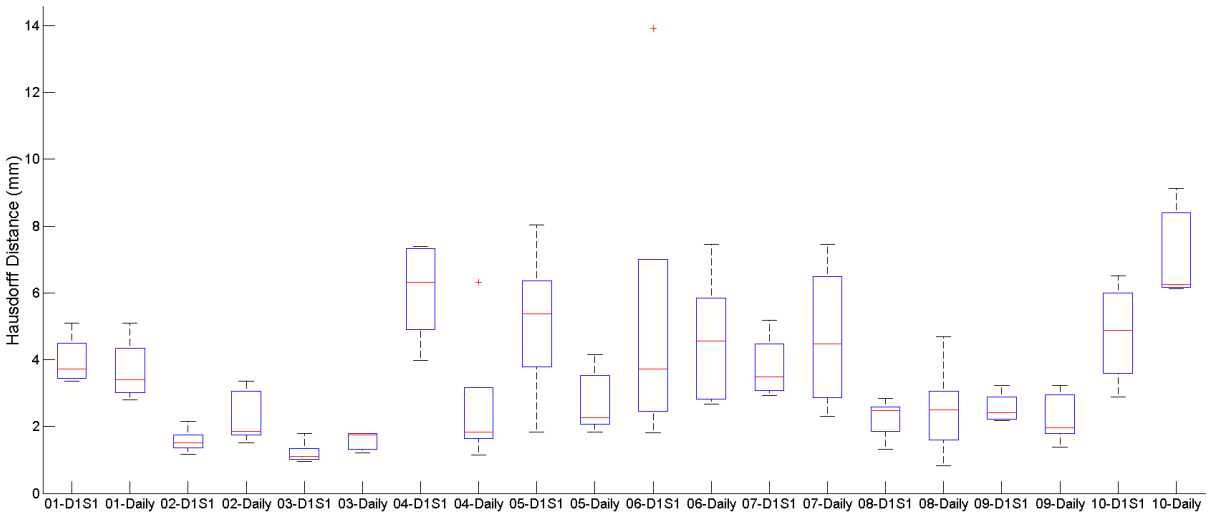

Figure 8.8 - Mean Hausdorff distance variations for the ITV for each volunteer. Both sets of results comparing a single reference scan (D1S1) or a daily S1 reference scan (daily) are presented.

The overlap of nearby OARs (duodenum, small bowel and stomach) with the PTV was also assessed. The variation for each volunteer is shown in figures 8.7 – 8.9 for when the overlap variation is assessed against the D1S1 overlap, as well as for the daily overlap. For all instances the S2 overlap volume is compared with the reference, whether that is the D1S1 overlap volume, or the S1 overlap volume on that corresponding day. When all volunteers and fractions are considered, the average overlap variation is -0.25% ± 9.58%, and when absolute overlap difference is considered, the average absolute OAR overlap variation is 9.93% ± 4.29% when compared against the D1S1 overlap. The OAR overlap varied from -20.74% to 26.30% for this comparison. Similarly, for the daily overlap, this average was -0.78% ± 5.76%, and when absolute OAR overlap variation is considered, this average was 7.86% ± 3.84%.

For the daily overlap, the variations ranged from -33.36% to 14.08%. The range of variation on a per volunteer basis was on average 17.79% ± 8.77% for the comparison against the D1S1 overlap, and 18.75% ± 12.93% for the daily overlap.

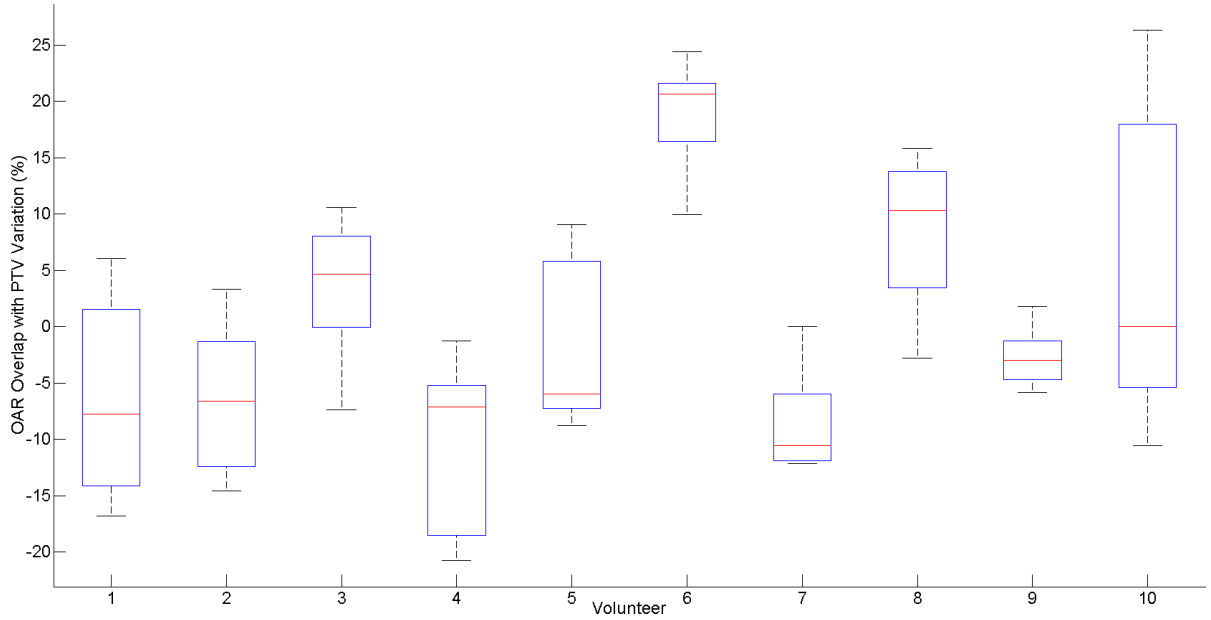

Figure 8.9 - OAR overlap variation with PTV when compared to D1S1.

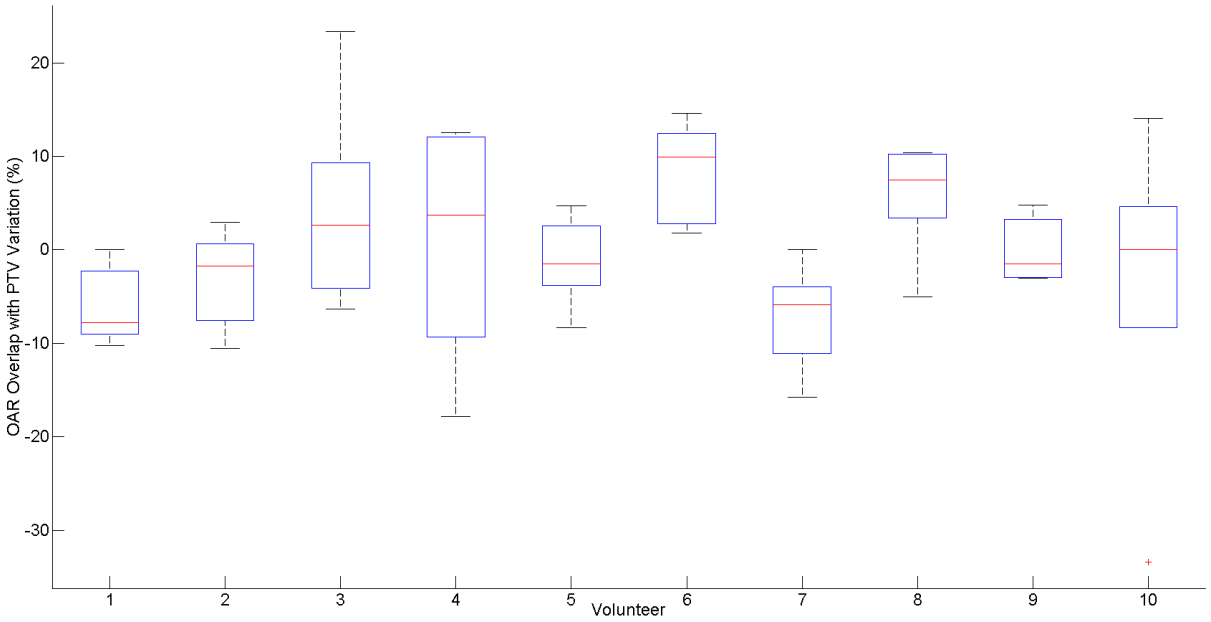

Figure 8.10 - OAR overlap variation with PTV when compared to a daily reference scan.

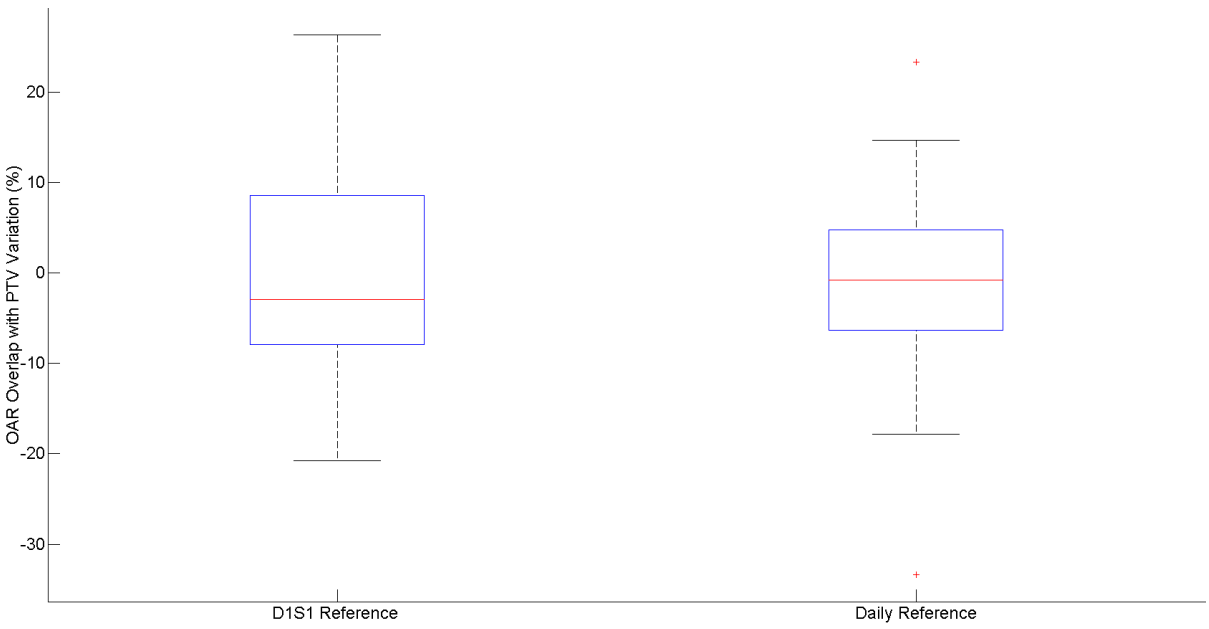

Figure 8.11 - OAR Overlap variation with PTV across the whole group of volunteers for comparison with the D1S1 overlap, as well as for the daily overlap.

8.4.3 Dose Assessment

Table 8.6 displays the mock treatment adaptation comparison as a whole, with each dose accumulation methodology averaged. Each target or OAR DVH parameter was compared to the corresponding reference DVH parameter depending on the reference plan, and the percentage difference for these across all volunteers was averaged and presented in the table. Considering some OAR DVH parameters had low absolute doses or percentage volumes, small changes in these produced large percentage differences. This was especially the case for the liver V12 comparison, and as such the liver D50 comparison is also presented. For the S2 vs D1S1 comparison, the reference plan generated on D1S1 of the volunteer dataset is propagated to the other S2 datasets through a rigid registration and the DVH parameters accumulated. Through a DIR of each S2 dataset back to the D1S1 reference dataset, the dose was also able to be recalculated according to the DIR for each S2 dataset and accumulated, with these results being the Deformed S2 vs D1S1. Considering a daily scan, each S1 scan was planned individually and recalculated on the S2 scan using a rigid registration, with DVH parameters accumulated. Lastly, each S2 was replanned to ensure that the plan achieved on D1S1 was still achievable with the change in internal organ anatomy. Figure 8.10 displays the DVH results for the comparisons to both the D1S1 plan and the daily plan using the rigid registration dose accumulation.

Table 8.6 - Dose accumulation summary considering the different scenarios. These DVH parameters have been averaged for all volunteers.

DVH Statistics	Rigid Accumulation Compared to D1S1 Plan	Rigid Accumulation Compared to Daily Plan	Deformed Dose Accumulation Compared to D1S1 Plan	Online Adaptive
PTV40 D95	-22.64% ± 19.59%	-23.85% ± 19.34%	-12.35% ± 23.94%	1.72% ± 3.82%
PTV40 D99	-33.17% ± 23.13%	-34.67% ± 19.61%	-18.20% ± 23.99%	1.03% ± 2.88%
PTV40_EVAL D90	-20.50% ± 11.55%	-21.12% ± 12.82%	-11.14% ± 20.97%	-0.72% ± 2.32%
ITV D99	-17.71% ± 16.56%	-19.60% ± 19.30%	-10.50% ± 26.22%	1.65% ± 5.11%
DUODENUM V30	-2.16% ± 62.10%	45.89% ± 127.15%	-2.70% ± 39.24%	-2.40% ± 44.44%
DUODENUM D0.5cc	6.64% ± 9.91%	9.14% ± 2.61%	4.62% ± 3.90%	-1.72% ± 2.60%
SMALLBOWEL V30	108.39% ± 365.82%	41.19% ± 84.98%	71.36% ± 289.63%	120.90% ± 365.07%
SMALLBOWEL D0.5cc	-2.29% ± 24.59%	5.53% ± 16.76%	-0.35 ± 10.67%	-10.34% ± 21.54%
STOMACH V30	763.98% ± 1601.03%	8.48% ± 17.89%	119.43% ± 334.87%	125.40% ± 312.29%
STOMACH D0.5cc	-11.26% ± 30.74%	47.59% ± 114.67%	2.42% ± 7.58%	-29.69% ± 29.34%
LIVER D50	0.12% ± 27.80%	17.47% ± 31.53%	6.69% ± 26.13%	-13.32% ± 30.81%
LIVER V12	596.07% ± 1327.11%	335.91% ± 587.53%	115.24% ± 277.93%	1507.54% ± 3335.22%
COMB_KIDNEYS V12	43.60% ± 73.88%	22.17% ± 33.86%	13.69% ± 46.36%	60.93% ± 185.91%

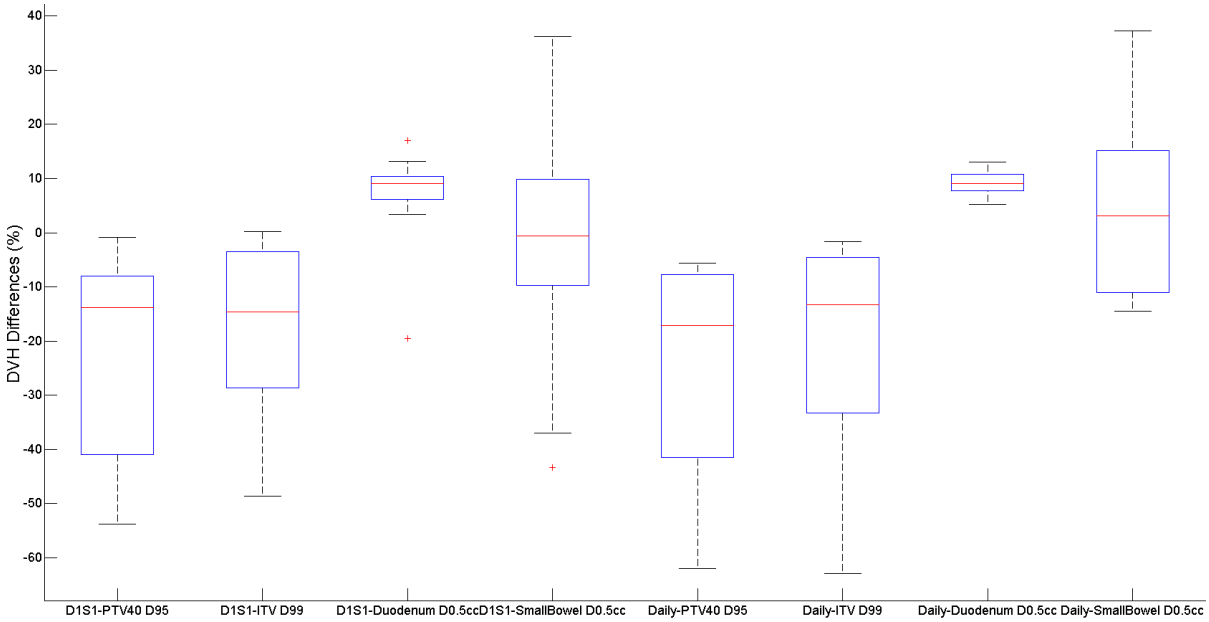

Figure 8.12 - DVH Differences between the D1S1 plan comparison and the Daily plan comparison.

The target volume coverage on average was reduced when considering the accumulated dose for both mock treatment with either a D1S1 reference plan or a daily reference plan as can be seen in figures 8.11 and 8.12 for comparison with the D1S1 plan, and figures 8.13 and 8.14 for comparison with a daily reference plan. The PTV40 D95 was on average reduced by -22.64% ± 19.59% when considering comparison to a D1S1 reference plan, and similarly reduced by -23.85% ± 19.34% when considering a daily reference plan. Small bowel and duodenum V30 increased for both sets of plan comparison as shown in figures 8.15 and 8.16 for the D1S1 reference plan comparison, and figures 8.17 and 8.18 for the daily reference plan comparison.

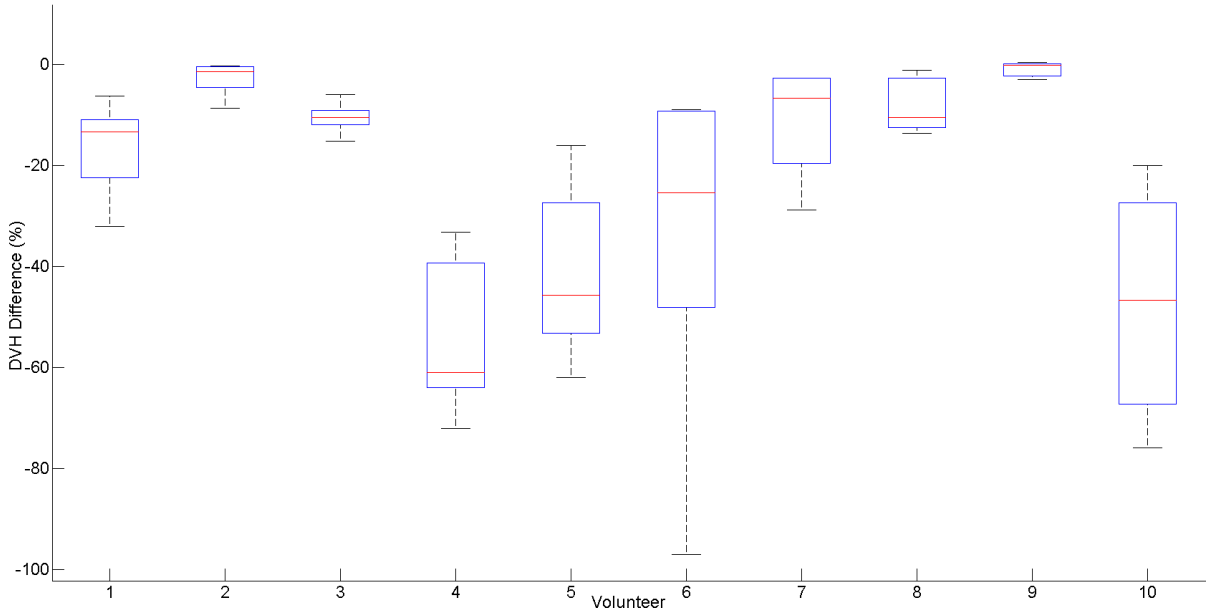

Figure 8.13 - PTV40 D95 for S2 vs D1S1.

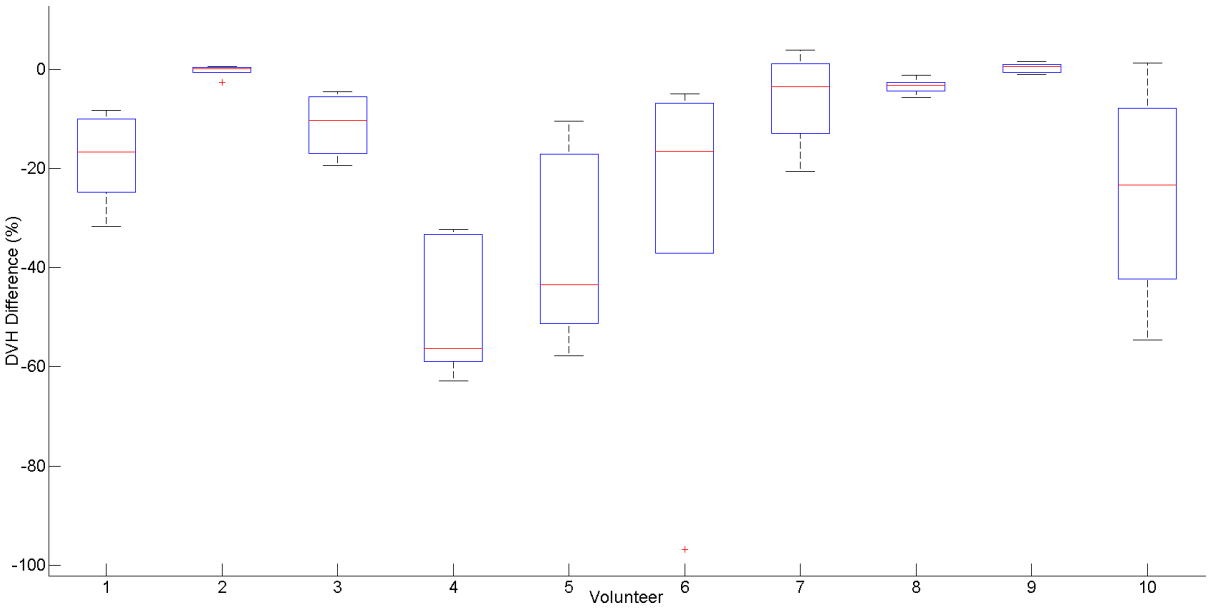

Figure 8.14 - ITV D99 for S2 vs D1S1.

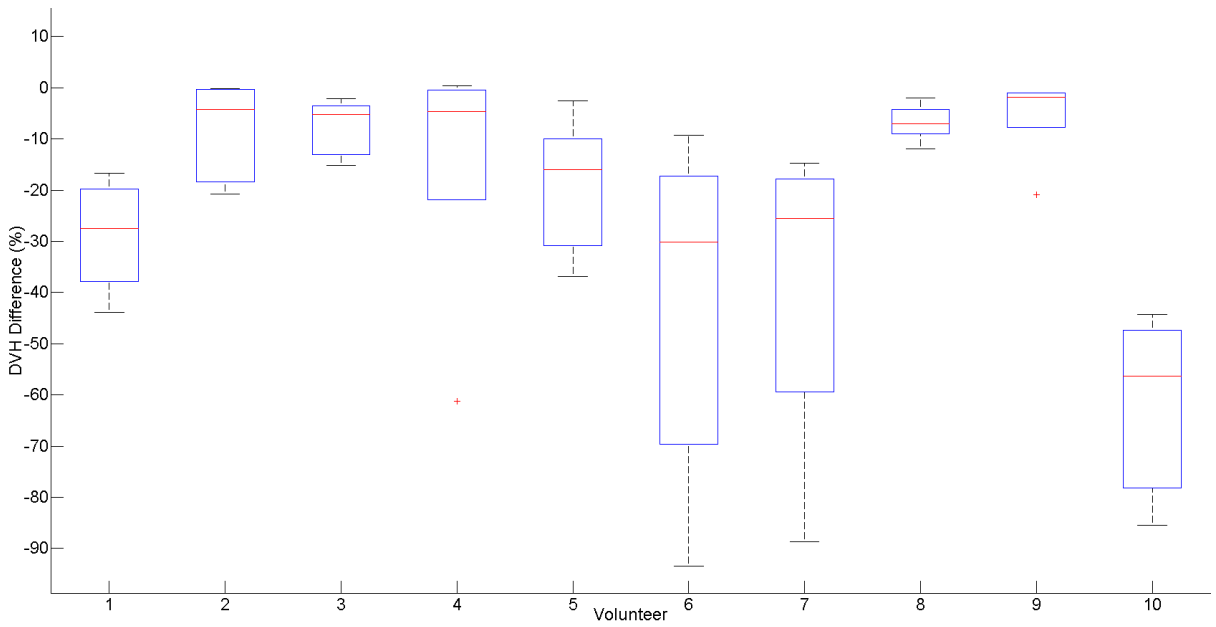

Figure 8.15 - PTV40 D95 vs Daily.

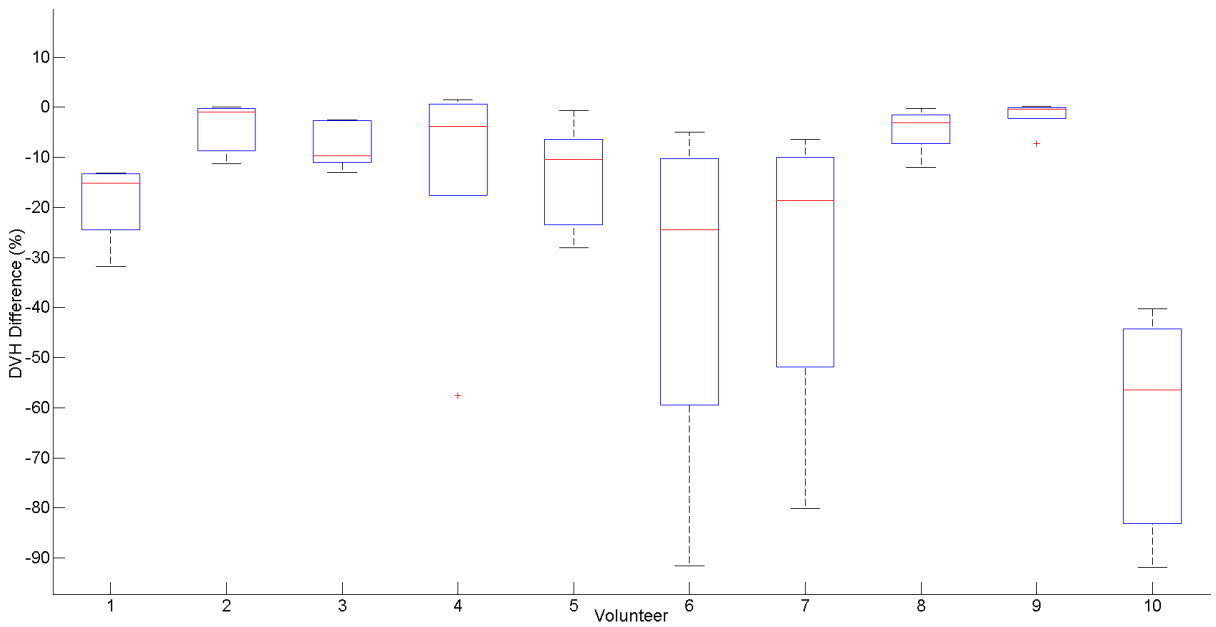

Figure 8.16 - ITV D99 vs Daily.

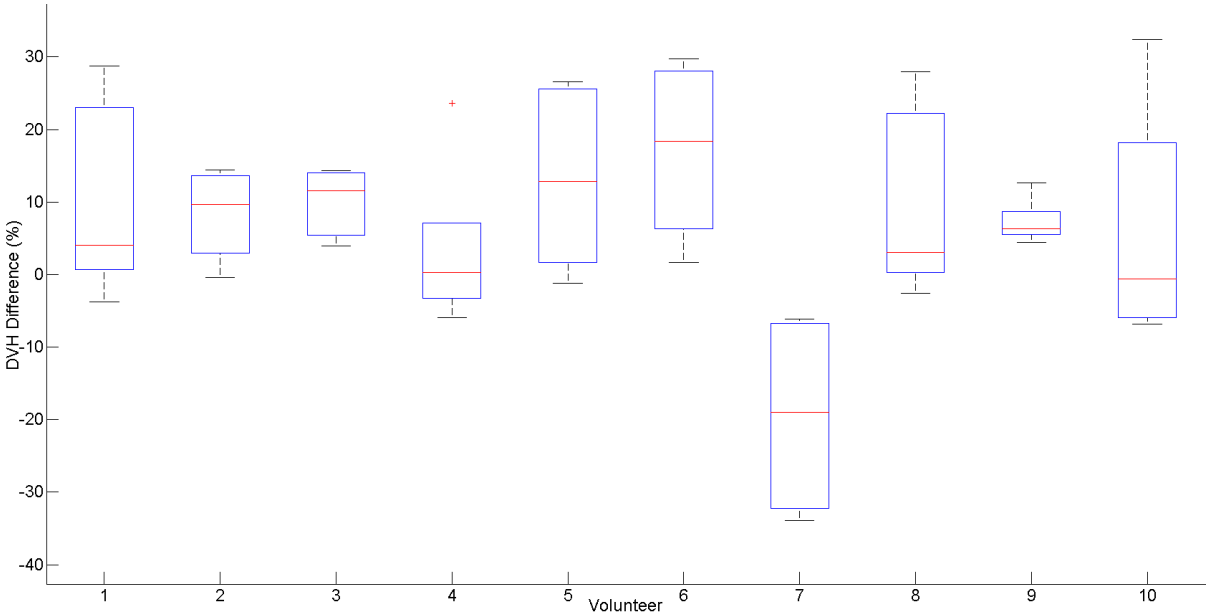

Figure 8.17 - Duodenum D0.5cc for S2 vs D1S1.

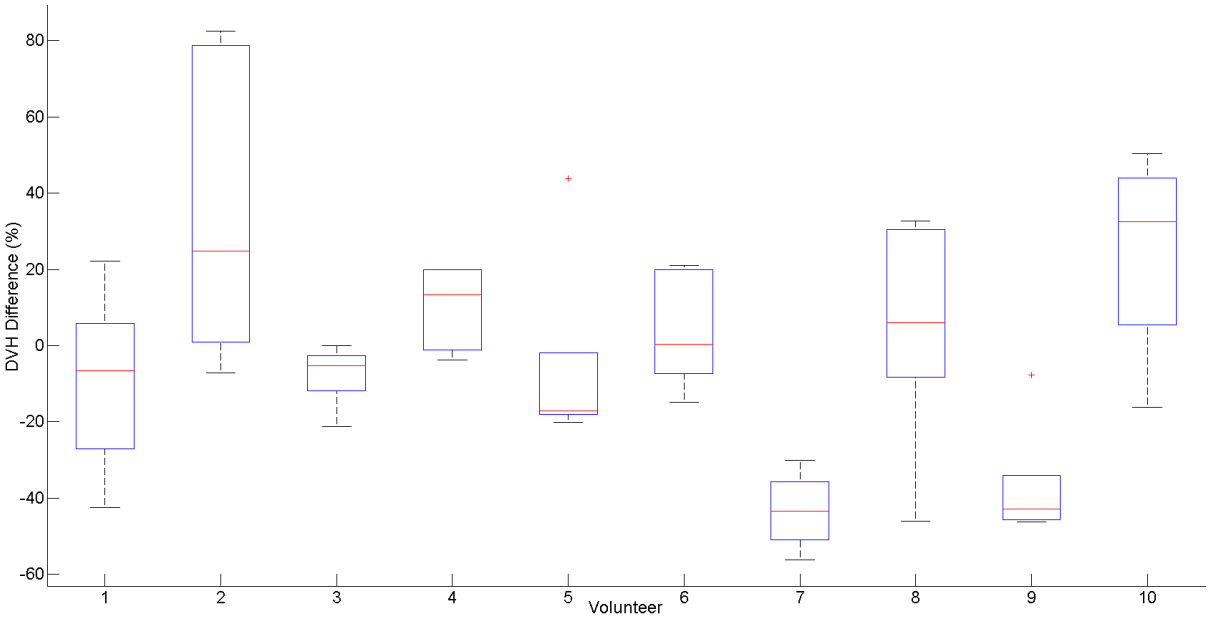

Figure 8.18 - Small bowel V30 D0.5cc for S2 vs D1S1.

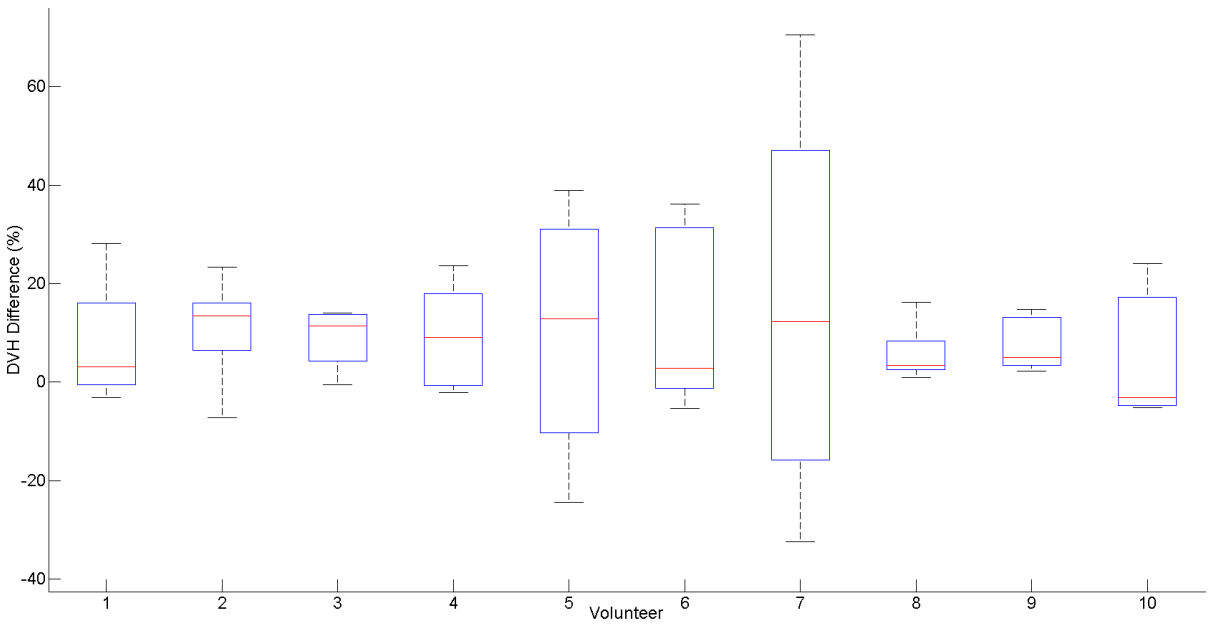

Figure 8.19 - Duodenum D0.5cc vs Daily.

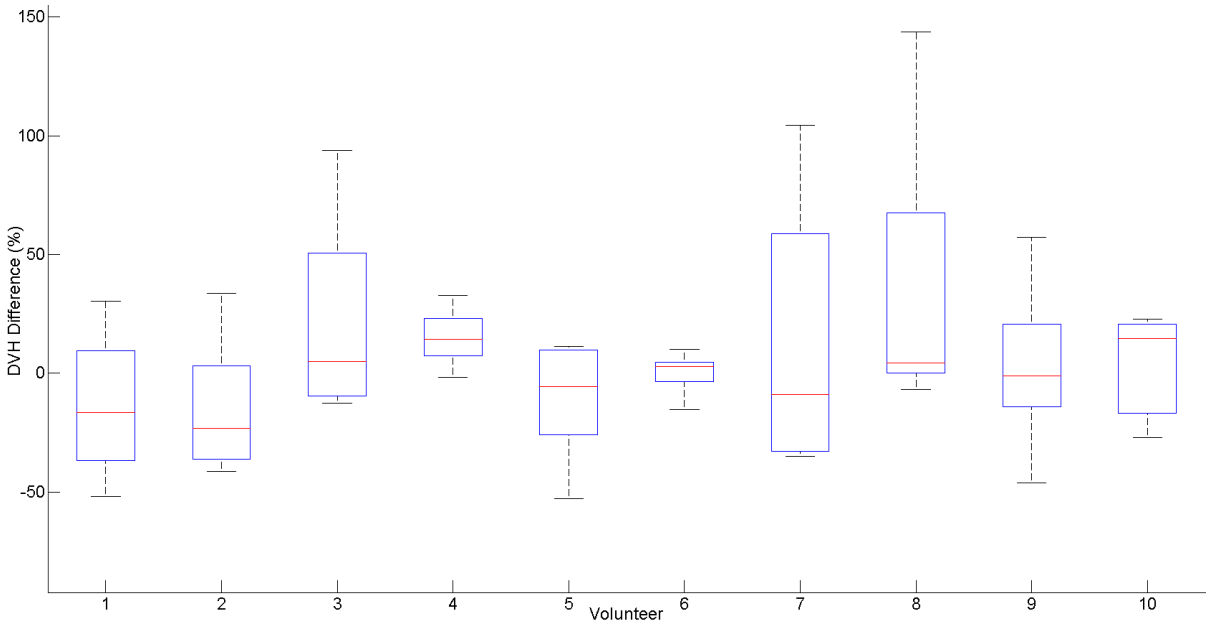

Figure 8.20 - Small bowel D0.5cc vs Daily.

The number of DVH parameters which did not exceed major violation criteria were assessed as per the number of acceptable fractions that did not exceed major violations, with the results shown in tables 8.7 and 8.8. The DVH criteria considered are in tables 8.2 and 8.3 (the max dose criteria were not considered in this analysis). Though neither the D1S1 comparison or the daily plan comparison yielded a fully acceptable treatment, some fractions had acceptable results in both cases, depending on the volunteer

anatomy on the day and imaging session. The differences between the D1S1 plan recalculated on each mock treatment session, and daily plan methodology were quite small in terms of number of acceptable DVH parameters, with on average 27.83% and 27.17% of fractions not exceeding major violations for the target DVH parameters, and 87.94% and 87.42% of fractions not exceeding major violations for OAR DVH parameters respectively. Considering the surrounding OARs, the duodenum had the smallest number of fractions which did not exceed major violations, at 77.08% and 76.09% respectively for D1S1 and daily replan comparisons. This was followed by small bowel at 84.38% and 84.78% respectively, and stomach at 90.63% and 89.13% respectively. Though the OARs had large percentage variations when compared to the appropriate reference plan, the majority still did not exceed major violations.

Table 8.7 - Fraction percentage for DVH parameters which did not exceed major violations.

	Total Pass Rate		Target Pass Rate		OAR Pass Rate	
Volunteer	D1S1 Fractions	Daily Fractions	D1S1 Fractions	Daily Fractions	D1S1 Fractions	Daily Fractions
1	67.27%	63.64%	0.00%	0.00%	92.50%	87.50%
2	78.18%	74.55%	53.33%	40.00%	87.50%	87.50%
3	70.91%	72.73%	26.67%	33.33%	87.50%	87.50%
4	61.82%	74.55%	0.00%	46.67%	85.00%	85.00%
5	65.45%	70.91%	0.00%	20.00%	90.00%	90.00%
6	67.27%	60.00%	20.00%	6.67%	85.00%	80.00%
7	84.09%	79.55%	50.00%	25.00%	96.88%	100.00%
8	74.55%	74.55%	46.67%	46.67%	85.00%	85.00%
9	89.09%	81.82%	73.33%	53.33%	95.00%	92.50%
10	56.82%	57.58%	8.33%	0.00%	75.00%	79.17%
Average	71.55%	70.98%	27.83%	27.17%	87.94%	87.42%

Table 8.8 - Fraction percentage for OAR DVH parameters which did not exceed major violations.

OAR	D1S1 Fractions	Daily Fractions
Duodenum	77.08%	76.09%
Small Bowel	84.38%	84.78%
Stomach	90.63%	89.13%

The use of DIR for dose accumulation was also applied to the comparison with the D1S1 reference plan. When the volunteer D1S1 plan was recalculated on each S2 dataset using the DIR, the dose agreement was much closer with the original D1S1 reference plan, though the target dose was still reduced, and the OAR doses generally increased. The use of DIR does deform the different organs closer to the original anatomy, showing closer agreement of the target volumes and OAR on average. Large deviations were still seen in some of the target volume DVH results, with some large outliers seen in figure 8.19 which presents the percentage DVH differences compared to the D1S1 plan for all patients using deformable dose accumulation.

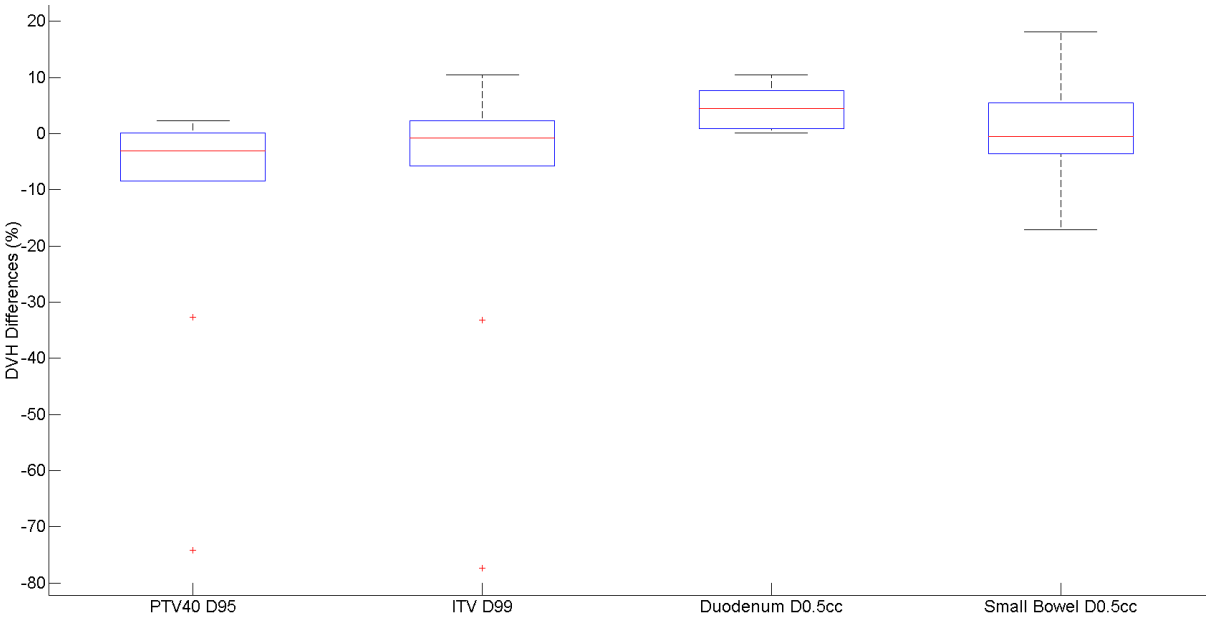

Figure 8.21 - DVH Differences between the Deformable Dose accumulation compared to a D1S1 plan, and for each mock treatment fraction replanned.

Results for the S2 mock treatment replan as would occur with daily online adaptive replanning is presented in table 8.6. All the DVH constraints were able to be met, or improved, with no major variations when compared to the planning criteria, and all would have been acceptable fractions. Each daily S2 set of MRI images was able to be planned to equivalent or better than the initial D1S1 reference plan, with the PTV40 D95 increased on average by 1.67%, and generally decreases in OAR doses. The average small bowel and stomach V30 was increased however all fraction doses were still within per protocol constraints. A comparison of the PTV, ITV, duodenum, and small bowel with the D1S1 parameters are shown in figure 8.20, with large percentage differences observed in the small bowel due to the lower doses for this parameter in addition to the day to day variation.

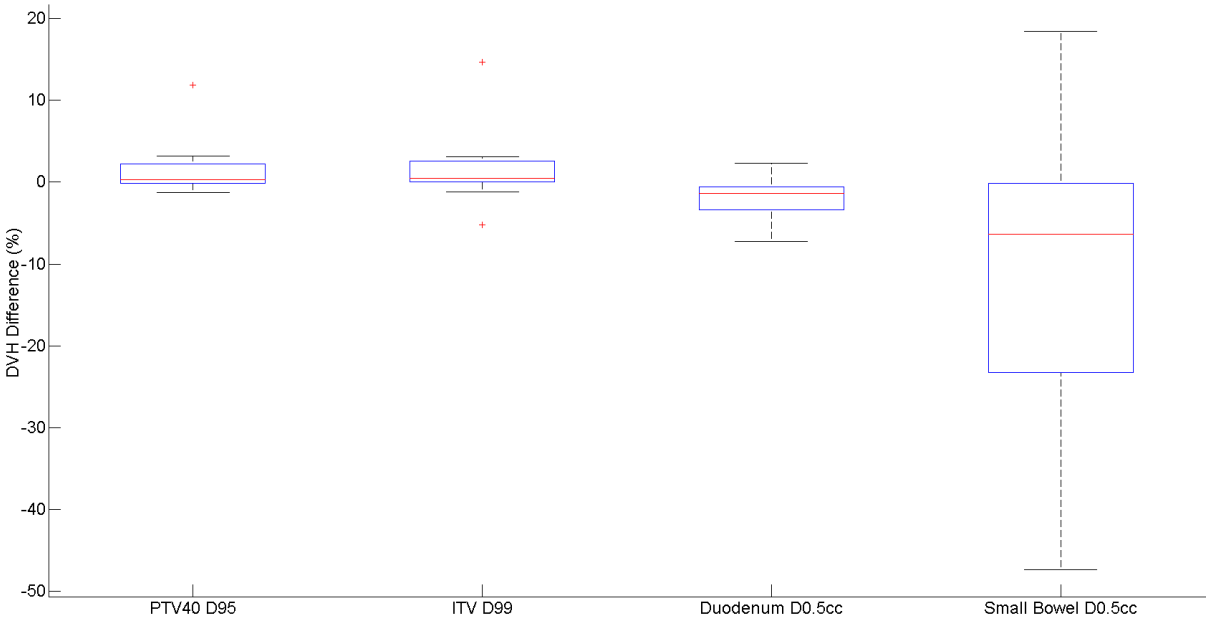

Figure 8.22 - DVH Differences for the mock treatment replan compared to the original D1S1 treatment plan. Large percentage differences are observed in the small bowel due to the lower doses for this parameter in addition to the day to day variation.

8.5 Discussion

This study considered the variation in internal anatomy between daily imaging sessions and over different days, and the variation in dose to target volume and nearby organs at risk for a simulated pancreas SBRT radiotherapy treatment. MR imaging was used for this comparison, with volunteers undertaking twice daily MRI simulation scans over 5 days within a 2 week period on a radiotherapy MRI simulator to simulate a 5 fraction treatment regime. A bulk density approach was used on the MRI data for treatment planning, with this approach initially tested on retrospective patient data.

The results show the need for online (on table) adaptive planning and treatment for accurate pancreas SBRT. Day to day and daily variations were observed in the ITV of similarly large magnitudes, in addition to internal organ motion and volume changes for both the target volume and OARs. These variations were observed between scans on different days in addition to scans on the same day. These differences ensured that neither a single reference treatment plan (such as a plan generated during pre-treatment simulation, or D1S1 in this study), or a daily reference treatment plan was sufficient to ensure suitable dose coverage with acceptable OAR doses for any of the mock treatments in this study.

It had been considered that a daily replanning exercise may be sufficient for this cohort of patients, especially in the absence of an MRI-guided linac. From table 8.5, the average DSC, mean Hausdorff and volume change had improved results for all volumes compared in the daily scans when compared to the results which compared the volumes back to the D1S1 reference scan. However the dosimetric results for the daily plans recalculated on the treatment scan of the day showed large variations in dose

coverage and OAR dose, with a similar percentage of fractions with acceptable DVH parameters as compared to the D1S1 reference plan. Poor compliance with instructions for food and drink between imaging sessions may have contributed to the large variations in organ location and volume within this study for the daily replan. Additionally, this cohort of patients would potentially be treated with an empty stomach each day for consistency, which did not occur in this volunteer study. This may have contributed to the day to day variations seen between scans.

The variation in internal volume anatomy has been studied previously. Heerkens et al. [33] studied MRI based tumor motion characterization, using sagittal and coronal cine MRIs of 60 seconds in 15 pancreatic cancer patients to quantify tumor motion. Tumour motion was largest in the craniocaudal direction, with an average amplitude of 15 mm and with a range of 6 – 34 mm. The average in the anterior – posterior direction was 5 mm, with range 1 – 13 mm, and in the lateral direction an average of 3mm, range 2 – 5 mm. Dolde et al. [34] used 4D MRI to analyse inter- and intra-fraction pancreas motion and deformation with different immobilization devices from 5 volunteers undertaking 10 imaging sessions with 3 different setup methods – a flat table top only, a vacuum bag and an abdominal corset to provide abdominal compression. Large pancreatic motion variations were observed, with mean inferior – superior motion amplitudes upto 28.5 mm and 21.9 mm for flat table top only and vacuum bag scanning. This study observed very patient specific pancreas motion amplitudes and day to day motion variations, with one volunteer having inferior – superior pancreatic motion amplitudes of 8.0 – 28.5 mm with large day to day variations up to 20.5 mm. The use of the abdominal corset reduced motion amplitudes in the anterior – posterior direction by up to 69%, with day to day fluctuations reduced by approximately 130%. Van Der Horst et al [5] studied anatomical changes in pancreatic cancer patients through retrospective analysis of daily cone beam CTs (CBCT) compared to the planning CT. From the daily CBCT the gastrointestinal gas was compared, and was found to vary considerably between fractions, ranging from 5 – 669 cm^3 for the 9 patients studied. Alam et al [35] looked at a pre-treatment, verification and post-treatment MRI for each abdominally compressed pancreas cancer patient treatment fraction, finding median (max) interfraction deformation for the stomach/duodenum and small bowel of 6.1 (25.8) mm and 7.9 (40.5) mm respectively, and median intrafraction deformation was 5.5 (22.6) mm and 8.2 (37.8) mm respectively. These large variations are similar for both inter- and intra-fraction motion, indicating large displacements for both, even with abdominal compression. Alam et al.'s study also reported median Dice similarity scores for the duodenum-stomach and small bowel of 0.7, which is similar to that reported in this study.

This study suffers from a lack of motion management, with large variations in ITV seen. This shows that a 4D ITV method may not be sufficient for these patients, with other motion management techniques [36, 37] such as gated techniques, implanted markers/tumour tracking or compression techniques able to reduce the variation in ITV on a daily basis, and potentially enable more accurate delivery of dose to the tumour whilst maintaining OAR doses [38, 39]. However this would not

necessarily reduce any interfraction motion of the OAR, which occurred throughout this study for all volunteers. Fiducial markers implanted in the target volume would be useful for determining the interfraction and intrafraction motion of the target. Though this study was able to visualize the target volume, fiducial markers would aid the accuracy of the registration back to reference images and plan, in particular for DIR accuracy in the target volume.

Bulk density was determined to be suitable for use for this study from the results of application of the bulk density correction to retrospective patients planned on CT. The results of the original treatment plans recalculated on the bulk density corrected datasets, and compared with the calculations on CT, were a point dose agreement of 0.01% ± 1.06%, and a 2%/2mm global gamma pass rate of 99.14% ± 0.97% for the 10 patient dataset. Hsu et al. [40] completed a similar planning study using ICRU 46 bulk density values in the abdomen, reporting a mean difference of -0.6% ± 0.3% for the PTV D99.9%, and concluding that that the ICRU values might be sufficient for electron density assignment of MRI for treatment planning. Bredfeldt et al. [41] also utilised a bulk density approach for the abdomen, with a fuzzy c-means segmentation method used to segment the image into different tissue classes before the appropriate HU was assigned. Maximum differences in the target volumes were less than 0.5 Gy, with median target dose metrics all within 0.1 Gy for this study. Liu et al. [42] investigated a deep learning based sCT generation method for liver SBRT, with no significant differences observed in the PTV and OAR DVH metrics in addition to an average 1%/1mm gamma pass rate of greater than 99% at the coronal plane. This suggests that incremental improvement may be achieved by using a more sophisticated sCT generation method, though the bulk density approach is acceptable for this anatomy and the adaptive planning comparisons made within this study.

When comparing the dose delivery considering only a single baseline plan, as well as comparing to a daily plan, the target dose was deficient in most days considered, due to anatomical changes. These variations included both nearby OAR variations, as well as changes in ITV generation due to the variability in volunteer breathing, which generated a different daily PTV volume for the day. It should be considered that if the ITV was smaller, that the previous dose coverage should still be sufficient for target coverage, however the average DSC of 0.594 ± 0.158, average Hausdorff distance of 3.66 mm ± 1.69 mm and average volume variation of -0.25% ± 19.70% would indicate that the ITV volume and position varied when compared to the D1S1 ITV. For the daily plan, these results were only slightly improved, with an average DSC of 0.615 ± 0.141, average Hausdorff distance of 3.41 mm ± 1.67 mm and average volume variation of 8% ± 18.95%.

Previous studies have investigated different dose accumulation methodologies in pancreatic cancer due to the day to day variations in anatomy in this region. Van Der Horst et al [5] chose to accumulate dose rigidly within their study as they utilized fiducial markers in the target volume. This study did conclude that the OARs did not move rigidly with the fiducial markers however were not able to view the nearby

OARs accurately, rather the gastrointestinal gas only due to being a CBCT study. Alam et al [35] utilized a Large Deformation Diffeomorphic Metric Mapping (LDDMM) DIR to accumulate dose to nearby OARs for a 5 patient retrospective study. This study showed accumulated doses for two patients exceeded institutional constraints, one of which experienced grade 1 acute and late abdominal toxicity. Some DIR algorithms implemented in commercial systems have been shown to lack accuracy even in prostate and head and neck anatomies [43, 44], with MR-MR DIR also not able to account for potential large volume changes seen in bladder or rectum [43]. Mittauer et al [45] conducted a heterogeneous anthropomorphic abdominal deformable phantom study to compare DIR algorithms available with MRIdian and MIM systems, benchmarking both systems for mean phantom DVFs of 5 mm and achieving mean, median dose differences of 0.3%, -0.3% for rigid dose accumulation and 4.1%, 0.6% for deformed dose accumulation, with a large difference seen with the different dose accumulation techniques. From the work presented in this chapter, differences were also observed with the use of different dose accumulation techniques. The use of DIR for dose accumulation did produce improved results when compared to the rigid dose accumulation method, however there were still large outliers in the target volume DVH results. The work described in this chapter however did not look at the accuracy of the DIR, for which further validation would be required, but rather the comparison of the deformable dose accumulation methodology with more conventional rigid techniques.

The conventional method of simulation and planning based off a single reference scan is not appropriate for this treatment site for a hypofractionated SBRT treatment as per the variations seen in this study. Scanning on the day and completing treatment planning with the scan on the day may be appropriate for some patients with appropriate motion management but still may have large variations in internal organ anatomy between the scan on the day and the treatment scan, particularly if strict protocols are not followed regarding intake. Online adaptive treatment is the best option for ensuring target dose coverage whilst minimizing dose to nearby OARs, particularly the duodenum, small bowel and stomach [46]. This methodology is current best practice and has been utilized with hybrid MRIg-linacs [8, 19-21, 47], allowing delivery of hypofractionated SBRT treatment for pancreatic cancer using real time adaptation of the dose distribution to account for day to day variations in organ shapes and position. This is currently not possible with conventional linear accelerators however, and a daily MRI scan in conjunction with daily plan adaptation and additional motion management techniques and tracking may allow more accurate treatment of pancreas SBRT whilst reducing dose to nearby OARs. A daily MRI scan for this cohort of patient being treated on conventional linacs may also yield additional information related to intrafraction motion, providing ability to better predict target dose coverage and OAR dose on the day. Further work is planned for the potential clinical translation of a daily MRI for pancreas SBRT patients within the department.

8.6 Conclusions

Daily online adaptive radiotherapy is required for accurate dose delivery for pancreas cancer in the absence of additional motion management and tumour tracking techniques, considering the inter- and intra-fraction variations present in this treatment site. Daily MRI is beneficial for this cohort of patients for assessment of intrafraction motion, particularly for centres without MRIg-linacs available. The use of different dose accumulation techniques produced different results, and further work is required to validate the deformable dose accumulation approach.

8.7 References

[1] Mahadevan A, Moningi S, Grimm J, Li XA, Forster KM, Palta M, et al. Maximizing Tumor Control and Limiting Complications With Stereotactic Body Radiation Therapy for Pancreatic Cancer. International Journal of Radiation Oncology* Biology* Physics. 2021;110:206-16.

[2] Courtney PT, Paravati AJ, Atwood TF, Raja N, Zimmerman CT, Fanta PT, et al. Phase I trial of stereotactic body radiation therapy dose escalation in pancreatic cancer. International Journal of Radiation Oncology* Biology* Physics. 2021;110:1003-12.

[3] de Geus SW, Eskander MF, Kasumova GG, Ng SC, Kent TS, Mancias JD, et al. Stereotactic body radiotherapy for unresected pancreatic cancer: A nationwide review. Cancer. 2017;123:4158-67.

[4] Reyngold M, Parikh P, Crane CH. Ablative radiation therapy for locally advanced pancreatic cancer: techniques and results. Radiation Oncology. 2019;14:95.

[5] van der Horst A, Houweling AC, van Tienhoven G, Visser J, Bel A. Dosimetric effects of anatomical changes during fractionated photon radiation therapy in pancreatic cancer patients. Journal of Applied Clinical Medical Physics. 2017;18:142-51.

[6] Akimoto M, Nakamura M, Nakamura A, Mukumoto N, Kishi T, Goto Y, et al. Inter-and intrafractional variation in the 3-dimensional positions of pancreatic tumors due to respiration under real-time monitoring. International Journal of Radiation Oncology* Biology* Physics. 2017;98:1204-11.

[7] Liu F, Erickson B, Peng C, Li XA. Characterization and management of interfractional anatomic changes for pancreatic cancer radiotherapy. International Journal of Radiation Oncology* Biology* Physics. 2012;83:e423-e9.

[8] Magallon-Baro A, Milder MT, Granton PV, Nuyttens JJ, Hoogeman MS. Comparison of daily online plan adaptation strategies for a cohort of pancreatic cancer patients treated with SBRT. International Journal of Radiation Oncology* Biology* Physics. 2021;111:208-19.

[9] Boldrini L, Cusumano D, Cellini F, Azario L, Mattiucci GC, Valentini V. Online adaptive magnetic resonance guided radiotherapy for pancreatic cancer: state of the art, pearls and pitfalls. Radiation Oncology. 2019;14:1-6.

[10] Paganelli C, Whelan B, Peroni M, Summers P, Fast M, Van de Lindt T, et al. MRI-guidance for motion management in external beam radiotherapy: current status and future challenges. Physics in Medicine & Biology. 2018;63:22TR03.

[11] Jayachandran P, Minn AY, Van Dam J, Norton JA, Koong AC, Chang DT. Interfractional uncertainty in the treatment of pancreatic cancer with radiation. International Journal of Radiation Oncology* Biology* Physics. 2010;76:603-7.

[12] Nakamura M, Akimoto M, Ono T, Nakamura A, Kishi T, Yano S, et al. Interfraction positional variation in pancreatic tumors using daily breath-hold cone-beam computed tomography with visual feedback. Journal of Applied Clinical Medical Physics. 2015;16:108-16.

[13] Gurney-Champion OJ, Versteijne E, van der Horst A, Lens E, Rütten H, Heerkens HD, et al. Addition of MRI for CT-based pancreatic tumor delineation: a feasibility study. Acta Oncologica. 2017;56:923-30.

[14] Ding Y, Campbell WG, Miften M, Vinogradskiy Y, Goodman KA, Schefter T, et al. Quantifying allowable motion to achieve safe dose escalation in pancreatic SBRT. Practical Radiation Oncology. 2019;9:e432-e42.

[15] Niedzielski JS, Liu Y, Ng SS, Martin RM, Perles LA, Beddar S, et al. Dosimetric uncertainties resulting from interfractional anatomic variations for patients receiving pancreas stereotactic body radiation therapy and cone beam computed tomography image guidance. International Journal of Radiation Oncology* Biology* Physics. 2021;111:1298-309.

[16] Feng M, Balter JM, Normolle D, Adusumilli S, Cao Y, Chenevert TL, et al. Characterization of Pancreatic Tumor Motion Using Cine MRI: Surrogates for Tumor Position Should Be Used With Caution. International Journal of Radiation Oncology*Biology*Physics. 2009;74:884-91.

[17] Chow PE, Chu F-I, Agazaryan N, Cao M, Tyran M, Yang Y, et al. Dosimetric quality of online adapted pancreatic cancer treatment plans on an MRI-guided radiation therapy system. Advances in Radiation Oncology. 2021;6:100682.

[18] Ermongkonchai T, Khor R, Muralidharan V, Tebbutt N, Lim K, Kutaiba N, et al. Stereotactic radiotherapy and the potential role of magnetic resonance-guided adaptive techniques for pancreatic cancer. World Journal of Gastroenterology. 2022;28:745.

[19] Hassanzadeh C, Rudra S, Bommireddy A, Hawkins WG, Wang-Gillam A, Fields RC, et al. Ablative five-fraction stereotactic body radiation therapy for inoperable pancreatic cancer using online MR-guided adaptation. Advances in Radiation Oncology. 2021;6:100506.

[20] Placidi L, Romano A, Chiloiro G, Cusumano D, Boldrini L, Cellini F, et al. On-line adaptive MR guided radiotherapy for locally advanced pancreatic cancer: Clinical and dosimetric considerations. Technical Innovations & Patient Support in Radiation Oncology. 2020;15:15-21.

[21] Nierer L, Eze C, da Silva Mendes V, Braun J, Thum P, von Bestenbostel R, et al. Dosimetric benefit of MR-guided online adaptive radiotherapy in different tumor entities: liver, lung, abdominal lymph nodes, pancreas and prostate. Radiation Oncology. 2022;17:1-14.

[22] Chetty IJ, Rosu-Bubulac M. Deformable Registration for Dose Accumulation. Seminars in Radiation Oncology: Elsevier; 2019. p. 198-208.

[23] Kieselmann JP, Kamerling CP, Burgos N, Menten MJ, Fuller CD, Nill S, et al. Geometric and dosimetric evaluations of atlas-based segmentation methods of MR images in the head and neck region. Physics in Medicine & Biology. 2018;63:145007.

[24] Ziegler M, Nakamura M, Hirashima H, Ashida R, Yoshimura M, Bert C, et al. Accumulation of the delivered treatment dose in volumetric modulated arc therapy with breath-hold for pancreatic cancer patients based on daily cone beam computed tomography images with limited field-of-view. Medical Physics. 2019;46:2969-77.

[25] Paganelli C, Meschini G, Molinelli S, Riboldi M, Baroni G. Patient-specific validation of deformable image registration in radiation therapy: Overview and caveats. Medical Physics. 2018;45:e908-e22.

[26] Weistrand O, Svensson S. The ANACONDA algorithm for deformable image registration in radiotherapy. Medical Physics. 2015;42:40-53.

[27] Bankman I. Handbook of medical image processing and analysis: Elsevier; 2008.

[28] Lee ES, Lee JM. Imaging diagnosis of pancreatic cancer: a state-of-the-art review. World Journal of Gastroenterology: WJG. 2014;20:7864.

[29] Miura F, Takada T, Amano H, Yoshida M, Furui S, Takeshita K. Diagnosis of pancreatic cancer. HPB. 2006;8:337-42.

[30] Schima W, Ba-Ssalamah A, Goetzinger P, Scharitzer M, Koelblinger C. State-of-the-art magnetic resonance imaging of pancreatic cancer. Topics in Magnetic Resonance Imaging. 2007;18:421-9.

[31] Heerkens HD, Hall W, Li X, Knechtges P, Dalah E, Paulson E, et al. Recommendations for MRI-based contouring of gross tumor volume and organs at risk for radiation therapy of pancreatic cancer. Practical Radiation Oncology. 2017;7:126-36.

[32] Oar A, Liney G, Rai R, Deshpande S, Pan L, Johnston M, et al. Comparison of four dimensional computed tomography and magnetic resonance imaging in abdominal radiotherapy planning. Physics and Imaging in Radiation Oncology. 2018;7:70-5.

[33] Heerkens HD, van Vulpen M, van den Berg CA, Tijssen RH, Crijns SP, Molenaar IQ, et al. MRI-based tumor motion characterization and gating schemes for radiation therapy of pancreatic cancer. Radiotherapy and Oncology. 2014;111:252-7.

[34] Dolde K, Dávid C, Echner G, Floca R, Hentschke C, Maier F, et al. 4DMRI-based analysis of inter—and intrafractional pancreas motion and deformation with different immobilization devices. Biomedical Physics & Engineering Express. 2019;5:025012.

[35] Alam S, Veeraraghavan H, Tringale K, Amoateng E, Subashi E, Wu AJ, et al. Inter-and intrafraction motion assessment and accumulated dose quantification of upper gastrointestinal organs during magnetic resonance-guided ablative radiation therapy of pancreas patients. Physics and Imaging in Radiation Oncology. 2022;21:54-61.

[36] Brandner ED, Chetty IJ, Giaddui TG, Xiao Y, Huq MS. Motion management strategies and technical issues associated with stereotactic body radiotherapy of thoracic and upper abdominal tumors: a review from NRG oncology. Medical Physics. 2017;44:2595-612.

[37] Campbell WG, Jones BL, Schefter T, Goodman KA, Miften M. An evaluation of motion mitigation techniques for pancreatic SBRT. Radiotherapy and Oncology. 2017;124:168-73.

[38] Arumugam S, Young T, Johnston M, Pavey D, Lee M. The delivered dose assessment in pancreas SBRT with the target position determined using an in-house position monitoring system. Frontiers in Oncology. 2022;12.

[39] Vinogradskiy Y, Goodman KA, Schefter T, Miften M, Jones BL. The clinical and dosimetric impact of real-time target tracking in pancreatic SBRT. International Journal of Radiation Oncology* Biology* Physics. 2019;103:268-75.

[40] Hsu S-H, Zawisza I, O'Grady K, Peng Q, Tomé WA. Towards abdominal MRI-based treatment planning using population-based Hounsfield units for bulk density assignment. Physics in Medicine & Biology. 2018;63:155003.

[41] Bredfeldt JS, Liu L, Feng M, Cao Y, Balter JM. Synthetic CT for MRI-based liver stereotactic body radiotherapy treatment planning. Physics in Medicine & Biology. 2017;62:2922.

[42] Liu Y, Lei Y, Wang T, Kayode O, Tian S, Liu T, et al. MRI-based treatment planning for liver stereotactic body radiotherapy: validation of a deep learning-based synthetic CT generation method. The British Journal of Radiology. 2019;92:20190067.

[43] Christiansen RL, Dysager L, Bertelsen AS, Hansen O, Brink C, Bernchou U. Accuracy of automatic deformable structure propagation for high-field MRI guided prostate radiotherapy. Radiation Oncology. 2020;15:1-11.

[44] McDonald BA, Vedam S, Yang J, Wang J, Castillo P, Lee B, et al. Initial feasibility and clinical implementation of daily mr-guided adaptive head and neck cancer radiation therapy on a 1.5T MR-linac system: Prospective r-ideal 2a/2b systematic clinical evaluation of technical innovation. International Journal of Radiation Oncology* Biology* Physics. 2021;109:1606-18.

[45] Mittauer KE, Hill PM, Bassetti MF, Bayouth JE. Validation of an MR-guided online adaptive radiotherapy (MRgoART) program: deformation accuracy in a heterogeneous, deformable, anthropomorphic phantom. Radiotherapy and Oncology. 2020;146:97-109.

[46] El-Bared N, Portelance L, Spieler BO, Kwon D, Padgett KR, Brown KM, et al. Dosimetric Benefits and Practical Pitfalls of Daily Online Adaptive MRI-Guided Stereotactic Radiation Therapy for Pancreatic Cancer. Practical Radiation Oncology. 2019;9:e46-e54.

[47] Tyagi N, Liang J, Burleson S, Subashi E, Scripes PG, Tringale KR, et al. Feasibility of ablative stereotactic body radiation therapy of pancreas cancer patients on a 1.5 Tesla magnetic resonance-linac system using abdominal compression. Physics and Imaging in Radiation Oncology. 2021;19:53-9.

9 Summary, Future Work and Final Conclusions

9.1 Summary and Significant Findings

As magnetic resonance imaging (MRI) utilization increases in radiotherapy for diagnosis, delineation, and image guidance for treatment, tools will be required for accurate treatment planning and to allow online adaptation of treatment plans to ensure patients receive the best possible treatment outcomes. The increased utilization of MRI-only treatment planning will enable MR-only radiotherapy, allowing MRI to be used consistently from diagnosis to simulation and for treatment guidance without the need to rely on computed tomography (CT) scanning. MRI has value for many anatomical regions due to the additional soft tissue contrast provided as well as potential biological and physiological information, with a variety of anatomical treatment sites investigated throughout this work. This thesis presents investigations of various tools and methods for MRI-only treatment planning, considering their utilization, validation, and potential application to different anatomical regions.

Chapter 3 investigated the impact of electron density assignment for synthetic CT (sCT) generation on MRI-only treatment planning calculations. This was evaluated on dose calculation and optimization accuracy for volumetric arc therapy (VMAT) plans for nasopharynx head and neck patients. Optimisation error is difficult to assess, as it would not result in incorrect doses, but rather a sub-optimal treatment plan, in terms of balance between target coverage and organ-at-risk doses. This work concluded that electron density correction using a bulk density approach in this anatomical site achieved dose uncertainties within 3%, and that the incorrect application of bulk density correction could potentially result in optimisation errors larger than dose calculation errors. Additionally, it was concluded that bulk density assignment was not appropriate for this treatment site and more advanced approaches should be considered for improved accuracy in dose calculations and to reduce potential optimisation errors. This work was published in the Australasian Physical and Engineering Sciences in Medicine Journal in 2018.

Chapter 4 presents the clinical validation of a deep learning sCT generation model for head and neck cancer patients. This work was carried out in conjunction with a commercial software partner. This work included comparison to a deformed CT in addition to the gold standard CT, assessing both anatomical accuracy as well as dosimetric accuracy of the sCTs generated. As the MRI dataset used for sCT generation for these patients did not encompass the entire patient outline, for a “like-for-like” comparison of the CT to MRI/sCT, cropping and deformation of the CT to match the MRI was attempted. Both with and without cropping were considered when considering the appropriateness of the deep learning methodology investigated. It was concluded that though the U-Net framework considered produced acceptable results for head and neck sCT datasets within the current limitations of the approach, further work is required on the framework to improve these results to be in line with

current literature. A publication is under preparation on this work, with this work establishing the collaboration with the commercial partner, which will continue through validation of the software as it is further developed to ensure it becomes more clinically applicable.

Chapter 5 explored various methods and aspects of lung sCT generation from a single MRI sequence, assessing the suitability of the SpiralVIBE sequence for sCT generation of MRI-only treatment planning for lung. SpiralVIBE has advantages for lung imaging as it produces 3D ultrashort echo time (UTE) images under free breathing, with UTE improving the quality of lung imaging due to the short T2 and T2* values in lung. A bulk density approach, an atlas approach and a hybrid method utilizing a Gaussian Mixture Model (GMM) were attempted for lung sCT generation from a single SpiralVIBE MRI sequence. It was concluded that the SpiralVIBE sequence used was not ideal for sCT generation due to this sequence triggering on a specific phase of the breathing cycle, and that none of the methods investigated produced sCT datasets suitable for clinical use. Further work is required in this treatment site for accurate and clinically acceptable sCT generation, such as utilisation of a 4D MRI sequence to allow better correlation with the average CT scans often used for treatment planning in lung. This work was presented at EPSM 2018, Engineering and Physical Sciences in Medicine, in Adelaide,

Chapter 6 investigated the possible time reduction of a MRI sequence for sCT generation in prostate radiotherapy, to enable reduction of potential patient and organ motion effects during the scan and to improve the patient experience, but still have adequate image quality for sCT generation for MRI-only treatment planning. The original standard sequence had a number of parameters adjusted to reduce the overall sequence time, and was tested on 10 volunteers. This study demonstrated that the MR imaging sequence time was able to be reduced by approximately 80%, with the sCT generated with this time reduced MRI sequence producing similar dosimetric results to those obtained with the sCT generated with the original standard sequence. This work was published in 2021 with the title “Effects of MR Imaging time reduction on substitute CT generation for prostate MRI-only treatment planning” and was awarded the 2022 Kenneth Clarke award for the best paper of the year on original work published in the (Australasian) Physical and Engineering Sciences in Medicine authored by a member of the Australasian College of Physical Scientists and Engineers in Medicine (ACPSEM). Chapter 7 followed up on this volunteer study with a real-world clinical validation, comparing the results of the most suitable time-reduced sequence from the volunteer study within a 10 patient cohort who were receiving radiotherapy as part of an MR-only clinical trial. This follow up study showed that the fast MRI sequence produced an sCT with similar anatomical and clinical dosimetric results compared to the sCT produced with the standard MRI sequence, demonstrating its potential in a clinical patient cohort for treatment planning. This work has been submitted to the Physical and Engineering Sciences in Medicine Journal, with a current revised manuscript under review and is being considered for implementation into clinical practice.

Chapter 8 investigated the variability of target and OAR volumes for different adaptive treatment regimens for pancreatic cancer, as part of an evaluation of the feasibility of utilizing daily MRI scans for daily adaptive planning for this difficult treatment site. A secondary aim was to investigate the differences in dose accumulation techniques available utilizing MRI-only treatment planning. This work assessed the suitability of using a treatment day MRI for treatment planning purposes, in addition to conventional treatment planning utilizing a single reference scan from the first imaging session on the first day (D1S1). Initially, it was considered that daily replanning may be sufficient to account for intra-fraction motion for pancreas cancer patients receiving hypofractionated SBRT treatment on a conventional linear accelerator, utilizing daily MRI simulator images for treatment planning. Due to the nature of the anatomy, and being a comparison of treatment plans to either a D1S1 reference plan, or a daily treatment plan, bulk density correction was considered sufficient for planning on the MRI datasets. Large variations were found in both target and OAR anatomies between mock treatment fractions and imaging sessions, with the doses considered in both the conventional treatment planning methods and a daily replan found to not be able to be delivered accurately. Doses were accumulated utilizing both a rigid methodology and a deformable method, with large variations in accumulated dose seen for both methods. This study concluded that daily online adaptive radiotherapy is required for accurate dose delivery for pancreas cancer, particularly in the absence of motion management or tumour tracking techniques. This work will contribute to the potential clinical translation of daily MRI for pancreas SBRT patients within the department, and a draft manuscript has been prepared for this work.

The work presented, taken as a whole, demonstrates the potential for MRI to move forward from its current complementary role to a primary role throughout the radiotherapy process, from simulation to treatment planning and to treatment guidance. In regards to MRI-only treatment planning, different sCT generation methods such as bulk density, multi-atlas, hybrid and deep learning approaches have been investigated and clinically validated for various anatomical treatment sites, including head and neck, lung, prostate and abdomen. For simple anatomy such as the abdomen, the bulk density approach may be suitable, whilst for more rigid anatomy such as the prostate, a multi-atlas approach has yielded clinically acceptable results. Deep learning approaches may be the best approach for more complex anatomy such as head and neck or lung, especially as these approaches continue to become more sophisticated and computing power continues to increase over time [1-3]. Considering the currently available sCT generation methods and the current training techniques for these methods, in addition to the different contrasts captured within MRI for different anatomy, it is difficult to find or predict a potential single overarching solution for sCT generation which will be suitable for all anatomy or generalizable for all MRI sequences. Very few studies have utilised the same sCT generation methodology for multiple anatomical treatment sites across the entire body, with the few that do generally utilizing a bulk density approach [4, 5], potentially as this is the most generalizable approach requiring only accurate segmentation. There are however MRI sequences and sCT generation methods

which in combination provide clinically acceptable dosimetric results when compared to CT for specific anatomical treatment sites [6, 7], especially after training the sCT generation method using the MRI sequence of choice for that particular anatomy. This is the approach utilised by current commercial sCT generation software [8-10], and potential standardisation of MRI sequences required for sCT generation for specific anatomical sites is likely to continue.

For MRI-only simulation, the effects of reducing imaging time for an MRI sequence required for sCT generation has been investigated in a volunteer cohort, and clinically validated within a patient cohort. The clinical validation of this time-reduced MRI sequence for sCT generation provides a potential framework for future studies which investigate improvements in either sCT generation or MRI sequence time for MRI-only treatment planning, as these may not necessarily include a gold standard CT image, but rather a baseline or standard MRI/sCT image. This will naturally progress as MRI-only treatment planning becomes accepted within the clinic and further incremental improvements are sought in the process. Though few studies investigate time reduction of MRI sequences specific for sCT generation, a study from Johansson et al. [11] investigated simulating time-reduced MR images for sCT generation in the brain, reconstructing the original MRI sequence images with reduced k-space spokes to simulate parallel imaging acceleration. These simulated time-reduced MR images produced sCT without any adverse effects on quality, though a hybrid bulk density approach was used for sCT generation.

In regards to treatment guidance, the need for MRI guidance in an adaptive radiotherapy setting is shown for the pancreas. The anatomical variations observed in the volunteer study presented in chapter 8 far outweigh the potential uncertainty in dose calculation using a bulk density approach, demonstrating the need for MRI guidance in treating this anatomical site. The use of MRI guidance for treatment, in addition to the ability to complete the dose accumulation directly on the MRI data through MRI-only treatment planning provides an ideal solution for difficult anatomical treatment sites which may suffer from large amounts of inter- and intra-fraction motion. Hunt et al. [12] and Farjam et al. [13] investigated deep learning based sCT generation using images from MRIg-linacs, with both studies demonstrating the possibility of making use of the daily MRI guidance images for MRI-only treatment planning purposes.

MRI-only treatment planning is necessary for a true MRI guided adaptive radiotherapy workflow. Additional improvements from faster MRI scan times, more sophisticated and accurate sCT generation, and seamless adaptive radiotherapy planning workflows will accelerate the implementation of MRI guidance in radiotherapy. As MRI-only treatment planning becomes clinically implemented for additional treatment sites, the benefits of MRI guidance and MRI-only adaptive radiotherapy will far outweigh the uncertainty from sCT generation.

9.2 Future Work

The accuracy required for MR-only treatment planning to be suitable as a replacement for CT based treatment planning has not been fully determined, and as such all techniques are benchmarked against the corresponding gold standard CT scan.

From chapters 3 and 4, further investigation is required for an appropriate deep learning architecture for this site considering the complexity of the head and neck anatomy. This may be an alternate deep learning methodology, such as a GAN architecture with additional steps or layers appropriate for the complexity of the head and neck anatomy, or further work on the model considered in the chapter such as potentially utilizing an alternate loss function which may produce improved results, or utilizing more appropriate training data. Additionally, an accurate, artefact-free large field of view (LFOV) MRI sequence, or a more appropriate method to expand a limited FOV dataset, is required for improved results in the head and neck treatment site. Dental implants and potential artefacts, and how an sCT generation method would manage these, should also be considered, as these impact on treatment planning and were not considered in this work. Further work will also continue in collaboration with the commercial software partner with a clinical trial planned for capture of appropriate LFOV training data and further clinical validation of the technique for head and neck cancer treatment as their software develops.

Further work from chapter 5 would consider investigation into an appropriate MRI sequence for lung imaging which may be used for accurate sCT generation. The most appropriate sCT generation method was also not found within the methods investigated within this chapter, and with new methods available (i.e. deep learning methods not considered at the time of this work) improved results may be obtained. The addition of 4D MRI scans may also be appropriate for sCT generation, with an average scan potentially able to be used, providing the best anatomy for treatment planning purposes. This would also match the use of the average CT scan generated from 4D CT commonly used for radiotherapy treatment planning in lung cancer.

The work from chapters 6 and 7 relate to a time-reduced MRI sequence for sCT generation for prostate cancer radiotherapy treatment planning. Additional validation of this sequence for sCT generation against true CT would be useful to ensure accurate agreement of the sCT against the gold standard imaging for treatment planning, as these studies were compared to a gold standard sCT. Further testing could include investigations into treatment planning optimisation uncertainty due to the variations in generated sCT. It should also be considered that as MRI-only treatment planning matures, validation against existing sCT techniques may become necessary in the absence of true CT being captured, so further work into potential techniques and analysis for this should be considered. This may become even more relevant as MRI sequences are improved or reduced in time, with the potential effects on the corresponding sCT generated needing to be assessed against a standard CT or sCT for suitability.

Additional MRI sequence and reconstruction techniques such as compressed sensing [14, 15], simultaneous multi-slice imaging [16] and artificial intelligence (AI) based reconstruction methods [17, 18] are now becoming commercially available which reduce MRI sequence acquisition time with no reduction in image quality – these may also be appropriate for sCT generation and should be investigated for the potential for clinical validation.

From chapter 8, further work could involve this mock study being repeated on a patient cohort for feasibility. If this volunteer study was expanded, the use of additional motion management in addition to stricter imaging conditions for these volunteers or patients could be implemented to assist in considering if these methods are appropriate for daily imaging and replan (particularly in the absence of an MRIg-linac). For patients receiving treatment with a conventional linac in a centre with an MRI-simulator, it may be possible for that patient to receive an MRI on the treatment day immediately prior to their radiotherapy treatment appointment, which may be correlated with the setup images. This may help improve dose delivery whilst reducing dose to nearby OARs for this treatment site, but further work should be undertaken in regards to the feasibility of this, with additional tools required for fast segmentation and potential plan adaptation in this scenario. In regards to the deformable dose accumulation method considered, an assessment of the accuracy of the DIR algorithm used for dose accumulation should also be undertaken.

From the work presented in this thesis as a whole, further future work would be related to the application of sCT methods to different clinical sites. At the current moment there is no single MRI sequence or sCT generation method which has been successful for all anatomical treatment sites, though deep learning approaches show promise. Therefore determination of which MRI sequences and sCT generation methodologies which would be appropriate for particular anatomical sites, especially as different anatomies provide their own unique challenges, should be considered. As sCT generation methodologies develop further or are improved over time, appropriate recommendations on consistent quality assurance (QA) of these new methods and workflows will need to be developed, and initial and regular QA undertaken to ensure appropriateness. Such QA processes will need to be systematic and standardised where possible to allow translation of these processes for different anatomical treatment sites. Additionally, currently QA procedures utilised clinically are complex, cumbersome and time consuming, as treatment planning systems may not provide the necessary tools to complete these procedures in an efficient manner. As MRI-only treatment planning becomes more common, these workloads will no doubt be reduced as new tools may become available, and existing QA procedures are streamlined. The standardisation, development and validation of these methodologies and workflows would accelerate the application of MRI-only treatment planning to different anatomical treatment sites.

A common theme for all chapters in regards to potential future work is related to the development of MRI sequences, and the increased value of MRI, particularly in the radiotherapy process [19, 20]. As MRI sequences develop, with new techniques becoming available which provide improved image resolution and contrast, reduced potential for artefacts and distortions, and reducing imaging time, these sequences may be appropriate for sCT generation for MRI-only treatment planning. This sequence development will occur for both MRI simulators and on MRIg-linacs, and would require clinical validation for both the application of MRI-only treatment planning, and MRI-only adaptive radiotherapy.

9.3 Final Conclusions

The work presented in this thesis adds new knowledge and contributes to the MRI-only radiotherapy body of research, in particular MRI-only treatment planning, covering a variety of anatomical treatment sites and investigating various sCT generation methods and validation of these sCT datasets. All aspects of this work relate to the development and utilization of MRI-only treatment planning in radiotherapy, considering both the effects on treatment plans and adaptive radiotherapy.

MRI-only radiotherapy shows great potential for improving outcomes for cancer treatment. MRI provides the additional soft tissue contrast which is lacking for CT scans, and coupled with MRI-only treatment planning tools which are in development, will provide a means for accurate adaptive radiotherapy to be carried out, especially in conjunction with hybrid MRIg-linacs. The future of hybrid MRIg-linacs will employ MRI-only tools to allow real time adaptive radiotherapy, holding the promise of better treatment delivery in the balance of dose to targets and OARs and hence better patient outcomes, including making safe treatment feasible for some sites where it previously wasn’t possible.

9.4 References

[1] Bahrami A, Karimian A, Arabi H. Comparison of different deep learning architectures for synthetic CT generation from MR images. Physica Medica. 2021;90:99-107.

[2] Boulanger M, Nunes J-C, Chourak H, Largent A, Tahri S, Acosta O, et al. Deep learning methods to generate synthetic CT from MRI in radiotherapy: A literature review. Physica Medica. 2021;89:265-81.

[3] Spadea MF, Maspero M, Zaffino P, Seco J. Deep learning based synthetic-CT generation in radiotherapy and PET: A review. Medical Physics. 2021;48:6537-66.

[4] Jonsson JH, Karlsson MG, Karlsson M, Nyholm T. Treatment planning using MRI data: an analysis of the dose calculation accuracy for different treatment regions. Radiation Oncology. 2010;5:62-.

[5] Korsholm M, Waring L, Edmund J. A criterion for the reliable use of MRI-only radiotherapy. Radiation Oncology. 2014;9:16.

[6] Edmund JM, Nyholm T. A review of substitute CT generation for MRI-only radiation therapy. Radiation Oncology. 2017;12:28.

[7] Johnstone E, Wyatt JJ, Henry AM, Short SC, Sebag-Montefiore D, Murray L, et al. Systematic Review of Synthetic Computed Tomography Generation Methodologies for Use in Magnetic Resonance Imaging–Only Radiation Therapy. International Journal of Radiation Oncology• Biology• Physics. 2018;100:199-217.

[8] Tyagi N, Fontenla S, Zhang J, Cloutier M, Kadbi M, Mechalakos J, et al. Dosimetric and workflow evaluation of first commercial synthetic CT software for clinical use in pelvis. Physics in Medicine & Biology. 2017;62:2961.

[9] Persson E, Jamtheim Gustafsson C, Ambolt P, Engelholm S, Ceberg S, Bäck S, et al. MR-PROTECT: clinical feasibility of a prostate MRI-only radiotherapy treatment workflow and investigation of acceptance criteria. Radiation Oncology. 2020;15:1-13.

[10] GmbH SH. MR-only RT planning for brain and pelvis with Synthetic CT White paper. Siemens Healthcare GmbH.

[11] Johansson A, Garpebring A, Asklund T, Nyholm T. CT substitutes derived from MR images reconstructed with parallel imaging. Medical Physics. 2014;41:082302.

[12] Hunt B, Zaki B, Russo G, Gill G, Asher G, Prioleau T, et al. Deep Learning-Based Synthetic CT Generation for MR-Only Adaptive Radiation Therapy on MR-Linacs. International Journal of Radiation Oncology, Biology, Physics. 2022;114:e584.

[13] Farjam R, Nagar H, Kathy Zhou X, Ouellette D, Chiara Formenti S, DeWyngaert JK. Deep learning-based synthetic CT generation for MR-only radiotherapy of prostate cancer patients with 0.35T MRI linear accelerator. Journal of Applied Clinical Medical Physics. 2021;22:93-104.

[14] Hollingsworth KG. Reducing acquisition time in clinical MRI by data undersampling and compressed sensing reconstruction. Physics in Medicine and Biology. 2015;60:R297-R322.

[15] Lustig M, Donoho D, Pauly JM. Sparse MRI: The application of compressed sensing for rapid MR imaging. Magnetic Resonance in Medicine: An Official Journal of the International Society for Magnetic Resonance in Medicine. 2007;58:1182-95.

[16] Barth M, Breuer F, Koopmans PJ, Norris DG, Poser BA. Simultaneous multislice (SMS) imaging techniques. Magnetic Resonance in Medicine. 2016;75:63-81.

[17] Behl N. Deep resolve—mobilizing the power of networks. MAGNETOM Flash (78). 2021;1:29-35.

[18] Hammernik K, Klatzer T, Kobler E, Recht MP, Sodickson DK, Pock T, et al. Learning a variational network for reconstruction of accelerated MRI data. Magnetic Resonance in Medicine. 2018;79:3055-71.

[19] van Beek EJ, Kuhl C, Anzai Y, Desmond P, Ehman RL, Gong Q, et al. Value of MRI in medicine: more than just another test? Journal of Magnetic Resonance Imaging. 2019;49:e14-e25.

[20] Glide-Hurst CK, Paulson ES, McGee K, Tyagi N, Hu Y, Balter J, et al. Task group 284 report: magnetic resonance imaging simulation in radiotherapy: considerations for clinical implementation, optimization, and quality assurance. Medical Physics. 2021;48:e636-e70.

10 Appendices

10.1 Appendix 1

10.1.1 EPSM 2016 Accepted Abstract

Assessment of Electron Density Effects for MRI Only Treatment Planning

Tony Young

Liverpool and Macarthur Cancer Therapy Centres and Ingham Institute, Sydney, Australia.

Institute of Medical Physics, School of Physics, University of Sydney, Sydney, Australia

Tony.Young@sswahs.nsw.gov.au (Presenting author)

David Thwaites

Institute of Medical Physics, School of Physics, University of Sydney, Sydney, Australia.

david.thwaites@sydney.edu.au

Lois Holloway

Liverpool and Macarthur Cancer Therapy Centres and Ingham Institute, Sydney, Australia.

University of New South Wales, Sydney, New South Wales, Australia

Institute of Medical Physics, School of Physics, University of Sydney, Australia.

Centre for Medical Radiation Physics, University of Wollongong, Wollongong,

New South Wales, Australia

lois.holloway@sswahs.nsw.gov.au

Introduction

The gold standard for radiotherapy simulation and treatment planning is Computed Tomography (CT) due to spatial accuracy, bony anatomy definition and electron density information for dose calculations. Initial use of MRI in radiotherapy was to improve visualisation of anatomy for accurate target definition and contouring, via fusion of the MRI scan with the CT scan. This introduces registration error and potential errors from variations in patient setup and internal organ motion [1]

MRI only treatment planning would remove current registration errors, approximately 2mm [2, 3], reduce patient discomfort and lower the workload and financial cost of additional scans.
MRI however lacks electron density information required for dose calculations. This may be overcome by applying manually segmented bulk density corrections for tissue, bone, lung and air, with results reported to be within approximately 2% compared to the same plan applied on a CT dataset [2, 4]. Further work includes an atlas based electron density mapping method to automatically segment and apply the appropriate bulk density correction, with some success reported for prostate cases [5]

Method

10 retrospective H&N patients had clinically acceptable VMAT plans created. These plans were recalculated on the data sets with no density correction (water equivalent) and with a bulk density correction for bone/air/tissue applied. Plans were also reoptimised on these two data sets, and recalculated. These plans were compared for dose calculation and optimization error through point dose comparison, DVH analysis and gamma analysis of dose.

Results

Bulk density corrections for bone and air provide dose calculations generally within expected uncertainties (2%) of the original treatment plans with appropriate corrections.

Conclusion

The bulk density approach to electron density correction achieves uncertainties within expected dose uncertainties, however more advanced approaches such as a direct conversion approach may improve accuracy, particularly at interface regions, and should be considered.

References/ Acknowledgements as applicable

1. Nyholm T, Jonsson J. Counterpoint: Opportunities and Challenges of a Magnetic Resonance Imaging–Only Radiotherapy Work Flow. Seminars in Radiation Oncology. 2014;24(3):175-80.

2. Karlsson M, Karlsson MG, Nyholm T, Amies C, Zackrisson B. Dedicated Magnetic Resonance Imaging in the Radiotherapy Clinic. International Journal of Radiation Oncology*Biology*Physics. 2009;74(2):644-51.

3. Roberson PL, McLaughlin PW, Narayana V, Troyer S, Hixson GV, Kessler ML. Use and uncertainties of mutual information for computed tomography/magnetic resonance (CT/MR) registration post permanent implant of the prostate. Medical Physics. 2005;32(2):473-82.

4. Lambert J, Greer PB, Menk F, Patterson J, Parker J, Dahl K, et al. MRI-guided prostate radiation therapy planning: Investigation of dosimetric accuracy of MRI-based dose planning. Radiotherapy and Oncology. 2011;98(3):330-4.

5. Dowling JA, Lambert J, Parker J, Salvado O, Fripp J, Capp A, et al. An Atlas-Based Electron Density Mapping Method for Magnetic Resonance Imaging (MRI)-Alone Treatment Planning and Adaptive MRI-Based Prostate Radiation Therapy. International Journal of Radiation Oncology*Biology*Physics. 2012;83(1):e5-e11.

10.2 Appendix 2

10.2.1 AAPM 2022 Accepted Abstract

Deep Learning for MRI-generated Synthetic CT: Dosimetric Evaluation for RT Planning in Head and Neck Cancers

JT Antunes[1]*, D Pittock[1], P Jacobs[1], AS Nelson[1], J Piper[1], T Young[2,3], S Deshpande[3,4]

(1) MIM Software Inc, Cleveland, OH, (2) Institute of Medical Physics, School of Physics, University of Sydney, Australia, (3) Liverpool And Macarthur Hospital, Liverpool, Australia, (4) South Western Sydney Clinical School, University of New South Wales, Sydney, Australia

JA, DP, PJ, AN, and JP are all employees of MIM Software Inc and were reimbursed for travel expenses.

Purpose: Modern radiation therapy (RT) utilizes both computed tomography (CT) and magnetic resonance imaging (MRI) for treatment planning purposes– CT providing electron density values and MRI providing superior soft-tissue contrast. MR-only guided RT would simplify the clinical workflow and reduce patient burden, but requires methods to derive electron density information from MR images. We present in this work a deep learning-based synthetic CT (sCT) generation framework using a single pre-contrast T1 MRI sequence, and evaluate the dose calculation accuracy in the context of head and neck cancers.

Methods: For 54 patients treated for head and neck cancer, a planning CT (pCT) was acquired the same day as a T1 Dixon MRI scan using the same patient positioning and immobilization. 46 registered MR-CT pairs were used to train a Unet-based convolutional neural network (CNN) to generate sCTs for dose calculation. The CNN included residual blocks and skip connections that transfer high resolution features. The network was trained iteratively to improve the quality of the sCT generated by reducing pixel-wise error with the pCT. The model was validated on 8 unseen MR-CT pairs, with the clinical pCT treatment plan recalculated on the sCT and compared using gamma analysis and dose volume histogram (DVH) comparison.

Results: Our CNN achieved a pixel-wise difference of 78.2±32.5 HU between pCTs and sCTs. DVHs calculated on sCTs were comparable (0.0±1.2 Gy difference) to those calculated on pCTs (Table 1), along with 3D Gamma Index pass rates (96.4-99.5%). Figure 1 displays qualitative comparisons of the sCT and pCT for one test subject, and the corresponding isodose maps and DVH plots.

Conclusion: The comparable calculated dose demonstrates the efficacy of sCT images in treatment planning. Adopting the proposed method offers the potential to eliminate unnecessary pCT scans and may enable MR-only guided RT.

Table 1: Differences in dose calculations using Monte Carlo simulation on both the planning CT and synthetic CT showing minimal differences in DVH metrics; the 3D gamma index pass rates (3%/3mm criterion) between these calculated doses were extremely high.

Contour	PTV High			PTV Med			PTV Low			Brain	Brain -stem	Chiasm	Mandible	Optic Nerve L	Optic Nerve R	Parotid L	Parotid R	Retina L	Retina R	Spinal Cord	3D Gamma Index
Dose Metrics	$\Delta_{D98\%}$ (Gy)	$\Delta_{D50\%}$ (Gy)	$\Delta_{D2\%}$ (Gy)	$\Delta_{D98\%}$ (Gy)	$\Delta_{D50\%}$ (Gy)	$\Delta_{D2\%}$ (Gy)	$\Delta_{D98\%}$ (Gy)	$\Delta_{D50\%}$ (Gy)	$\Delta_{D2\%}$ (Gy)	$\Delta_{D1\%}$ (Gy)	Δ_{D1cc} (Gy)	Δ_{Max} (Gy)	$\Delta_{D1\%}$ (Gy)	Δ_{Max} (Gy)	Δ_{Max} (Gy)	Δ_{Mean} (Gy)	Δ_{Mean} (Gy)	$\Delta_{D1\%}$ (Gy)	$\Delta_{D1\%}$ (Gy)	Δ_{D1cc} (Gy)	Global Gamma Pass Rate (%)
Test Patient 1	-0.5	0.0	0.2	-0.9	0.0	0.1	-1.9	0.2	0.2	0.0	0.1	-0.4	0.1	-0.5	0.3	-0.2	0.1	0.1	-0.1	0.0	98.3
Test Patient 2	-2.6	0.3	0.9	0.2	0.7	0.9	-1.2	-0.1	0.6	0.0	0.4	-0.4	-0.3	2.2	0.3	0.0	0.3	0.2	0.0	-0.1	99.5
Test Patient 3	0.3	0.4	0.5	-0.5	0.1	0.4	-1.3	0.0	0.4	0.0	0.0	0.3	0.1	-0.1	0.0	0.0	0.1	-0.1	-0.1	0.2	96.4
Test Patient 4	-7.6	0.0	0.1	-5.6	-0.1	0.1	-1.6	-0.2	0.1	0.0	-0.4	0.0	-0.4	-0.1	0.0	-0.1	0.3	0.0	0.0	0.2	99.1
Test Patient 5	0.0	0.0	-0.1	0.0	0.1	0.1	0.1	0.2	0.0	-0.1	-0.1	1.2	-0.4	0.4	-0.1	0.2	0.0	0.0	-0.1	-0.1	99.2
Test Patient 6	3.7	0.0	-0.2	6.5	0.9	-0.2	5.5	-0.1	-0.1	0.1	0.1	0.0	-0.7	-1.0	0.7	-0.1	-0.2	0.4	-0.1	0.3	98.3
Test Patient 7	-0.2	0.0	-0.2	-2.0	0.0	-0.2	-1.7	0.0	-0.1	1.4	0.1	-0.1	0.1	0.0	0.0	-0.1	0.0	--	--	0.0	97.0
Test Patient 8	1.3	0.0	0.0	0.4	0.0	0.0	0.0	0.0	0.0	0.0	0.0	0.0	0.0	--	--	0.0	0.1	--	--	0.0	97.1
Abs. Avg.	**2.4**	**0.1**	**0.1**	**2.3**	**0.3**	**0.3**	**1.9**	**0.1**	**0.2**	**0.1**	**0.2**	**0.4**	**0.3**	**0.7**	**0.3**	**0.1**	**0.2**	**0.1**	**0.1**	**0.1**	**98.5**

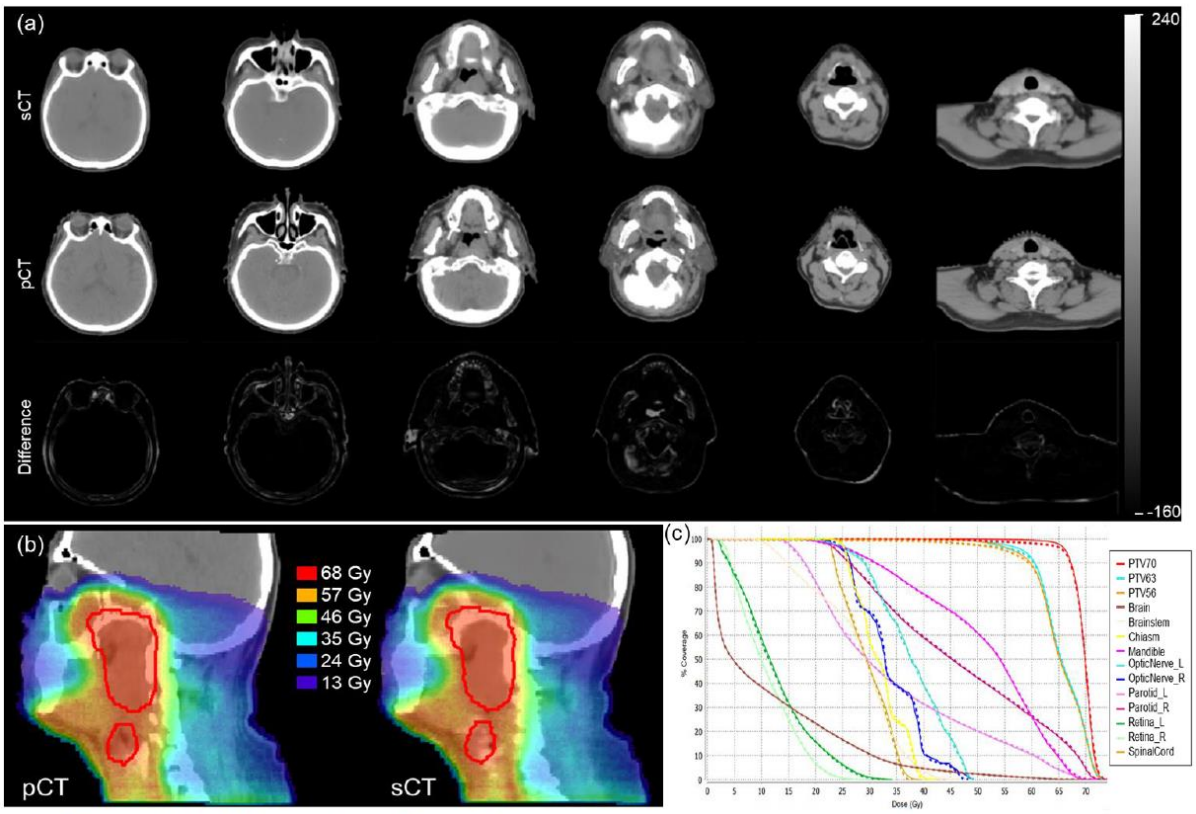

Figure 1: (a) Different slices of the sCT generated appear anatomically similar to the corresponding slices on the pCT, with difference maps showing minor differences at boundaries of the image and tissue transitions for one test patient. (b) Isodose maps for both the pCT and sCT based on calculated doses overlaid with the PTV70 contour (red). (c) Corresponding DVHs for different PTVs and OARs for that same test patient, showing similar trends.

10.2.2 ASTRO 2022 Accepted Abstract

Title: Assessing Multiple MRI sequences in Deep Learning-Based Synthetic CT Generation for MR Only-Guided Radiation Therapy of Head and Neck Cancers

Authors: Jacob T. Antunes, PhD[1], Dane Pittock[1], Paul Jacobs[1], Jon Piper[1], Tony Young[2,3], Shrikant Deshpande, PhD[3,4].

[1]MIM Software Inc, Beachwood, OH, United States

[2]Institute of Medical Physics, School of Physics, University of Sydney, Sydney, Australia

[3]Liverpool and Macarthur Hospital, Liverpool, Australia

[4]South Western Sydney Clinical School, University of New South Wales, Sydney Australia

Purpose/Objective(s):

MRI is often utilized in radiation therapy (RT) planning for contouring due to its superior soft-tissue contrast. However, a planning CT is still required to provide electron density information for dose calculation. Reducing the need for multiple modalities for quality RT planning would improve clinical workflow and reduce patient burden. Synthetic CT generation based on MRI is a promising solution, but it is not yet known which set of MR sequences generates the most accurate synthetic CT. In this work, we assessed 14 combinations of MR sequences as inputs to a deep learning-based synthetic CT generator in the context of MR-guided treatment planning for head and neck cancers.

Materials/Methods:

26 patients who underwent RT for head and neck cancer were retrospectively identified and included in this study based on availability of 3 pretreatment MR Dixon sequences (T1pre-contrast, T1post-contrast, T2) and a planning CT. Each Dixon sequence generated an in-, opposed-, fat-only-, and water-only-phase image, yielding 12 MR images per patient. MR and planning CT images were acquired on the same day, with patients scanned in the same treatment position and immobilization. CT images were registered to a primary MR sequence, masked to eliminate background elements, and clipped to a fixed intensity range. Our synthetic CT generator comprised a 2D autoencoder with skip connections, designed for a variable subset of MR inputs. For each combination of MR sequences, the deep learning model was trained using 21 patients and validated on 5 patients. Dose was computed on both the planning and synthetic CT via Monte Carlo simulation using the clinical RT plan. Performance was

measured in terms of mean absolute error (MAE) as well as 3D global gamma (3% / 3mm) between the planning and synthetic CT and their respective doses.

Results:

MR sequences yielded average MAE ranges from 78.9 - 86.5 HU. More MR sequences only moderately correlated with lower MAE (R^2 = 0.613, p > 0.05). T2 was the lowest performing sequence. No differences were observed between synthetic CTs generated using T1pre- and T1post-contrast sequences. All combinations of MR inputs yielded synthetic CTs with dose plans yielding extremely high average gamma indexes (99.5 - 99.8%).

Conclusion:

No significant differences were found amongst individual MR sequences; the acquisition of more MR sequences for synthetic CT generation did not yield additional improvement in terms of clinical efficacy. Using our proposed method offers the potential for clinically viable MR-guided RT without having to acquire additional sequences for synthetic CT generation.

MR Sequences	nSeq	Avg MAE (HU)	Avg Gamma Index (%)
$T1pre_{all}$ + $T1post_{all}$ + $T2_{all}$	12	78.9	99.8
$T1pre_{all}$ + $T1post_{all}$	8	80.4	99.5
$T1pre_{all}$ + $T2_{all}$	8	81.4	99.7
$T1pre_{in}$ + $T1post_{in}$ + $T2_{in}$	3	81.9	99.7
$T1post_{all}$ + $T2_{all}$	8	82.0	99.6
$T1pre_{in}$ + $T1post_{in}$	2	82.5	99.7
$T1pre_{all}$	4	82.5	99.7

$T1post_{all}$	4	82.9	99.6
$T1pre_{in}$ + $T2_{in}$	2	83.1	99.5
$T1post_{in}$	1	83.8	99.6
$T1pre_{in}$	1	84.0	99.5
$T1post_{in}$ + $T2_{in}$	2	84.4	99.5
$T2_{all}$	4	85.1	99.8
$T2_{in}$	1	86.5	99.8

10.2.3 EPSM 2022 Accepted Abstract

Comparison of synthetic CTs derived from 2D versus 3D convolutional neural networks via Head and Neck MRIs for RT planning

JT Antunes

MIM Software Inc, Cleveland, OH

jantunes@mimsoftware.com (presenting author)

D Pittock

MIM Software Inc, Cleveland, OH

dpittock@mimsoftware.com

P Jacobs

MIM Software Inc, Cleveland, OH

pjacobs@mimsoftware.com

K Chatterjee

MIM Software Inc, Cleveland, OH

kchatterjee@mimsoftware.com

AS Nelson

MIM Software Inc, Cleveland, OH

anelson@mimsoftware.com

J Piper

MIM Software Inc, Cleveland, OH

jpiper@mimsoftware.com

T Young

Institute of Medical Physics, School of Physics, University of Sydney, NSW, Australia

South Western Sydney Cancer Services, NSW Health, Sydney, NSW, Australia

Ingham Institute, Sydney, NSW, Australia

tony.young@health.nsw.gov.au

S Deshpande

South Western Sydney Cancer Services, NSW Health, Sydney, NSW, Australia

Ingham Institute, Sydney, NSW, Australia

shrikant.deshpande@health.nsw.gov.au

Introduction: MR-only guided Radiation Therapy (RT) requires electron density information, usually acquired from a planning CT (pCT). Several works propose utilizing deep-learning to generate synthetic CT (sCT) from MR. However, most have focused on 2D implementations. We present in this work the efficacy of a 3D-convolutional neural network (CNN) for sCT generation from MR for head and neck cancers and compare its output to its 2D-CNN implementation.

Methods: 54 head and neck cancer patients who were scanned simultaneously with Dixon-MR sequences and pCT using fixed immobilization were included. A UNet-based CNN was constructed with residual blocks. 2D and 3D implementations were trained on 46 patients to generate sCT from Dixon-MR phases, iteratively reducing pixel-wise error between the sCT and pCT. For 3D experiments, varying patch sizes were assessed. Dose was calculated on the sCTs and pCTs using a Monte-Carlo algorithm. Performance was evaluated on 8 patients using mean absolute error (MAE), global gamma analysis (3%/3mm), and qualitative assessment.

Results: All 3D-CNN experiments yielded similar or better MAE compared to 2D-CNN (Table 1). Noticeable improvement in bone reconstruction was observed with 3D-CNN outputs compared to 2D-CNN, primarily in sagittal and coronal planes (Figure 1). A 3D patch of 96 row-pixels yielded

significantly lower MAE than 2D-CNN (73.4±6.5 HU versus 79.5±8.4, $p<0.05$). Minimal differences were measured in terms of Gamma pass rate (99.5±0.4% versus 99.4±0.7%, $p\geq0.05$).

Conclusion: Generating sCTs for MR-only guided RT planning may benefit from 3D-CNNs over 2D-CNNs due to lower MAE, better bone reconstruction and limited impact on calculated dose.

Table 1: Quantitative comparison of sCTs derived from 2D- versus 3D-CNN.

Experiment	**Patch (row-pixels)**	**MAE (HU)**	**Global Gamma Pass Rate (%)**
2D-CNN	256	79.5±8.4	99.4±0.7
3D-CNN	32	81.7±6.4	98.7±0.9
	64	74.5±5.6	99.0±0.9
	96	**73.4±6.5***	**99.5±0.4**
	128	73.6±6.1	99.4±0.4

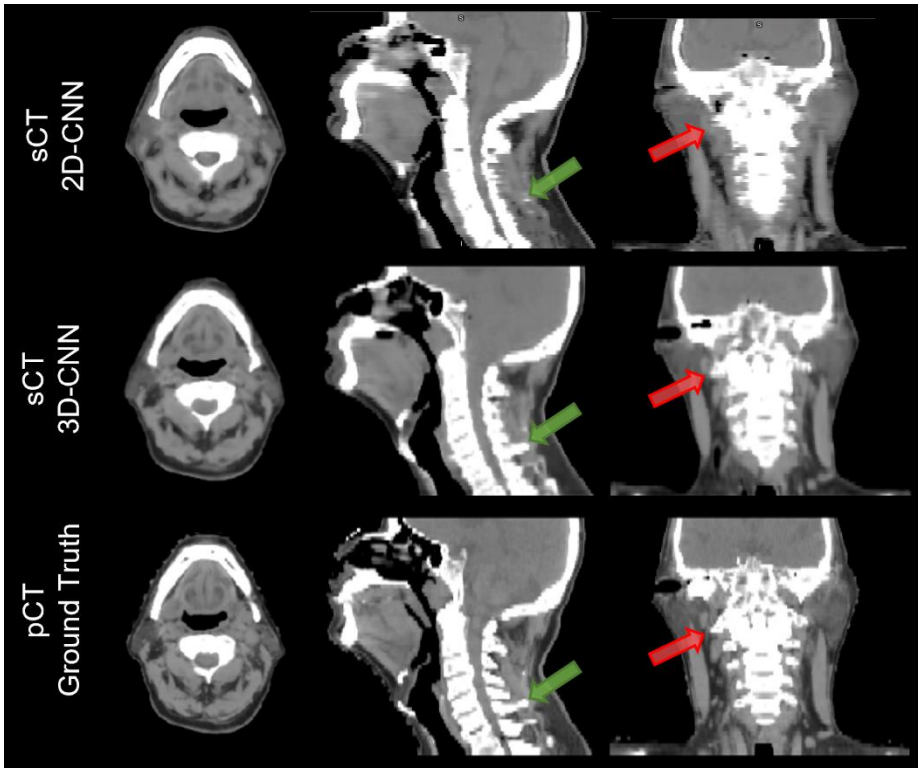

Figure 1: Qualitative comparison of sCTs derived from 2D-versus 3D-CNN.

10.3 Appendix 3

10.3.1 EPSM 2018 Accepted Abstract

MRI-Only Treatment Planning for Lung Cancer Using a Single MRI Sequence

T Young

Liverpool and Macarthur Cancer Therapy Centres and Ingham Institute, Sydney, Australia.

Institute of Medical Physics, School of Physics, University of Sydney, Sydney, Australia

Tony.Young@health.nsw.gov.au (Presenting author)

J Dowling

CSIRO Health and Biosecurity, The Australian e-Health & Research Centre, Australia

South Western Sydney Clinical School, University of New South Wales, Australia

Institute of Medical Physics, University of Sydney, Australia

School of Mathematical and Physical Sciences, University of Newcastle, Australia

Jason.Dowling@csiro.au

D Thwaites

Institute of Medical Physics, School of Physics, University of Sydney, Sydney, Australia.

david.thwaites@sydney.edu.au

S Kumar

Liverpool and Macarthur Cancer Therapy Centres and Ingham Institute, Sydney, Australia

University of New South Wales, Sydney, New South Wales, Australia

Shivani.Kumar@health.nsw.gov.au

R Rai

Liverpool and Macarthur Cancer Therapy Centres and Ingham Institute, Sydney, Australia.

University of New South Wales, Sydney, New South Wales, Australia

Robba.Rai@health.nsw.gov.au

S Vinod

Liverpool and Macarthur Cancer Therapy Centres, Sydney, Australia

University of New South Wales, Sydney, New South Wales, Australia

Shalini.Vinod@health.nsw.gov.au

G Liney

Liverpool and Macarthur Cancer Therapy Centres and Ingham Institute, Sydney, Australia

University of New South Wales, Sydney, New South Wales, Australia

Centre for Medical Radiation Physics, University of Wollongong, Wollongong,

New South Wales, Australia

Gary.Liney@health.nsw.gov.au

A Stemmer

Siemens Healthcare, Erlangen, Germany

alto.stemmer@siemens-healthineers.com

S Josan

Siemens Healthcare, Erlangen, Germany

sonal.josan@siemens-healthineers.com

L Holloway

Liverpool and Macarthur Cancer Therapy Centres and Ingham Institute, Sydney, Australia.

University of New South Wales, Sydney, New South Wales, Australia

Institute of Medical Physics, School of Physics, University of Sydney, Australia.

Centre for Medical Radiation Physics, University of Wollongong, Wollongong,

New South Wales, Australia

lois.holloway@health.nsw.gov.au

Introduction

The need for an MRI-only workflow which provides electron density information for hybrid Magnetic Resonance Imaging guided Linear Accelerators (MRIg-linacs) in radiotherapy has increased. Investigations into segmented bulk density corrections to tissue, bone and lung have reported results for point dose calculations in lung within 2% [1]. However, a more recent study investigating the effect on dose volume parameters concluded that this approach may not be appropriate for lung MRI only planning [2]. Other correction methods including atlas and voxel based methods have been used in sites such as brain and prostate for MRI only treatment planning with success [3]. In this study the accuracy of an atlas based auto segmentation method to generate substitute CT (sCT) for lung patients from a single MRI sequence was investigated.

Method

Simulation CT and MRI scans were completed on 11 lung cancer patients. 3D ultrashort-echo-time (UTE) images were acquired on a Siemens MAGNETOM Skyra 3T MRI under free breathing using a prototype spoiled gradient echo sequence utilizing a variable TE stack-of-spirals trajectory (SpiralVIBE) [5, 6]. The SpiralVIBE MRI scans were converted to sCT using an existing methodology validated for the male pelvis [4]. All generated sCT were compared against the original CT dataset for Hounsfeld Unit (HU) differences, and 10 sCT datasets were evaluated for dosimetric differences against the clinical treatment plan.

Results

The mean error for the 11 generated sCT datasets was 17.2HU (SD 71.3HU), and the mean absolute error was 162HU (SD 66.7HU). For dose calculations, 9/10 datasets met a 3% point dose tolerance.

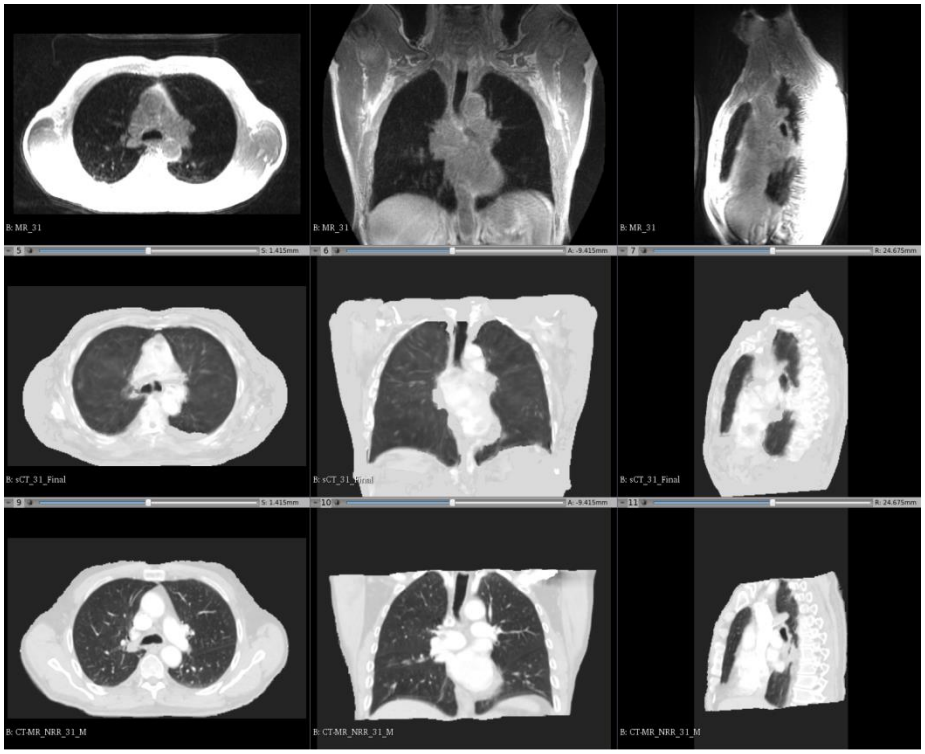

Figure 1 – An example of a patient MRI (top), clinical CT scan (bottom) and generated sCT (middle)

Conclusion

Lung MRI datasets were converted to sCTs for treatment planning with reasonable agreement with the original CT datasets, and treatment plans.

References/ Acknowledgements as applicable

1. Jonsson J, Karlsson M, Karlsson M, Nyholm T (2010) Treatment planning using MRI data: an analysis of the dose calculation accuracy for different treatment regions. Radiation Oncology 5 (1):62

2. Phil P, Xinfeng C, Elizabeth G, Candice J, Allen LX (2017) Technical Note: Is bulk electron density assignment appropriate for MRI-only based treatment planning for lung cancer? Medical Physics 44 (7):3437-3443. doi:doi:10.1002/mp.12267

3. Johnstone E, Wyatt JJ, Henry AM, Short SC, Sebag-Montefiore D, Murray L, Kelly CG, McCallum HM, Speight R (2018) Systematic Review of Synthetic Computed Tomography Generation Methodologies for Use in Magnetic Resonance Imaging–Only Radiation Therapy. International Journal of Radiation Oncology• Biology• Physics 100 (1):199-217

4. Dowling JA, Sun J, Pichler P, Rivest-Hénault D, Ghose S, Richardson H, Wratten C, Martin J, Arm J, Best L (2015) Automatic substitute computed tomography generation and contouring for magnetic resonance imaging (MRI)-Alone external beam radiation therapy from standard MRI sequences. International Journal of Radiation Oncology* Biology* Physics 93 (5):1144-1153

5. John P. Mugler, III, Samuel W. Fielden, Craig H. Meyer, Talissa A. Altes, G. Wilson Miller, Alto Stemmer, Josef Pfeuffer, and Berthold Kiefer. Breath-hold UTE Lung Imaging using a Stack-of-Spirals Acquisition. Proc. Intl. Soc. Mag. Reson. Med. 23 (2015) #1476.

6. Samuel Fielden , John Mugler , Wilson Miller , Alto Stemmer , Josef Pfeuffer , Berthold Kiefer , and Craig Meyer. A Variable-TE Stack-of-Spirals Sequence for 3D UTE Imaging. Proc. Intl. Soc. Mag. Reson. Med. 24 (2016) #1062

10.4 Appendix 4

10.4.1 EPSM 2017 Accepted Abstract

The Effect of MRI Sequence Variations on Substitute CT Generation for MR-Only Planning

Tony Young

Liverpool and Macarthur Cancer Therapy Centres and Ingham Institute, Sydney, Australia.

Institute of Medical Physics, School of Physics, University of Sydney, Sydney, Australia

Tony.Young@sswahs.nsw.gov.au (Presenting author)

David Thwaites

Institute of Medical Physics, School of Physics, University of Sydney, Sydney, Australia.

david.thwaites@sydney.edu.au

Jason Dowling

CSIRO Health and Biosecurity, The Australian e-Health & Research Centre, Australia

South Western Sydney Clinical School, University of New South Wales, Australia

Institute of Medical Physics, University of Sydney, Australia

School of Mathematical and Physical Sciences, University of Newcastle, Australia

Jason.Dowling@csiro.au

Gary Liney

Liverpool and Macarthur Cancer Therapy Centres and Ingham Institute, Sydney, Australia

University of New South Wales, Sydney, New South Wales, Australia

Centre for Medical Radiation Physics, University of Wollongong, Wollongong,

New South Wales, Australia

Robba Rai

Liverpool and Macarthur Cancer Therapy Centres and Ingham Institute, Sydney, Australia.

University of New South Wales, Sydney, New South Wales, Australia

Peter Greer

Calvary Mater Newcastle Hospital, Newcastle, New South Wales, Australia

School of Mathematical and Physical Sciences, University of Newcastle, Australia

Lois Holloway

Liverpool and Macarthur Cancer Therapy Centres and Ingham Institute, Sydney, Australia.

University of New South Wales, Sydney, New South Wales, Australia

Institute of Medical Physics, School of Physics, University of Sydney, Australia.

Centre for Medical Radiation Physics, University of Wollongong, Wollongong,

New South Wales, Australia

lois.holloway@sswahs.nsw.gov.au

Introduction

The current gold standard imaging for radiotherapy simulation and treatment planning is computed tomography (CT) due to spatial accuracy, bony anatomy definition and electron density information for dose calculations. MRI provides improved visualisation of soft tissue anatomy for accurate target definition and contouring, via fusion of the MRI with CT scans. This introduces registration error and potential errors from variations in patient setup and internal organ motion [1].

MRI only treatment planning would remove registration errors, reduce patient discomfort, workload and cost of additional scans [2,3]. MRI however lacks electron density information required for dose calculations. This may be overcome by applying manually segmented bulk density corrections for tissue, bone, and air, with results reported to be within 2% [2,4]. Other methods include atlas based electron density mapping to automatically segment and apply the appropriate bulk density correction [5]. In this study the robustness of an atlas based auto segmentation method to generate substitute CT (sCT) from a range of MRI sequences was investigated.

Method

A volunteer was scanned on a Siemens Skyra 3T MRI. Sequences included a 3D T2-weighted (T2-w) SPACE used for sCT conversion as published [5], along with variations in bandwidth (781Hz vs 200Hz) and repetition time TR (1200, 1310, 1700 ms). Additionally, a fast 2D T2-w turbo spin echo with large slice thickness as published for potential use with the future MR-Linac [6] was tested to further evaluate the robustness of the sCT generation. These image datasets were converted to sCT and evaluated for changes in contour and dosimetric differences for a standard VMAT plan.

Results

Small volume variations within 5% were observed in autocontoured bony anatomy for all sCT datasets. Dosimetrically, all plans agreed within previously published uncertainties.

Conclusion

The sCT method investigated was robust and insensitive to changes in MRI sequence parameters for comparable slice thickness and voxel size.

References/ Acknowledgements

1. Nyholm T, Jonsson J (2014) Counterpoint: Opportunities and Challenges of a Magnetic Resonance Imaging–Only Radiotherapy Work Flow. Seminars in Radiation Oncology 24 (3):175-180. doi:http://dx.doi.org/10.1016/j.semradonc.2014.02.005

2. Karlsson M, Karlsson MG, Nyholm T, Amies C, Zackrisson B (2009) Dedicated Magnetic Resonance Imaging in the Radiotherapy Clinic. International Journal of Radiation Oncology*Biology*Physics 74 (2):644-651. doi:http://dx.doi.org/10.1016/j.ijrobp.2009.01.065

3. Roberson PL, McLaughlin PW, Narayana V, Troyer S, Hixson GV, Kessler ML (2005) Use and uncertainties of mutual information for computed tomography/magnetic resonance (CT/MR) registration post permanent implant of the prostate. Medical Physics 32 (2):473-482. doi:doi:http://dx.doi.org/10.1118/1.1851920

4. Lambert J, Greer PB, Menk F, Patterson J, Parker J, Dahl K, Gupta S, Capp A, Wratten C, Tang C, Kumar M, Dowling J, Hauville S, Hughes C, Fisher K, Lau P, Denham JW, Salvado O (2011) MRI-guided prostate radiation therapy planning: Investigation of dosimetric accuracy of MRI-based dose

planning. Radiotherapy and Oncology 98 (3):330-334. doi:http://dx.doi.org/10.1016/j.radonc.2011.01.012

5. Dowling JA, Sun J, Pichler P, Rivest-Hénault D, Ghose S, Richardson H, Wratten C, Martin J, Arm J, Best L, Chandra SS, Fripp J, Menk FW, Greer PB (2015) Automatic substitute CT generation and contouring for MRI-alone external beam radiation therapy from standard MRI sequences. International Journal of Radiation Oncology • Biology • Physics. doi:10.1016/j.ijrobp.2015.08.045

6. Whelan B, Liney GP, Dowling JA, Rai R, Holloway L, McGarvie L, Feain I, Barton M, Berry M, Wilkins R, Keall P (2017) An MRI-compatible patient rotation system — design, construction, and first organ deformation results. Medical Physics 44 (2):581-588. doi:10.1002/mp.12065

10.4.2 EPSM 2020 Accepted Abstract

Can we reduce imaging time and still generate acceptable Substitute CT for Prostate MRI Only Treatment Planning?

Tony Young

Liverpool and Macarthur Cancer Therapy Centres and Ingham Institute, Sydney, Australia.

Institute of Medical Physics, School of Physics, University of Sydney, Sydney, Australia

Tony.Young@health.nsw.gov.au (Presenting author)

Jason Dowling

CSIRO Health and Biosecurity, The Australian e-Health & Research Centre, Australia

South Western Sydney Clinical School, University of New South Wales, Australia

Institute of Medical Physics, University of Sydney, Australia

School of Mathematical and Physical Sciences, University of Newcastle, Australia

Jason.Dowling@csiro.au

Robba Rai

Liverpool and Macarthur Cancer Therapy Centres and Ingham Institute, Sydney, Australia.

University of New South Wales, Sydney, New South Wales, Australia

Gary Liney

Liverpool and Macarthur Cancer Therapy Centres and Ingham Institute, Sydney, Australia

University of New South Wales, Sydney, New South Wales, Australia

Centre for Medical Radiation Physics, University of Wollongong, Wollongong,

New South Wales, Australia

Peter Greer

Calvary Mater Newcastle Hospital, Newcastle, New South Wales, Australia

School of Mathematical and Physical Sciences, University of Newcastle, Australia

David Thwaites

Institute of Medical Physics, School of Physics, University of Sydney, Sydney, Australia.

david.thwaites@sydney.edu.au

Lois Holloway

Liverpool and Macarthur Cancer Therapy Centres and Ingham Institute, Sydney, Australia.

University of New South Wales, Sydney, New South Wales, Australia

Institute of Medical Physics, School of Physics, University of Sydney, Australia.

Centre for Medical Radiation Physics, University of Wollongong, Wollongong,

New South Wales, Australia

lois.holloway@health.nsw.gov.au

Introduction

The introduction of MRI linear accelerators (MR-linacs) requires improved approaches to MRI-only radiotherapy. MRI provides excellent soft tissue visualisation for target and organ definition, but no electron density information for dose calculation, obtained instead from registering CT images[1]. MRI-only radiotherapy would remove registration errors and reduce patient discomfort, workload and cost [2, 3]. Electron density requirements may be addressed in different ways, from manually applying bulk density corrections [2, 4], to more computationally intensive methods, such as atlas based techniques [5] which automatically segment and apply bulk density corrections to produce substitute CT datasets (sCT). Reducing MRI imaging time would reduce potential artefacts from intrafraction motion and patient discomfort. This study investigated the effects of MRI imaging time reduction on sCT generation for prostate MRI-only treatment planning.

Method

10 volunteers were scanned on a Siemens Skyra 3T MRI. Sequences included the 3D T2-weighted (T2-w) SPACE used for sCT conversion as previously validated against CT [5], along with variations to this sequence in repetition time (TR), turbo factor, and combination of these to reduce the imaging time. Additionally, a T1 DIXON scan was taken to test the robustness of the sCT technique. All scans were converted to sCT and evaluated for anatomical changes and dosimetric differences for a standard VMAT plan compared to the previously validated SPACE sequence.

Results

Compared to the previously validated T2-w SPACE sequence [5], scan times were reduced by up to 80%. The external volume and bony anatomy were compared, with most meeting a DICE coefficient of 0.9 or better, with the largest variations occurring at the edges of the external body volume. Dosimetrically, most plans agreed within 2% at isocentre.

Conclusion

This study demonstrates that MRI sequence imaging times can be reduced significantly with clinically acceptable sCT accuracy for dose calculation.

References/ Acknowledgements as applicable

[1] Nyholm T, Jonsson J. Counterpoint: Opportunities and Challenges of a Magnetic Resonance Imaging–Only Radiotherapy Work Flow. Seminars in Radiation Oncology. 2014;24:175-80.

[2] Karlsson M, Karlsson MG, Nyholm T, Amies C, Zackrisson B. Dedicated Magnetic Resonance Imaging in the Radiotherapy Clinic. International Journal of Radiation Oncology*Biology*Physics. 2009;74:644-51.

[3] Roberson PL, McLaughlin PW, Narayana V, Troyer S, Hixson GV, Kessler ML. Use and uncertainties of mutual information for computed tomography/magnetic resonance (CT/MR) registration post permanent implant of the prostate. Medical Physics. 2005;32:473-82.

[4] Lambert J, Greer PB, Menk F, Patterson J, Parker J, Dahl K, et al. MRI-guided prostate radiation therapy planning: Investigation of dosimetric accuracy of MRI-based dose planning. Radiotherapy and Oncology. 2011;98:330-4.

[5] Dowling JA, Sun J, Pichler P, Rivest-Hénault D, Ghose S, Richardson H, et al. Automatic substitute computed tomography generation and contouring for magnetic resonance imaging (MRI)-Alone

external beam radiation therapy from standard MRI sequences. International Journal of Radiation Oncology* Biology* Physics. 2015;93:1144-53.

10.5 Appendix 5

10.5.1 EPSM 2022 Accepted Abstract

Dose Variation in Pancreas SBRT – A planning study based on daily MR imaging

Tony Young

Liverpool and Macarthur Cancer Therapy Centres, Sydney, Australia.

Ingham Institute, Sydney, Australia

Institute of Medical Physics, School of Physics, University of Sydney, Sydney, Australia

Tony.Young@health.nsw.gov.au (Presenting author)

Mark Lee

Liverpool and Macarthur Cancer Therapy Centres, Sydney, Australia.

Meredith Johnston

Liverpool and Macarthur Cancer Therapy Centres, Sydney, Australia.

Theresa Nguyen

Liverpool and Macarthur Cancer Therapy Centres, Sydney, Australia.

Rebecca Ko

Liverpool and Macarthur Cancer Therapy Centres, Sydney, Australia.

Sankar Aramugam

Liverpool and Macarthur Cancer Therapy Centres and Ingham Institute, Sydney, Australia.

Ingham Institute, Sydney, Australia

Institute of Medical Physics, School of Physics, University of Sydney, Sydney, Australia

University of New South Wales, Sydney, New South Wales, Australia

Introduction

Pancreatic Cancer is associated with significant morbidity and mortality, with the treatment outcomes remaining poor compared to other cancers. Even in patients with resectable disease, the 5 year overall survival is less than 25% [1]. The use of SBRT (1-5 fractions) to treat pancreatic cancer has improved survival [2]. The aim of this study was to investigate dosimetric variations that occur over a simulated SBRT course for pancreatic cancer using daily MR images.

Method

Five healthy volunteers were scanned on a Siemens Skyra 3T MRI over two sessions, approximately 3hrs apart, per day over 5 days to simulate an SBRT daily simulation scan for treatment planning, and a pretreatment scan for patient setup and treatment. A 4D MRI scan was taken at each session for ITV generation and assessment. For each volunteer a treatment plan was generated in the Raystation TPS following departmental protocols on the day one, first session dataset, with bulk density overrides applied to enable dose calculation. This treatment plan was propagated through other imaging sessions, and the calculated dose, as well as the deformed dose for the second session of each day was accumulated as per treatment. These accumulated mock treatment doses were assessed against the original treatment plan through DVH comparison of the PTV and OAR volumes.

Results

The generated ITV varied on average 18.4% (1.6% - 43.2%) between imaging sessions compared to the first session ITV. The PTV D95 varied from -53.8% to -2.7% for the rigid accumulated dose and -32.7% to +0.1% considering the deformed dose. Surrounding OARs had large variations in delivered dose, with the duodenum D0.5cc differences ranging from +3.5% to +17.1% for the rigid accumulated dose and +0.6% to +10.5% considering the deformed dose.

Conclusion

Pancreas SBRT would benefit from daily adaptive planning to account for changes in anatomy.

References/ Acknowledgements

[1] Mahadevan A, Moningi S, Grimm J, Li XA, Forster KM, Palta M, et al. Maximizing Tumor Control and Limiting Complications With Stereotactic Body Radiation Therapy for Pancreatic Cancer. International Journal of Radiation Oncology* Biology* Physics. 2021;110:206-16.

[2] de Geus SW, Eskander MF, Kasumova GG, Ng SC, Kent TS, Mancias JD, et al. Stereotactic body radiotherapy for unresected pancreatic cancer: A nationwide review. Cancer. 2017;123:4158-67.